SYNTHESIS AND CHARACTERIZATION OF NICKEL OXIDE BASED HETRO NANOSTRUCTURES FOR ENERGY STORAGE

Thesis Submitted for the Award of the Degree of

DOCTOR OF PHILOSOPHY

in

Physics

By

Sandeep

Registration Number: 11919641

Supervised By

Dr. Kawaljeet Singh (16468)
Department of Physics (Professor)
Lovely Professional University

LOVELY PROFESSIONAL UNIVERSITY, PUNJAB

2024

DECLARATION

I, hereby declared that the presented work in the thesis entitled "**Synthesis and Characterization of Nickel Oxide based Hetro- nanostructures for Energy Storage**" in fulfilment of degree of **Doctor of Philosophy (Ph. D.)** is outcome of research work carried out by me under the supervision of Dr. Kawaljeet Singh Samra, working as Professor in Department of Physics at School of Chemical Engineering and Physical Science, Lovely Professional University, Punjab, India. In keeping with general practice of reporting scientific observations, due acknowledgements have been made whenever work described here has been based on findings of another investigator. This work has not been submitted in part or full to any other University or Institute for the award of any degree.

(Signature of Scholar)
Name of the scholar: Sandeep
Registration No.: 11919641
Department/school: Chemical Engineering and Physical Science
Lovely Professional University,
Punjab, India

CERTIFICATE

This is to certify that the work reported in the Ph. D. thesis entitled "**Synthesis and Characterization of Nickel Oxide based Hetro- nanostructures for Energy Storage**" submitted in fulfillment of the requirement for the award of degree of **Doctor of Philosophy (Ph.D.)** in the Physics, Lovely Professional University, Phagwara (Punjab) India, is a research work carried out by Sandeep (11919641), is bonafide record of his/her original work carried out under my supervision and that no part of thesis has been submitted for any other degree, diploma or equivalent course.

(Signature of Supervisor)
Name of supervisor: Dr. Kawaljeet Singh Samra
Designation: Professor
Department/school: Department of Physics
University: Lovely Professional University
Punjab, India

ABSTRACT

Chapter 1 explores the potential of supercapacitors (SCs) as an advanced energy storage (ES) solution, highlighting their superior performance compared to traditional storage systems. SC devices are characterized by high power density (P_D), and extended cycle life, rendering them particularly suitable for applications, portable electronics, and electric vehicles. The chapter reviews the fundamental components of SCs, including their classification and the associated development challenges. Study about different electrode materials including, carbon-based materials, conducting polymers (CPs), and transition metal oxides (TMOs). Among of these, TMOs are frequently utilized in SCs due to their high theoretical capacitance and acceptable conductivity. In TMOs nickel oxide (NiO) is identified as a standout candidate for SC electrodes due to its ecofriendly nature, and cost-effectiveness. The discussion covers the contributions of these materials to enhancing SC performance, while also addressing ongoing challenges and outlining future perspectives for the optimization of SC technologies.

Chapter 2 examines the role of NiO in SCs, emphasizing its high theoretical capacity, environmental sustainability, and cost-effectiveness. It reviews recent advancements in NiO-based materials, focusing on their morphology, composite structures, and performance enhancements relevant to SC applications. The chapter discusses the controlled fabrication of NiO in various morphologies—zero-, one-, two-, and three-dimensional—and their unique electrochemical properties that benefit SCs. It also explores the development of NiO-based composites, including those doped with transition metals, NiO/metal oxide (MO) composites, NiO/carbon nanomaterials, NiO/CPs, and NiO/metal sulfides, highlighting their influence on charge storage capacity and cycle stability. Furthermore, the chapter identifies current research gaps, such as the challenges of achieving consistent material properties and scaling advanced composites. Future research objectives are outlined, focusing on optimizing NiO's morphology and composite structures to enhance energy density (E_D) and cycling performance. This comprehensive analysis provides essential insights into material design strategies aimed at improving the performance of NiO-based SCs.

Chapter 3 provides an in-depth examination of the materials, synthesis methods, and characterization techniques essential for advancing SC technology. A comprehensive list of chemicals used in the study is included, ensuring reproducibility. The synthesis of materials is carried out using three main techniques: hydrothermal, sol-gel, and microwave

methods. Each technique is discussed in detail, highlighting its role in the preparation of advanced materials for ES applications and offering a versatile framework for optimizing material properties tailored to specific SC applications. The characterization techniques employed to analyze electrode materials. Various methodologies are explored, including XRD for phase identification and crystallinity assessment, Raman spectroscopy for molecular vibrational analysis, and FESEM for morphological studies. EDS is utilized for elemental composition analysis, while XPS provides insights into the electronic state of elements on the electrode surface. The application of Brunauer-Emmett-Teller (BET) theory for SA measurements, along with High-Resolution Transmission Electron Microscopy (HRTEM) for structural evaluation, are also discussed. Electrochemical techniques, including cyclic voltammetry (CV), galvanostatic charge–discharge (GCD), and electrochemical impedance spectroscopy (EIS), are highlighted to assess the performance characteristics of the materials. The integration of these methods offers a holistic understanding of the properties and behaviors of electrode materials, facilitating advancements in SC technology.

Chapter 4 investigates the change in electrochemical performance and morphology of NiO by changing the reaction temperature and urea concentration. At 110°C temperatures through hydrothermal method with a 1:2 ratio of nickel nitrate hexahydrate to urea in the growth solution achieved nanosheets. Additional, same repeat and grown on nickel foam achieved highly porous microspheres NiO morphology. At 1 A/g, the porous microspheres NiO electrode was exhibited specific capacity of 418 C/g (1045 F/g). After one thousand cycles, this electrode demonstrated remarkable retention rate of 87.5% at 14 A/g. Furthermore, E_D of 22.5 Wh/kg was achieving by assembled asymmetric supercapcitor (ASC) at P_D OF 0.9 kW/kg.

Chapter 5 presents the synthesis of MoS_2@NiO heterostructures via a simple hydrothermal method, aimed at enhancing electrochemical performance as electrode materials. The effect of varying MoS_2 concentrations within the composite is systematically explored to optimize performance. The most optimized MoS_2@NiO heterostructure-based electrode demonstrates an impressive specific capacity of 419.5 C/g (1048.75 F/g) at 1 A/g, outperforming MoS_2 and NiO-based electrodes by 60% and 45%, respectively. The investigation reveals that Faradic or diffusion processes predominantly govern the charge storage mechanisms. Leveraging the synergistic interactions between MoS_2 and NiO, the ASC configuration, MoS_2@NiO//graphite-activated carbon (GAC), achieves a notable E_D of 47.43 Wh/kg at a P_D of 0.825 kW/kg. Furthermore, developed device maintains approximately 80% of its Cs and around 85% Coulombic efficiency after 5000 cycles at 2 A/g, demonstrating robust cyclic stability.

Chapter 6 presents the synthesis of CoS_2@NiO heterostructures via a simple hydrothermal method, aimed at enhancing electrochemical performance as electrode materials. By exploiting the synergistic effects of CoS_2's superior electrical conductivity and NiO's exceptional electrochemical stability. The optimized CoS_2@NiO electrode exhibits specific capacity of 475 C/g (1187.5 F/g), significantly surpassing conventional NiO and CoS_2 electrodes by approximately 46% and 42%, respectively. At P_D of 0.825 kW/kg, the assembly of ASC device (CoS_2@NiO//GMC) was demonstrating E_D of 50.18 Wh/kg. After 5000 cycles, the device further demonstrates excellent durability, retention rate of 82%. This study emphasizes the effectiveness of compositional tuning and heterostructure formation in enhancing electrochemical performance, paving the way for advancements in high-performance SC applications.

Chapter 7 presents the synthesis of CuS@NiO heterostructures via a simple hydrothermal method, aimed at enhancing electrochemical performance as electrode materials. CuS NPs and NiO nanosheets are synthesized using hydrothermal and annealing methods, respectively, and subsequently combined to form the composite. Characterization techniques, including XRD, XPS, FESEM, BET analysis, CV, GCD and EIS confirm the successful formation of the CuS@NiO composite and highlight its enhanced structural and electrochemical properties. At 1 A/g, the composite electrodes exhibit a specific capacity of 392 C/g (980 F/g), and excellent retention rate of 80.08% after five thousand cycles. CV and GCD tests demonstrate that the CuS@NiO composite offers a higher charge storage capacity and E_D compared to individual CuS and NiO electrodes. EIS results indicate a lower intrinsic resistance of 0.4 ohms and higher ionic conductivity of 0.56×10^{-4} S/cm for the composite. At P_D of 0.825 kW/kg ,assembled ASC device (CuS@NiO//EGA) was demonstrate E_D of 44 Wh/kg and maintains a Coulombic efficiency of 77.62% after five thousand cycles. This study highlights how compositional tuning and heterostructure formation can significantly improve electrochemical performance, marking a step forward in advancing high-performance SC applications.

ACKNOWLEDGEMENT

I am deeply grateful to God for blessing me with the gift of learning and the curiosity to explore further. I hope that this work serves as a guiding light for myself, and everyone connected to me, now and in the future.

I would like to express my sincere gratitude to my research supervisor, Dr. Kawaljeet Singh, for his constant support and invaluable guidance throughout this journey. His insightful feedback and suggestions have greatly enhanced the quality of this work.

I owe a profound debt of gratitude to my mother, Smt. Krishna, whose unwavering love and selfless sacrifices have been the foundation of my achievements, both in academia and beyond. I am equally thankful to my father, Sh. Satparkash, whose steadfast support has carried me through the challenges of my PhD journey.

A special thanks to my wife, Kalpana, for her continuous encouragement and support throughout this process. I am also immensely thankful to my colleagues Ajay Nain, Rohit Malik, Kapil Yadav, Pawan Bhaker, Seema Sharma, and Shakra Jabeen, who have supported me in every possible way.

I extend my heartfelt appreciation to my senior, Prashant Kumar, for his exceptional support and guidance over the years; this work would not have been possible without him.I am also grateful to the faculty and staff of the Department of Physics at Lovely Professional University for their encouragement. A special note of thanks goes to Dr. Kailash Juglan (HOS) for his genuine support and motivation.

Table of contents

List of Tables

List of Figures

LIST OF ACRONYMS AND ABBREVIATIONS

Acronym and Abbreviations	Description
0D	Zero-dimensional
1D	One dimensional
2D	Two dimensional
3D	Three dimensional
BET	Brunauer-Emmett-Teller
CNT	Carbon nanotube
CPE	Constant phase element
CV	Cyclic voltammetry
Cs	Specific Capacitance
CE	Counter electrode
CTAB	Cetyltrimethylammonium bromide
CP	conducting polymer (CP)
EDLC	Electric double-layer capacitor
EIS	Electrochemical impedance spectroscopy
EDS	Energy-dispersive X-ray spectroscopy
Eq.	Equation
ES	Energy Storage
EL	Electrolyte
E_D	Energy density
eg.	for example,
FESEM	Field emission scanning electron microscopy
Fig.	Figure
GCD	Galvanostatic charge-discharge

GO	Graphene oxide
HRTEM	High-resolution transmission electron microscopy
MWCNT	Multiwalled carbon nanotube
JCPDS	Joint Committee on Powder Diffraction Standards
Ltd.	Limited
MOs	Metal Oxides
MWCNT	Multiwall carbon nanotube
NP	Nanoparticle
NMP	n-methyl-2-pyrrolidone
PANI	Polyaniline
Ppy	Polypyrrole
PTFE	Polytetrafluoroethylene
P_D	Power density
PVDF	Polyvinylidene fluoride
PC	Pseudo capacitor
RE	Reference electrode
SEM	Scanning electron microscopy
SAED	Selected area electron diffraction
SC	Supercapacitor
SA	Surface Area
SSA	Specific Surface Area
TMOs	Transition metal oxides
TEM	Transmission electron microscopy
v	Scan rate
WE	Working electrode
XRD	X-ray diffraction
XPS	X-ray photoelectron spectroscopy

LIST OF UNITS

Unit	Description
A	Ampere
cm	centimeter
cc	Cubic-centimeter
C	Coulomb
eV	electron-Volt
F	Farad
g	gram
h	hour
K	Kelvin
kg	kilo-gram
KHz	Kilo-Hertz
kW	kilo-Watt
MHz	Mega-Hertz
m	meter
µm	micro-meter
mA	milli-Ampere
mF	milli-Farad
mL	milli-liter
mV	milli-Volt
nm	nano-meter
Ω	ohm
s	second
S	Siemens
Wh	Watt-hour
W	Watt

Chapter 1
Introduction

1.1 Needs of a Supercapacitor for Energy Storage

Fossil fuels have been the main source of energy source throughout the past century, but their extensive use has led to the depletion of natural resources and has contributed to numerous environmental issues that adversely affect human health [1-3]. However, it is possible to generate energy from renewable sources such as bioenergy, hydroelectric, and solar power [4,5]. Although renewable energy sources can generate substantial amounts of energy, they require localized storage solutions capable of managing large bursts of energy [6]. Without appropriate ES systems, harnessing power from these sources may not fully address the energy challenges. Currently, the storage of electrical energy is limited to devices such as, fuel cell, capacitors, and batteries, each of which has its own Pros and cons in terms of capacity, efficiency, and scalability [7]. Capacitor's store energy through electrostatic means, allowing for rapid charge and discharge cycles. While capacitors offer high power density (P_D) and excel in applications demanding quick bursts of power, their Energy density (E_D) is comparatively low, limiting their capacity for long-term ES. In contrast, Fuel cells convert chemical energy into electrical energy, making them well-suited for applications requiring sustained energy output and high Ed. However, fuel cells generally exhibit lower P_D compared to other technologies [8]. Battery technology is frequently regarded as the most advanced and economically viable option for storing electrical energy [9]. However, the limited charging speed, bulky size, and relatively short lifespan of batteries pose significant barriers to their widespread adoption. Additionally, the presence of hazardous and highly toxic chemicals in many battery types presents serious environmental risks, necessitating stringent handling and recycling procedures [10]. In recent years, lithium-ion (Li-ion) technology has gained popularity due to its high E_D and reduced toxicity. Despite its widespread use in ES applications, the relatively low P_D of Li-ion technology remains a significant limitation, hindering its broader deployment [11]. Therefore, advancing ES technologies is essential for fully harnessing the potential of renewable energy and maintaining a stable, reliable power supply.

A new category of devices known as SCs has emerged, offering high P_D without relying on vigorous chemical reactions [8]. Unlike batteries, these devices are lightweight, non-toxic, and do not require bulky electrodes, thereby eliminating complex disposal challenges. This makes

SCs a promising alternative for applications that demand both high power output and environmental sustainability [12]. SCs exhibit a capacitance that is over 10^6 times greater than that of conventional capacitors. They also surpass lithium-ion batteries and fuel cells in P_D while offering higher E_D compared to traditional capacitors. Consequently, it is crucial to invest substantial effort into the development and integration of SC technology within ES systems. SCs provide substantial advantages over traditional physical capacitors and batteries, including cost-effectiveness, extended cyclic lifespan, rapid charge-discharge capabilities, and high- P_D [13,14].

SC devices offer several advantages compared to other ES systems, making them favorable for ES applications. These advantages are discussed below.

- *High* Power density*:* Electrochemical SCs exhibit substantially greater P_D compared to lithium-ion batteries. This enhancement arises from the SCs' method of charge storage, which occurs at both the surface and within the bulk of the electrodes. SCs can achieve significantly faster charge and discharge rates, translating into higher P_D in ES systems [15,16].
- *Extended Life Expectancy*: The long-life cycle of SCs is largely due to their electrostatic ES mechanism, which minimizes wear compared to chemical batteries. Their use of durable materials, low internal resistance, and high charge/discharge efficiency also contributes to their longevity [17-20].
- *Long Shelf Life:* SCs offer a significant advantage in terms of shelf life. Unlike rechargeable batteries, which lose functionality over time due to self-discharge during extended periods of inactivity, SCs can retain their capacitance and be recharged to their original state. Although prolonged self-discharge may result in some voltage reduction, SCs can remain unused for several years while retaining their initial performance characteristics [21].
- *High Efficiency:* SCs exhibit high efficiency due to their reversible charge and discharge properties, which are consistent across the entire voltage range of operation. They experience minimal energy loss as heat during these processes, simplifying heat management and resulting in a cycle efficiency of approximately 95% [22].
- *Environmental Friendliness:* SCs are devoid of harmful or toxic substances, and their waste materials can be disposed of with ease. This environmental advantage highlights their sustainability compared to other ES systems.

- *Broad Temperature Range:* SCs can operate efficiently across a broad temperature range of -40 to 70 °C. This extensive operational temperature range provides a distinct advantage over batteries, especially in applications requiring reliable performance in diverse temperature conditions, such as military operations [23,24].
- *Safety:* Under standard operating conditions, SCs are considerably safer than batteries, due to the absence of harmful chemicals in their construction [25,26].

SC devices have gained significant traction across various fields due to their numerous advantages. They have emerged as the favored option for various application, mobile phones, including electric vehicles, hybrid electric vehicles, digital cameras, digital communication devices, electrical tools, pulse laser technologies, uninterruptible power supplies, and ES systems for solar cells. In digital cameras, SCs provide quick bursts of energy for high-power functions such as flash photography. In electrical tools, SCs are used to improve power delivery, efficiency, and durability. They provide quick bursts of energy for tasks that require high power, such as drilling and cutting. In Pulse laser SCs help stabilize the power supply, ensuring consistent pulse generation without fluctuations. They also enable faster recharge cycles between laser pulses, improving operational efficiency and reducing downtime in applications like precision cutting, medical procedures, and scientific research. In solar cell systems, SCs are used to store and release energy efficiently. They efficiently capture surplus energy produced by solar panels during peak sunlight and release it during times of reduced sunlight or increased demand. In electric vehicles, which require high P_D to meet peak load demands during acceleration or climbing, SCs offer a solution with their extended lifespan and superior P_D [20,27,28]. By integrating SCs with batteries, hybrid electric vehicles can achieve improved performance, such as enhanced acceleration, energy recovery during braking, better cold weather starting, and a prolonged battery lifespan. Looking ahead, SC manufacturers are likely to concentrate on sectors such as transportation, with particular emphasis on hybrid electric vehicles and metro trains [29,30].

1.2 Constituents of Supercapacitors

SCs share several similarities in their Constituents and design with batteries. The main constituents of a SC device include electrolyte (EL), current collector, binder, separators, and electrode material as illustrated in Fig. 1.1. The SC includes two electrodes, two current collectors, a separator, a binder, and an EL. Of these components, the electrode materials and the EL are regarded as the device's active elements, as the maximum E_D and overall performance of SCs largely depend on these two elements. The remaining three Constituents the current collector, binder, and separator are classified as passive parts. While these passive components play essential roles in the functionality of the device, their impact is relatively minor compared to the active components [31].

Electrolyte: Selecting an appropriate EL material is essential for the advancement of SCs. The E_D, internal resistance, and cyclic stability of SCs are contingent upon both the type and molar concentration of the EL. The EL's type also affects the operational temperature range and self-discharge behavior of the SC [32]. The ionic size and capacitance of the EL are closely related. A reduction in the size of EL ions can significantly enhance the SC’s overall efficiency. The EL's conductivity directly influences the SC’s E_D; increased ionic conductivity facilitates the movement of ions towards the electrode surface, thereby reducing resistance. Ionic conductivity is indicative of the quantity of charge carriers, their mobility, and their valency. Aqueous ELs generally exhibit higher conductivity than non-aqueous alternatives. Consequently, achieving high electrochemical performance often necessitates the use of aqueous, organic, or ionic liquid ELs [33-35]. Aqueous ELs possess a higher ion concentration compared to organic ELs, leading to lower resistance and consequently higher E_D in SCs. Additionally, aqueous ELs are easier to manufacture and use without stringent preparation

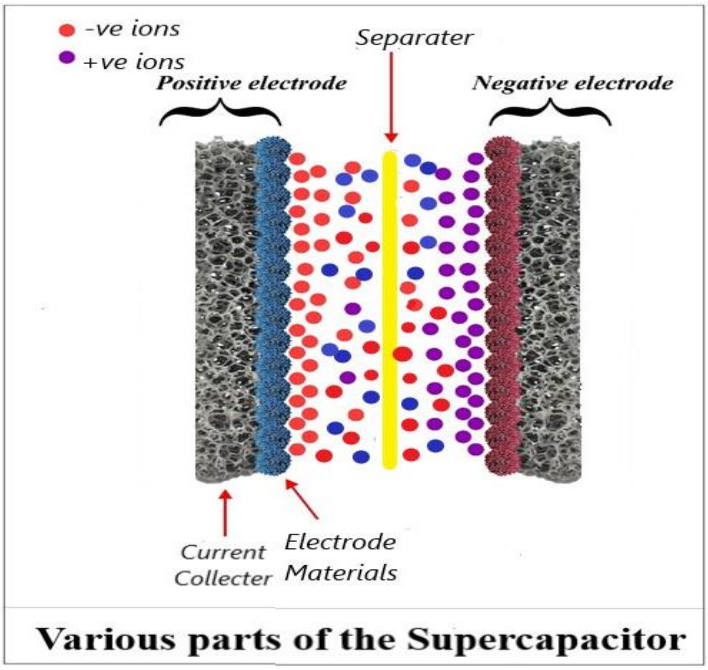

Fig. 1.1. Various parts of the SC

controls. However, their voltage range is more limited compared to organic ELs, which reduces their potential to improve E_D and P_D. Common examples of aqueous ELs include H_2SO_4, KOH, Na_2SO_4, and NH_4Cl [36,37]. Organic ELs offer a broader potential window (approximately 3.5 V) compared to aqueous ELs (approximately 1.2 V). The primary solvents used in organic ELs are acetonitrile and propylene carbonate. However, organic ELs have several disadvantages, including higher costs, lower specific capacitance (Cs), reduced conductivity, and safety concerns due to their flammability and volatility. Additionally, they require complex purification and assembly processes to eliminate contaminants that could otherwise impair performance and lead to significant self-discharge issues [38].

Ionic liquids, or molten salts, are formed when heat is applied to salt, counterbalancing the lattice energy, and causing the salt to become liquid. These ELs exhibit desirable properties exceptional thermal and chemical stability, minimal flammability, and conductivity of approximately 10 mS/cm. There is drawback of low conductivity at low temperature [39-41]. To address low conductivity issues at sub-room temperatures, ionic liquids can be mixed with organic solvents. This approach, however, introduces additional concerns such as safety hazards, toxicity, flammability, and limited temperature ranges [42-46].

Current Collector: For SC, the choice of current collector is primarily determined by the type of EL and electrode materials. In systems with strong acid-based ELs, corrosion-resistant metal foils, such as gold, are commonly used as current collectors. On the other hand, for SCs using alkaline ELs, nickel (Ni)-based current collectors are typically favored [47,48]. Nickel foam has gained popularity due to its higher surface area (SA) compared to nickel foil. This increased SA enhances of the active electrode material in alkaline EL based SCs [49]. The choice of current collector is crucial for optimizing the Cs of a SC. Incompatibility between current collectors and electrodes or ELs can result in a rise in resistance, which adversely affects the ES capability of the SC device.

Binders: The performance of SCs can be significantly influenced by the type of binder employed. Binders are used in conjunction with active electrode materials to facilitate adhesion between these materials and the current collector. Common examples of binders include polyvinylidene fluoride (PVDF), polytetrafluoroethylene (PTFE), Nafion, natural cellulose, polyvinylpyrrolidone (PVP), polyacrylic acid (PAA), and various conductive polymers such as polypyrrole (Ppy) and polyaniline (PANI). While binders are essential for ensuring stable adhesion and structural integrity, their use can also reduce the conductivity of the electrode. This increase in resistance can negatively impact the SC’s electrochemical performance by reducing conductivity and decreasing the effective active SA. Consequently, significant research efforts have been directed towards developing binder-free electrodes to enhance electrochemical activity and mitigate these adverse effects [50-54].

Separators: Separators in SCs do not contribute to the capacitive performance of the device. The separator is put between electrodes, which prevent direct physical contact and to facilitate the movement of ions between them. Various materials are employed in the construction of separators, including polypropylene, PVDF, PTFE, and cellulose polymer membranes. An effective separator is characterized by several key properties, including electrical insulation, ion transfer capability, high mechanical strength, and appropriate thickness and porosity. These attributes are essential for ensuring the proper operation and longevity of the SC [55, 56].

Electrode Materials: The materials selected for the electrodes considerably affect the performance of the SC. There are various types of electrode materials, including carbon-based materials, CPs, and MOs, among others [57- 60]. Electrode materials are active components of the SC device because the device performance directly depends on them [61,62].

1.3 Classification of Supercapcitor

SC can be classification on the based upon electrode materials and design.

1.3.1 Based upon electrode materials:

Based on electrode materials, SCs can be categorized into three main types: electrochemical double-layer capacitors (EDLCs), pseudocapacitors (PCs), and hybrid capacitors.

Electric Double-Layer Capacitor (EDLC): EDLC employs carbon-based materials such as carbon nanotubes (CNTs), carbon aerogel, activated carbon, carbon fiber cloth, and graphene for its electrodes. These carbon nanomaterials are distinguished by their high SSA, excellent chemical and mechanical stability, superior electrical conductivity, and cost-effectiveness. In EDLCs, charge storage occurs through a non-Faradaic mechanism, meaning that charge is accumulated electrostatically on the electrode surfaces [63-65]. The operating voltage range of EDLCs is primarily determined by the choice of EL, which is limited by the EL's stability. When an electric potential is applied, charge accumulates on the electrode surfaces as cations and anions from the EL diffuse through the separator to the electrodes with opposite charges. The E_D of EDLCs increases with larger SA and decreases as the distance between the electrodes increases. This lack of chemical change leads to minimal alterations in the volume or morphology of the electrode material, contributing to the EDLCs long cycle life [66,67].

Pseudocapacitor: Electrode materials commonly used in PCs include CPs and MOs. PCs primarily store charge through a Faradaic process, where charge transfer occurs between EL and electrode, involving in redox reactions. This mechanism allows PCs to achieve higher energy densities compared to EDLCs [68,69]. CPs are favored for their high capacitance, excellent electrical conductivity, low equivalent series resistance, and relatively low cost compared to the materials used in EDLCs. MOs, on the other hand, are noted for their high Cs and low series resistance, making them well-suited for commercial applications [70-73]. The enhanced ES capabilities of PCs result from these Faradaic processes, which provide a significant advantage over EDLCs in applications requiring higher E_D.

Hybrid Capacitor: A typical hybrid capacitor consists of one electrode similar to that in EDLCs, storing charge via a non-Faradaic process, and another electrode similar to that in PCs, storing charge via a Faradaic process. [74-76]. Hybrid capacitors were developed to leverage the advantages of both EDLCs and PCs, combining their strengths for improved performance. [77-79]. This combination results in a device that integrates the characteristics of both EDLCs and PCs, achieving higher E_D and P_D than either type alone. The hybrid capacitor's unique structure, which merges the high E_D of PCs with the high- P_D of EDLCs, mitigates the limitations inherent in each component. This integration leads to increased Cs and enhances electrochemical performance. [80].

1.3.2 Based upon designs

A SC can be designed in various ways depending on the materials used for its electrodes.

Symmetric SC device: In a symmetric SC, both the anode and cathode are constructed from the same material. This design approach ensures that both electrodes have identical properties, contributing to the overall performance of the SC [81]. Symmetric SCs typically have a lower operating voltage range compared to their asymmetric counterparts but offer advantages such as a longer cycle life and simpler construction [82].

Asymmetric Supercapacitors (ASC)device: An ASC device uses different materials for its anode and cathode electrodes. Unlike symmetric SCs, where both electrodes are made from the same material, an ASC combines materials with distinct properties for each electrode. One electrode might be constructed from high-capacitance materials like carbon, while the other could use materials with high E_D, such as MOs or conductive polymers. This varied approach optimizes both ES and power delivery, improving the device's overall performance and efficiency [83].

1.4 Issues concerning Supercapacitors: While SCs offer several advantages as discus above, they face specific challenges that hinder their ability to meet the demands of modern applications.

- *High Cost:* The commercialization of SC devices remains challenging due to the high costs associated with raw materials and manufacturing. A significant portion of this expense stems from the electrode materials, with carbon and ruthenium oxide being the most used in commercial SCs. Both materials are expensive, and the overall cost is further escalated by the separator and EL. Particularly, the use of organic ELs in electrochemical capacitors can substantially increase costs [84].

- *Low Energy density:* SCs generally exhibit lower E_D compared to batteries. Applications requiring substantial energy capacity necessitate the use of larger SCs, which further raises costs. Enhancing the E_D of SCs is therefore essential, necessitating extensive research and development efforts [18].
- *High Self-Discharge Rate:* SCs are characterized by a high self-discharge rate, with energy losses ranging from 10% to 40% per day. This significant rate of self-discharge presents a considerable barrier to their widespread adoption in certain real-world applications [27].

To meet the demands of modern applications, it is essential to overcome the challenges associated with SC devices. This requires focused research in the field of SCs, particularly on their components. As mentioned earlier, the electrode material is a critical active part of the device, and much of the device's performance depends on it. Therefore, selecting suitable electrode materials and working on their improvement is crucial for increasing the electrochemical performance of SC devices.

1.5 Electrode Materials for Supercapacitor

Electrode materials are the primary component of SC systems, and their electrochemical performance is central to the functionality of the device [85]. The electrode material is an important component of SC devices, profoundly affecting their electrochemical performance. To ensure optimal performance, the electrode material must have high SSA, which enhances Cs [86-88]. It has high electrical conductivity, which is essentials for efficient charge and discharge processes. For the high cyclic stability and longevity, materials have high thermal and chemical stability [89,90]. The different types of electrodes materials used in SC device such as carbon-Based electrode materials, CP, and metals oxides.

Carbon-based materials are extensively used as electrode materials for EDLCs, due to their properties, including chemical stability, substantial SA, and low processing and manufacturing costs. [57,58]. These materials store charge through a non-Faradaic process, making their capacitance performance highly dependent on their SA. Due to heteroatoms and functional groups, carbon materials contribute to a high SA, which enhances their electrochemical performance [91-95]. But the performance of carbon-based electrodes can be compromised by high series resistance, which arises from significant contact resistance between carbon atoms.

In contrast, pseudocapacitive materials exhibit Cs that is 10 to 100 times greater than that of EDLC materials due to their Faradaic charge storage processes [96]. This has led to substantial research interest in developing pseudocapacitive electrode materials for enhanced the ES capability of SC device. CPs are favorable choices for SC applications due to their low cost, high conductivity, variable redox activity, wide operational potential, and environmental friendliness [97-99]. Examples of CPs include polyaniline PANI, PPy, and polythiophene derivatives. [100-103]. Charge storage in CP-based electrodes involves both surface and bulk processes [104]. However, these materials often suffer from degradation, leading to a diminished Cs after approximately 1000 cycles [105-107,118].

The MOs as electrode materials in SCs has been shown to improve ES efficiency compared to traditional carbon materials. In PC applications, CPs often suffer from poor cycle stability. Consequently, TMOs are frequently utilized in PCs due to their high theoretical capacitance and acceptable conductivity [108]. Notable TMOs include Co_3O_4, MoO_3, MnO_2, V_2O_5, NiO, and $NiCo_2O_4$. [60] The performance of MO-based electrodes is influenced by factors such as SSA, crystallinity, and particle size. [109-113]. TMOs generally meet most of the criteria for highly efficient electrode materials. This discussion will focus primarily on the use of TMOs as electrode materials in SCs. Ruthenium oxide (RuO_2) is highly regarded for its high theoretical Cs, high electrical conductivity, and broad potential window. Despite these advantages, RuO_2 faces limitations due to high crystalline density and power constraints, which prevent it from achieving its theoretical capacitance value [114,115]. However, the commercialization of RuO_2-based SC devices is limited by high costs and environmental concerns associated with the material [116]. Cobalt oxides exhibit intercalative pseudocapacitance characteristics, making them promising candidates for SC electrodes. They are noted for their high theoretical capacitance, exceeding 2000 F/g, and have been extensively researched due to their high capacity, durability, and corrosion resistance [117-119]. However, Co_3O_4 has limitations in practical applications primarily due to its narrow potential window, which restricts its effectiveness in SC devices [120]. Iron, forms various oxides, including Fe_2O_3, Fe_3O_4, and FeO. Iron oxides are utilized in diverse applications beyond ES, such as photocatalysis and photoelectrochemical water splitting. Despite their relatively high conductivity compared to other TMOs, iron oxides do not exhibit high Cs, which limits their commercial use in SCs [121]. Manganese oxide (MnO_2) has emerged as an alternative to RuO_2, because MnO_2 have some advantage like cost-effectiveness, and environmental friendliness. MnO_2 possesses a high theoretical Cs and is more affordable and sustainable compared to RuO_2 [122-124]. Nonetheless, the conductivity of MnO_2 electrodes significantly impacts their capacitive performance and power characteristics [125]. Improving the capacitive characteristics of MnO_2 is challenging due to its low electrical conductivity, which ranges from 10^{-5} to 10^{-6} S/cm [126-128]. Vanadium oxides have distinctive electrical, optical, and electrochemical properties. Vanadium forms several oxygen compounds, including VO, V_2O_3, VO_2, V_2O_5, V_3O_7, and V_4O_9 [129]. These compounds exhibit varied properties based on their oxidation states and structural configurations [130]. However, V_2O_5 faces limitations related to its poor electrical conductivity, low P_D, and limited cyclic stability, which constrain its effectiveness in SC applications.

NiO offers several advantages as an electrode material for SCs, including high theoretical capacitance, cost-effectiveness, good thermal and chemical stability, and pseudocapacitive behavior. In addition to these benefits, NiO's low toxicity, availability, and eco-friendly nature. Additionally, its relatively low cost and abundance make it an attractive option for large-scale ES applications [131]. NiO NPs are particularly suitable due to their diverse range of beneficial characteristics, such as the ability to exist in multiple oxidation states within a certain potential range. NiO exhibits a significant SA, high theoretical capacitance, and better cyclic stability, fulfilling most of the criteria required for effective SC electrodes [132]. NiO typically exhibits a theoretical Cs of around 2573 F/g, which is significantly higher than many other transitions MOs, making it particularly appealing for high-performance ES devices. Its electrochemical performance can be further enhanced by tailoring its morphology, such as creating nanostructured forms like nanoflakes, nanowires, or nanospheres, which provide a higher SA and shorter ion diffusion paths [133].

1.6 Conclusion: In conclusion, the increasing demand for efficient ES solutions underscores the essential role of SCs in modern applications. Their unique properties, including high P_D and long-life cycles, make them especially appealing for various ES applications. To meet this demand, it is crucial to enhance E_D. Research should focus on developing advanced electrode materials, because ES capability of SC device directly depend on electrode materials. NiO stands out as a superior choice compared to traditional materials such as CPs, carbon-based materials, and other MOs. NiO possesses a high theoretical capacitance and exhibits pseudocapacitive behavior, allowing for rapid charge and discharge cycles. Additionally, its cost-effectiveness, low toxicity, abundant availability, and eco-friendly nature make it an attractive option for sustainable ES solutions. By optimizing NiO as an electrode material, we can significantly enhance the performance and viability of SCs.

Chapter 2

Recent Progress in Nickel Oxide-Based Materials for Supercapacitors: Morphology, Composites, and Performance

Nickel Oxide (NiO) has become a highly promising material for diverse applications, such as gas sensing, catalysis, lithium-ion batteries, supercapacitors, and magnetic devices. [134,135]. Nanostructured NiO can be effectively synthesized by calcining various nickel-based precursors e.g., nickel hydroxide [136-138]. The pseudocapacitive properties of NiO are predominantly dependent on morphology, crystallinity, and electrical conductivity, making these factors critical for optimizing its performance in ES and conversion systems [139].

2.1 Properties of NiO

NiO has a cubic crystal structure, like rock salt, with a lattice constant of about 4.17 Å. Its Ni and O atoms are arranged in a stable octahedral coordination. The lattice constant of NiO is affected by various factors, including synthesis methods and particle size. Nanostructured NiO can be synthesized in different morphologies, such as NPs, spherical, hierarchical and nanowires, providing a high SA, which is beneficial for catalytic processes and ES applications. Although NiO exhibits good thermal stability, it can experience partial reduction to metallic nickel at high temperatures. These structural properties enhance its suitability for applications in SCs and batteries. NiO is antiferromagnetic below 523 K and often exhibits defects like nickel vacancies, affecting its properties [136-138]. NiO exhibits remarkable optical properties, primarily due to its wide bandgap, which typically ranges from 3.6 to 4.0 eV. As a transparent p-type semiconductor, NiO demonstrates substantial transmittance in the visible spectrum while exhibiting strong absorption in the ultraviolet range. The optical characteristics of NiO are influenced by various factors, including its nanostructure, thickness, and the presence of defects or dopants, all of which can alter its bandgap and light absorption behavior [140,141]. NiO exhibits intermediate thermal and mechanical properties. Its thermal conductivity ranges from 10 to 20 W/m·K. The specific heat capacity of NiO is approximately 0.72 J/g·K. This moderate thermal conductivity supports efficient heat dissipation during the charging and discharging processes, whereas its mechanical strength contributes to the structural integrity of SC electrodes [136-138]. The conductivity and charge storage mechanisms in NiO are critical factors influencing its performance in SCs. As a p-type semiconductor, the conductivity of NiO primarily arises from the generation of holes due to oxygen vacancies and structural defects.

These holes facilitate charge transport within the material, thereby enhancing its overall conductivity. The charge storage mechanism involves faradaic processes, wherein lithium ions (or other cations) intercalate into the NiO structure during the charging phase [140,141]. This intercalation is a reversible process, enabling efficient ES and subsequent release. Additionally, NiO can undergo redox reactions, with nickel oxidation states transitioning between Ni^{2+} and Ni^{3+} during charge and discharge cycles. This transformation significantly enhances the overall charge storage capacity, contributing to a higher E_D in SCs. The electrochemical activity of NiO is further amplified by its nanostructured forms, which enhanced the SA and provide additional active sites for ion interactions [136-138]. The SA and porosity of NiO are crucial determinants in enhancing its charge storage capacity, as a larger SA promotes improved ion accessibility during charge-discharge cycles. Additionally, the intrinsic electrical conductivity of NiO is influenced by structural defects and the oxidation state of nickel; optimizing these characteristics can significantly enhance charge transfer rates. The selection of synthesis method such as sol-gel, hydrothermal, or thermal decomposition affects the resultant morphology, which can range from NPs to nanostructures, thereby increasing the number of active sites and SA. Furthermore, electrochemical stability is an essential consideration, as maintaining structural integrity during cycling is critical to mitigate capacity fading due to phase transitions or material degradation [142-144].

2.2 Fabrication of NiO with Controlled Morphology for Supercapacitor Applications

NiO can manifest in various dimensional configurations, including zero-dimensional NPs, one-dimensional (1D), two-dimensional (2D), and three-dimensional (3D). Different dimensional morphology has differences properties like different particle size, and specific surface area (SSA). All these terms are play a pivotal role in ES capability of SCs [145].

2.2.1 Zero-dimensional *NiO morphology for Supercapacitor applications*

Zero-dimensional (0D) nickel oxide (NiO) particles are predominantly synthesized through sonochemical and sol-gel methods. The sonochemical method for synthesizing nanocrystals involves the application of ultrasonic waves to a precursor solution. The sonochemical method is favored for its ability to produce high-purity nanomaterials at relatively low temperatures, offering precise control over particle characteristics and enhancing the uniformity of the final product [146,147]. The sonochemical method has the potential of simplifying the reaction pathway, thereby enhancing the reaction rate, and decreasing the activation energy required for the process. The manipulation of NiO NP sizes is achievable through the regulation of ultrasound frequency and intensity [148,149]. The sol-gel is highly preferred due to the simplicity and cost-effectiveness in synthesizing materials. This multistep technique involves hydrolysis, condensation, and drying processes, during which significant chemical and physical transformations occur. Initially, particles in solution convert into a gel under carefully controlled conditions. The sol-gel process enables the mixing of precursor chemicals in solution at relatively low temperatures, allowing precise control over the composition at the atomic level [150,151]. Additionally, the sol-gel is valued for its versatility, as variations in reaction time, solvents, and temperature can be employed to achieve different material morphologies [152]. **Duraisamy, et al. (2016)** synthesized 0D NiO NPs via the sonochemical method, exploring the effects of varying calcination temperatures. The NPs subjected to calcination at 250°C exhibited average (avg.) NPs size of 6 nm, Cs of 448.5 F/g was achieved at 0.3 A/g. In contrast, at the same current density other the particles calcined at 450°C displayed an increased size of 21 nm and a reduced Cs of 298.5 F/g. Additionally, the NPs calcined at 650°C reached a size of 41 nm, resulting in a significant decline in Cs to 39 F/g [153]. **Chatterjee, et al. (2017)** synthesized 0D NiO NPs of particle size 21 nm by using sol-gel method. At 5 mV/s, these NPs exhibited the Cs of 810 F/g [154]. **Jahromi, et al. (2015)** synthesized NPs with 0D morphology of NiO using the sol-gel method at various calcination temperatures. At 1 A/g, particles calcined at 300°C have a size of 8 nm, archived the Cs of 379 F/g. At the same current density, other which particles have calcined at 400°C, size of 12 nm, archived Cs of 250 F/g. Similarly, Particles calcined at 500°C have a size of 22 nm and a Cs of 97 F/g [155]. **Kim, et al. (2013)** synthesized NiO NPs of 0D morphology using the sol-gel method. At 0.5 A/g, these NPs exhibited a Cs of 260 F/g [156]. **Pandurangan, et al. (2017)** synthesized nanoclusters with 0D morphology of NiO using the precipitation method of different size. At 1 A/g, particles have a size of 4 nm, demonstrate the Cs of 62 F/g. Cs of 303 F/g was demonstrated by particles have a size of 1.5 nm under the identical current condition. Particles have a size of 0.75 nm, demonstrate the Cs of 449 F/g under the identical current condition [157]. From above reported research articles its concluded that the size of NiO NPs, synthesized through various methods, varies significantly, impacting their electrochemical performance. Smaller NPs exhibit the ability to pack more densely, which reduces ion diffusion distances and enhances Cs. These smaller particles generally have a more porous structure and a higher number of electrochemically active sites. Moreover, the calcination temperature is critical in controlling particle size; as the temperature increases, particle crystallinity and size grow due to crystal expansion along specific directions, reducing surface energy. Typically, higher annealing temperatures result in larger, rougher particles with reduced Cs. Maintaining a uniform smaller particle size enhances the extent of EL ion intercalation within the NiO electrode, thereby improving overall electrochemical performance [158,159].

2.2.2 One-dimensional (1D) NiO morphology for Supercapacitor applications

NiO 1D nanostructures, such as **nanorods, nanofibers, and nanotubes**, have been widely studied for their application in SCs. These 1D nanomaterials offer several advantages for enhancing electrochemical performance. Their continuous pore structure allows for improved ion diffusion at the EL/electrode interface, promoting better charge transport. Additionally, the porous nature of 1D nanostructures provides sufficient space to accommodate volume changes, thereby reducing structural degradation during cycling [160,161]. Commonly employed methods for fabricating 1D NiO-based SC electrodes include electrospinning and hydrothermal/solvothermal techniques. The hydrothermal approach has gained significant popularity among scientists and technicians from several disciplines, especially in the past fifteen years. Hydrothermal/solvothermal synthesis is a commonly used one-pot synthesis process for preparing a diverse array of TMOs [162,163]. The word "hydrothermal" typically describes a heterogeneous reaction that occurs in under the condition of high pressure and temperature. [164,165]. In hydrothermal method for reaction, a sealed autoclave made of stainless steel and lined with Teflon are used. The temperature utilised is often above 100 °C, resulting in the automated generation of pressure within a sealed system. By using the hydrothermal method/ solvothermal method, different types of morphology and degrees of crystallinity are obtained by changing the reaction time and temperature [166]. Electrospinning is a method for synthesizing nanofibers by applying a high-voltage electric field to a polymer solution or melt, which forms fine fibers collected on a surface. It allows control over fiber size and structure, is scalable, and works with a variety of materials. Electrospun fibers are used in applications such as ES, filtration, and tissue engineering due to their high SA and customizable properties, making them ideal for enhancing performance in fields like SC electrode fabrication [167-169]. **Su et, al. (2012)** utilized the solvothermal method for synthesized NiO nanowire structures, which show a Cs of 348 F/g and SSA of 85.18 m^2/g [170]. **F. Dar et, al. (2013)** synthesized 1D nanoporous NiO using an electrodeposition method. The morphology of NiO evolved into nanotubes following annealing at 450°C for 25 minutes. When annealed for 300 minutes, NiO developed a nanorod-like structure. At 5 mV/sec, the Cs of the NiO nanorods and nanotubes was measured at 797 F/g and 2,093 F/g, respectively. These findings indicate that the morphology of NiO can be significantly altered by varying the annealing duration [171]. **Liu, et al. (2016)** synthesized NiO nanotubes with pore radius ranging from 2.5 to 10 nm using the solvothermal method. At 1 A/g, these nanotubes show Cs of 919 F/g [172]. Similarly, **Xiong, et al. (2011)** synthesized NiO nanotubes with a pore radius of 7.1 nm using the solvothermal method. At 1A/g, the NiO was demonstrating a Cs of 405 F/g [173]. **Ren, et**

al. (2013) employed the electrospinning method to synthesize NiO nanofibers with an avg. radius of 50–60 nm. At 1 A/g, nanofibers like NiO were exhibited Cs of 336 F/g [174]. **Kundu et, al. (2015)** synthesized NiO nanofibers having avg. radius of 140–200 nm by electrospinning. At 1 A/g, the NiO nanofibers was showing Cs of 773 F/g [175]. **Paravannoor, et al. (2013)** synthesized NiO nanowires which has avg. radius of 32.5 nm by using the solvothermal process. At 1 A/g, the highly porous NiO exhibited Cs of 750 F/g [176]. **Vidhyadharan, et al. (2014)** synthesized NiO nanofibers with diameters ranging from 50 to 70 nm using electrospinning. At 1 A/g, these was exhibited Cs of 670 F/g [177]. **Zang, et al. (2014)** synthesized the NiO nanofibers with a pore radius of 1.85 nm by using solvothermal method. At 1 A/g, nanofibers like NiO were yielding Cs of 884 F/g [178]. **Wang, et al. (2012)** developed NiO nanobelts with a pore radius of 5 nm via the solvothermal method. At 1 A/g, these nanobelts of NiO exhibited a Cs of 1126 F/g [179]. **Yao, et al. (2015)** synthesized NiO nanotubes of pore radius of 2.35 nm using the solvothermal method. At 1 A/g, these nanotubes of NiO were demonstrating a Cs of 1260 F/g [180]. **Zhang, et al. (2015)** synthesized of NiO nanofibers of avg. pore radius of 40 nm using the electrospinning method. At 1 A/g, these nanofibers exhibited a Cs of 700 F/g [181]. **Lastly, et al. (2011)** synthesized NiO macrotubes of pore diameters of 2–3 μm via electrospinning. At 1 A/g, these macrotubes achieving a Cs of 701.2 F/g [182].

It can be concluded from the above survey of research articles that 1D NiO nanomaterials feature mesoporous or macroporous structures, which provide significant advantages for SC applications. 1 D porous architecture reduces the diffusion distance for EL ions, while the larger pore diameters of mesopores and macropores enhance ion diffusion, improve electron transport efficiency, and boost ES capacity.

2.2.3 Two-dimensional NiO morphology for Supercapacitor applications

2D NiO structures include nanosheets, nanoplates, nanoflakes, and other similar configurations [183–187]. These 2D NiO nanomaterials typically exhibit a high SA, a large surface-to-volume ratio, and optimized pore sizes, all of which facilitate enhanced EL penetration and shorten the ion diffusion pathways. The properties of these materials, including in-plane charge transport, wettability, and bandgap characteristics, are significantly influenced by the nanosheet thickness. This reduction in thickness of nanosheets enhances the performance, making them more effective for electrochemical applications [188,189]. Chemical precipitation is a straightforward and effective method for synthesizing materials such as TMOs and hydroxides in large quantities, typically in micro- or nano-sized forms. This process entails the coprecipitation of soluble metal cation salts (e.g., nitrates), followed by drying the precipitate (e.g., hydroxides) and after annealing obtained the MOs. [190,191]. Another method for synthesizing 2D NiO nanomaterials is microwave-assisted synthesis. This is a modern and efficient technique for producing micro- and nano-sized crystalline materials. This method is distinguished by its accelerated reaction rates and reduced reaction times, often achieving complete reactions within minutes [192]. Microwave irradiation is widely used in both industrial and academic settings due to its simplicity, speed, cost-effectiveness, uniform heating, and energy efficiency. It is commonly applied to synthesize a variety of materials, including porous substances [193], inorganic complexes [194], and nanocrystalline particles [195]. Despite its advantages, such as reduced reaction time, precise control over the morphology of MOs remains challenging in microwave-assisted synthesis. **Khairy, et al. (2013)** synthesized NiO nanoplatelets having SSA of 161 m^2/g and a pore radius of 1.7 nm using a microwave-assisted method. At 1 A/g, these nanoplatelets of NiO demonstrated Cs of 1,200 F/g in a 2 M NaOH EL. In contrast, At the same current density and EL nanoslices of NiO, which had a SSA of 145 m^2/g and a pore radius of 1.95 nm, were synthesized using the same method and demonstrate a Cs of 600 F/g [196]. **Xiao, et al. (2016)** synthesized NiO nanoflakes through a solvothermal method, achieving a SSA and pore diameter of 89.56 m^2/g and 2.31 nm respectively. At 1 mA/cm^2, these nanoflakes exhibited the Cs of 870 mF/cm^2 [197]. **Behm, et al. (2013)** synthesized NiO nanoplates via a solvothermal method, achieving the SSA and a pore diameter of 95 m^2/g and 2.5 nm respectively. At 1 A/g, these nanoplates exhibited a Cs of 85 F/g [198]. **Zhang, et al. (2010)** employed a hydrothermal synthesis method to synthesis NiO with diverse morphologies by adjusting the pH of the solution using NaOH. Nickel oxide (NiO) nanocolumns were synthesized, exhibiting a SSA of 102.4 m^2/g and a pore radius ranging from 1 to 2.5 nm. At 1 A/g, these nanocolumns demonstrated a Cs of 390 F/g. Additionally, NiO nanoslices, characterized by a SSA of 11.4 m^2/g and a pore radius of 5 to 15 nm, at 1 A/g exhibited Cs of 176 F/g. Furthermore, NiO nanoplates having a SSA of 20.2 m^2/g and a pore radius ranging from 5 to 12.5 nm were synthesized. At 1 A/g, these nanoplates showing a Cs of 285 F/g [199]. **Zhu, et al. (2012)** synthesized nanoplates like NiO via a solvothermal method, achieving a SSA of 95 m^2/g and a pore radius of 1.205 nm. At 1 A/g, these nanoplates demonstrated a Cs of 286.7 F/g [200]. **Alammar, et al. (2012)** synthesized NiO nanosheets having SSA of 92.84 m^2/g and a pore radius of 7.5 nm using an ultrasound-assisted method. At 1 A/g, these nanosheets exhibited a Cs of 199.4 F/g [201]. **Yuan, et al. (2013)** synthesized NiO nanosheets having SSA of 156 m^2/g and a pore radius of 2.85 nm through a chemical precipitation method. At 1 A/g, these nanosheets demonstrated a Cs of 168 F/g [202]. **Sun, et al. (2011)** synthesized NiO nanosheets featuring a SSA of 318.29 m^2/g and a pore radius of 3.425 nm using a chemical precipitation method. At 1 A/g, these nanosheets exhibited a Cs of 1025 F/g [203]. **Sun, et al. (2013)** synthesized NiO nanoflakes with a SSA of 42 m²/g through a chemical precipitation method. At 1 A/g, these nanoflakes demonstrated a Cs of 410 F/g [204]. **Liu et al. (2014)** synthesized nanoflakelet structure like NiO by using a solvothermal method. The pure NiO show a Cs of 480 F/g. Subsequently, the NiO was converted to NiO/Ni by calcining in hydrogen (H_2). At 20 A/g, the NiO/Ni composite demonstrated a Cs of 760 F/g [205]. **Purushothaman et al. (2013)** reported the Cs of 989 was achieved by synthesised NiO of nanosheet-assembled microstructures by using a solvothermal method at 3 mV/s [206]. **Yuan et al. (2012)** employed the chemical precipitation method for synthesized the mesoporous NiO nanoplatelets. At 2 A/g, these nanosheets electrodes exhibited a Cs of 1,124 F/g. The mesoporous NiO nanoplatelets demonstrated a SSA of 137 m²/g and notable porosity [207]. **Xiao et al. (2016)** employed the solvothermal method to fabricate NiO nanosheet structures, which demonstrated a SSA of 116.9 m²/g. At 0.5 A/g, these nanosheets was showing a Cs of 81.67 F/g. Additionally, these NiO electrodes showed a retention of 78.5% after three thousand galvanostatic charge-discharge (GCD) cycles [208]. **Jagadale et al. (2013)** synthesized NiO with a nanoflake-like structure using an electrochemical deposition. The NiO demonstrated a Cs of 222 F/g [209]. **Zheng et al. (2012)** synthesized flake-like NiO morphologies via a solvothermal method, at 0.2 A/g, these flake like NiO was achieving Cs of 137.7 F/g and demonstrating retentions rate of 91.6% after 1000 GCD cycles. The NiO nanoflakes exhibited a width ranging from 50 to 80 nm and a thickness of 20 nm [210]. **Vijayakumar et al. (2013)** synthesized nanoflake-like NiO using a microwave-assisted and as surfactant using the cetyltrimethylammonium bromide (CTAB). The research indicated that CTAB is inhibiting the agglomeration of nanocrystals. The NP-based flake structure facilitates enhanced electron conduction while reducing ion diffusion pathways. The research also investigated the impact of annealing temperature on Cs. At 0.5 mA/cm², NiO annealed at 300°C, 400°C, and 500°C exhibited Cs of 401 F/g, 240 F/g, and 206 F/g, respectively. The voltage drop observed in the discharge curves was directly proportional to the increase in current density and inversely proportional to the decrease in Cs. At lower current densities, the hydroxide ions (OH^-) have a longer time to diffuse between the EL and the NiO surface, resulting in an increased Cs [211].

In conclusion, SSA is crucial for the ES capability of 2D NiO-based SC electrode materials. A larger SA provides more active sites for electrochemical reactions, and an overall improvement in ES capability of materials used for SCs. However, it is noteworthy that higher annealing temperatures tend to reduce the SA of NiO materials, which can adversely affect their electrochemical performance. Therefore, optimizing the annealing process is essential to balance SA and performance in NiO-based SC applications.

2.2.4 Three-dimensional (3D) NiO morphology for supercapacitor applications

3D NiO morphology, including **microspheres, flower-like formations, and other hierarchical architectures**, have been widely investigated for SC applications due to their high SA. Hydrothermal/solvothermal techniques, have been mainly utilized to fabricate these 3D NiO electrode materials, offering enhanced electrochemical properties and improved charge storage capabilities. These structures provide an optimal framework for ion diffusion and electron transport, making them promising candidates for advanced ES systems [212–214]. **Abbas, et al. (2016)** successfully synthesized NiO microspheres using solvothermal method, achieving SSA of 295 m^2/g, pore radius 4.6 nm, and pore volume 0.64 cm^3/g. At 10 A/g, these microspheres show Cs of 1140 F/g [215]. **Du, et al. (2014)** successfully synthesized NiO microspheres using solvothermal method, achieving SSA of 149.6 m^2/g, pore radius 5.25 nm, and pore volume 0.36 cm^3/g. At 1 A/g, this microsphere was showing Cs of 762 F/g. At 15 A/g, showing the retention rate of 96 % % after 1000 cycles [216]. **Yao, et al. (2015)** synthesized NiO flowers using a solvothermal method, achieving SSA of 135 m^2/g, and pore radius 1.7– 4.9 nm. At 1 A/g, these NiO flower was exhibited Cs of 1860 F/g. At 20 A/g, these was showing a cyclic stability of 92 % % after five thousand cycles [217]. **Wang, et al. (2016)** synthesized NiO ball-flower by using an solvothermal method, achieving a high SSA of 163.1 m^2/g, pore radius 5.4 nm, and pore volume 0.376 cm^3/g. At 1 A/g, these NiO ball flower was exhibited an impressive Cs of 734 F/g and also, showing retention rate of 82 % % after 2000 cycles [218]. **Kim, et al (2013)** successfully synthesized NiO nanoflowers using sol−gel. The nanoflowers like NiO show a high SSA of 159 m^2/g, an avg. pore radius of 8.35 nm, and a pore volume of 0.66 cm^3/g. At 1 A/g, these nanoflower was showing a Cs of 480 F/g [219]. **Wang, et al. (2014)** synthesized NiO nanospheres using an nano casting method, achieving SSA of 200 m^2/g. At 0.5 A/g, these nanospheres was demonstrate impressive Cs of 1201 F/g. Also show retention rate of 70% after 5000 cycles, when current increased by sex times [220]. **Cao, et al (2012)** synthesized NiO nanotube arrays using electro-deposition methods, achieving SSA of 165 m^2/g. At 2 A/g, these NiO nanotube was achieved an impressive Cs of 675 F/g. Also, demonstrate the retention rate of 93.2% % after ten thousand cycles, under the identical current density [221]. **Cao, et al. (2011)** synthesized NiO hollow spheres by using an Microwave-assisted method, achieving SSA of176 m^2/g, and pore radius 2 nm. At 2 A/g, these NiO hollow sphere achieved an impressive Cs of 770 F/g. At 5 A/g, these also show retention rate of 95 % % after 1000 cycles [222]. **Fan et al. (2014)** synthesized flower-like NiO structure by solvothermal method. This innovative morphology shows a SSA of 95.63 m^2/g. At 1 A/g, these NiO structure was demonstrate Cs of 619 F/g [223]. **Patil et al. (2008)** synthesized a honeycomb-like $Ni(OH)_2$ structure with the chemical bath deposition. Upon annealing, the honeycomb $Ni(OH)_2$ transformed into a spherical grain-like NiO structure. The Cs of 119 F/g and 157 F/g were achieved by the resulting NiO in 0.5 M and 2 M KOH ELs, respectively. This suggests that the Cs of NiO increases with the molar concentration of KOH used as the EL, underscoring the effect of EL concentration on the electrochemical performance of NiO [224]. **Feng et al. (2015)** synthesized a chestnut-like porous nanosphere structure of NiO having SSA of 174.1 m^2/g, by using a solvothermal method. At 1 A/g , these porous NiO a show the Cs of 982 F/g [225].

The SC performance of 3D NiO electrode materials are largely governed by key factors such as SA, pore diameter, and pore volume. In comparison to 0D, 1D, and 2D NiO nanomaterials, the 3D NiO nanostructures demonstrate significantly higher Cs. This superior performance is primarily attributed to the distinctive nanostructure of 3D NiO, which, through its enhanced SSA and porosity, thereby enhancing the material's overall electrochemical performance.

2.3 NiO-Based Composites for supercapacitor application

Several studies have shown that the archived Cs of NiO observed in the researcher's investigations is significantly lower than its theoretical value. The investigated reason behind the lower Cs is low conductivity of NiO. So, need to increase the conductivity of NiO to archived higher Cs. Incorporating other MOs, carbon-based materials, CPs, and doping with transition metals are widely used strategies for increased the conductivity and ES capability of electrode materials [226-228].

2.3.1 Transition Metal Element Doping in NiO

The introduction of doping elements into NiO induces the formation of lattice defects, which substantially enhanced the ES capability of NiO by increasing the number of electrochemically active sites [229]. Various transition metals, including rare earth elements like Co, Mn, Cu, and La, have been used to dope NiO. Research indicates that specific dopant ions, such as Co^{2+} and La^{3+}, can significantly alter the morphology of NiO materials. Doping not only mitigates particle agglomeration but also facilitates the development of a porous structure, thereby increasing the SSA and conductivity. This enhanced structural design directly contributes to improved electrochemical performance in ES applications [230-232]. By using sol-gel method, study the Ce-doping vartion in NiO from 0.5 to 2%. There has been seen, the transformation of nanosheets to flowers after doping. Among of all variation Ce 1% sample achived higher SSA and pore volume of 226 m^2/g and 1.41 cm^3/g. At 1 A/g and 5mV/sec, Ce 1% dopped materials electrode was exhibited the Cs of 1725 F/g, and 2444 F/g respectively [233]. By using various chemical Co/Mn co-doped NiO composite materials can be synthesized [234]. Research indicates that $Ni_{0.95}Co_{0.025}Mn_{0.025}O_{1}$-δ composite materials demonstrate a remarkable Cs of up to 673.73 F g^{-1}. because of the synergistic effects of Co/Mn co-doping and the introduction of crystal defects, which collectively increased the ES capability of electrode materials. Cu^{2+} ions can effectively substitute for cation sites within the NiO lattice, leading to the formation of numerous positive defects. This substitution not only enhances the probability of proton transport but also facilitates electron transmission within the material [235,236].

In conclusion, the incorporation of doping elements into NiO significantly enhances its electrochemical performance by creating lattice defects that increase the numbers of active sites of electrode materials. The use of various transition metals, including Co, Mn, Cu, and rare earth elements like La, has proven effective in modifying the morphology of NiO, leading to improved charge storage capabilities. These findings highlight the importance of strategic doping in optimizing the ES capability of NiO, which also opening avenues for the creation of advanced electrode materials.

2.3.2. NiO/Metal Oxide Composites

Firstly, the incorporation of NiO with diverse MOs optimizes the electrical conductivity and electrochemical activity of the composite. The presence of multiple MOs facilitates the formation of a more conductive network, thereby enhancing charge transfer capabilities and overall conductivity. This enhanced conductivity is vital for efficient charge storage and rapid response times during charge-discharge cycles. Additionally, the synergistic interactions between NiO and other MOs can enhance the electrochemical reactions taking place at the electrode surface. The unique redox properties of various MOs introduce additional faradaic reactions, thereby increasing the overall charge storage capacity. This multifacet E_D approach enables the achievement of higher Ed compared to single-component systems. Furthermore, the structural stability of these composite materials is crucial for improving cycling stability. The mechanical properties of one oxide can reinforce the structural integrity of the other, thereby minimizing the risk of degradation and capacity fading during repeated cycling. This increased stability is particularly critical for practical applications, where longevity and reliability are of utmost importance [237,238]. **Wei et al. (2017)** reported that the Cs of 992.85 F/g were exhibited $NiCo_2O_4$/NiO electrode by at 1 A/g. and materials exhibit a SSA of 127.09 m^2/g, and particle size of 8.82 nm. At 10 A/g, these electrodes retention rate of 79.82% after five thousand cycles. Also, an ASC was successfully fabricated using $NiCo_2O_4$/NiO and activated carbon (AC). This $NiCo_2O_4$/NiO//AC device achieved a high E_D of 47.43 kW/kg at

0.389 Wh/kg [239]. **Wang et al. (2017)** reported that the Cs of 493.0 F/g were exhibited by NiO at 0.2 A/g. Under the same conditions, NiO@Co_3O_4 and NiO@Co_3O_4@MnO_2 demonstrate significantly improved Cs of 868.5 F/g and 1055.3 F/g, respectively.[240] **Wang et al. (2021)** reported that the specific capacities of 1394 C/g and 560 C/g were achieved by the NiO/ZnO electrode at 1 A/g and 20 A/g, respectively. Also, maintaining a capacitance of 538 C/g after 2000 cycles at 5 A/g. BET analysis revealed a SSA, pore diameter, and pore volume of NiO/ZnO were 47.951 m^2/g, 2.55, nm and 0.477 cm^3/g. [241] **Xiaoli et al. (2020)** successful synthesis of hierarchical structures of MnO_2@NiO by utilizing a combination of MnO_2 nanosheets and NiO nanowires. At 0.25 A/g, the binder-free electrodes of MnO_2@NiO exhibit a Cs of 374.6 F/g and demonstrating exceptional retention rate of 92.7% after five thousand cycles. At 9360 W/kg, ASC achieved an E_D of 15.4 W/kg. [242] **Yi et al. (2019)** synthesized NiO and NiO@CeO_2 samples containing 2.5, 5.0, and 7.5 wt% using a solvothermal method. At 1 A/g, the NiO@CeO_2 (5.0 wt%) electrode exhibited the highest Cs, achieving values of 2155.6 F/g. Additionally, Cs of 960.4 F/g was archived by this electrode at 20 A/g, and retention rate of approximately 95.84% after 10,000 GCD cycles. Furthermore, the NiO and NiO@CeO_2 (5 wt%) electrodes exhibited excellent E_D of approximately 25.0 Wh/kg and 54.8 Wh/kg, respectively, at P_D (of around 2 kW/kg.[243] **Zuo et al. (2016)** reported that the SSA of 176.5 m^2/g for Co_3O_4/NiO. At 2 A/g, the Co_3O_4/NiO electrode archived Cs of 710 F/g after 500 cycles. [244] Xu et al. (2019) reported that the Cs of 1982.3 F/g were archived by $NiMoO_4$/NiO nanoflowers at 1 A/g. Under the identical current density, exhibited retention rate of 98.6% after 3000 cycles. The $NiMoO_4$/NiO structure also exhibited a high SSA, pore size, and pore volume of 79.47 m^2/g, 5.61 nm, and 0.34 cm^3/g, respectively. At 96.2 W/kg, the $NiMoO_4$/NiO//AC ASC demonstrated an impressive E_D of 38.0 Wh/kg [245]. The performance of SCs based on NiO and MO composites with varying compositions and morphologies has been extensively investigated. These composites typically demonstrate lower electrical resistance and higher Cs values compared to NiO. It can be concluded that the incorporation of NiO with TMOs significantly enhances SC properties through several key factors, including hierarchical morphology, improved electrical conductivity, increased SA, and the formation of heterostructures. Collectively, these attributes contribute to superior electrochemical performance, positioning NiO-based composites as promising candidates for advanced SC applications.

2.3.3 NiO/Carbon Nanomaterial Composites

Mesoporous carbon, carbon nanofibers, carbon spheres, CNTs, and graphene are frequently employed in the fabrication of NiO/carbon composites [246-249]. The higher SSA of these carbon materials increases the availability of active sites in composite nanomaterials. Additionally, mechanical strength along with the excellent conductivity of carbon materials enhance capacitance values and cycling stability in NiO/carbon composites. In composites formed with carbon spheres and NiO NPs, an encapsulated structure is created. The outer carbon layer acts as an electron transfer pathway while preventing the aggregation of the inner NPs [250-253]. Many carbon shells have the mesoporous characteristics, which help to increase the interaction between the EL and composite materials. Moreover, active functional groups, such as N or O, after treatment, promoting the oriented growth along with specific morphologies of NiO, which present in the porous carbon nanospheres [254]. Graphene has emerged as one of the most extensively studied carbon materials due to its numerous advantages, including exceptional mechanical stability, high SSA, and excellent chemical and electrical conductivity [255,256]. Multiwalled carbon nanotubes (MWCNTs) are recognized for their desirable properties, including a mesoporous network, mechanical strength, and chemical stability. In hybrid materials composed of NiO/MWCNTs, the CNTs facilitate the dispersion of NiO NPs, resulting in a uniform surface morphology, enhanced SSA and providing electronic transmission channels [257-259]. **Wen et al. (2016)** reported that Cs of 972 F/g was demonstrated by pure NiO at 1 A/g. In comparison, the NiO@CNTs composite showed a significantly higher SSA of 186.4 m^2/g, leading to an enhanced Cs of 1844 F/g under identical current conditions in a 6 M KOH EL. At 1 A/g, the NiO@CNTs composite demonstrated superior cyclic stability, retaining 88.9% of cyclic stability after 1000 charge-discharge cycles [260]. **Zhao et al. (2014)** reported that the Cs of 166 F/g was exhibited by pure NiO at 1 A/g. In contrast, NiO/graphene spheres, with a SSA of 185 m^2/g, showed significantly enhanced ES capability, achieving a Cs of 555 F/g under identical current conditions. Additionally, the NiO/graphene spheres demonstrated excellent cyclic stability, retaining 98.8% after 2000 GCD cycles under identical current conditions [261]. **Xiang et al. (2017)** reported that Cs of 929 F/g was demonstrated by the NiO/carbon nanofibers at 1 A/g. Furthermore, the material demonstrated excellent long-term stability, retaining 88% after 5000 cycles under identical current conditions [262]. **Lv et al. (2018)** reported that Cs of 1062 F/g was demonstrated by the NiO/graphene nanoflakes at 1 A/g. The material demonstrated robust cyclic stability, retaining 90.6% after 5000 GCD cycles, when the current density become two times [263]. **Xu et al. (2013)** reported that carbon coated mesoporous NiO NPs show a SSA of 107.6 m^2/g. At 2 A/g, these NPs was demonstrated a Cs of 931 F/g. Moreover, they demonstrate the notable, maintaining Cs of 93% after 6000 cycles under identical current conditions [264]. **Liu et al. (2018)** reported that NiO/ rGO flower-like structures exhibited a SSA of 255 m^2/g.

At 0.5 A/g, these structures demonstrated a Cs of 900 F/g. Furthermore, the electrodes exhibited E_D of 31.6 Wh/kg at 397 W/kg in aqueous 6 M KOH, 49 Wh/kg at 868.5 W/kg in an organic LiPF6 solution, and 146 Wh/kg at 1 kW/kg in an ion gel polymer EL [265]. **Jinlong et al. (2017)** reported that NiO/graphene nanoflakes having a SSA of 231.6 m^2/g. At 1 A/g, these nanoflakes demonstrated an impressive Cs of 1782 F/g. Furthermore, the material exhibited significant cyclic stability, retaining 90.2% after 5000 GCD cycles under identical current conditions [266]. **Li et al. (2016)** reported that Cs of 782 F/g was exhibited NiO/reduced graphene oxide (rGO) nanosheets at 0.5 A/g. After 3000 GCD cycles, the electrode shows the retention rate of 94.1% at 2 A/g. At P_D of 375 W/kg, an ASC configuration utilizing NiO/RGO in conjunction with AC show E_D of 32.5 Wh/kg [267]. **Feng et al. (2016)** reported that NiO/carbon (C) nanofibers having SSA of 156.208 m^2/g. At 1 A/g, these nanofibers structure like NiO/C electrode was demonstrated a remarkable Cs of 2048 F/g. Nanofiber like electrode also show the excellent cyclic stability, retaining 97% after 8000 cycles, when current density increased by twenty times [268].

Carbon materials typically facilitate the uniform growth of NiO nanocrystals and prevent their aggregation. Consequently, the composites formed from NiO and carbon nanomaterials exhibit substantially higher SAs and Cs compared to pure NiO. The presence of π–π bonding and intermolecular forces within the NiO/carbon nanomaterial composites further contributes to the improved properties, enhancing SA, conductivity, porosity, and hydrophilicity. Collectively, these factors lead to enhanced charge storage capabilities, making these composites more effective for ES applications.

2.3.4 NiO/conducting polymer (CP) composites

Recent investigations have focused on NiO composites with CPs, specifically PANI and PPy, for SC applications [269]. PANI exhibits several advantageous characteristics, including its doping, high electrical conductivity, environmental stability, and straightforward synthesis [270]. The ion doping, and de-doping processes induce significant volumetric changes within the PANI structure during charge and discharge cycles. To improve the cycling stability of PANI, hybrid materials that incorporate PANI with MOs have been developed. NiO, recognized for its high SSA and cost-effectiveness, serves as a critical component in PANI-MO hybrids. In this capacity, When NiO added with PANI increased the conductivity, thus providing a synergistic enhancement of the properties of composite [271]. **Sun et al. (2016)** reported the Cs of 2565 F/g was achieved by the flower-like PANI-NiO structures at 1 A/g. At 10 A/g, this Cs was reduced and remained 1795 F/g [272]. The PANI-graphene nanosheet (GNS)/NiO composites developed by **Wu's research group** by composition of PANI and NiO exhibit markedly improved Cs and increased electrochemical reversibility compared to pure PANI and NiO electrodes. This performance enhancement of the composites can be primarily attributed to the capacity of PANI to improve the electrochemical properties of NiO [273]. For NiO, PPy facilitates the creation of electrically conductive pathways, while concurrently mitigating mechanical stress arising from volumetric changes during operation. This property positions PPy as a highly suitable choice for incorporation into SC electrode materials [274]. **Vijeth et al. (2020)** reported that the Cs of 581.77 F/g was achieved by the NiO/PNT (Ppy nanotubes decorated with NiO) composite at 1 A/g. The Cs of PNT, measured at 337.44 F/g under identical conditions [275]. **Han et al. (2019)** successfully fabricated Tremella-like NiO and fish-scale-like PPy microspheres using solvothermal and in situ polymerization techniques. When utilized as electrode materials for SCs, the combination of NiO and PPy exhibits a beneficial synergistic effect. At 3 A/g, the NiO/PPy composite with a NiO to PPy molar ratio of 6, designated as NiO/PPy-6, demonstrated an exceptional Cs of 3648.6 F/g. At 2399.99 W/kg, the ASCs device was achieved an E_D of 333.3 W h/kg [276]. **Fu's research group** developed NiO@PPy nanocomposites and examined their Cs. The addition of a PPy coating layer resulted in composite materials that demonstrate enhanced flexibility and substantially improved electrochemical performance relative to pure NiO, achieving a 75% increase in capacitance [277].

In conclusion, recent studies highlight the promising integration of NiO-based composites with \CPs for SC applications. The unique properties of PANI, including its high electrical conductivity and stability, are enhanced through hybridization with NiO, leading to improved cycling stability and capacitance retention. Similarly, the incorporation of PPy facilitates the formation of conductive pathways and alleviates mechanical stress during charge-discharge cycles, further enhancing the electrochemical performance of NiO composites. Notable advancements include the synthesis of flower-like PANI-NiO structures and NiO/PPy composites, which have demonstrated exceptional Cs and E_D values. These findings underscore the potential of NiO-conductive polymer hybrids in advancing ES technologies, offering avenues for the development of more efficient and durable SC systems.

2.3.5 NiO/Metal Sulfide Composites

Metal sulfides are often preferred due to their layered structures and intrinsic electrical conductivity, which make them ideal candidates for a variety of applications. Transition metal sulfides, including MoS_2, SnS, WS_2, CuS, and ZnS, have been widely employed in diverse fields such as ES, energy conversion, and photocatalysis. These materials' unique properties enhance their performance across these technological domains, contributing to their extensive use in advanced applications [278,279]. In the study conducted by **Moradlou et al. (2020)** reported that the NiO/$NiCo_2S_4$-based electrode was demostrated a remarkable Cs of 1984 mF/cm^2 at 1 mA cm^{-2}. Subsequently, an ASC device was fabricated, achieved an E_D of 0.254 Wh/m^2 at a P_D of 7.82 W m^{-2} [280]. **Wang et al. (2018)** reported that Cs of 1063 F/g was demonstrated by the $(NiO)_{0.1}(NiS)_{0.9}$ composite electrode at 2 A/g. Remarkably, even current increased by fifty times, the electrode retained a Cs of 486 F/g after 10,000 charge-discharge cycles. Furthermore, Cs of 58.5 F/g was exhibited by the $(NiO)_{0.1}(NiS)_{0.9}$‖activated carbon ASC device at 2 A/g [281]. In the study by **Yang et al. (2018)** reported that the Cs of 1620 F/g was exhibited CoS/NiO electrode at 1.0 A/g, significantly outperforming the pristine CoS and NiO electrodes. At 3 A/g, the CoS/NiO//NC ASC maintained, retaining 93.5% of its capacitance after 3,000 cycles [282]. **Yi et al. (2020)** reported that ZnS@Co_3S_4@NiO nanosheets exhibited an initial Cs of 1418.7 F/g, which increased to 1550.9 F/g after 5,000 cycles, calculated retention rate of 109.3% at 5 A/g. In comparison, ZnS@Co_3S_4 nanorods demonstrated a lower initial Cs of 708.7 F/g and maintained 716.4 F/g, calculated retention rate of 101.1% after same number of cycles [283]. **Kim et al. (2018)** reported that, Cs of 386.7 F/g was exhibited by the NiO/NiS at 1 A/g. At 5 A/g, demonstrating impressive retention rate. Notably, the electrode retained 97.6% after undergoing 3,000 cycles [284].

In conclusion, metal sulfides, particularly transition metal sulfides, demonstrate significant promise in various applications due to their favorable layered structures and inherent electrical conductivity. Studies highlight the impressive performance metrics of various composite electrodes, showcasing their potential in ES and conversion systems. Noteworthy findings include exceptional capacitance values and outstanding cycling stability across multiple research efforts, illustrating the advancements in SC technology. These developments not only emphasize the effectiveness of these materials in enhancing device performance but also pave the way for future innovations in ES solutions. The continued exploration of metal sulfide-based electrodes could lead to more efficient and sustainable energy systems.

2.4 Research gap: Despite the established importance of morphology, synthesis techniques, and electrochemical properties of NiO electrode materials in enhancing SC performance, significant gaps remain in understanding the optimal structural configurations and their relationships to capacitance. While the nanoscale structure of NiO is known to facilitate electron transfer and ion diffusion, and while larger SSA and pore diameters are associated with increased ES capacity. There is need to explore variation of reaction temperature and ratio proportion precursors during NiO synthesis. Additionally, the inherent low conductivity of NiO necessitates further investigation into the comparative electrochemical performance of binder-based versus binder-free electrodes.

The development of innovative NiO-based hetero nanostructures is a critical strategy for advancing SC electrode materials. Although synergistic effects from composites, heterostructures, and lattice defects are known to enhance conductivity and electrochemical performance, there remains a significant knowledge gap regarding the integration of NiO with specific metal sulfides. Investigating the potential of metal sulfides such as MoS_2, CuS, and CoS_2 in conjunction with NiO is essential for optimizing the hetero nanostructure. Currently, there is a lack of dedicated research addressing the combinations of NiO with these metal sulfides, highlighting the necessity for further studies to explore their synergistic effects and implications for SC applications.

2.5 Research objectives

The objectives of the research work are:

1. To synthesis NiO nanostructures and its characterization.
2. Synthesis of NiO based hetro nanostructures and their optimization.
3. Development of hetro nanostructures-based electrodes and their relevant characterization.

Chapter 3

Materials and Methods

3.1 Materials Used: All the chemicals used in this research are listed in **Table 3.1.1**, which includes their manufacturer details, chemical formula, molecular weight, and general information about these chemicals. All chemicals were used as provided by the company, without any further modifications.

3.2 Synthesis Techniques: In the current study, hydrothermal, sol-gel, and microwave methods were employed for the synthesis of materials. A detailed explanation of these methods is provided below.

Hydrothermal: The hydrothermal approach has garnered significant attention among researchers and technicians across various scientific disciplines, especially over the last fifteen years. Hydrothermal or solvothermal synthesis is a widely adopted one-pot method for fabricating a wide range of TMOs [162,163]. The word "hydrothermal" typically describes a heterogeneous reaction that occurs in under the condition of high pressure and temperature. [165]. Originally rooted in geology, the term was first introduced by the British geologist Sir Roderick Murchison to describe processes in which water, subjected to elevated temperatures and pressures, induces transformations within the Earth's crust, leading to the formation of diverse minerals and rocks. This technique is well-regarded for its ability to synthesize oxide-based materials with high crystallinity and excellent morphological control [167]. Typically, the hydrothermal process involves heating a mixture of reactants in a sealed autoclave, usually made of stainless steel with a Teflon lining. Under these conditions, precursors for MOs dissolve and recrystallize as the solvent operates at elevated temperatures and pressures. The reaction temperatures commonly exceed 100°C, leading to the automatic generation of pressure within the system. One of the key advantages of the hydrothermal/solvothermal method is its environmentally friendly nature, as it eliminates the need for harmful catalysts, yielding products of high purity. Additionally, by varying reaction parameters like time and temperature, this method enables precise control over the morphology, crystallinity, and phase composition of the resulting MOs [168].

Chemical precipitation method: This method is a versatile and widely employed technique for synthesizing various materials, particularly nanoparticles, thin films, and crystalline structures. This method involves the formation of a solid precipitate from a solution when the solubility product of a compound is exceeded, typically achieved by mixing two or more

Table 3.1: A comprehensive list of the chemicals utilized in the current research.

S.No	Chemical Name	Chemical Formula	Molecular weight (g/mol)	Procured from (Company)	General Information
1.	Hydrochloric acid	HCL, (35% purity)	36.46	LOBA Chemie (India)	Highly odorous, hazardous & density: 1.18 g/cm^3.
2.	Thiourea	CH_4N_2S, (99% purity)	76.12	LOBA Chemie (India)	Reducing agent, hazardous & Melting Point:174-178 °C
3.	Ethanol	C_2H_5OH, (99.5% purity)	46.06	LOBA Chemie (India)	Highly flammable, organic solvent & density: 0.778
4.	Urea	NH_2CONH_2 (99.5% purity)	60.06	LOBA Chemie (India)	Colorless or white, odorless, highly soluble, & Melting point: 132- 133 °C
5.	Nickel Nitrate Hexahydrate	$Ni(NO_3)_2.6H_2O$ (99% purity)	290.80	LOBA Chemie (India)	Highly soluble, green crystalline solid & Melting Point:56°C
6.	Potassium Hydoxide Pellets	KOH (85% purity)	56.11	LOBA Chemie (India)	Water soluble , Odorless, & Melting Point :360–406 °C
7.	Hexamine	$C_6H_{12}N_4$	140.19	LOBA Chemie (India)	Colorless, Soluble, & Melting point: 280°C
8.	Cobalt Nitrate Hexahydrate	$Co(NO_3)_2.6H_2O$ (98% purity)	291.03	LOBA Chemie (India)	Odorless, Soluble, & Melting point: 55 °C
9.	N-Methyl 2-Pyrrolidone (NMP)	C_5H_9NO (98% purity)	99.13	LOBA Chemie (India)	Highly Chemical and thermal stability, colorless liquid, & Boiling point: 202 °C
10.	Acetone	$(CH_3)_2CO$ (99% purity)	58.08	LOBA Chemie (India)	Highly flammable, colorless liquid, boiling point of 56.05°C, & density of 0.7845 g/cm^3
12.	Graphite	C (99.9% purity)	12	Sigma Aldrich Ltd. (India)	Inert, heat resistant
13.	Polyvinlidene Fluoride (Pvdf)	$(C_2H_2F_2)_n$	-	LOBA Chemie (India)	High thermal stability & mechanical strength
14.	Acetylene Black	ClCH=CHCl, (98% purity)		Sigma Aldrich Ltd. (India)	High electrical and thermal conductivity

15.	Activated Carbon (AC)	C	12.1	Merck (USA)	Large surface area (SA)
16.	Copper sulfate pentahydrate	$CuSO_4 \cdot 5H_2O$	249.685	LOBA Chemie (India)	Blue crystalline, Soluble in water, and Odorless
17	Thioacetamide	CH_3CSNH_2	75.14	Sigma Aldrich Ltd. (India)	Soluble in water & reacts with salts of heavy metals.

reactant solutions under controlled conditions. These reactants are dissolved in appropriate solvents, and their interaction can be triggered by altering key parameters such as pH, temperature, ionic strength, or concentration. Common examples include the addition of a precipitating agent, such as ammonium hydroxide or sodium hydroxide, to a metal salt solution to produce metal hydroxides or oxides. Several factors influence the characteristics of the precipitate, including reaction kinetics, nucleation rate, and growth mechanisms. Precise control over these parameters allows tailoring of the material's properties, such as particle size, morphology, and crystallinity. For instance, slower nucleation and growth rates often yield larger, more uniform particles, while rapid precipitation may lead to smaller, less crystalline particles. The chemical precipitation method is advantageous due to its simplicity, scalability, cost-effectiveness, and ability to produce high-purity materials. It is extensively used in diverse applications, including the preparation of catalysts, semiconductors, pigments, ceramics, and environmental remediation agents [152].

Microwave-assisted synthesis: This Techniques is a relatively recent and efficient for synthesis the micro- and nano-sized crystalline materials. Compared to conventional methods, it significantly accelerates the reaction rate and reduces the overall reaction time, often completing the process within just a few minutes [192]. This rapid and energy-efficient approach leverages microwave irradiation, a widely used heating technology in both industrial and academic settings due to its simplicity, speed, cost-effectiveness, uniform heating, and energy efficiency. Microwave-assisted synthesis has been successfully employed in the production of various materials, such as porous materials [193], inorganic complexes [194], and nanocrystalline particles [195]. Despite its many advantages, one of the challenges associated with this method is achieving precise control over the morphology. This limitation arises from the difficulty in regulating the rapid and localized heating that occurs during microwave irradiation [192]. However, the benefits of microwave-assisted synthesis, particularly its ability to drastically reduce reaction times and energy consumption, make it an attractive method for producing nanomaterials.

3.3 Electrode fabrication*:* The working electrodes were fabricated using a weight percent ratio of 8:1:1 for active materials, acetylene black (as the conducting material), and PVDF (as the adhesive), respectively. NMP was supplemented to the mixture and then stirred continuously for three hours at a temperature of 70°C, resulting in the creation of a consistent slurry. Subsequently, a consistent layer of the slurry was spread evenly on the cleaned Ni foam, which had dimensions of 1 cm x 1 cm. The coated foam was then subjected to a drying process at 80 °C for a duration of 12 hours in an oven. The cathode was developed with exfoilated graphite (20%) and activated charcoal (80%). To prepare the expanded graphite powder, graphite powder was first mixed with a 30% solution of sulfuric acid for 12 hours. The filtered materials were dried for 12 hours. The remaining steps were the same as those described for the anode.

3.4 Characterization Techniques: Characterization techniques are essential in research because they provide a detailed understanding of a material's physical, chemical, structural, and functional properties, ensuring it meets the required specifications for specific applications. This detailed insight allows researchers to optimize and enhance materials by adjusting factors like composition or SA, leading to improved performance and efficiency. Additionally, characterization supports quality control and standardization, ensuring reproducibility and consistency, which are vital for both experiments and industrial applications. Moreover, new properties and phenomena discovered through these techniques often lead to innovations, driving advancements in areas such as SCs, batteries, and semiconductors. Characterization techniques used during this research are discus bellow in details.

3.4.1. X-Ray Diffraction (XRD)

XRD is commonly used in materials science, chemistry, and physics to study crystalline materials like metals, ceramics, and polymers. When X-rays are directed onto a sample, they are scattered in specific patterns based on the atomic arrangement in the material. By analyzing the diffraction pattern, XRD can reveal information about the material's crystal structure, phase composition, lattice parameters, and crystallite size [285,286].

The fundamental principle of XRD relies on the constructive interference of X-rays scattered by atoms within a crystalline material. XRD is based on Bragg's Law, which relates the wavelength of incident X-rays to the diffraction angle and the spacing between atomic planes in the crystal lattice. This relationship is expressed by the equation (3.1): [287]

$$2d \sin(\theta) = n \lambda \qquad (3.1)$$

In this equation, d, θ, n, and λ denote the interplanar spacing, Bragg's angle, order of diffraction, and X-ray wavelength, respectively. The XRD data collected by the diffractometer is compared with reference databases such as the Joint Committee on Powder Diffraction Standard

Table 3.4.1 XRD instrumentation specification used in present work.

Instrument used	**Available at**	**X-rays Wavelength**	Scanning range 2θ (Degrees)
1.Bruker D8 Advance, USA	CIF, Lovely Professional University, India.	Cu Kα1 = 1.54 Å	10 - 90º

Table 3.4.2 XRD peak positions of NiO.

2 θ	Planes
37.2°	111
43.3°	200
62.9°	220
75.4°	311
79.4°	222

Table 3.4.3 Instrumentation details used for Raman in the present work.

Instrument Used	**Available at**	**Laser used**	**Spectral Range**
Renishaw-Invia-Reflex	USIF, AMU, Aligarh, India	532 nm	100-2000 cm^{-1}

Table 3.4.4 Distinct vibrational bands in NiO.

Vibrational bands	Raman Shift position (cm^{-1})
1P	354
1P	512
2P	680
2P	802
2P	1059

(JCPDS) to identify the material composition [288]. The X-ray source, sample, and detector are the three primary components of XRD technology. A copper X-ray source emits radiation with a specific wavelength. The XRD technique can be used to analyze various types of samples, including powders, single crystals, or thin films. In this technique, a diffracted beam emitted by a monochromator is scattered from the sample's surface and detected by an oscillating detector positioned near the avg. diffraction point. The resulting diffraction pattern consists of a series of peaks, corresponding to angles (2θ) where constructive interference occurs. The position of these peaks is linked to the interplanar spacing (d-spacing), while their intensity provides information about the atomic arrangement and the types of atoms present in the crystal. It is commonly used to identify different crystalline phases by comparing the diffraction patterns with known standards. XRD can also provide information about the degree of crystallinity, as well as calculate lattice parameters, which reveal the dimensions of the unit cell. Additionally, it is useful in analyzing material texture and strain, and can quantify the proportion of phases in multi-phase systems. XRD analysis is the use of the Scherrer equation to estimate crystallite size from the broadening of diffraction peaks. This equation is expressed

$$D = K\lambda / \beta \cos \theta \qquad (3.2)$$

as where D represents the grain size, K denotes the shape factor (typically around 0.9), λ denotes the X-ray wavelength, β represent the full width at half maximum of the peak, and θ represents the Bragg angle. The Scherrer equation is particularly effective for analyzing small crystals, typically less than 100 nm, where peak broadening results from the finite size of the crystallites [289,290].

3.4.2 Raman characterization: Raman spectroscopy is a commonly used non-destructive technique that offers detailed insights into the vibrational, structural, and chemical properties of materials. It works by measuring the inelastic scattering of monochromatic light, typically from a laser, as it interacts with the sample. During this interaction, the scattered light experiences an energy shift due to molecular vibrations, phonons, or other excitations in the material, a phenomenon known as the Raman effect. This energy shift is associated with specific vibrational modes of the molecules, enabling the Raman spectrum to act as a molecular fingerprint for the material. In material science, Raman spectroscopy plays a crucial role in characterizing MOs, Raman spectroscopy can offer valuable information about the material's phase purity, bonding environment, and oxidation states. Additionally, Raman spectroscopy is particularly sensitive to nanostructures, enabling researchers to analyze composite materials and investigate interactions between different phases, such as in carbon-metal oxide hybrids. Raman spectroscopies include its non-destructive nature, minimal sample preparation, and the ability to perform both surface and bulk analyses. It can also be used for in situ monitoring of phase transitions or chemical changes during the operation of SCs, making it a valuable tool for understanding and improving material performance [291-294].

3.4.3. Field Emission-Scanning Electron Microscopy (FESEM): FESEM provides high-resolution imaging for analyzing the surface features and microstructure of materials. It functions by directing a focused electron beam onto the sample's surface, where it interacts with the atoms of the material to generate signals that are utilized to create detailed images. FESEM is distinguished from conventional SEM by its use of a field-emission electron source, which provides a highly focused electron beam, resulting in much finer surface details, often at the nanoscale. This makes FESEM particularly useful for analyzing the structural and morphological properties of materials used ES devices like SCs [295,296].

Table 3.4.5 Instrumentation specifications used for FESEM and EDS analysis in the current study.

Instrument Used	Available at	Magnifications
1. JEOL JSM-7610F Plus 2. EDS (OXFORD EDS LN2)	CIF, LPU, Punjab, India	100 µm- 100 nm

FESEM provides critical information about surface features such as porosity, particle size, and surface roughness, all of which directly influence the charge storage capability of materials. In the case of MOs, such as NiO MnO_2, TiO_2, or RuO_2, FESEM enables the examination of nanoscale characteristics such as particle distribution and morphology, which are crucial for enhancing ion diffusion and overall capacitance. Furthermore, in hybrid materials, such as carbon-metal oxide composites, FESEM provides insights into the distribution of phases, interface quality, and potential defects, helping researchers optimize material design for better performance [297-299]. FESEM include its ability to provide high-resolution images at the nanoscale, allowing detailed surface analysis without extensive sample preparation [300].

3.4.4. Energy Dispersive X-Ray Spectroscopy (EDS): EDS is an effective analytical method for identifying the elemental composition of materials. When combined with electron microscopy techniques like SEM or FESEM, EDS functions by detecting X-rays emitted from a sample that is subjected to a high-energy electron beam. Since these X-rays are unique to specific elements in the material, this enables precise elemental analysis.EDS provides both qualitative and quantitative data on the presence and concentration of elements, enabling researchers to map the elemental distribution across a sample's surface. In the context of SC materials, EDS is invaluable for confirming the presence of desired elements in electrode materials, such as MOs, or doped compounds. For example, in MO electrodes (e.g., NiO or ZnO), EDS helps verify the stoichiometry and detect any impurities that may affect the material's performance. When studying composite materials, such as carbon-metal oxide hybrids, EDS mapping can provide insights into the spatial distribution of elements within a material, offering insights into the uniformity of the composite and the interaction between phases. EDS is its ability to provide localized elemental analysis, even at the nanoscale, without requiring extensive sample preparation. This makes it an essential tool for complementing morphological studies, ensuring that the material's elemental composition aligns with its expected performance characteristics [301-303].

3.4.5 High-Resolution Transmission Electron Microscopy (HRTEM): HRTEM is an advanced form of TEM that allows for imaging materials at atomic resolution. HRTEM uses a highly focused beam of electrons transmitted through an ultra-thin sample to produce images with atomic-level detail. The technique relies on phase contrast imaging, where variations in the electron wave phase, caused by interactions with the sample's atomic structure, are converted into contrast in the final image.

The principle of HRTEM relies on the interaction between a high-energy electron beam and a thin sample, during which the transmitted electrons experience both elastic and inelastic scattering. As the electrons traverse the sample, they undergo phase shifts resulting from their interactions with the atomic structure. These phase shifts contain detailed information about the arrangement of atoms within the material. In HRTEM, electromagnetic lenses are used to focus the transmitted electrons and form an image, which is based on phase contrast. The contrast in the image arises from differences in the electron wave phase and amplitude, reflecting the atomic-level structure of the sample. By using a highly focused electron beam and taking advantage of the short wavelength of electrons, HRTEM can achieve atomic resolution, allowing for the visualization of individual atoms, lattice planes, and crystal defects. HRTEM is helpful for studying the fine structural details of materials at the atomic scale. HRTEM is widely used for atomic-scale imaging, allowing direct visualization of atomic arrangements in various materials, such as metals, semiconductors, and nanomaterials. HRTEM is also key in characterizing nanostructures like NPs, nanowires, and quantum dots, offering detailed insights into their morphology and structure at the atomic level. Additionally, it is commonly employed to investigate interfaces in composite materials and thin films, where atomic-level interactions significantly impact material behavior. HRTEM's ability to resolve lattice fringes also makes it invaluable for phase identification in materials with complex atomic structures. In catalysis research, HRTEM is used to study the atomic structure of catalysts, aiding in the optimization of their performance in chemical reactions [304,305].

3.4.6 Selected Area Electron Diffraction (SAED): SAED is typically performed in conjunction with HRTEM to obtain crystallographic information about the sample. In SAED, a high-energy electron beam is utilized, and a circular aperture is placed in the back focal plane of the objective lens, permitting electrons from a specific sample area to pass through while blocking the rest. As the electrons interact with the crystalline regions of the sample, they scatter in specific directions, generating a diffraction pattern on a detector. This pattern consists of a series of spots (or rings for polycrystalline samples) that reflect the periodic arrangement of atoms within the crystal lattice. By analyzing these diffraction patterns, one can determine the crystallographic orientation, unit cell dimensions, and possible crystal structures. Together, HRTEM and SAED are powerful tools for characterizing the structure of materials, making them essential in fields such as materials science, nanotechnology, and solid-state physics. SAED, often used alongside HRTEM, is a powerful tool for crystallographic analysis. SAED

Table 3.4.6 Instrumentation specifications used for HRTEM in the present study.

Instrument Used	Available at	Magnifications	Software Used
JEOL Model: JEM 2100 Plus	CIL, PU, Punjab, India	10nm - 500 nm	ImageJ

provides detailed information about a material's crystal structure and symmetry by generating diffraction patterns based on the interaction of electrons with atomic planes. It is frequently used for phase identification, distinguishing between different crystalline phases in multi-phase materials. SAED also helps determine grain size and orientation in polycrystalline samples, which is important for understanding their physical properties. By analyzing diffraction patterns, SAED allows for precise measurement of lattice parameters, aiding in the identification of unknown materials. In the study of nanomaterials, SAED provides information on crystallinity, phase, and defects, while in strained films or heterostructures, it is used to assess strain and lattice distortions through shifts in diffraction patterns [305,306].

3.4.7 BET theory: BET analysis is a commonly used to assess the SA and porosity of materials through gas adsorption measurements. In this method, a gas typically nitrogen is adsorbed onto the material's surface at a constant temperature, with the quantity of adsorbed gas being recorded relative to pressure. The BET theory is then used to interpret this data and determine the SSA, a key property for materials utilized in ES devices like SCs. For SCs, BET analysis is crucial in evaluating the SSA and pore size distribution of materials. This analysis ensures that the material provides sufficient active sites for ion adsorption and storage, optimizing its performance in ES applications. Additionally, for materials like MOs or nanocomposites, BET can reveal information about the material's porosity, which affects ion transport and the overall capacitance performance. A well-defined pore structure, especially in mesoporous or microporous materials, can significantly enhance charge storage by allowing easy access for EL ions. The main advantage of BET characterization is its ability to provide detailed information on SA and porosity, which are critical for optimizing the performance of SCs. By analyzing the surface properties, researchers can better design materials with the ideal balance of SA and pore size, leading to improved ES capabilities [307,308].

3.4.8 X-ray photoelectron spectroscopy (XPS): XPS is a highly sensitive method used to analyze the surface composition, chemical states, and electronic structure of materials. When a material is irradiated with X-rays, it emits photoelectrons from its surface atoms. By measuring the energy of these emitted photoelectrons, XPS can determine the elements present and their chemical bonding environments Due to its surface sensitivity, typically probing

Table 3.4.7 Instrumentation specifications used for BET in the present study.

Instrument used	**Available at**	Degassing Temperature	**Degassing Time**
1. Quantachrome Instruments version 5.21, Austria.	SAIF, Chandigarh, India	200 °C	3 h
2. NOVA touch 2LX	Scientium Analyze Solution, Jaipur, Rajasthan, India	200 °C	3 h

Table 3.4.8 Instrumentation details used for XPS in the present work.

Instrument Used	**Available at**	**Range**
1.ThermoScientific NEXA Surface analyzer	CIF, IIT Jammu	0- 1350 eV

Table 3.4.9 Here is a suggested format for presenting the B.E values for nickel (Ni) and oxygen (O) in a table format suitable for XPS characterization of NiO:

Element	**B.E (eV) (Approximate)**	**Description**
1. Ni	855	Ni $2P_{3/2}$ and
	872.6	Ni $2P_{1/2}$
	861	Ni $2P_{3/2}$ (Satellite Peaks)
	879	Ni $2P_{1/2}$ (Satellite Peaks)
2. O	529.8	metal-oxygen bonds
	531	surface-adsorbed oxygen

depths of 1–10 nm, XPS is particularly effective for studying thin films, coatings, and surface modifications. In SC research, XPS have important role in characterizing the surface chemistry of electrode materials, as surface interactions directly influence electrochemical performance. For MOs like NiO, TiO_2, or RuO_2, XPS helps determine the oxidation states of the metal ions, which are critical for understanding the pseudocapacitive behavior of the material. The ability of XPS to detect trace elements or contaminants also helps ensure that the material's surface composition is optimized for ES applications. XPS is advantageous because it not only identifies the elemental composition of the surface but also provides detailed chemical state information. This is a useful method for analyzing the impact of surface modifications, such as doping or functionalization, on the electrochemical performance of SCs [311,312].

3.4.9 Electrochemical Techniques: The electrochemical characterization of SCs includes techniques such as CV, GCD, and EIS. These methods provide accurate measurements of various electrochemical characteristics, including Cs, E_D, P_D, cyclic stability, and impedance. The CV technique measures the current generated in an electrochemical cell as the voltage is linearly ramped over time. CV is widely used to assess the electrochemical properties of

Table 3.4.10 Instrumentation specifications used for electrochemical technique in the present study.

Instrument used	Available at
1. Metrohm: Multi-Channel Autolab	CIF, LPU, Punjab, India

materials, including capacitance, oxidation/reduction reactions, and the electrochemical stability of SCs. GCD technique used to evaluate the performance of SCs device, by applying a constant current to charge and discharge the device while measuring the voltage responseover time. GCD is commonly used to determine key performance metrics like capacitance, E_D, and P_D. EIS is used to measure the impedance of an electrochemical system over a range of frequencies. It provides insights into the electrochemical behavior of materials, such as charge transfer resistance, and ion diffusion in SCs. Electrochemical techniques are applicable for evaluating the performance of SCs within electrochemical systems, effectively demonstrating their capabilities in the context of three- and two-electrode setups. There are three types of main electrode used during electrochemical techniques. All three main electrodes used during the electrode techniques explain below.

- **Counter electrode (CE):** In an electrochemical cell, the current circuit is completed using an electrode known as the CE, also referred to as the auxiliary electrode. This electrode typically comprises an inert material, such as platinum, gold, graphite, or glassy carbon, and serves as the site for the half-redox reaction not under investigation. To prevent kinetic limitations in the electrochemical processes being studied, the total SA of the CE (acting as both the source and sink of electrons) must exceed that of the WE, as the current flows between the two.
- **Reference electrode (RE):** RE is characterized by a stable and well-established electrode potential, serving as a reference point in an electrochemical cell for controlling and measuring potential. This reference electrode potential is typically established using a redox system that maintains consistent concentrations of all participants in the redox reaction, achieved through buffering or saturating the solution.
- **Working electrode (WE):** The WE in which the specific half-redox reaction of interest occurs in an electrochemical system. Typical materials for working electrodes include unreactive substances such as Au, Ag, Pt, glassy carbon, Hg drops, and film electrodes. The dimensions and configuration of the working electrode vary depending on the specific application.

Basic principle of a potentiostat/ galvanostat (PGSTAT): When the PGSTAT is set to potentiostatic mode, it precisely controls the potential difference between the WE and the RE to match a user-specified value. Simultaneously, the potential of the CE relative to the working electrode is also accurately regulated. In galvanostatic mode, the WE and CE can control the current flow. Continuous monitoring is performed to track the current flowing between the CE and WE, as well as the potential difference between the RE and WE [313,314].

Formula used: To calculate the Cs (in F/g) of the electrode from the CV curve, the following equation (4.3) is used:

$$\text{Cs} = \frac{Area\ under\ the\ curve}{2 \times m \times V \times v} \tag{4.3}$$

Where , the area under the curve is in square meters (m^2), m is the active mass deposited on electrode (in grams), V is the Potential window (in Volts), and v is the Scan rate (mV/sec). To calculate the Cs (in F/g) of the electrode from the GCD curve, the following equation (4.4) is used:

$$\text{Cs} = \frac{I \times t}{m \times V} \tag{4.4}$$

For, Cs (in C/g)

$$\text{Cs} = \frac{I \times t}{m} \tag{4.5}$$

Where , I is the current applied (in A), and t is the discharging time (in sec).

To calculate the E_D (in Wh/Kg) of the SC device ,the following equation (4.6) is used:

$$E_D = \frac{Cs \times V \times V}{2 \times 3.6} \tag{4.6}$$

To calculate the P_D (in kW/kg) of the SC device ,the following equation (4.7) is used [315]:

$$P_D = \frac{Ed \times 3.6}{t} \tag{4.7}$$

Electrochemical techniques are important for the evaluating the performance of SCs by providing detailed insights into their ES capacity, efficiency, and long-term durability. One commonly used technique is CV, which helps study the charge-discharge behavior and provides information on capacitance, charge storage mechanisms, and overall stability. GCD, another important method, measures Cs, E_D, and P_D by charging and discharging the SC at a constant current. It also helps assess internal resistance through the analysis of charge-discharge curves. EIS is used to investigate internal resistance, ion diffusion, and charge-transfer processes by measuring the system’s response to alternating current across different frequencies. This technique aids in analyzing the frequency-dependent behavior and optimizing device performance [313,314]

Chapter 4

3D highly porous microspherical morphology of NiO nanoparticles for Supercapacitor application

4.1 Introduction

Throughout the past century, fossil fuels have primarily fulfilled the demand for energy. However, their extensive use has led to the depletion of natural resources and contributed to numerous environmental issues that harm human health. This has driven the need to develop green energy sources and more sustainable ES devices. Currently, electrical ES is limited to devices such as fuel cells, capacitors, and batteries, each with its own advantages and disadvantages regarding of ES device. Supercapacitors (SCs) have surfaced as a viable alternative offering high power density without relying on intense chemical reactions [316-318]. Unlike batteries, SCs are lightweight, non-toxic, and don't require bulky electrodes, which minimizes disposal challenges. This makes them particularly suitable for applications that require cost-effectiveness, long cyclic life, rapid charge-discharge capabilities, and high-power density.[319-320] SCs can be categorized main types based on their electrode materials: EDLCs and PCs [321,322]. PCs primarily store charge through a Faradaic process involving redox reactions at the electrode surface, allowing them to achieve higher energy densities compared to EDLCs [323]. The choice of electrode material is critical in determining the electrochemical performance of any SC. TMOs are commonly used in PCs due to their high theoretical capacitance and reasonable conductivity. Notable TMOs include ruthenium oxide (RuO_2), cobalt oxide (Co_3O_4), molybdenum trioxide (MoO_3), manganese dioxide (MnO_2), vanadium pentoxide (V_2O_5), nickel oxide (NiO), and nickel cobalt oxide ($NiCo_2O_4$) [324-326]. For example, RuO_2 is valued for its high theoretical capacitance, and high electrical conductivity. However, its high cost and environmental concerns limit its commercial use in SC devices. Similarly, while Co_3O_4 is promising, its narrow potential window restricts its practical effectiveness. MnO_2 is another material commonly used, yet its low electrical conductivity poses a challenge for enhancing its capacitive performance and power output. On the other hand, NiO presents several advantages, including high theoretical capacitance, cost-effectiveness, good thermal and chemical stability, and environmentally friendly properties. NiO are especially well-suited for SC electrode materials due to their high SA, stability, and ability to exist in multiple oxidation states within a particular potential range, achieving a theoretical capacitance of around 2573 F/g [327]. NiO can be synthesized through various methods, including hydrothermal, sputtering, electrochemical, and sol gel approaches [328-332]. Among these, the hydrothermal/solvothermal method is especially environmentally friendly, requiring no harmful catalysts and producing high-purity products. This method also allows precise control over morphology, crystallinity, and phase composition by adjusting reaction parameters like time and temperature [328]. An ideal electrolyte (EL) can improve E_D, power output, and cycle life while reducing internal resistance and self-discharge rates of SCs. For instance, Dhas et al. reported that NiO performs well in alkaline KOH compared to Na_2SO_4 due to KOH's high ionic conductivity. Moreover, the surface morphology of the electrode material significantly impacts performance, as innovative nanostructures can greatly enhance conductivity and active SA, contributing to more efficient and powerful SCs [333]. The surface morphological characteristics of the electrode material have a considerable impact on its performance as its conductivity and active SA can be considerably increased by creating innovative nanostructures. For example, Ali et al. [334] reported a very high Cs of 1782 F/g was demonstrated by 3D NiO grown on Ni foam at 1 A/g. By increasing the Ni concentration in the NiO material, Ci et al. [335] were able to produce NiO microflowers with enhanced electrochemical performance, i.e. 1828 F/g at 0.5 A/g. Cao et al. reported the preparation and characterization of hierarchical porous array of NiO nanotubes for SC applications. The Cs of 675 F/g was exhibited by NiO microflowers at 2A/g [336]. The Cs of 762F/g was demonstrated by synthesized flower-like microspheres of nano-NiO as an electrode material at 1A/g [337]. It is well acceptable that the electrode's performance is affected by a variety of factors, such as the material's SA, porosity and morphology, and so, more studies on these factors are still under pursual. By changing the reaction temperature and the concentration of reactants, it is possible to control the size, growth, and morphology of the electrode material during synthesis.

The concentration of the reactant controls the pH of the growth solution. While synthesizing NiO NPs, the pH of the growth medium can also be easily regulated by varying the concentration of urea [338]. Here, we report on the impact of urea concentration and reaction temperature on the electrochemical performance of NiO NP-based electrodes. This article examines how complexing agents affect the morphology of NiO. This article also compares the electrochemical performance of binder-enriched paste electrodes with that of binder-free electrodes.

4.2 Material synthesis and electrode preparation

First, 0.1 M $Ni(NO_3)_2 \cdot 6H_2O$ and 0.2 M urea were mixed in 60 mL of deionized (DI) water and stirred for 20 minutes. The solution was then placed in an autoclave and maintained at 110 °C, 150 °C, or 200 °C for 6 hours. The resulting $Ni(OH)_2$ precipitates were filtered, rinsed with DI water, ethanol, and acetone, and subsequently dried in an oven at 70 °C. The complete synthesis process is described by the following reactions:

$$(H_2N)_2CO + H_2O \rightarrow 2NH_3 + CO_2 \qquad (4.1)$$

$$NH_3 + H_2O \rightarrow NH_4 + OH \qquad (4.2)$$

$$2Ni(NO_3) \rightarrow Ni^{+2} + 2NO^{-3} \qquad (4.3)$$

$$Ni^{+2} + 2OH \rightarrow Ni(OH)_2 \qquad (4.4)$$

Finally, the $Ni(OH)_2$ precursors synthesized at various temperatures were heated at 300 °C for 2 hours to yield different NiO nanoparticles. The same approach was applied to produce another set of NiO nanoparticles by adjusting the nickel nitrate-to-urea ratios to 01:01, 01:02, 01:05, and 01:08. The resulting samples were labeled as S:1, S:2, S:5, and S:8.

4.3 Result and discussion

4.3.1 Structural and morphological analysis: The XRD patterns of NiO (S:2) NPs synthesized at different reaction temperatures, i.e. 110 °C, 150 °C and 200 °C, are shown in Fig. 4.1a. The peaks at 37.2°, 43.3°, 62.9°, 75.4° and 79.4°, are observed in the diffraction curves of all studied reaction temperatures, displaying the presence of (111), (200), (220), (311) and (222) planes, respectively.The peak positions of all XRD patterns are well-mapped with the PDF (ICSD) 01–089-5881, which confirms the formation of cubic NiO NPs. The sharpening of the prominent peaks was noticed with the increase of reaction temperature, indicating the growth of crystalline size. The crystallite size of NiO NPs synthesized at 110 °C, 150 °C and 200 °C was measured as 29 nm, 34 nm and 41 nm, respectively [339, 340], which suggests that the NPs synthesized at 110°C would be more suitable as an active electrode

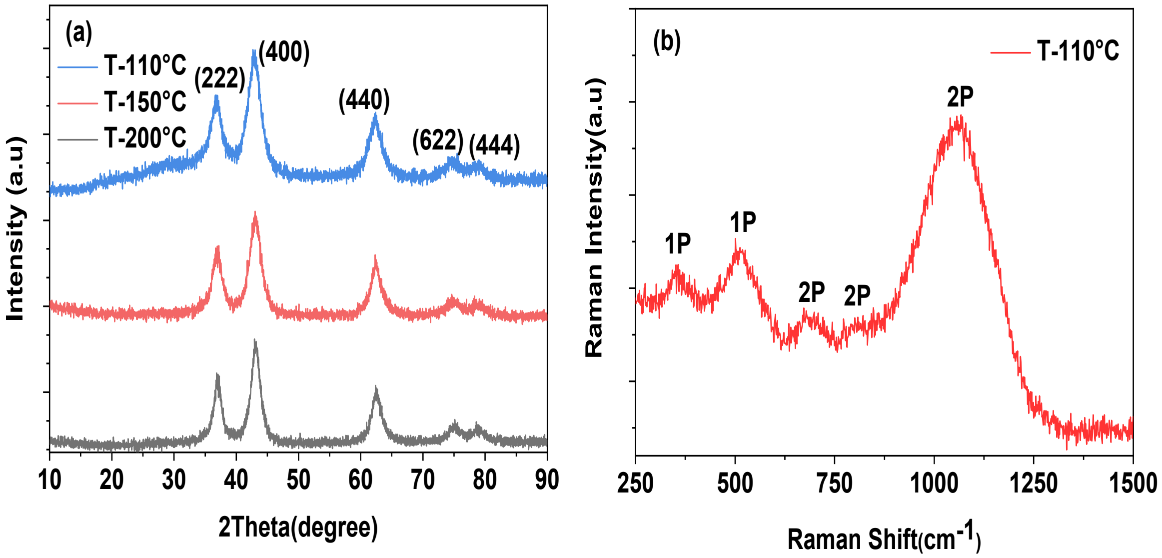

Fig. 4.1 The XRD patterns of NiO (S:2) NPs synthesized at different reaction temperatures (a). Raman spectrum of NiO NPs synthesized at 110 °C (b)

material for SC application as it can provide more SA for electrochemical interactions. The formation of NiO NPs was further confirmed through Raman analysis. The Raman spectrum of S:2 sample synthesized at 110 °C is shown in Fig. 4.1b. The presence of all five vibrational

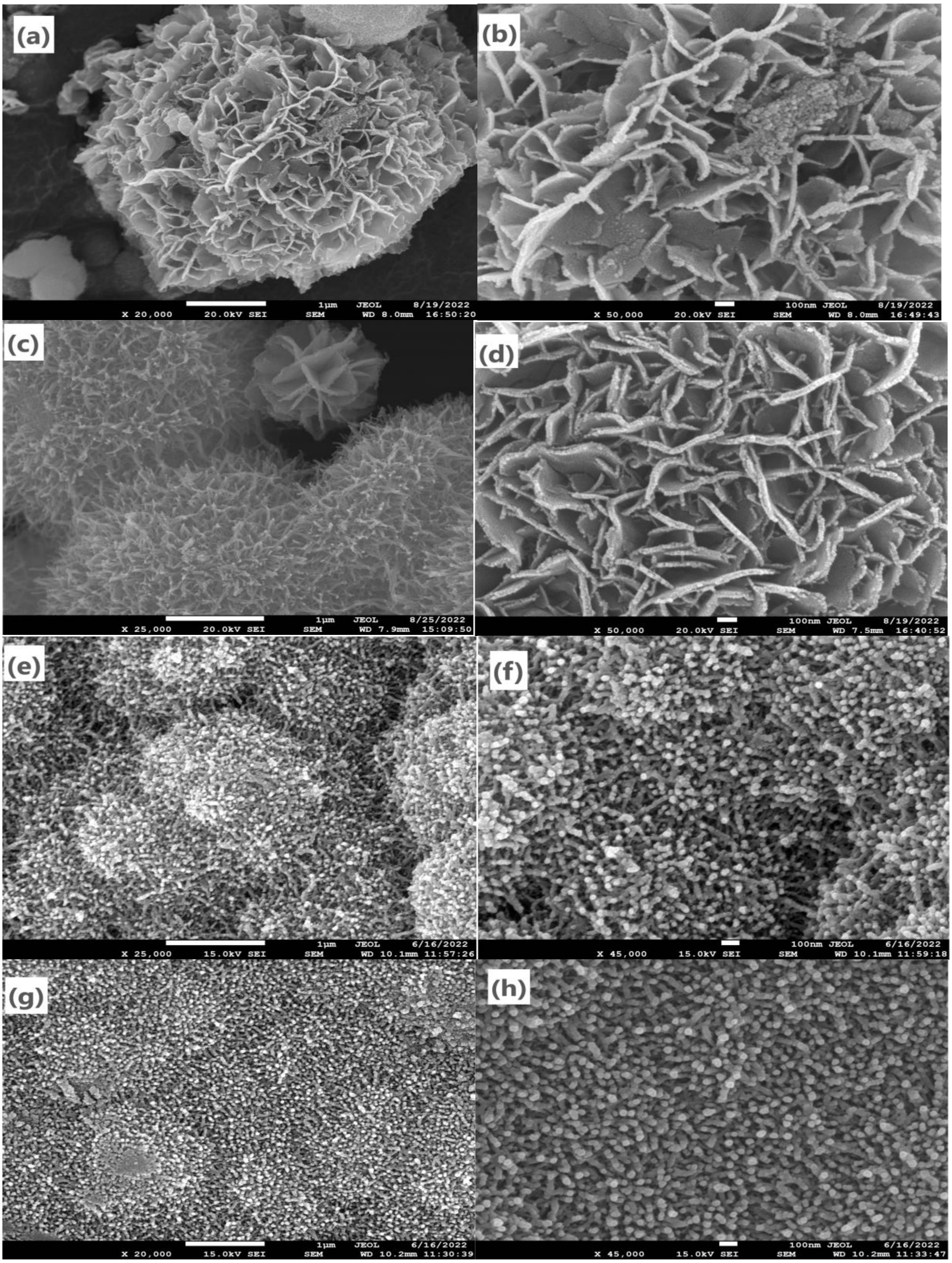

Fig. 4.2 FESEM images at different magnifications a, b S:1, c, d S:2, e, f S:5 and g, h S:8

bands, i.e. single phonon (1P) vibrations at 354 cm^{-1} and 512 cm^{-1}, and double phonon (2P) vibrations at 680 cm^{-1}, 802 cm^{-1} and 1059 cm^{-1}, clearly reveals the formation of NiO NPs and corroborates the findings of XRD analysis [341, 342]. The microstructural and morphological details of the NiO NPs synthesized at 110 °C with different urea concentrations, i.e. S:1, S:2, S:5 and S:8, are explored with FESEM, and their micrographs at different magnifications are displayed in Fig. 4.2a–h. A periodical array of nanosheets is unveiled, when the concentration of urea was less, i.e. S:1 and S:2, but as the concentration of the complexing agent was

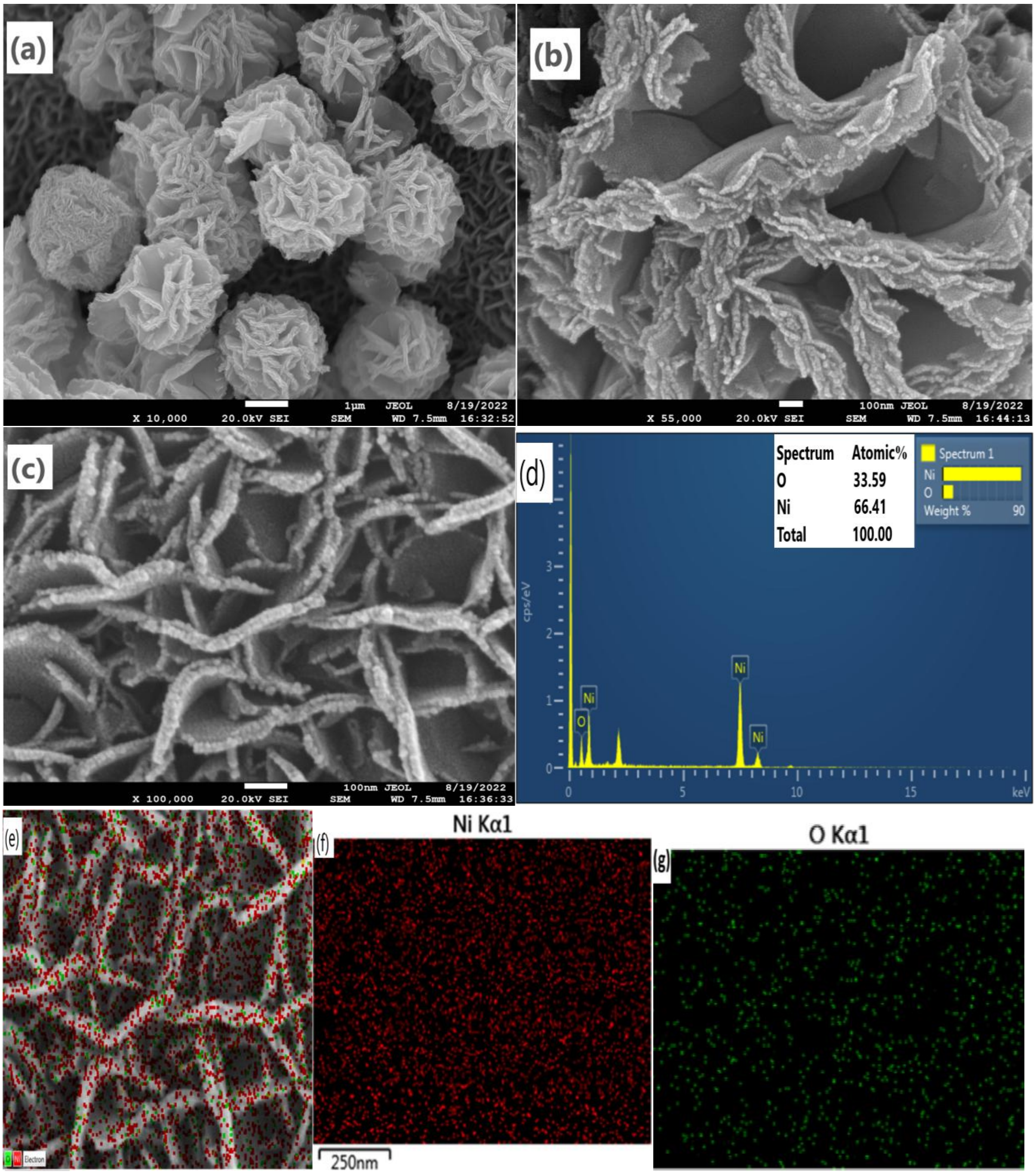

Fig. 4.3 FESEM images of NiO (S:2) nanostructures deposited on nickel foam **(a, b and c)** and their EDS mapping **(d–g)**

increased, i.e. S:5, the shape of the NPs become nanospheres, whose size was further reduced when the concentration of urea during the reaction mechanism was increased eight times the nickel nitrate, i.e. S:8. It is observed from Fig. 4.2 that the porosity of NiO nanosheets was maximum when the proportion of nickel nitrate and urea in the growth solution was 1:2, i.e. S:2. It is further noticed that various nanosheets were collecting together to form highly porous microsphere to adjust their surface energy, as can be seen from Fig. 4.2c. It is analysed from the FESEM images that the NPs associated with S:2 sample can be a more suitable candidate as an electrode material due to their enhanced SA and highly porous morphology. On contrary, when synthesize was done with higher concentration of urea, the size of the NiO NPs was reduced considerably, and they packed themselves so densely as shown in the Fig. 4.2e–h. This morphology is not suitable for the electrochemical processes as it may increase the diffusion resistance by trapping the ions. In Fig. 4.3a–c, FESEM images of NiO nanostructures (S:2) synthesized at 110 °C and successfully grown on nickel foam are displayed. Their EDS mapping shown in Fig. 4.3d–g is manifesting the uniform distribution of Ni and O. Availability of large number of highly porous microspheres, as can be seen in the Fig. 4.3a, is disclosing the accessibility of large SA for electrochemical interaction. The presence of minute nanostructure on the edges of the nanosheets (Fig. 4.3b) is further endorsing the enhanced SA and highly porous character of the synthesized material. The SSA of S2 was meticulously calculated using the BET technique, which involved analyzing the nitrogen (N_2) sorption isotherms at 77 K. The specimens were subjected to a degassing process for 3 hours at 200 °C to remove any adsorbed moisture or gases that could interfere with the measurement.

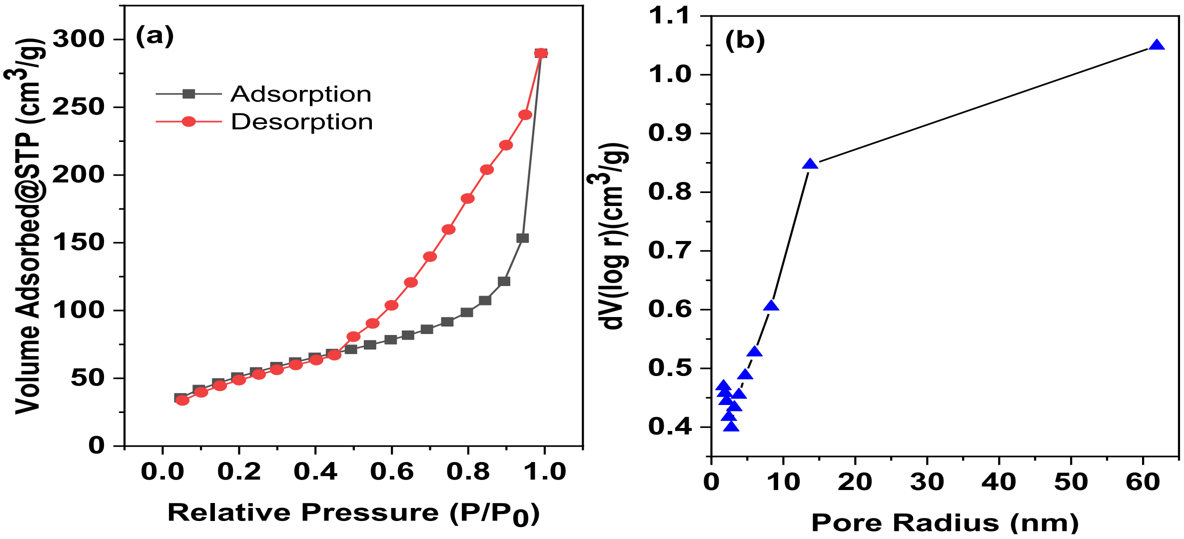

Fig. 4.4 Nitrogen adsorption–desorption isotherm **(a)** and plot between pore volume and pore radius **(b)** of NiO NPs

The resulting N_2 adsorption-desorption isotherms exhibited distinct hysteresis loops, indicative of the textural properties of the materials, as depicted in Fig. 4.4. Upon examination of the plots, the BET surface-area values were measured as 185.6 m2/g. The avg. pore size in the synthesized NiO was determined to be 4.8 nm [333, 337]. These results of BET and BJH analysis are further supporting the finding of FESEM and XRD analysis and suggesting the potential use of the synthesized NiO nanosheets in the SC application.

4.3.2 Electrochemical analysis: The electrochemical performance of NiO NPs deposited on nickel foam with binder (NiO@NFBE) and without binder (NiO@NFBF) has been assessed by CV, GCD measurement and EIS was conducted using a three-electrode setup with 6 M KOH as the EL. CV curves were recorded within a potential window of -0.01 to 0.5 V. Figure 4.5a presents the CV curves of NiO (S:2) nanoparticles synthesized at various reaction temperatures. A comparison reveals that the CV curve area for NiO@NFBE prepared with nanoparticles synthesized at 110 °C is larger than those prepared at 150 °C and 200 °C. The variation in specific capacities with reaction temperature is plotted in Figure 4.5b, indicating a decrease in specific capacity with increasing reaction temperature. The maximum specific capacity achieved was 394 C/g (788 F/g) for NiO@NFBE with nanoparticles synthesized at 110 °C. This enhancement may be attributed to the smaller crystallite size of the NiO nanoparticles formed at lower temperatures, which provides a larger surface area for electrochemical reactions [339, 340]. Figure 4.5c illustrates the CV curves of NiO@NFBE prepared with nanoparticles synthesized at 110 °C under varying urea concentrations., i.e. S:1, S:2, S:5 and S:8, at a scan rate (v) of 10 mV/s. It is observed that the CV curve of NiO@NFBE prepared with S:2 sample has encompassed more area as compared to those of S:1, S:5 and S:8. The variation of their specific capacities with different urea concentration is plotted in Fig. 4.5d. It is observed that the value of specific capacity was maximum, i.e. 394 C/g (788 F/g) for NiO@NFBE prepared with the NPs of S:2 sample. This may be ascribed to the highly porous periodical array of NiO nanosheets as is seen in FESEM analysis, which were able to provide large SA for the interaction between the electrode material and the EL. The dependence of nitrate/urea ratio played a crucial role in the synthesis of NiO nanostructures, as excess urea enhances the basicity of the solution, which in turn affected the morphology of the synthesized NPs. As compared to other ratios of nitrate and urea, probably 01/02 ratio was able to provide the most optimized concentration for the development of the nanostructures with enhanced SA and highly porous morphology. Further, the effect of binder was analysed under the same conditions by plotting the CV curves of NiO@NFBE and NiO@NFBF prepared with the nanosheets of S:2 (110 °C) sample as shown in Fig. 4.5e. It is noticed that the binder-free electrode displayed considerably higher specific capacity, i.e. 408 C/g (815 F/g) as compared to the binder-enriched electrode. The superior CV performance of the binder-free electrode can be attributed to the direct growth of highly porous microspheres, composed of a periodic array of NiO nanosheets on the nickel substrate, along with the elimination of resistive binder effects. Figure 4.5f shows the CV curves of NiO@NF (S:2) across various scan rates (v), from 10 to 200 mV/s. The presence of a redox peak pair across the full v range reflects the Faradic capacitive nature of the binder-free electrode. The anodic peak between 0.25 and 0.4 V is associated with the reduction of NiO to NiOOH, while the cathodic peak between 0.1 and 0.25 V corresponds to the oxidation of NiOOH back to NiO. The CV curve shape remains consistent, and the area under the curve increases with higher scan rates, indicating good

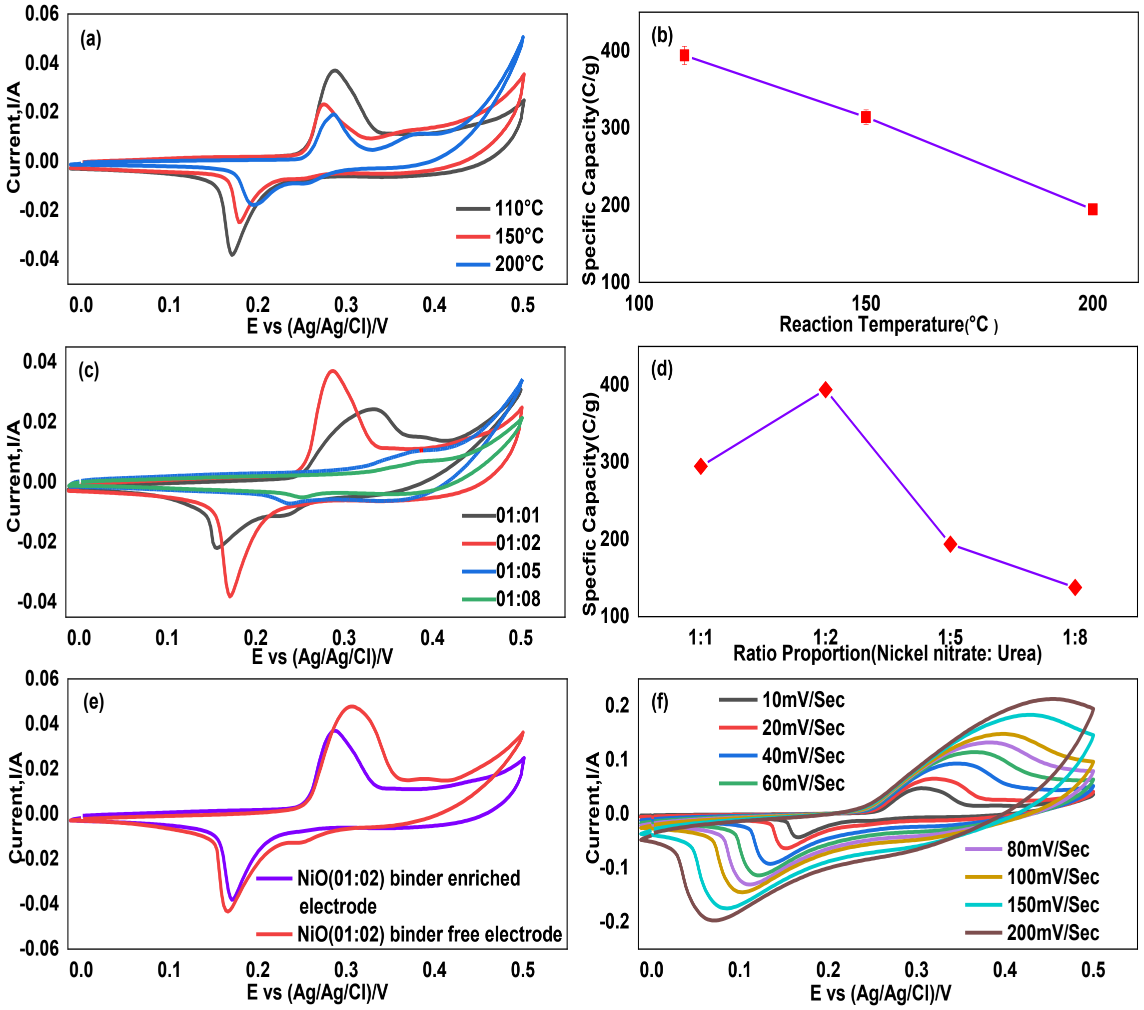

Fig. 4.5 a The CV curve NiO (01:02) NPs synthesized at different reaction temperatures at 10 mV/s. b Graph representing the variation between specific capacity and reaction temperature. **c** The CV curves of NiO NPs synthesized by varying the concentration of urea at 10 mV/s. **d** Graph representing the variation between specific capacity and urea concentration at 10 mV/s. **e** The CV curves of NiO (01:02) NP-based binder-enriched and binder-free electrode at 10 mV/s. **f** The CV curves of NiO (01:02) NP-based binder-free electrode at various v.

electrochemical reversibility. The anodic and cathodic peak shifts to higher and lower potentials, respectively, with increasing v, are due to rapid charge transfer at the electrode-electrolyte interface. The influence of reaction temperature and urea concentration on the measurements conducted between 0 and 0.4 V.The GCD curves at a current density of 1 A/g,

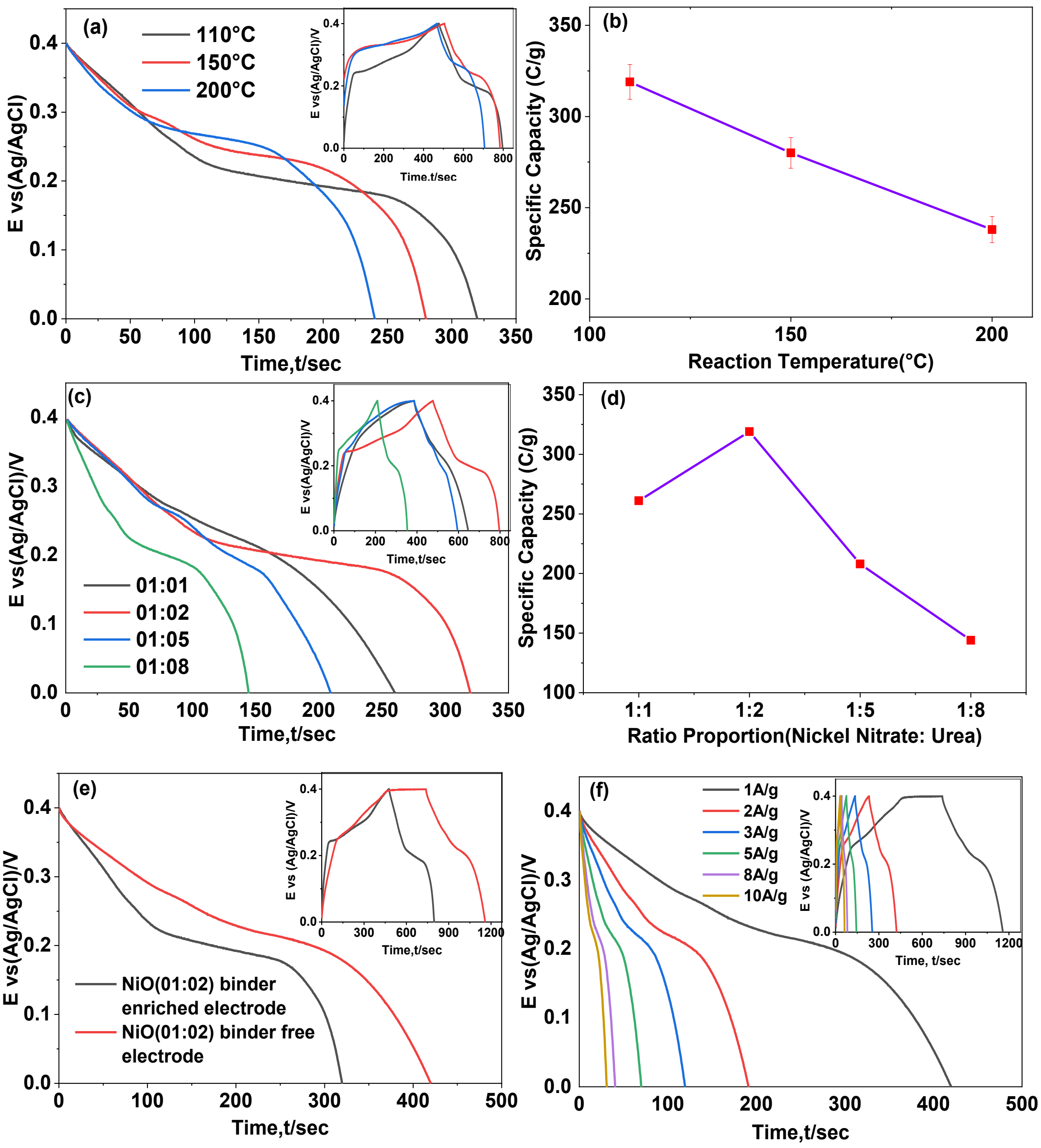

Fig. 4.6 **a** The GCD curve NiO (01:02) NP synthesized at different reaction temperatures at constant current density of 1A/g. **b** Graph representing the variation between specific capacity and reaction temperature. **c** The GCD curves of NiO NPs synthesized by varying the concentration of urea at constant current density of 1A/g. **d** Graph representing the variation between specific capacity and urea concentration at 10 mV/s. **e** The GCD curves of NiO (01:02) NP-based binder-enriched and binder-free electrode at 10 mV/s. **f** The GCD curves of NiO (01:02) NP-based binder-free electrode at various current densities. The insets are representing the complete charging and discharging behaviours of the studied electrodes.

for NiO@NFBE synthesized at different reaction temperatures and with various urea concentrations, are shown in Figures 4.6a and 4.6c, respectively. It is marked that the variation of specific capacities with reaction temperature and urea concentration as shown in Fig. 4.6b and d, respectively, is exactly replicating the same trend, as was noticed in the CV. This replication confirmed that NiO@NFBE prepared with S:2 nanoparticles synthesized at 110 °C outperforms the other studied electrodes. The maximum specific capacity of the binder-enriched electrode, calculated from GCD measurements, was 319 C/g (797.5 F/g). This improvement is likely due to the highly porous periodic array of NiO nanosheets, as observed in CV and FESEM analyses. Additionally, Figure 4.6(e) shows that the binder-free electrode NiO@NFBF, prepared with S:2 nanosheets (110 °C), achieved a significantly higher specific capacity of 418 C/g (1045 F/g) compared to the binder-enriched electrode. The lack of binder resistance and the direct growth of highly porous microspheres on the nickel substrate enable faster ion kinetics and maximize the availability of redox reaction sites. Figure 4.6f displays the GCD curves for NiO@NFBF (S:2) at current densities from 1 to 10 A/g. The specific capacities calculated are 418 C/g (1045 F/g), 381 C/g (952.5 F/g), 355 C/g (888.75 F/g), 347.5 C/g (868 F/g), and 316 C/g (790 F/g) at 1 A/g, 2 A/g, 3 A/g, 5 A/g, 8 A/g, and 10 A/g, respectively. A decrease in discharge duration and specific capacity for NiO@NFBF (S:2) was observed at higher current densities, likely due to limited interaction time between Els ions and

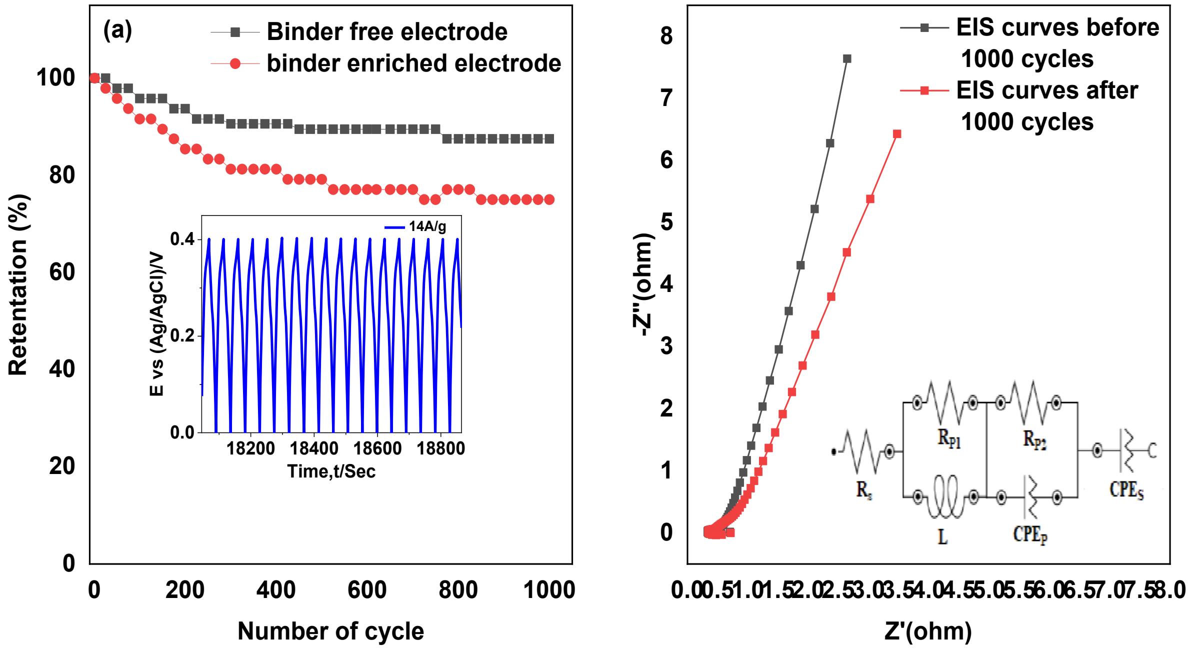

Fig. 4.7 a The variation in the retention percentage of specific capacity with the number of cycles at 14A/g. **b** The EIS curves of the binder-free and their equivalent circuit diagram.

Table 4.1. The reported electrochemical performance of NiO nanostructure-based electrodes under different experimental conditions

S. No	Material Synthesis	Method	Weight loading per cm^2	Electrolyte (EL)	Specific Capacitance (F/g)	Current Density/ V	Cyclic Stability	Ref.
1	NiO NP	Hydrothermal method	41.8 mg/cm^2	1M KOH And 1M Na_2SO_4	132 F/g in KOH and 79 F/g in Na_2SO_4	5 mV/s	75% retention after 500 cycles	[333]
2	NiO NP	Microwave method	0.8 mg/cm2	2M KOH	401 F/g	0.5 mA/cm2.	91.6% retention after 1000 cycle	[346]
3	NiO microspheres	Hydrothermal method	Not Given	6 M KOH	515 F/g	1 A/g	-	[347]
4	Hierarchical porous NiO-nanotube	Electro-deposition	1.2 mg/cm^2	2 M KOH	675 F/g	2 A/g	93.2% retention after 10000 cycles	[326]
5	Flower-like microspheres of nano-NiO	Hydrothermal method	2 mg/cm^2	6 M KOH	762 F/g	1 A/g	96% retention after 1000 cycle	[337]
6	Porous NiO nanosheets	Multistep preparation	0.7 mg/cm^2	2M KOH	600 F/g	10 A/g	-	[348]
7	mesoporous NiO nanoflake	Hydrothermal method	2 mg/cm^2	2M KOH	400 F/g	2 A/g	-	[328]
8	NiO NP	Sol-gel method	2 mg/cm^2	1M KOH	549 F/g	1 mV/s	81.8% retention after 10000 cycles	[339]
9	NiO NP	One-step green synthesis	Not Given	0.1M KOH	644 F/g	0.5 A/g	124% after 10,000 cycles.	[349]
10	NiO NP	Hydrothermal method	0.74 mg/cm^2	6M KOH	418 C/g (1045 F/g)	1A/g	89.5% retention after 1000 cycles	This work

reaction sites on the electrode at these increased rates [343]. GCD measurements were conducted over 1,000 cycles at 14 A/g, as shown in Figure 4.7a, to evaluate the long-term stability of both binder-free and binder-enriched NiO@NF (S:2) electrodes.The binder-free NiO@NF (S:2) based electrode retained a noteworthy, i.e. 87.5% of its initial specific capacity after 1000 cycles. However, the same number of cycles binder-enriched electrode was able to retain only 74.2% of its initial specific capacity. The EIS was performed to explore the charge transfer rate of EL ions between NiO@NFBF (S:2) electrode and EL. The Nyquist plots recorded between 0.1 Hz and 100 kHz, before and after 1000 cycles, and their equivalent circuit are displayed in Fig. 4.7b. The portrayed equivalent circuit is composed of an equivalent resistance (R_S) connected in series with two impedances and a constant phase element (CPE_S). The first impedance element is consisting of a resister R_{P1} and an inductor (L) connected in parallel, and the second impedance element contains a resistor R_{P2} coupled parallelly with another constant phase element (CPE_P). The bending of EIS curve in the fourth quadrant at higher frequency region is ascribed to the inductive effect resulting from the improper wiring so is modelled with first impedance element [344]. However, the second impedance element is

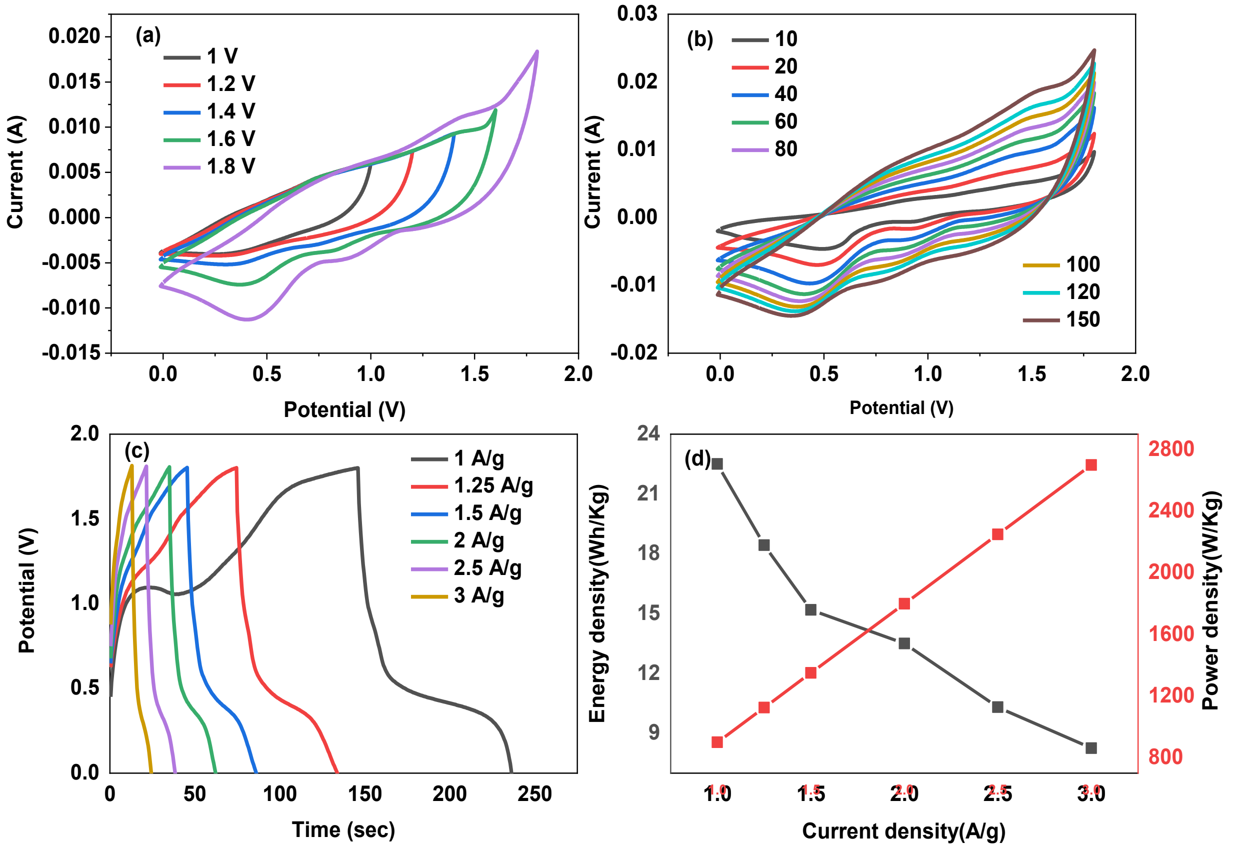

Fig.4.8 **a** The CV curves of ASC at different potential windows, at the constant v of 60 mV/s. **b** The CV curves of the device at different v between the potential window of 0 to 1.8 V. **c** The GCD curve of SC at various current density in the potential window of 0 to 1.8 V. **d** The variation of energy and power densities of SC device

associated with the reduction and oxidation reactions happening at anode and cathode, respectively, and CPEs is representing the diffusion of the ions deeper into the electrode material because it is the slow process and is being observed at the low frequency end of the spectrum. The fitted values of R_S, R_{P1} and R_{P2} are 0.73 Ω, 1.73 Ω and 0.05 Ω, respectively, which are favouring the charge transfer process. The measured values of the distributing factor for CPE_P and CPE_S are 0.72 and 0.77, suggesting the capacitive nature of both CPEs [345]. The analysis suggests that the in-situ growth of NiO nanosheets on nickel foam provided a highly porous structure and increased electrochemical surface area with abundant electroactive sites, facilitating efficient charge transport. The primary factor influencing the electrochemical performance of the NiO@NFBF (S:2) electrode is ion diffusion from the electrolyte to the electrode surface. After 1,000 charge-discharge cycles, a slight decrease in the slope of the EIS curve indicates some electrode degradation due to reduced diffusion. The binder-enriched electrode showed limited performance, as the binder restricted ion movement on the electrode surface. Conversely, in the binder-free electrode, the lack of binder reduced diffusion resistance, enhancing the reaction rate across the entire electrode surface. The electrode performance of previously reported results of NiO has been compared with the best performing electrode of the present investigation and is presented in Table 4.1. It is unveiled that the electrochemical performance of binder-free NiO nanosheets (S:2) based electrode is at par over other reported results on similar material. An ASC was assembled by considering NiO nanosheet (S:2)-based electrode as anode, activated carbon-based electrode as the cathode and 6 M KOH/PVA-based gel as EL. The total mass loading of the active materials on both electrodes was 6.9 mg. with current density. The CV curves were recorded at 60 mV/s, as shown in Fig. 4.8a, in different potential ranges, i.e. 1.0 to 1.8 V to find the appropriate and stable potential window for the assembled ASC device. Figure 4.8b illustrates the CV curves at different v in the stable potential window, i.e. between 0 and 1.8 V. The shape of the curves was retained at all v, which indicated the good rate performance of the assembled device, and it also suggests the Faradic nature of the electrode. The GCD curves were recorded at different current densities which are displayed in Fig.4.8c. The calculated specific capacity of the device was 90 C/g (200 F/g), 74 C/g (164 F/g), 61 C/g (135 F/g), 54 C/g (120 F/g), 41 C/g (92 F/g) and 33 C/g 73(F/g) at 1, 1.25, 1.5, 2, 2.5 and 3 A/g, respectively. The variation of energy and power densities of the SC device with current density are illustrated in Fig. 4.8d. The maximum E_D delivered by the ASC was 22.5 Wh/kg at 0.9 kW/kg.

4.4 Conclusions

The NiO nanosheets were successfully synthesized with hydrothermal method by varying the urea concentration and reaction temperature. It is disclosed that the crystallite size of NiO NPs was increasing with the increase of reaction temperature. The synthesis at 110°C using a hydrothermal method with a 1:2 molar ratio of nickel nitrate hexahydrate to urea successfully produced NiO nanosheets. When this synthesis was repeated on nickel foam, a highly porous microsphere morphology was achieved. At 1 A/g, the binder-free NiO nanosheet electrode demonstrated an specific capacity of 418 C/g (1045 F/g), along with an excellent retention rate of 87.5% after 1,000 cycles at 14 A/g. Additionally, E_D of 22.5 Wh/kg was achieved by the ASC at P_D of 0.9 kW/kg, showcasing the potential of this electrode material in high-performance energy storage applications

Chapter 5

Augmented Electrochemical Capacities of Microporous MoS_2@NiO Heterostructures

5.1 Introduction

With the burgeoning and pressing demand for efficient renewable clean energies, research on high-performance portable electronic devices has gained momentum in recent years. SCs, a sustainable electrochemical ES technology, outperform rechargeable batteries in terms of P_D but lag in E_D [350,351]. Consequently, the quest for superior electrode materials remains a fundamental challenge in modern SC research. Materials possessing a substantial SA and high electrical conductivity are deemed suitable for SCs [352]. In recent times, the use of transition metal-based oxides and dichalcogenides has emerged as a significant factor in advancing SC technology. There are numerous transition MO materials like Co_3O_4, MoO_3, MnO_2, V_2O_5, NiO, $NiCo_3O_4$, etc. Among these options, NiO stands out and is preferred due to its excellent electrochemical stability, provide relatively more specific capacitance as it supports charge storage process at the surface by reversible and fast redox reactions, low cost, high chemical/thermal stability, wide availability, and minimal environmental impact [353,354]. However, the inherent low conductivity characteristic of NiO hinders the transport of ions and electrons at elevated electrical rates, thus restricts their utility in high-efficiency charge storage devices [354]. Many researchers work on the composites of NiO with graphene and CNT for energy-storage utilizations. Graphene and CNTs have captivated significant focus for ES due to their unique properties. However, exploring other materials for storing energy is crucial to overcome limitations and enhance the performance of NiO. For this reason, sulfidized transition metal are often preferred ascribed to their layered structure and intrinsic conductivity. In fact, this characteristic makes them ideal for various applications. MoS_2, SnS, WS_2, CuS, and ZnS are examples of transition metal dichalcogenides that have found widespread application in various fields, including the storage and conversion of energy, as well as photocatalytic processes. Among several materials, molybdenum sulfide (MoS_2) stands out as a particularly noteworthy substance due to its layered crystal structure, high intrinsic ionic conductivity, capable to display rich intercalation chemistry and have high charge storage capacity. Furthermore, MoS_2 have abundant active edge sites, large SA and exhibits multiple oxidation states. But concurrently it suffers from restacking, poor rate-capability and cycling stability [278, 279].

Many researchers have conducted investigations on the compositing of MOs with dichalcogenides. The synthesis of the Manganese-doped SnO_2@MoS_2 composite was carried out applying a hydrothermal method, resulting in 242 F/g at 0.5 A/g. After 5,000 cycles of consistent charge and discharge, a retention rate of 83.95% of the initial capacitance was observed [279]. The WO_3-ZnS nanocomposites were synthesized using the microwave-supported technique. These nanocomposites demonstrated 215 F/g [355]. The MoS_2/CeO_2 heterostructure developed by the hydrothermal method to investigate the electrochemical characteristics using various ELs, including the neutral Na_2SO_4, the acidic H_2SO_4, and the basic NaOH. The heterostructure of MoS_2/CeO_2 demonstrated 166.6 F/g when subjected to 5 mV/s in 1 M NaOH, which is classified as a basic solution [356]. At current density of 1 A/g, the MoS_2-RuO_2 composite displayed Cs of 972 F/g. This measurement was obtained by subjecting the composite to an EL solution consisting of 1 M KOH [357]. At 1 A/g, the nanocomposite of PANI/MoS_2-MnO_2 electrode was demonstrated Cs 469 F/g. Additionally, the nanocomposite attenuated 6% after four thousand cycles. Furthermore, Ed of 35.97 Wh/kg was exhibited by the ASC exhibited at 500 W/kg. Moreover, it retained 94.1% of its overall performance even after undergoing 4000 cycles. [358]. NiO/MoS_2 nanocomposite developed by the hydrothermal synthesis route resulted in 289 F/g at 1A/g [359]. The nanocomposite consisting of Cu_2O/MoS_2/rGO synthesized by microwave methods. The nanocomposite material had remarkable pseudocapacitive characteristics, with a significantly improved 388 F/g when subjected to current density of 1 A/g. Moreover, the cyclic endurance of the nanocomposite remained at around 96% after undergoing 3000 cycles [360]. The CuO/MoS_2 (p-n) composite was synthesized by the hydrothermal route, resulted in 268 F/g. Furthermore, the composite attenuated by ~10% after undergoing 5000 cycles [361]. It was found that the use of a hybrid p-n junction effect leads to improved electrochemical performance through the enhancement of redox reactivity sites [362]. Another mesoporous composite of NiO/ZnO, was synthesized by using facile hydrothermal procedure. Notably, broad potential range of 0.6 V and a greater specific-capacity of 1394 C/g, and 560 C/g was demonstrated by the NiO/ZnO at 1 A/g, and 20 A/g [354].

Our research addresses a notable gap in the existing literature by delving into the synergistic effects of combining MoS_2 with NiO, an aspect yet to be extensively explored. Building upon a comprehensive review of prior studies, we embark on a systematic investigation aimed at optimizing the concentration of MoS_2 within the MoS_2@NiO composite. Through this approach, we seek to unravel the combined impact of MoS_2 and NiO on electrochemical performance, shedding light on their synergistic interactions and elucidating the underlying mechanisms. By elucidating these previously unexplored synergies, our research plays a role in advancing the understanding of composite materials for ES applications.

Notably, our study reveals compelling results, with the most optimized MoS_2@NiO hetero-structure-based electrode demonstrating a remarkable specific-capacity of 419.5 C/g (1048.75 F/g) at 1 A/g. This performance surpasses that of both MoS_2 and NiO-based electrodes by substantial margins, underscoring the efficacy of our composite approach. Furthermore, our ASC MoS2@NiO//GAC exhibits an impressive E_D of 47.43 Wh/kg at 0.825 kW/kg, underscoring its prospect for high-performance energy-storage utilizations.

5.2 Synthesis and electrode preparation

Synthesis of NiO: The experiment commenced with the mixing of 0.2 M $Ni(NO_3)_2 \cdot 6H_2O$ with 60 mL of distilled water. Thereafter, the solution was heated and agitated using a magnetic stirrer. Following this, 3 mL of ammonia was gradually introduced into the mixture. The pH of solution after adding ammonia was 9. The resulting $Ni(OH)_2$ precipitates were effectively separated through a filtration process. The reaction mechanism of formation of $Ni(OH)_2$ is given below [353]:

$$NH_3 + H_2O \rightarrow NH_4 + OH \quad \text{(i)}$$
$$2Ni(NO_3) \rightarrow Ni^{+2} + 2NO^{-3} \quad \text{(ii)}$$
$$Ni^{+2} + 2OH \rightarrow Ni(OH)_2 \quad \text{(iii)}$$

The obtained precipitates were then rinsed with distilled water, ethanol, and acetone and then dry in oven. The $Ni(OH)_2$ precipitates were then calcinated at 300 °C for 2 hours, resulting in the formation of NiO NPs.

Synthesis of MoS_2: In the initial step, a solution was prepared by dissolving 1000 mg of $(NH_4)_6Mo_7O_{24}.4H_2O$ and 700 mg of NH_2CSNH_2 in 70 mL of DI water with magnetic stirring for 15 minutes. The resulting uniform solution was placed in an autoclave operating at 180 °C for 6 hours. The reaction mechanism of MoS_2 formation is shared below [363,364]:

$$CSN_2H_4 + 2H_2O \rightarrow 2NH_3 + CO_2 + H_2S \quad \text{(iv)}$$
$$(NH_4)_6Mo_7O_{24} \rightarrow 6NH_3 + 7MoO_3 + 3H_2O \quad \text{(v)}$$
$$MoO_3 + 3H_2S + H_2O \rightarrow MoO_2 + SO_4^{2-} + 2H^+ \quad \text{(vi)}$$
$$MoO_2 + 2H_2S \rightarrow MoS_2 + 2H_2O \quad \text{(vii)}$$

The yield of MoS_2 NPs obtained was around 80 mg.

Synthesis of MoS_2@NiO composite: A total of 720 mg of NiO was homogenized with 70 mL of distilled water by ultrasonication of 1 hour. Subsequently, an equal amount of $(NH_4)_6Mo_7O_{24}.4H_2O$ and NH_2CSNH_2 was added, and the aforementioned process, as outlined in the synthesis of MoS_2, was repeated. This procedure resulted in the formation of 10% MoS_2@NiO after filtration. The same procedure was applied to synthesize additional nanocomposites with 20, 30, 40, and 50% MoS_2 in the MoS_2@NiO composite, with the corresponding proportions of NiO being 320, 186, 120, and 80 mg, respectively. The resulting specimens with 20, 30, 40, and 50% MoS_2 in the MoS_2@NiO composite were labelled as M1, M2, M3, M4, and M5, respectively.

5.3 Results and discussion

5.3.1. Structural and morphological analysis The XRD pattern of MoS2 NPs is depicted in Fig. 5.1(a). The diffraction curves exhibit conspicuous peaks at 32.4°, 33.4° and 58.3°, corresponding to the (100), (101) and (110) planes, respectively, closely resembling those described in PDF (ICSD): 00–006–0097. These peaks confirm the presence of the 2H phase, characterized by a hexagonal crystal structure, of the synthesized MoS2 NPs. In this phase, each molybdenum atom is surrounded by six sulfur atoms, forming a trigonal prismatic coordination geometry. The layers of MoS2 are stacked together via weak intermolecular forces, leading to a lamellar configuration. The 2H phase is one of the most common and stable phases of MoS2, exhibiting significant electronic, optical, and mechanical properties. The

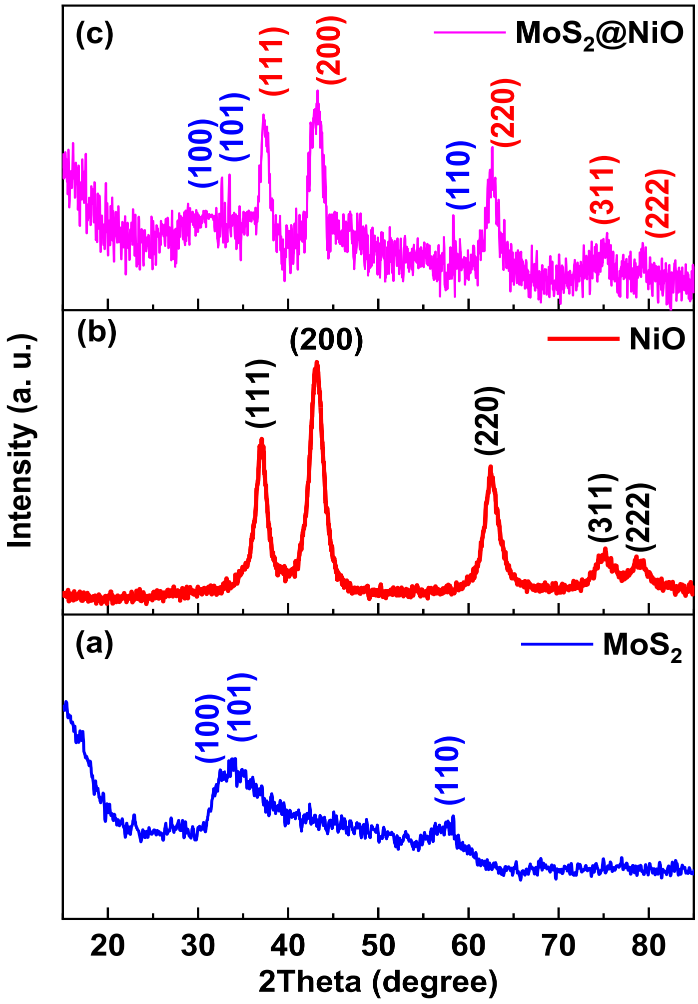

Fig. 5.1 XRD spectra of (a) MoS_2, (b) NiO and (c) MoS_2@NiO.

diffraction pattern of NiO NPs depicted in Fig. 5.1(b) is in good alignment with PDF (ICSD): 01–071–1179. The diffraction curve shows distinct peaks at 37.2°, 43.3°, 62.9°, 75.4°, and 79.4°, manifesting (111), (200), (220), (311), and (222) planes, sequentially, attesting to the cubic crystal structure of the NiO NPs. The XRD pattern of the MoS2@NiO composite is shown in Fig. 5.1(c). It is observed that the sharpness and intensity of the prominent planes, such as (111), (200), and (220) of NiO NPs, are considerably reduced after the addition of MoS2 in the composite, ascribed to the amorphous character of the 2H phase of MoS_2. Furthermore, visible peaks at approximately 33.4°, 33.4° and 58.4° in Fig. 1(c) suggests the formation and presence of MoS_2 in the MoS_2@NiO composite. The XPS analysis was employed to explore the elemental composition and oxidation states of the MoS_2@NiO hetero-structures, as illustrated in Figs. 5.2(a–e). Using the Gaussian fit method, all simulated peaks were compared with the database. In Figs. 2(b), the peaks corresponding to the Ni $2p_{3/2}$ and Ni $2p_{1/2}$ orbitals were observed at approximately 855 eV and 872.6 eV, in their sequence, along with their satellite peaks at around 861 eV and 879 eV, respectively, suggesting the

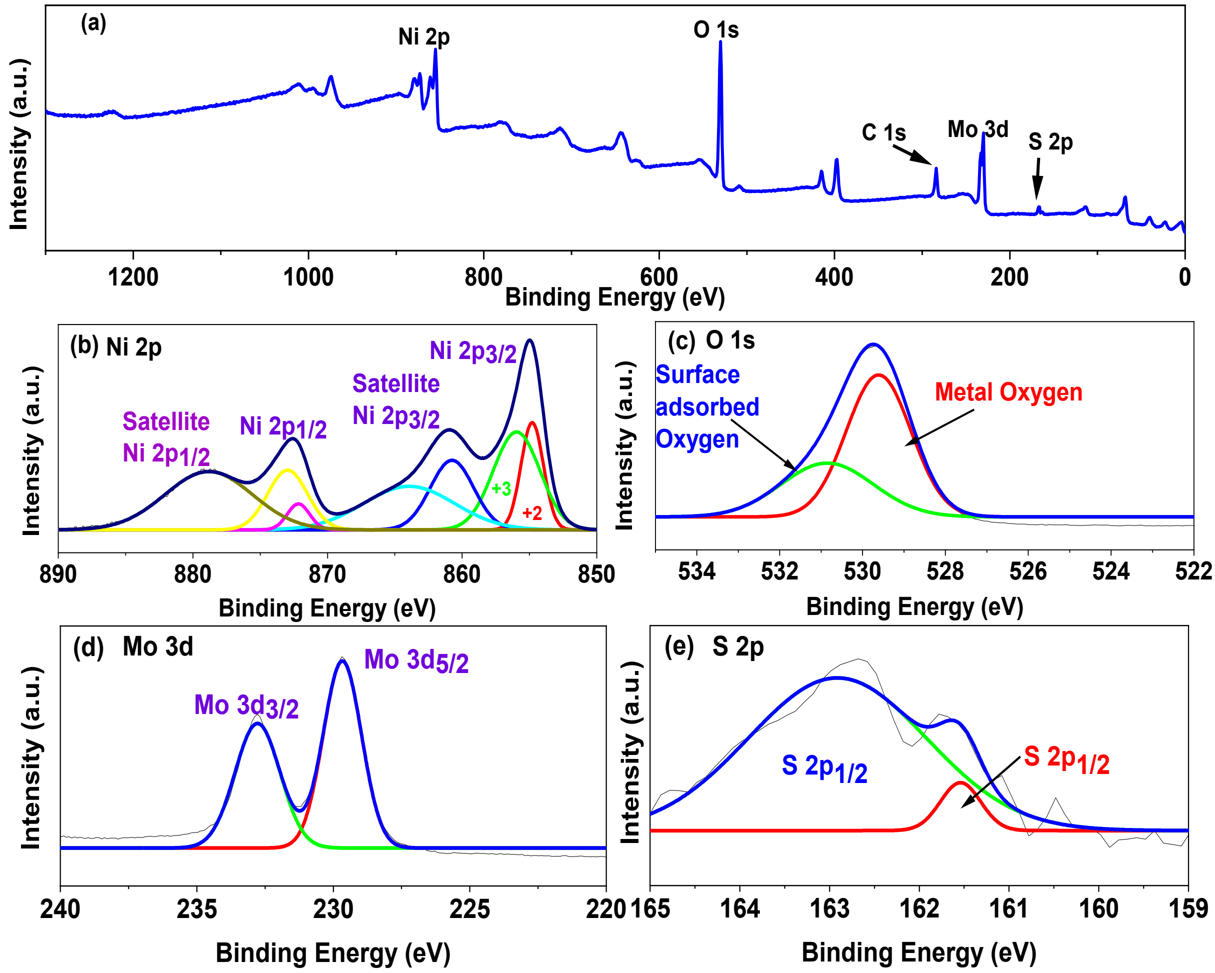

Fig. 5.2 XPS spectra of MoS_2@NiO (M3) composite: (a) Survey scan and core-level spectra of (b) Ni 2p, (c) O 1s, (d) Mo 3d and (e) S 2p.

manifestation of the +2 oxidation state of nickel and the formation of NiO in the composite. However, the deconvolution of the Ni $2p_{3/2}$ peak into two peaks, approximately at 854.5 eV and 586 eV, indicates the existence of the +3 oxidation state of nickel. The O 1 s high-resolution spectrum shown in Figs. 5.2(c) exhibits two deconvoluted peaks at 529.8 eV and 531 eV, corresponding to metal-oxygen bonds and surface-adsorbed oxygen, sequentially, validating the coexistence of the +2 and +3 oxidation states of nickel. The surface-adsorbed oxygen may transform into negatively charged species by accepting electrons from the NiO available on the

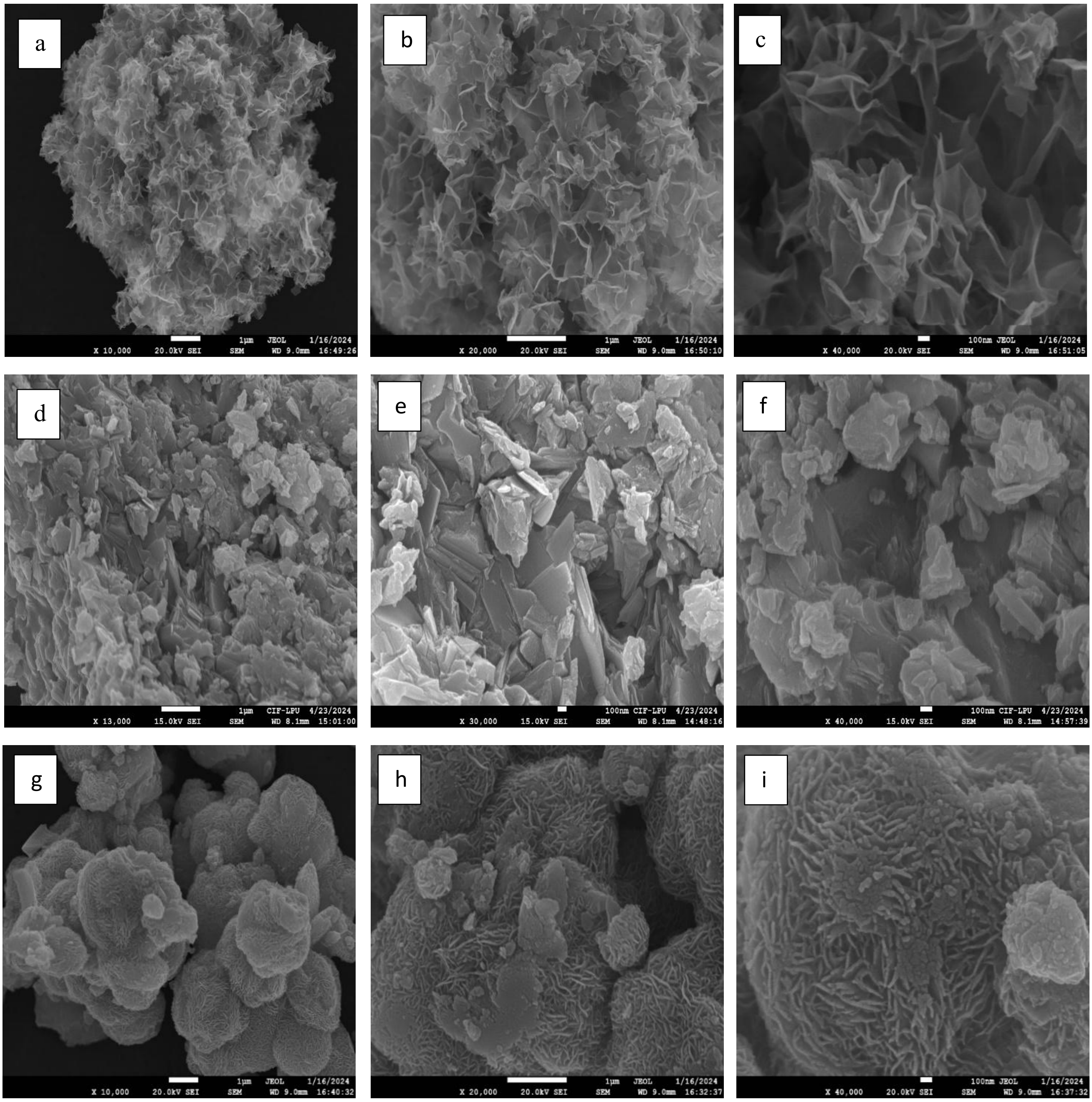

Fig. 5.3 FESEM images (a, b and c) of NiO, (e, f and g) of MoS_2 and (g, h and i) of MoS_2@NiO (M3) composite.

surface, thereby converting Ni^{2+} into Ni^{3+} to maintain the charge neutrality of the composite [363]. In Figs. 5.2(d), the Mo $3d_{5/2}$ and Mo $3d_{3/2}$ peaks linked with MoS_2, displayed at 229.6 eV and 232.7 eV, in the specified order, reveal the +4 oxidation state of molybdenum. Similarly, the S 2p deconvoluted doublet, i.e., S $2p_{3/2}$ and S $2p_{1/2}$ observed in Fig. 5.2(e) at 161.4 eV and 162.7 eV, respectively, confirm the -2-oxidation state of sulfur The XPS core-level spectra of molybdenum and sulfur confirm the presence of the 2H-phase in MoS_2, as previously observed in the XRD analysis. FESEM was utilized to assess the microstructural and morphological characteristics of both NiO, MoS_2 and MoS_2@NiO (M3) heterostructures. The FESEM micrographs at various magnifications of the NiO particles are depicted in Fig. 5.3(a-c), revealing a microflower like arrangement. Validation of the uniform presence of nickel and oxygen atoms is provided by the EDS mapping shown in Fig. S1. The stacked microsheets of MoS_2 are depicted in Fig. 5.3 (d-f). Their EDS mapping (Fig. S2) is clearly indicating the uniform distribution of Mo and S in the scanned area. Similarly, FESEM images captured at different magnifications of the M3 sample are illustrated in Fig. 5.3(g-i). Notably,

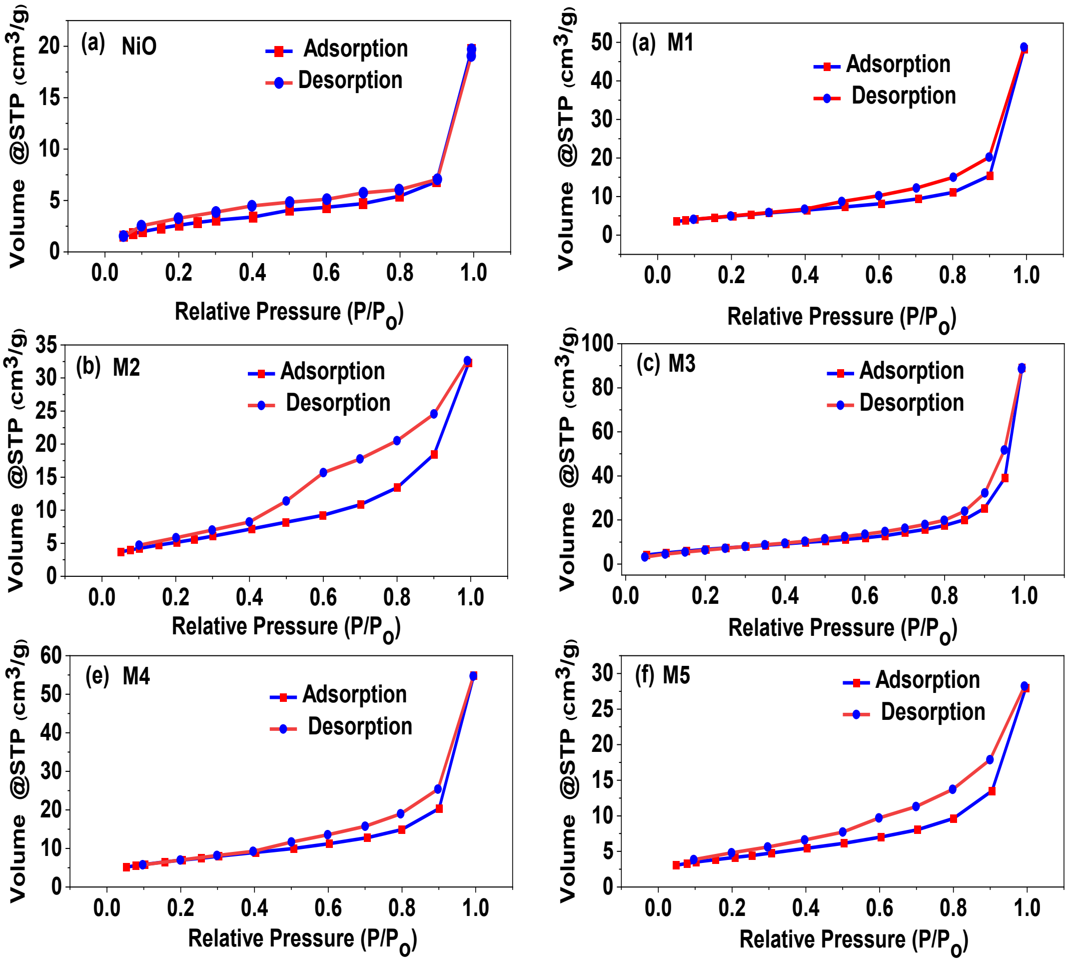

Fig. 5.4 The nitrogen adsorption-desorption isotherm of (a) NiO, (b) M1, (c) M2, (d) M3, (e) M4 and (f) M5 composites.

be readily distinguished. Upon closer examination, MoS_2 particles appear randomly dispersed

MoS_2 and NiO particles can among the NiO nanosheets. This heterogeneous distribution likely enhances porosity, underscoring the potential suitability of the MoS_2@NiO composite as an effective electrode-material. The SA per unit wight of NiO and MoS_2@NiO heterostructures was determined using the BET method. BET technique, which involved analyzing the nitrogen (N_2) sorption isotherms at 77 K. The specimens were subjected to a degassing process for 3 hours at 200 °C to remove any adsorbed moisture or gases that could interfere with the measurement. The resulting N_2 adsorption-desorption isotherms exhibited distinct hysteresis loops, indicative of the textural properties of the materials, as depicted in Fig.5.4. Upon examination of the plots, the BET surface-area values were measured as 12.8, 17.8,18.9, 25.9, 24.2 and 14.5 m2/g, for of NiO, M1, M2, M3, M4 and M5 composites, respectively. This clearly indicates that in M3 composite, a twofold increase in active SA following the addition of MoS_2 to NiO. Furthermore, the BJH pore size variation curves of the NiO and MoS_2@NiO composite samples are presented in Fig. S4. The avg. pore size in the synthesized NiO was determined to be 3.6 nm, but in MoS_2@NiO heterostructures it was around 1.9 nm, indicating that the porosity of NiO was switched from mesoporous to microporous character, after the addition of MoS2. This finding of increased porosity suggests the appearance of numerous sites for adsorption and diffusion for electrochemical reactions. The FESEM micrographs of NiO and MoS2@NiO (M3) composite are also supporting the finding of reduced pore size after the incorporation of MoS2 in NiO.

5.3.2 Electrochemical analysis Fig. 5.5(a) shows the CV profiles of NiO, MoS_2, and different MoS_2@NiO heterostructure based electrodes taken at 10 mV/*sec*, covering a potential window of - 0.01 to 0.5 V. All electrochemical characterization were carried out using a 4 M potassium hydroxide (KOH) EL solution. It is noteworthy that each voltammogram exhibits the presence of two pairs of peaks, suggesting the Faradic nature and structural stability of all studied electrodes. All MoS_2@NiO based electrodes exhibited notably enhanced current densities and increased areal capacity compared to both NiO and MoS_2 electrochemical capacitance through the process of ion exchange. Among the five composites, the MoS_2@NiO (M3) composites encompassed the highest integral area attributed to its enhanced SA available for electrochemical interactions, suggesting a greater specific capacity. Fig. 5.5(b) displays the CV curves of the M3 electrode at multiple v. Furthermore, it is relevant to observe that the curve shape remained unaltered, but the redox peaks of the M3 composite-based electrode displayed a progressive migration towards a broader potential range with the increase of the v. This may be attributed to increased polarization effect and diffusion limitation at higher v. As the capacitance properties of the electrodes are predominantly governed by Faradaic reactions, so the probable redox reactions can be defined as [365,366]:

$$MoS_2 + OH^- \rightleftharpoons MoS_2OH + e^- \quad \text{(viii)}$$

$$NiO + OH^- \rightleftharpoons NiOOH + e^- \quad \text{(ix)}$$

In MoS_2@NiO, initially, MoS2 and NiO react with OH^- ions to form MoS_2OH and NiOOH, respectively, while releasing electrons. And under certain conditions, the products (MoS_2OH) and NiOOH) release the captured electrons to revert back to the original materials (MoS_2 and

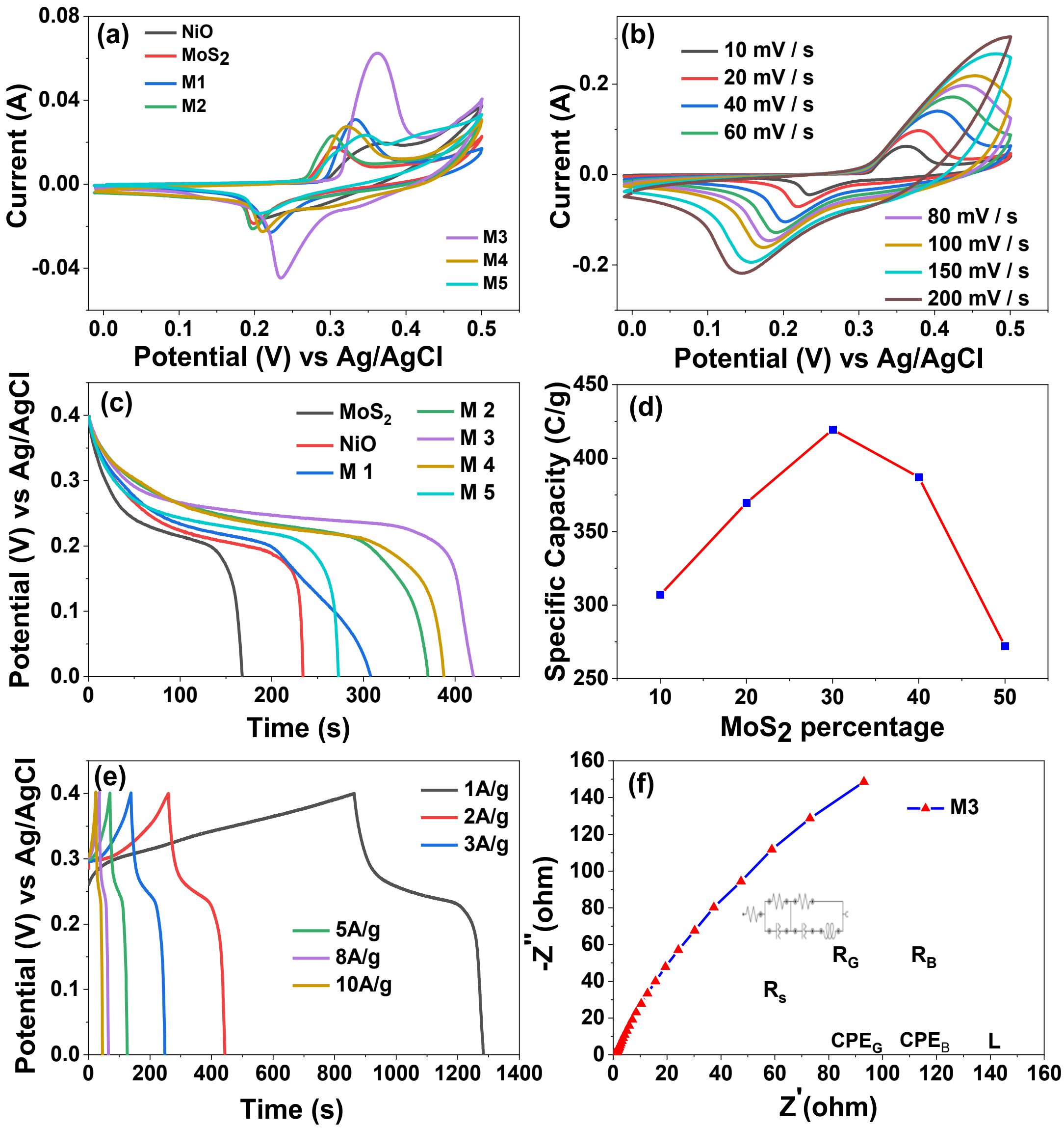

Fig. 5.5 (a) The CV curves of the NiO, MoS_2, and MoS_2@NiO composite-based electrodes obtained at a v of 10 mV/s.(b) The CV curves of the M3 electrode were obtained at various v. (c) The galvanostatic discharging curves of the NiO, MoS_2, and MoS_2@NiO composite-based electrodes analyzed at a current density of 1 A/g. (d) The graph illustrates the relationship between the specific capacity and the proportion of MoS_2 in the composite. (e) The GCD curves of the M3 electrode analyzed at various current densities. (f) EIS plot of the MoS_2@NiO (M_3) composite-based electrode and its equivalent circuit.

NiO) and release OH^- ions. Fig. 5.5(c) depicts the core-level (GCD) curves of NiO, MoS_2, and various MoS_2@NiO heterostructure-based electrodes within the voltage window of 0 to 0.4 V and at 1A/g. These curves exhibit an asymmetric shape, indicative of dominant Faradic behavior [367]. Notably, MoS_2@NiO-based electrodes exhibit longer discharge times compared to MoS_2 and NiO electrodes, underscoring their higher specific capacity. Specifically, the specific capacity of MoS_2-based and NiO-based electrodes is measured at 167 C/g (417.5 F/g) and 233.5 C/g (583.75 F/g), sequentially. Fig. 5(d) illustrates the variation in specific capacity among M1, M2, M3, M4, and M5 electrodes with varying concentrations of MoS_2 in NiO. The measured capacities range from 272 C/g (680 F/g) to 419.5 C/g (1048.75 F/g) at 1 A/g, with the MoS_2@NiO-based electrode containing 30 % MoS_2 demonstrating the superlative performance among the studied electrodes. In fact, the M3 electrode outperformed MoS_2 and NiO-based electrodes by 60 % and 45 %, respectively. The extended discharge time and heightened specific capacity of MoS2@NiO-based electrodes can be ascribed to the synergistic effect leading from the combination of MoS_2 and NiO in the composite electrode. While MoS_2 have layered structure, and high intrinsic ionic conductivity, NiO offers better electrochemical stability. The synergistic interaction between these materials enhances charge storage capabilities and overall electrode performance. Moreover, the presence of MoS_2 increases the active SA available for electrochemical reactions due to its layered structure, providing numerous sites for ion adsorption and diffusion. Additionally, the incorporation of MoS_2 into NiO may lead to the formation of additional active sites and defects, further enhancing the electrode's electrochemical performance. Fig. 5.5(e) presents the GCD curves of the M3 electrode at various current densities. A reduction in discharge time is observed as the electrode operates at higher current densities. Specifically, the specific capacity of the M3 electrode measures 419.5, 366, 330, 280, 236, and 210 C/g at 1, 2, 3, 5, 8, and 10 A/g, in the specified order. The observed 50 % decrease in rate capability with a tenfold increase in current density can be ascribed to limited ion diffusion within the electrode material at higher current densities. Furthermore, at higher current densities, ion depletion at the electrode surface may result in concentration polarization, reducing the effective driving force for ion migration and consequently diminishes the electrode's capacity. Additionally, the cyclic and Coulombic efficiency of the M3 composite based electrode depicted in Fig. S5 is done for 1000 cycle, revealed its robust nature. To analyze the reaction kinetics, Nyquist plot was generated for MoS_2@NiO (M3) electrode across 10^{-2} to 10^5 Hz, as depicted in Fig. 5.5 (f). An equivalent circuit model based on discrete-component elements was applied to represent the impedance

Table 5.1 The fitted values of various components of equivalent circuit.

Sample	**R_S (ohm)**	**R_B (ohm)**	**R_G (ohm)**	**Ionic conductivity (S/cm)**
NiO	0.67	1.9	2200	2.2×10^{-5}
MoS_2	0.6	1.83	1750	2.8×10^{-5}
M 1	0.55	1.8	1620	3×10^{-5}
M 2	0.539	1.78	1500	3.3×10^{-5}
M 3	0.353	0.617	581	8.6×10^{-5}
M 4	0.388	1.07	977	5.1×10^{-5}
M 5	0.597	1.81	1690	3.1×10^{-5}

characteristics, as portrayed in the same figure. This circuit comprises a resistance (R_S) in series with two other impedance components. R_S is influenced by factors such as EL's ionic impedance, contractual limitations between the conducting substrate and coated material, and internal limitations of the Ni-foam [368]. The leading impedance-component comprises a resistor (R_G) and a constant-phase component (CPE_G), which are associated with grain boundaries. Meanwhile, the other component consists of a resistance (R_B), and a phase element (CPE_B) in alliance with bulk composite material, representing charge-transfer resistance and interfacial or Helmholtz boundaries, respectively. The impedance of the constant-phase element is expressed as ω^{-n}/A, where ω, n and A represent the angular frequency, dispersing factor and a constant, sequentially. In the circuit, when n equals 1, it embodies the behavior of an ideal capacitor, while at n equals 0, it reflects the characteristics of an ideal resistor [369]. The fitted value of R_B (0.37 Ω) indicates favorable charge-transport character of the M3 composite material, as corroborated by CV and GCD analyses. It is noteworthy that the total resistance employed by the linking cables, ionic solution, and nickel foam is very small (0.35 Ω). Conversely, the substantial grain boundary or interfacial resistance (581 Ω) may result from bond elongation due to EL ion penetration into the microporous composite material. Moreover, the calculated 'n' values for bulk and grain boundaries were 0.79 and 0.95, sequentially, indicating the capacitive nature of both phase elements. For comparison, the EIS plots of NiO, MoS_2 and MoS_2@NiO composites-based electrodes are recorded and depicted in Fig. S6. The fitted values of different components of equivalent circuit is reported in Table 5.1. After comparing the reported values of R_S, R_B and R_G, it is noted that M3-based electrode is the most optimized electrode among all studied electrodes. Moreover, the ionic conductivity of all electrodes was calculated by considering their bulk and grain-boundary resistances. It is noticed that the ionic conductivity of the M3-based electrode was highest i.e. 8.6×10^{-5} S/cm. Further, the electrical conductivity was measured by four-probe method. The calculated values are 11.5, 9.3 and 14.2 S/cm for NiO, MoS_2 and MoS_2@NiO (M3) composite, respectively, which is further supporting the elevated behavior of M3-based electrode.

Concurrently, we undertook an in-depth analysis of the charge storage kinetics of the NiO and MoS_2@NiO electrodes through the examination of CV data concerning the v (v) and current (i) relationship: $i = \alpha v^{\beta}$ [370]. Here, ’α’ represents a constant contingent upon the character of the synthesized material, while ’β’ falls within the range of 0.5 to 1.0, determined from the slope of the log(v) and log(i) plot. A ’β’ value near 0.5 implies a battery-like or diffusion-controlled process, whereas a value approaching 1.0 indicates a capacitive or surface-controlled process. As depicted in Fig. 5.6(a) and (d), the calculated ’β’ values for the anodic peaks of NiO and MoS_2@NiO based electrodes are 0.757 and 0.539, respectively. This suggests that the charge storing process of the MoS2@NiO electrode predominantly follows diffusion-controlled processes, while NiO based electrode predominantly stores charge through a

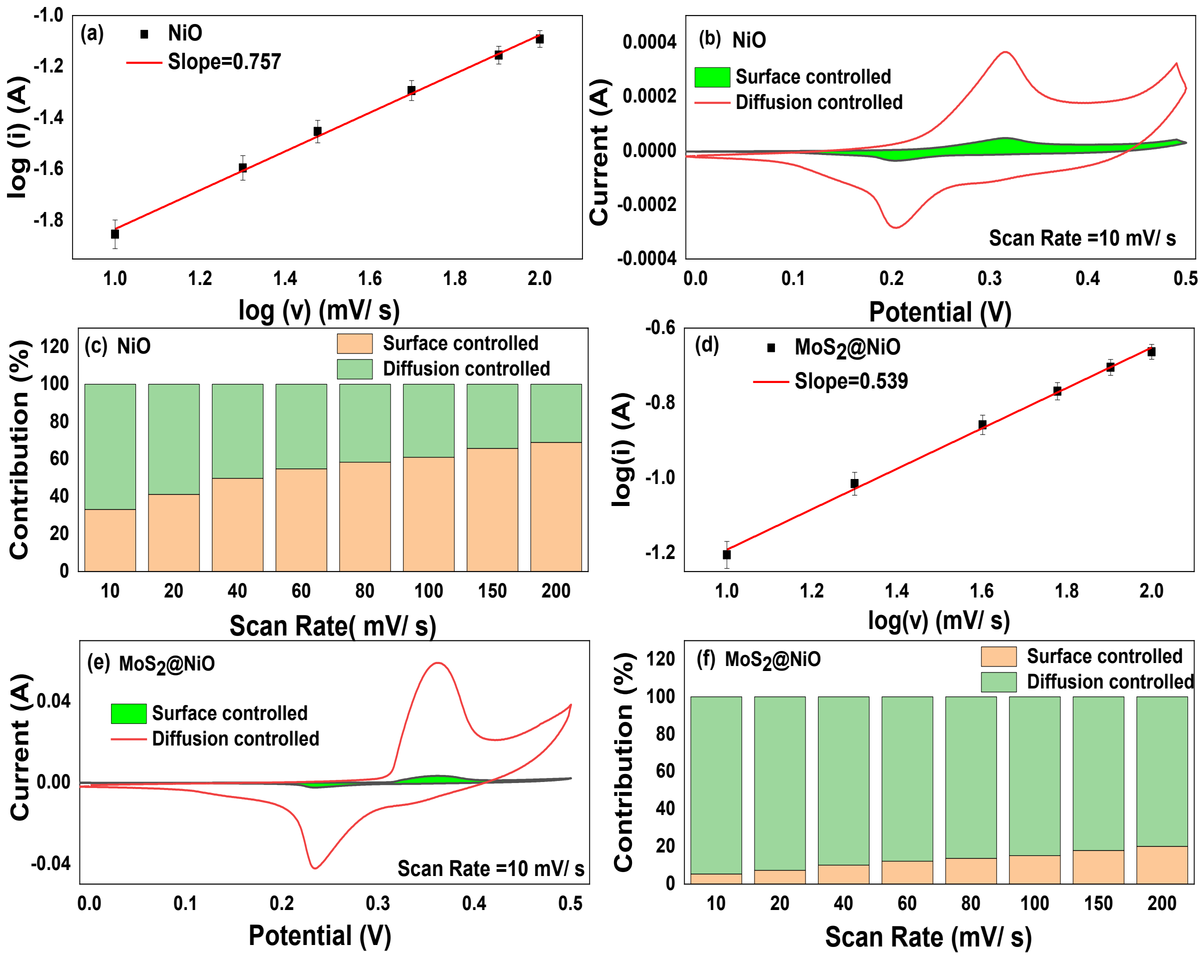

Fig. 5.6 (a) The graph between log (i) vs log (v) plotted for b parameter estimation for NiO. (b) The surface and diffusion contributions in NiO electrode at 10 mV/sec. (c) The percentage contribution of surface and diffusion current in NiO at different v. (d) The graph between log (i) vs log (v) plotted for b parameter estimation for MoS_2@NiO composite-based electrode. (e) The surface and diffusion contributions in MoS_2@NiO electrode at 10 mV/sec. (f) The percentage contribution of surface and diffusion current in MoS_2@NiO electrode at different v.

capacitive-surface controlled process. Moreover, Dunn’s equation [371] posits that the observed electrical current at a specific voltage stem from a composite effect, encompassing both surface-controlled (k1v) and diffusion-controlled phenomena ($k_2v^{1/2}$): $i(V) = k_1v + k_2v^{1/2}$. Here, ’k_1’, and ’k_2′ denote the constants. By plotting $i(V)/v^{1/2}$ against $v^{1/2}$ at various potentials, one can determine the values of k_1 (slope) and k_2 (intercept) at a predetermined voltage. Fig. 5.6(b) and (e) present the quantitative capacitive study of ES behavior, with specific consideration on the capacitive (green) and diffusion contributions for NiO and MoS_2@NiO electrodes at 10 mV/s. The total capacitance contribution via diffusion and capacitive mechanism at various v for NiO and MoS_2@NiO electrodes is depicted in Fig. 5.6(c) and (f).

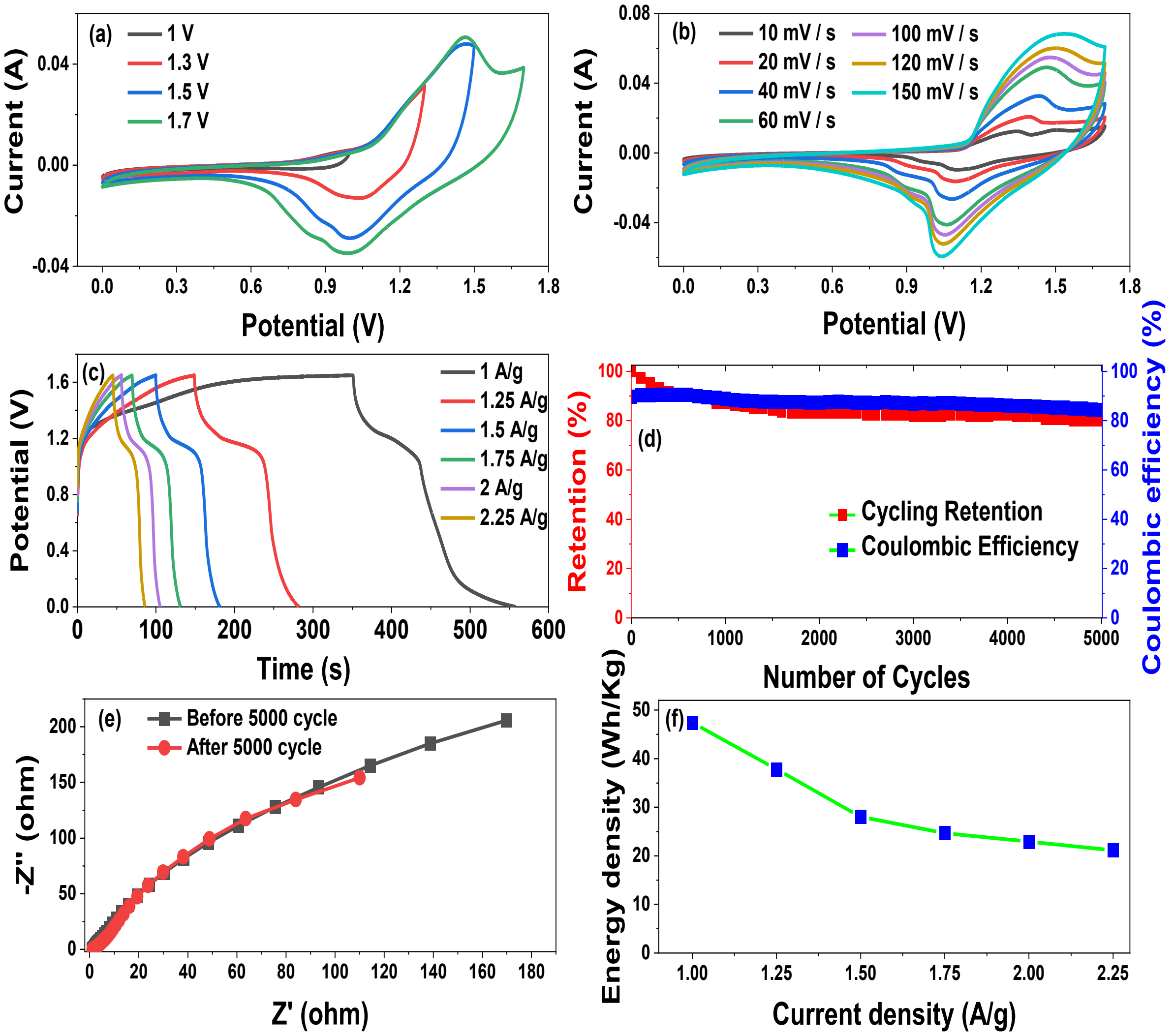

Fig. 5.7 (a) The CV curves of the ASC, obtained at a constant v of 60 mV/s, while utilizing various potential windows. (b) The CV curves of the device obtained by varying the v while maintaining a potential window of 0 to 1.7 V. (c) The current density-dependent GCD curve of the SC device. (d) The graph illustrates the variation of percentage retention of Cs and coulombic efficiency with number of cycles. (e) The EIS curve of the device was measured both before and after subjecting it to 5000 cycles of GCD. (f) The variation of E_D of the device with current density.

Table 5.2 Comparative analysis of the electrochemical performance of MoS_2 and transition MO-based electrodes and devices.

S. No.	**Material synthesis**	**Method**	**Electrolyte (EL)**	**Specific capacitance of electrode (F/g) by three-electrode setup**	**Current Density (A/g)**	**Energy Density (E_D) of device (Wh/kg) by two- electrode setup**	**Ref**
1	Mn-doped SnO_2@MoS_2	Hydrothermal	2M KOH	242	0.5	-	[279]
2	MoS_2/CeO_2	Hydrothermal	1M NaOH	166	5mV/sec	-	[356]
3	MoS_2-RuO_2 Composite	Hydrothermal	1M KOH	719	1	35.92 Wh/kg at 0.6 kW/kg	[357]
4	PANI/MoS_2- MnO_2	Hydrothermal	1M H_2SO_4	479	5mV/sec	35.97 Wh/kg at 0.5 kW/kg	[358]
5	NiO/MoS_2	Hydrothermal	1M KOH	289	1	-	[359]
6	Cu_2O/MoS_2/rGO	Microwave	6M KOH	388	1	-	[360]
7	CuO/MoS_2	Hydrothermal	2M KOH	268 g	1	26.66 W h/kg at 1.6 kW/kg	[361]
8	WS_2@NiO	Chemical exfoliation	1M Na_2SO_4	64.5 mF/cm^2	5 mV/s	-	[372]
9	MoS_2/Co_3O_4	Hydrothermal	1M KOH	69	0.5	-	[373]
10	MoS_2@NiO	Hydrothermal	4M KOH	1048.75	1	47.43 Wh/kg at 0.825 kW/kg	This work

At v varying from 10 to 200 mV/*sec*, the diffusion-controlled proportions in the NiO electrode decrease progressively from 66.69 % to 31.09 %, while those of the MoS_2@NiO electrode diminish from 94.65 % to 79.80 %. From Fig. 5.6(f), it is evident that the diffusion process overwhelmingly governs the total charge storage mechanism in the MoS_2@NiO electrode. Furthermore, it is observed that the diffusion mechanism primarily dictates the behavior at low v in both electrodes. However, with an escalation in v, the contribution of surface-controlled phenomena becomes more pronounced, particularly in the NiO-based electrode. This may be ascribed to the slower kinetics associated with diffusion processes compared to surface-controlled phenomena. At lower v, there is enough time for ions to intercalate into and out of the electrode material, resulting in a greater contribution from diffusion-controlled processes. An ASC configuration was established by pairing a MoS2@NiO-(M3) based electrode for oxidation with an expanded graphite and activated carbon (GAC) based electrode for reduction phenomena as displayed in Fig. S7. The electrochemical capability of the ASC device i.e. MoS_2@NiO//GAC, was assessed through CV measurements, employing a v of 60 mV/s across a potential window spanning from 1.0 V to 1.8 V, as illustrated in Fig. 5.7 (a). The principal objective of this measurement was to delineate the optimal and enduring potential range for the ASC device. The CV curves presented in Fig. 5.7(b) exhibit the electrochemical behavior across varying v, particularly within the stable potential range extending from 0 to 1.7 V. The consistent morphology of the curves at different v underscores the robust operational characteristics of the device across a broad range of rates. Additionally, the discernible presence of redox peaks hints at the Faradic attributes manifested by the device. The Cs of the ASC was measured at various v, yielding values of 581, 463, 363, 321, 256, 237, and 216 F/g at 10, 20, 40, 60, 100, 120, and 150 mV/*sec*, respectively. Based on these measurements, the Ed of the developed device was calculated to be 58.3, 46.5, 36.4, 25.7, 23.8, and 21.7 Wh/kg at the corresponding v. Fig. 5.7(c) showcases GCD profiles of the developed device obtained at diverse current densities. The device demonstrated Css of 501.8, 400, 296.4, 260.9, 242.4, and 223.6 F/g at 1, 1.25, 1.5, 1.75, 2, and 2.25 A/g, in the specified sequence. Driven by the synergistic interactions of MoS_2 and NiO within the MoS_2@NiO electrode material, ASC achieved a commendable E_D of 47.43 Wh/kg at 0.825 kW/kg. Fig. 5.7(d) clearly indicates that the developed device retained approximately 80 % of its Cs and around 85 % of Coulombic efficiency after 5000 cycles at 2 A/g, indicative of its robust cyclic stability. The decision to set the optimal current density at 2 A/g was driven by the need to balance E_D with cycle stability. Fig. 7(e) presents the Nyquist plots of the device pre and post 5000 cycles across the frequency spectrum of 0.1 Hz to 10^5 Hz, revealing negligible variation and affirming the structural integrity of the electrodes. Lastly, Fig. 5.7(f) delineates the variations in energy densities of the device concerning current density, highlighting a decrement in E_D with escalating current density due to heightened internal resistance or diffusion constraints. Table 5.2 provides a comparative analysis of the electrochemical capability of MoS_2 and TMO-based electrodes and devices. Notably, the MoS_2@NiO (M3) based electrode and the ASC device MoS_2@NiO//GAC exhibited remarkable superiority over recently reported counterparts employing similar materials. This remarkable performance is attributed to the synergistic effects between MoS_2 and NiO, such as enhanced SA facilitating electrochemical activities, heightened ionic and electrical conductivities for improved charge transport, resulting in enhanced charge storage kinetics, increased E_D, and enhanced cyclic stability.

5.4 Conclusion In conclusion, this study successfully synthesized MoS_2@NiO heterostructures via a facile hydrothermal method, aiming to boost their electrochemical-capability as electrode-materials. Through systematic structural, morphological, and electrochemical characterizations, the optimized MoS_2@NiO heterostructure-based electrode demonstrated a remarkable specific capacity of 419.5 C/g at 1 A/g, surpassing both MoS_2 and NiO-based electrodes by significant margins. It is revealed that the Faradic or diffusion-controlled process overwhelmingly governs the total charge-storing phenomenon in the MoS_2@NiO based electrode. Leveraging the synergistic interactions between MoS_2 and NiO, the ASC MoS_2@NiO//GAC exhibited an impressive E_D of 47.43 Wh/kg at 0.825 kW/kg. Notably, the developed device exhibited robust cyclic stability, retaining approximately 80 % of its Cs and around 85 % of Coulombic efficiency after 5000 cycles at 2 A/g. These findings underscore the prospect of MoS_2@NiO heterostructures as propitious electrode-material for advanced energy-storage deployments.

Chapter 6

High Efficiency CoS_2@NiO Heterostructures: Synthesis, Characterization, and Electrochemical Performance

6.1 Introduction

From last few years, SCs have captivated significant attention as innovative energy storehouses, due to their excellent electrical capacity, quick charging ability, long cycle life, and efficient Coulombic performance. The primary obstacle hindering its commercial use is the comparatively restricted E_D. The effectiveness of SCs is primarily dependent on the Cs, charge-discharge rate, ES capacity, and power delivery of electrodes [350]. Therefore, the current study is centred on the creation of electrode materials with superior performance. The electrode is the most crucial part that influences the electrochemical functionality of any ES device. Therefore, creating a highly effective electrode is an important area of focus. There is a requirement to create affordable, safe, and easily accessible alternative materials that have better electrochemical performance. As a result, numerous researchers have begun investigating the ES capability of various oxide materials such as Co_3O_4, MoO_3, MnO_2, V_2O_5, NiO, and $NiCo_3O_4$. Among these, NiO is less toxic, have high theoretical capacitance, offering comparatively higher specific capacitance as it facilitates storage of charges on the surface by reversible and swift redox reactions, excellent electrochemical stability, affordable, chemically/thermally stable, readily accessible, and environmentally friendly [353]. Even so, the inherent property of low conductivity in TMOs hinder the movement of charged species at high v, thereby restricting their application in high-performance charge storage. Still, it is needed to investigate alternative materials for ES purposes to overcome constraints and improve the efficiency of NiO. Therefore, in order to enhance the efficiency of SCs, it is crucial to develop and manufacture innovative high-efficiency electrode materials that can surmount this constraint [374–376]. An efficient approach is to create heterojunctions by combining different materials which possess different band gaps [377]. Heterostructures can demonstrate unique physical phenomena and advantages that cannot be accomplished by a single component, through the application of energy level asymmetry. Additionally, the internal field has the ability to segregate the electrons and holes, so preventing their reunification at the interface. This allows them to move through distinct phases, facilitating effective charge extraction [378,379]. For these transition metal sulfides are frequently favored due to their layered structure and inherent conductivity. Moreover, they have been extensively applied across various domains, encompassing ES and conversion, alongside photocatalytic processes [278]. Molybdenum sulfide (MoS_2), Tin sulfide (SnS), Tungsten disulfide (WS_2), Copper sulfide (CuS), and Zinc sulphide (ZnS) are some examples of transition metal dichalcogenides. Cobalt sulphide, which includes several stoichiometric compositions such as CoS, CoS_2, Co_3S_4, and Co_8S_9, etc., are notable for their exclusive benefit of the multi-electron impact occurring by the hydrogen ion dissociation, significantly enhancing their theoretical Cs. CoS_2 shines out from other cobalt sulfide materials ascribed to its high redox activity, variable reaction valency, and remarkable electrical conductivity. Because of this, CoS_2 is sometimes thought to be a metal but at the same time as other sulphides it has concerns related to inferior rate capability and cyclic longevity [380].

Several researchers have studied the compositing of MOs with metal dichalcogenides (MDs). At 10 mV/s, the Co_3O_4@CoS composite demonstrates a significant 887.5 F/g. After undergoing 5000 cycles, demonstrate the retention rate of 78.1% at 5 A/g. [381] The ZnO@CoS_2 material demonstrates a notable 898.9 C/g when tested at 3 mA/cm^2 in a 3 M potassium hydroxide solution. At 1039.1 W/kg, the ASC demonstrates the Ed 45.2 Wh/kg [382]. The Cs of 242 F/g was obtained by the Mn-doped SnO_2@MoS_2 at 0.5A/g. Which was synthesized by an aqua-thermal process. During five thousand cycles of continuous charging and discharging, 83.95% longevity of the original capacitance was reported [279]. The microwave-assisted approach was utilized to successfully synthesize the WO_3-ZnS nanocomposites. It was demonstrated that these nanocomposites had 215 F/g [355]. The Cs of 972 F/g at 1 A/g in 1 M potassium hydroxide is exhibited by the composite material composed of MoS_2 and RuO_2 [357]. The Cs of 469 F/g was demonstrated by the PANI/MoS_2-MnO_2 based electrode when it was subjected to 1 A/g. After 4000 cycles, the nanocomposite demonstrated a cycling stability of over 94%, which is an extraordinary achievement. At 500 W/kg, the device demonstrated the E_D of 35.97 Wh/kg. Additionally, even after being subjected to 4000 cycles of charge-discharge, it was able to maintain 94.1% of its overall performance quality [358]. The hydrothermal approach was used to create a heterostructure nanocomposite composed of NiO and MoS_2, which resulted in 289 F/g when presented with 1 A/g [359]. The microwave approach was used to conduct the synthesis of the nanocomposite that was composed of Cu_2O/MoS_2/rGO. The active electrode material exhibited outstanding pseudocapacitive properties, with a Cs that was greatly improved to 388 F/g after being subjected to 1 A/g. Furthermore, after being subjected to three thousand cycles, the nanocomposite maintained a cyclic stability equivalent to approximately 96% [360]. The CuO/MoS_2 heterostructures were developed, which achieved 268 F/g. The composite demonstrated a capacitance retention of 90.02% following five thousand cycles [361]. The electrode materials consist of $NiCo_2O_4$@CoS, where CoS is coated on $NiCo_2O_4$ to create heterojunctions. The $NiCo_2O_4$@CoS_2 heterojunctions have superior electronic conductivity compared to any individual component. The heterojunction-based electrode has a remarkable 1902.5F/g when tested at 1 A/g. Assembled ASC consisting of $NiCo_2O_4$@CoS and activated carbon (AC) as electrodes. At 425 W/kg, ASC demonstrates the E_D of 32.91 Wh/kg. Additionally, it demonstrates 81.5% retention after undergoing 5000 cycles [383].

Building upon the insights gleaned from the preceding literature review, this manuscript sets out to investigate the potential of composite heterostructures comprising CoS_2 and NiO as electrode materials, with the aim of enhancing electrochemical performance. The primary objective is to explore the synergistic effects stemming from the union of better electrical conductivity of CoS_2 and remarkable electrochemical stability of NiO, thereby fabricating a CoS_2@NiO composite. By varying the composition of CoS_2, we endeavor to tailor the properties of the composite to optimize its electrochemical behavior. Ultimately, the focus lies on optimizing CoS_2@NiO composite-based electrodes materials for advanced energy stockpiling purposes.

6.2 Experimental details

6.2.1 Synthesis details and electrode fabrication

Synthesis of nickel oxide (NiO): The experiment began by mixing 0.1 M nickelnitratehexadrate, 0.05 M hexamine, and 0.05 M urea with 90 mL of DI water. Subsequently, the stirring process started using a magnetic stirrer. Next, the solution was subjected to three consecutive irradiation exposures in a microwave for 180 seconds, 120 seconds, and 90 seconds, using a multimode cavity operating at 900 W. Then, the solution was separated by filtration using filter paper, successfully isolating the $Ni(OH)_2$ precipitates. The reaction scheme is given below [353]:

$$NH_3 + H_2O \rightarrow NH_4 + OH \qquad \text{(i)}$$
$$2Ni(NO_3) \rightarrow Ni^{2+} + 2NO^{3-} \qquad \text{(ii)}$$
$$Ni^{2+} + 2OH \rightarrow Ni(OH)_2 \qquad \text{(iii)}$$

The resultant precipitate was subsequently washed through a series of washing processes, which included water, alcohol, and acetone. Then, the $Ni(OH)_2$ precipitate annealed at 300 °C for 2 hours, leading to the development of NiO nanostructures.

Synthesis of cobalt disulphide (CoS_2): Initially, 1000 mg of $Co(NO_3)_2 \cdot 6\ H_2O$ and 650 mg of thiourea were mixed in 70 mL of water using magnetic agitation for a duration of 20 minutes. Afterwards, the solution was kept in autoclave, which was operated at 180 °C for 7 hours. The reaction scheme is shared below [384]:

$$CSN_2H_4 + 2H_2O \rightarrow 2NH_3 + CO_2 + H_2S \quad \text{(iv)}$$
$$2Co(NO_3) \rightarrow Co^{2+} + 2NO^{3-} \quad \text{(v)}$$
$$Co^{2+} + 2H_2S + 4NH_3 \rightarrow CoS_2 + 4NH_4^{+} \quad \text{(vi)}$$

Following the cooling process to reach ambient temperature, the solution underwent filtration and subsequent multiple washes using DI water, acetone, and ethanol in order to obtain CoS_2 NPs. Subsequently, the CoS_2 NPs underwent a drying process at 70 °C for 10 hours. The quantity of CoS_2 nanostructures acquired was 100 mg.

Synthesis of the composite CoS_2/NiO heterostructure: A solution was prepared by combining 400 mg of NiO with 70 ml of DI water, followed by ultrasonic agitation for a duration of 1 hour. Next, an equal quantity of cobalt (II) nitrate hexahydrate and thiourea was combined, and the repeat the procedure described for the synthesis of CoS_2 was repeated. After filtration, obtained the composite materials of CoS_2@NiO. The obtained composite has combination of 20% CoS_2 and 80% NiO. The same method was used to create additional composite heterostructures of CoS_2@NiO. The amount of NiO was systematically varied at specified quantities of 400, 233, 150, and 100 mg to ensure 20, 30, 40 and 50% of CoS_2 in CoS_2@NiO composite. The specimens were marked as K2, K3, K4, and K5, respectively.

6.3 Results and discussion

6.3.1. Microstructural, elemental, and morphometric assessments

The diffraction curve depicted in Fig. 6.1(a) reveals distinct peaks associated with CoS_2 NPs, indicating the presence of crystal planes 111, 200, 210, 220, and 311 at diffraction angles of 27.1°, 32.4°, 36.1°, 46.7°, and 54.8°, respectively. These observations align precisely with the diffraction pattern indexed by the JCPDS card number: 41-1471, thereby validating the successful development of CoS_2 NPs. In Fig. 6.1(b), the XRD pattern corresponding to NiO NPs reveals characteristic peaks ascribed to 111, 200, 220, 311, and 222, planes observed at diffraction angles of 37.2°, 43.3°, 62.9°, 75.4°, and 79.4°, respectively. These peak positions are in agreement with the PDF(ICSD): 01-089-5881, affirming the formation of cubic NiO NPs. Fig. 6.1(c) illustrates the XRD pattern of the CoS_2@NiO (K4) composite, wherein the presence of prominent peaks attributed to both CoS_2 and NiO validates the successful formation of the nanocomposite. Fig. 6.2 (a-e) display the HRTEM image of CoS_2@NiO composite materials. The measured value of d spacing of 0.249 nm belong to (210) plane of CoS_2 and 0.21 nm belong to (200) plane of NiO. That's conform the existence of CoS_2 and NiO in composite materials. Fig. 6.2 (e) displaying the selected area electron diffraction (SAED) pattern of CoS_2@NiO materials, which indicates the the polycrystalline nature of the composite materials. The ring indexed to (200) and (220) corresponds to CoS_2 and Similarly (200), (400), and (311) planes correspond to NiO. Result of HRTEM and SAED again give the conformation of successful formation of CoS_2@NiO composite materials. XPS measurement was applied to investigate the chemical makeup and valence states of the CoS_2@NiO heterostructures, as depicted in Figs. 6.3(a-e). In Fig. 3(b), peaks associated with Ni 2$p_{3/2}$ and Ni 2$p_{1/2}$ electron shells were noticed at ~ 855 eV and 873 eV, respectively, along with their subsidiary peaks at ~ 861 eV and 879 eV, in sequence. These observations indicate the presence of +2 valance state of Ni, confirming the successful synthesis of nickel oxide in the nanocomposite. On the other hand, the separation of the Ni 2$p_{3/2}$ peak into a pair of peaks, at ~ 853.7 eV and 855.2 eV, suggests the coexistence of both +2 and +3 valance states of Ni. The O 1 s high-resolution spectrum shown in Figs. 6.3(c) exhibits two deconvoluted peaks at 529.2 eV and 531 eV, corresponding to metal-oxygen bonds and surface-adsorbed oxygen, sequentially, validating the coexistence of the +2 and +3 oxidation states of nickel. Surface-bound oxygen has the potential to convert into negatively charged entities through electron acceptance from the

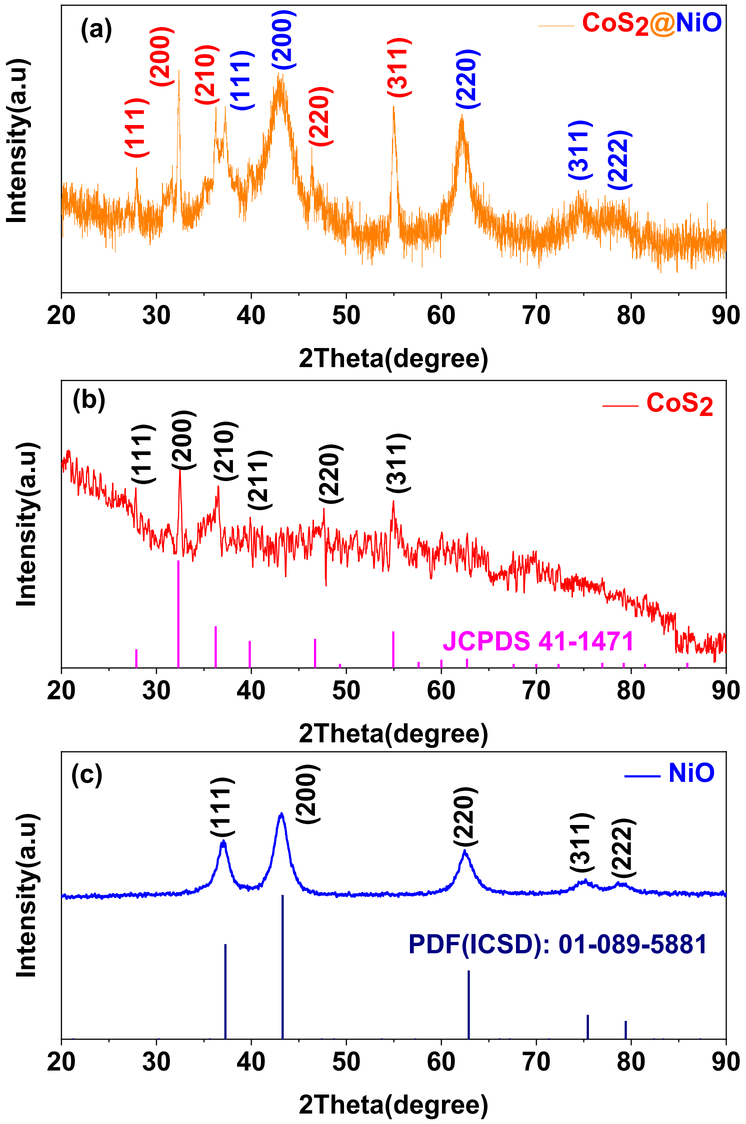

Fig. 6.1 XRD spectra of (a) CoS_2@NiO, (b) CoS_2 and (c) NiO.

nickel, and oxide present on the surface. This process facilitates the transformation of Ni^{2+} into Ni^{3+} to ensure the composite's electrical neutrality [359]. Fig. 6.3(d) illustrates peaks at 778.7, 780.7 and 784.7 eV are corresponded to $2p_{3/2}$ and 793.7 to 802 eV are corresponded to $2p_{1/2}$ in the high-resolution Co 2p spectra. The presence of peaks at 784.7 and 802 eV are two satellite peaks. The S 2p deconvoluted doublet in Fig. 6.3(e) at 161.3 and 162.6 eV confirms the -2- valance state of Sulphur. [385–387]. The FESEM image in Fig. 6.4(a-d) reveals the flower-like morphology of NiO. CoS_2 has a spherical cluster of nanosheets and nanorodes in Fig. 6.4(e-i). There is agglomeration of nanosheets and nanorodes clearly seen in morphology. Zoomed FESEM images of CoS_2@NiO (K4) heterostructures, presented in Fig. 6.5(a-d), reveal the distinct morphologies of the CoS_2 and NiO NPs within the composite. The flower like entities observed correspond to NiO, while the nanosheets and nanorods are representing CoS_2 particles. When the CoS_2 grows on the NiO flower-like structure, there is not any agglomeration in morphology. Nanorodes and nanosheets of CoS_2 with flowers like NiO are clearly visible in the higher magnification image in Fig. 6.5. (d and e). These distinct and varied morphologies within the CoS_2@NiO (K4) heterostructures underscore the porous nature and extensive SA of the synthesized nanocomposite, which are critical attributes for facilitating efficient electrochemical reactions. Furthermore, the EDS Spectroscopy visualization

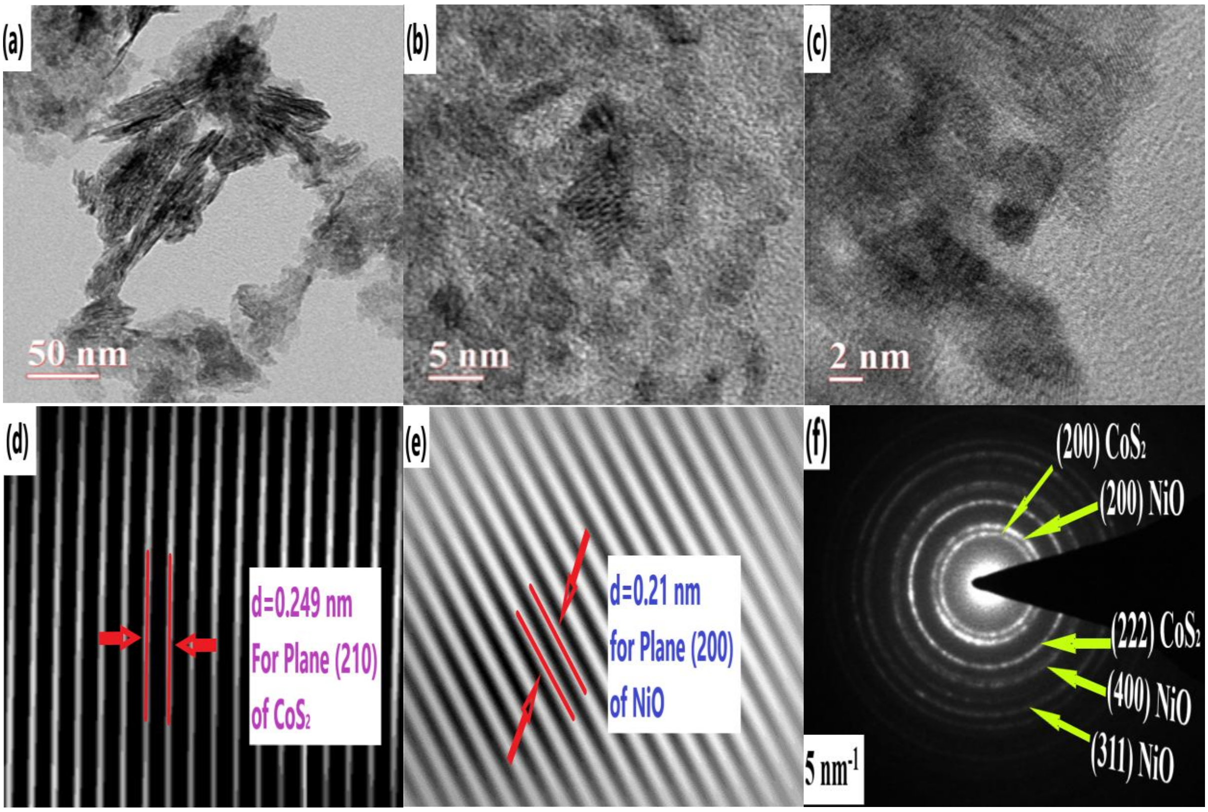

Fig 6.2 HRTEM Image (a, b ,c ,d, and e) and SAED pattern (f) of CoS_2@NiO composite materials

illustrated in Fig. 6.5(e-f) confirms the presence and even spread of Co, S, Ni, and O atoms throughout the heterostructure. This uniform distribution is essential for ensuring consistent electrochemical functionality and improving the interaction between the electroactive materials and the EL. The SSA of NiO and CoS_2@NiO (K4) hetero nanostructures was meticulously calculated using the BET technique, which involved analyzing the nitrogen (N_2) sorption isotherms at 77 K. The specimens were subjected to a degassing process for 3 hours at 200 °C to remove any adsorbed moisture or gases that could interfere with the measurement. The resulting N_2 adsorption-desorption isotherms exhibited distinct hysteresis loops, indicative of the textural properties of the materials, as depicted in Fig. 6.6. The BET SA derived from these isotherms were 8.7 m^2/g for the NiO nanosheets, 10.211m^2/g for CoS_2 and 18.902 m^2/g for the K4 heterostructures. This data demonstrates that the SA of the CoS_2@NiO heterostructures is

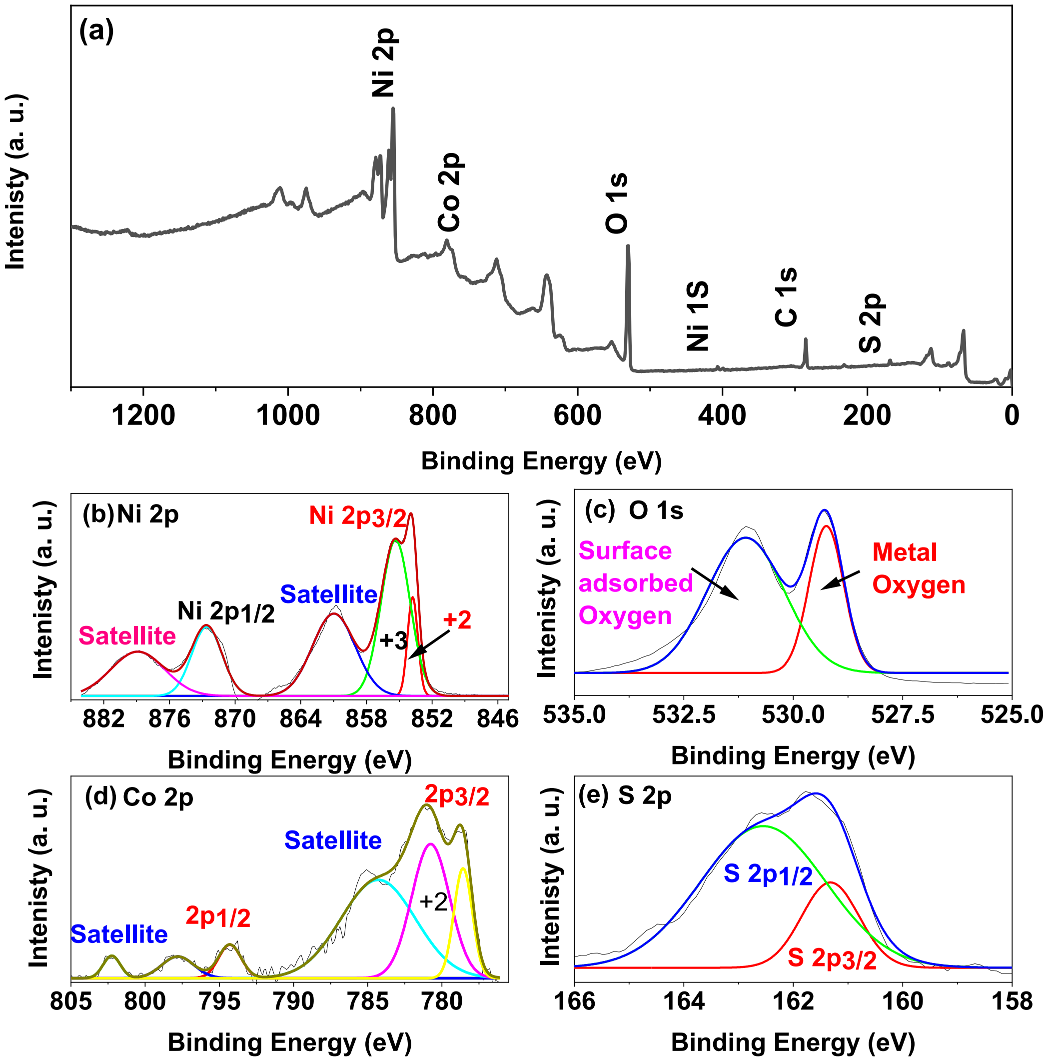

Fig. 6.3 XPS spectra of CoS_2@NiO (K4) nanocomposite: (a) Survey scan and core-level spectra of (b) Ni 2p, (c) O 1s, (d) Co 2p and (e) S 2p.

significantly enhanced, being 2.17 times greater than that of the NiO nanosheets alone and 1.85 times greater than that of the CoS_2 nanosheets alone. This increase in SA is likely due to the incorporation of CoS_2, which introduces additional porosity and surface complexity. Fig. 6.6(d, e, & f) further provides insights into the porosity characteristics through the Barrett-Joyner-Halenda (BJH) pore size variation plots for both NiO, CoS_2 and the K4 composite samples. The NiO nanosheets exhibited an avg. pore size of 3.6 nm, classifying them as mesoporous. In contrast, the synthesized CoS_2@NiO (K4) heterostructures displayed an avg. pore size of 1.8 nm, indicating a transition to microporous structures. This shift from mesoporous to microporous architecture is significant as it augments not only the SA but additionally

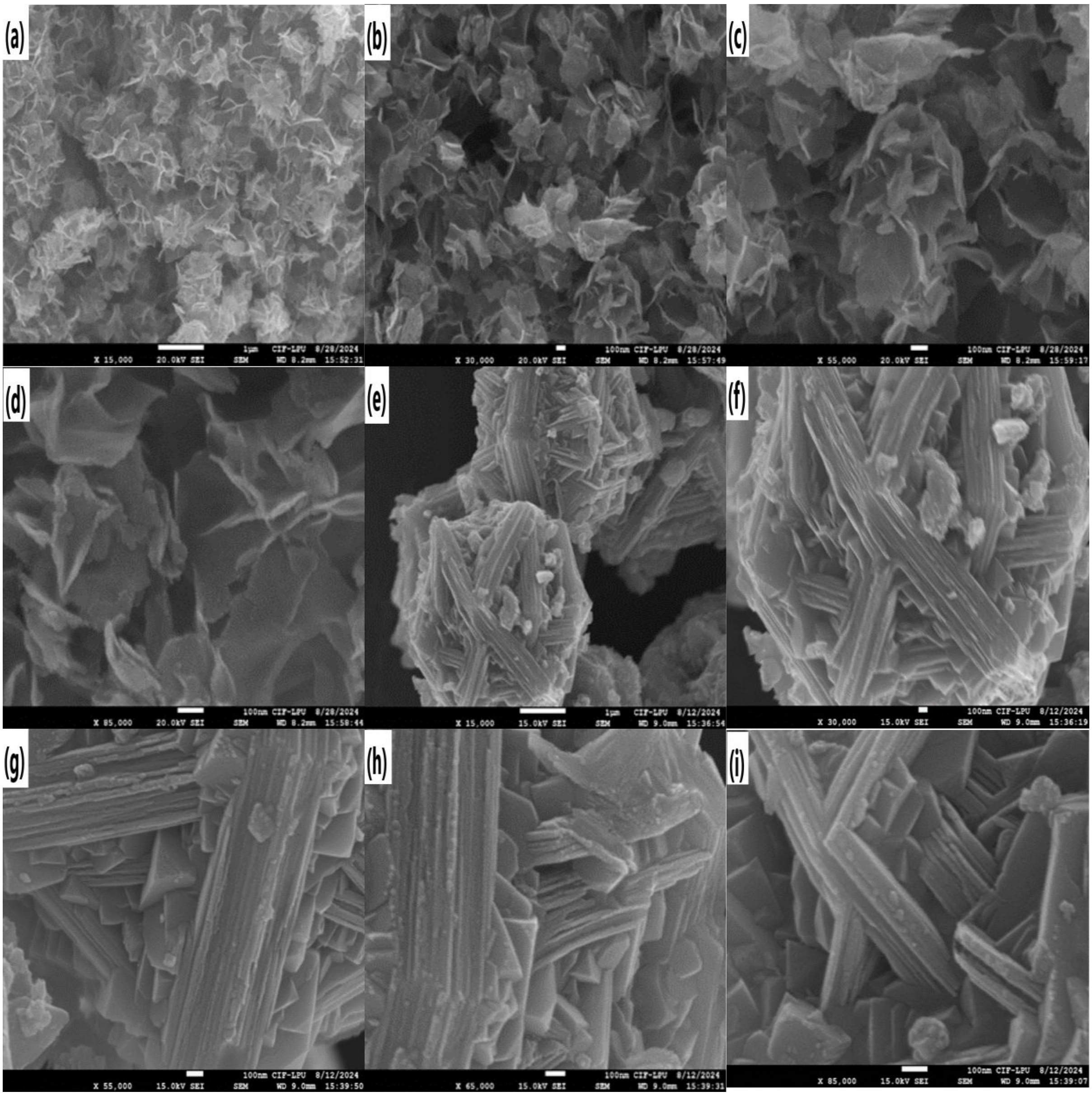

Fig. 6.4. FESEM images of NiO NPs (a-d) and FESEM images of CoS_2 NPs (e- i).

introduces a greater number of active sites. These characteristics are crucial for enhancing electrochemical interactions, especially during the engagement with ELs, thus potentially may improve the functionality of these heterostructures in ES applications.

6.3.2. Electrochemical analysis

The CV analysis of NiO, CoS_2, and different CoS_2@NiO heterostructures (K2, K3, K4, and K5) as competent electrode materials was conducted within 0 to 0.5 V potential range. The CV

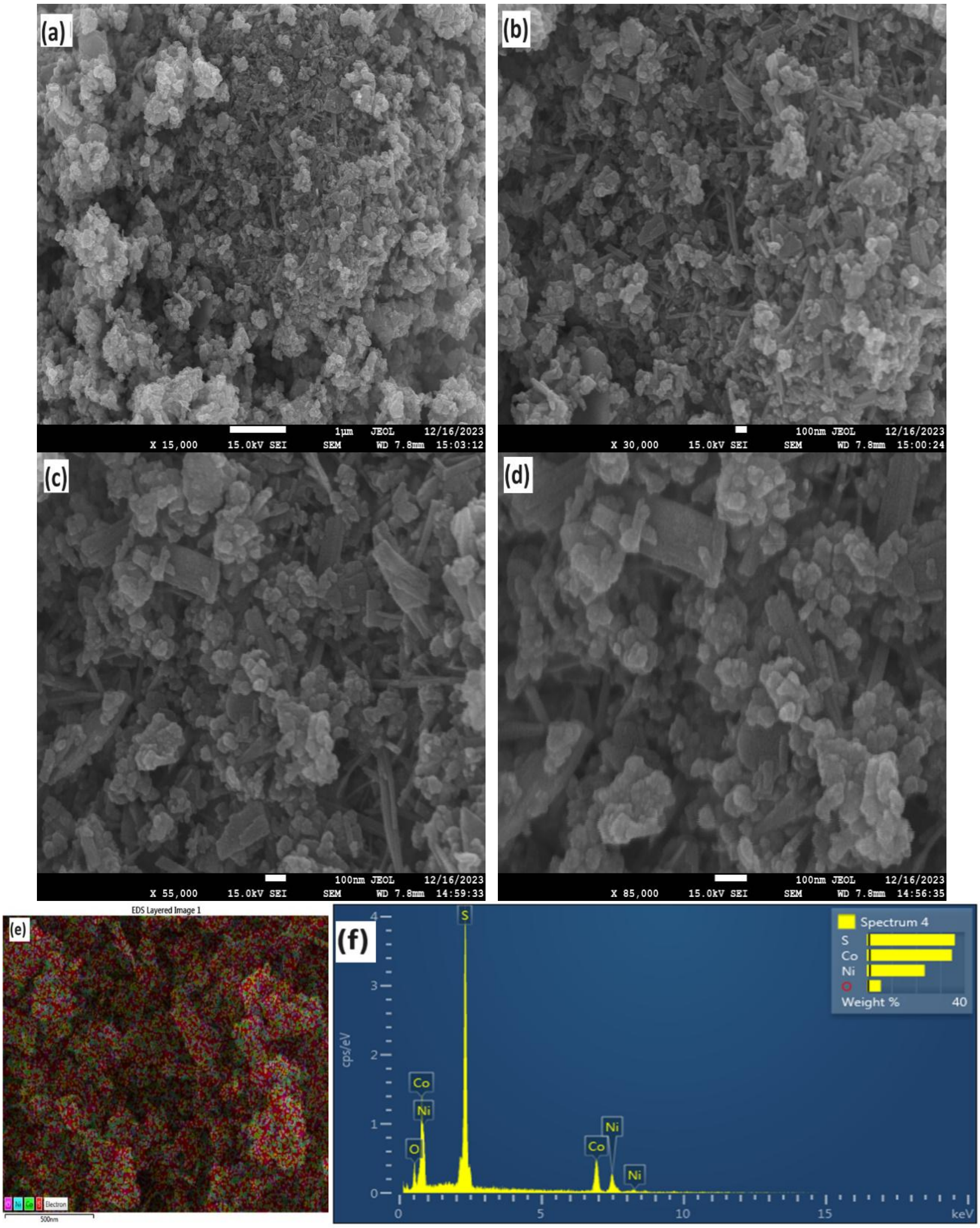

Fig. 6.5 FESEM images (a- d) and EDS mapping (e and f) of CoS_2@NiO (K4) nanocomposite

scans were performed at 10 mV/s, as depicted in Fig. 6(a). CV curve for the K4 electrode exhibited a larger enclosed area compared to the other studied cases, suggesting its superior ES rates. The observed shifts in the cathodic and anodic peaks towards lower and higher voltages, sequentially, can be attributed to decreased ion migration at higher scan speeds. The electrodes specific capacity of 272 C/g (680 F/g), while NiO exhibited 255 C/g (637.5 F/g). The specific capacities for K2, K3, K4, and K5 were 317.5 C/g (793.75 F/g), 340.92 C/g (852.3 F/g), 475 C/g (1187.5 F/g), and 381 C/g (952.55 F/g) at 1A/g. This indicates that the K4 electrode offers approximately 46% and 42% better charge storage capabilities compared to NiO and CoS_2-based electrodes, respectively. Moreover, Fig. 6.7(d) presents the GCD patterns of the K4 electrode under different current densities. For the K4 electrode recorded specific capacity values as follows: 475 C/g at 1 A/g, 460 C/g at 2 A/g, 435 C/g at 3 A/g, 405 C/g at 5 A/g, 376 C/g at 8 A/g, and 250 C/g at 10 A/g. Fig. 5(e) show the variation of Cs verse the current density of NiO, CoS_2, and the CoS_2@NiO composite electrodes. The observed decline in specific capacity at higher v (Fig. 6.7b) and current densities (Fig. 6.7(d & e)) can be ascribed to redox activities, caused by the decreased migration of EL ions within the active regions of the

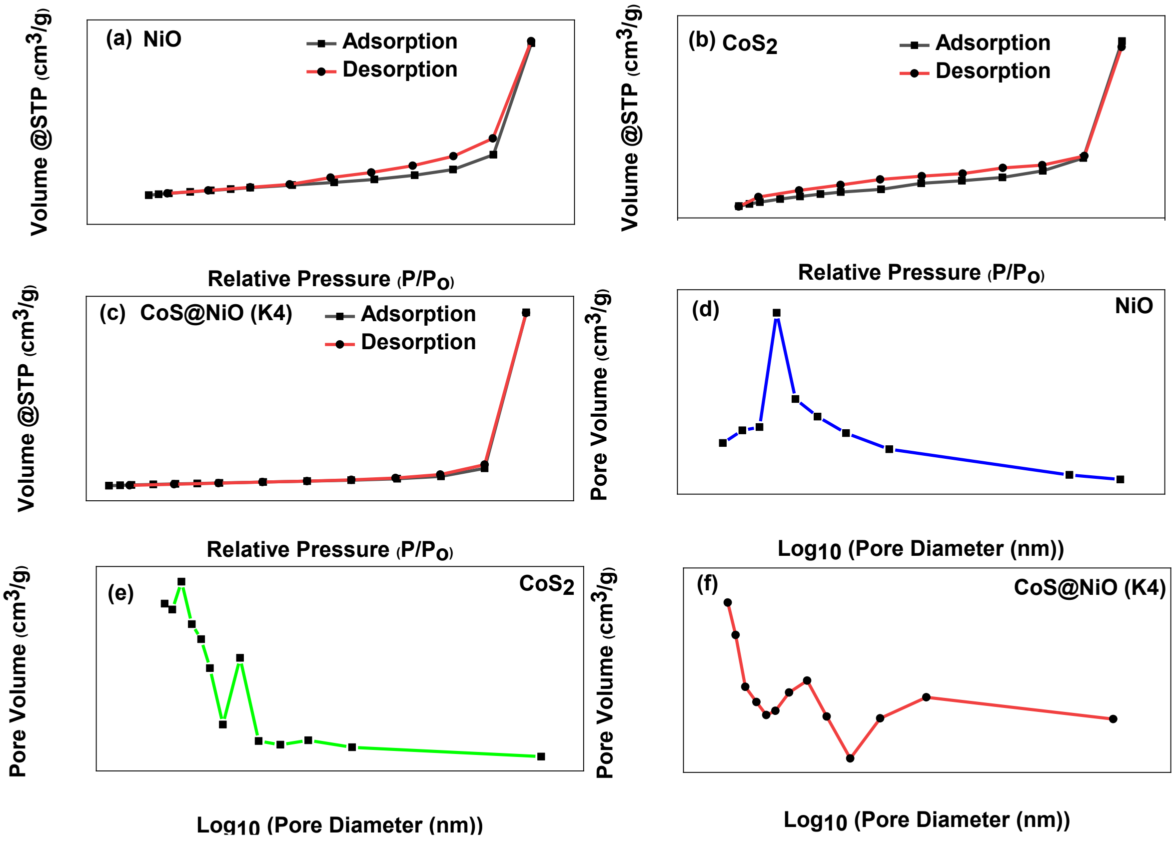

Fig. 6.6 The nitrogen adsorption-desorption isotherm of (a) NiO, (b) CoS_2 and CoS_2@NiO (K4) NPs. The variation of pore volume with pore diameter of (d) NiO, (e) CoS_2 and (f) CoS_2@NiO (K4) NPs.

capability.

electrode. The ES capability of the CoS_2@NiO (K4) based electrode is compared with other similar composite electrodes comprising MOs and MDs in Table 6.1. The data clearly show that the optimized K4 electrode outperforms most of these other composites. This outstanding ES capability is attributed to the synergistic contribution of CoS_2 and NiO, which together uplift the electrochemical properties in composite. The Nyquist plots of NiO, CoS_2, and CoS_2@NiO (K4) composite-based electrodes, along with their equivalent circuit, are illustrated in Fig. 6(f). The steeper slope observed for the K4 electrode compared to NiO and CoS_2 indicates superior diffusion kinetics, underscoring the enhanced ES performance of the K4 electrode. The equivalent circuit model comprises a series resistance (R_S) connected in series with two reactive components, each consisting of a resistance ($R_{G \text{ or }} R_{GB}$) and a CPE ($PE_{G \text{ or }} PE_{GB}$). The first reactive component represents the grain resistance, while the second is associated with grain boundary resistance. The fitted values of the components for NiO, CoS_2, and CoS_2@NiO (K4) electrodes are detailed in Table 6.2. Notably, the K4 electrode exhibits

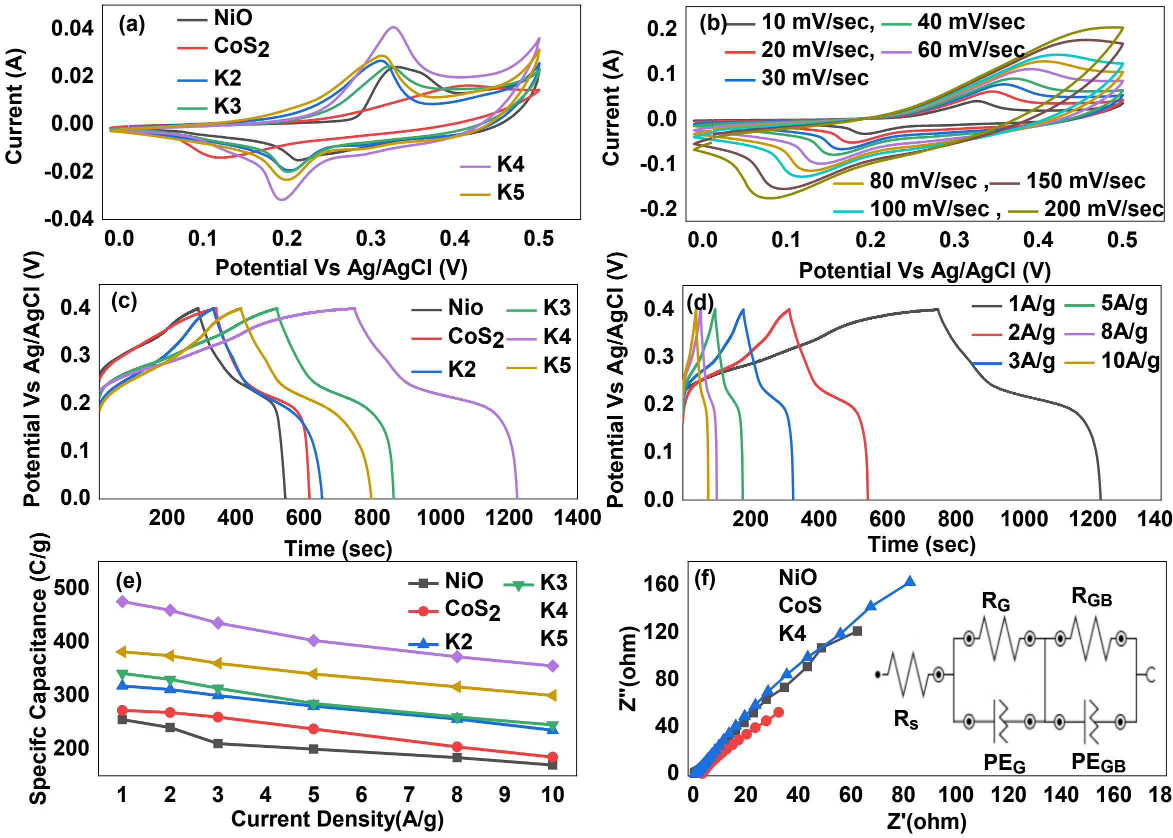

Fig. 6.7 (a) The CV curves of the NiO, CoS_2, and CoS_2@NiO nanocomposite-based electrodes obtained at a v of 10 mV/s.(b) The CV curves of the K4 electrode were obtained at various v. (c) The GCD curves of the NiO, CoS_2, and CoS_2@NiO nanocomposite-based electrodes analyzed at a current density of 1 A/g. (d) The GCD curves of the K4 electrode analyzed at various current densities. (e) The graph illustrates the variation of the specific capacity with current density of NiO, CoS_2, and CoS_2@NiO nanocomposite-based electrodes. (f) EIS plots of NiO, CoS_2 and CoS_2@NiO (K4) nanocomposite-based electrode and equivalent circuit.

Table 6.1 The electrochemical performance of composite electrodes consisting of TMOs and transition metal dichalcogenides.

S. No	**Composite**	**Method**	**Electrolyte (EL)**	**Specific capacitance (F/g)**	**Current density/ v**	**Energy Density (E_D) (Wh/kg)**	**Ref**
1	Co_3O_4@CoS	Hydrothermal	1M KOH	887.5	10mV/s	-	[381]
2	ZnO@CoS	Hydrothermal	3M KOH	898.9 C/g	3 mA/cm^2	45.2 at 1.0391 kW/kg	[282]
3	MoS_2-RuO_2 Composite	Hydrothermal	1M KOH	972	1A/g	35.92 at 0.6 kW/kg	[357]
4	PANI/MoS_2 MnO_2	Hydrothermal	1M H_2SO_4	479	5mV/sec	35.97 at 0.5 kW/kg	[358]
5	NiO/MoS_2	Hydrothermal	1M KOH	289	1A/g	-	[359)]
6	Cu_2O/MoS_2/rGO	Microwave	6M KOH	388	1A/g	-	[360]
7	CuO/MoS_2	Hydrothermal	2M KOH	268	1A/g	26.66 at 1.59 kW/kg	[361]
8	$NiCo_2O_4$@CoS	Hydrothermal	2M KOH	1902.5	1 A/g	32.91 at 0.42 kW/kg	[384]
9	WS_2@NiO	Chemical exfoliation	1M Na_2SO_4	64.5 mF/cm^2	5 mV/s	-	[372]
10	CoS_2@NiO	Hydrothermal	4M KOH	1187.5 (475C/g)	1A/g	50.18 at 0.82 kW/kg	This Paper

Table 6.2. The fitted values of various components of equivalent circuit.

Electrode	**R_S (ohm)**	**R_G (ohm)**	**R_{GB} (ohm)**	**Ionic Conductivity (S/cm)**
NiO	0.718	0.494	755	0.6×10^{-4}
CoS_2	3.19	0.119	278	1.7×10^{-4}
CoS_2@NiO (K4)	0.602	5.62	248	1.9×10^{-4}

the lowest resistance at the electrode- EL interface, measured as 0.60 Ω. Furthermore, the ionic conductivities calculated from the grain and grain boundary resistances for NiO, CoS_2, and CoS_2@NiO (K4) electrodes are 0.6×10^{-4} S/cm, 1.7×10^{-4} S/cm, and 1.9×10^{-4} S/cm, sequentially. These values clearly demonstrate the superior charge transport and reaction kinetics of the K4 electrode compared to its NiO and CoS_2 counterparts. The enhanced electrochemical activity of the C4 electrode are attributed to the synergistic effect of the composite, combining the high electronic conductivity of CoS_2 with the increased surface area of NiO. This synergy results in a microporous composite characterized by superior electrical conductivity and a large SA, facilitating more effective electrode-EL interactions. These properties collectively contribute to the outstanding performance of the K4 electrode in ES applications.

Based upon the above discussion, following can be the probable reaction mechanisms between NiO/CoS_2 and KOH [365,388]:

$$NiO + OH^- \rightleftharpoons NiOOH + e^- \qquad (vii)$$
$$CoS_2 + OH^- \rightleftharpoons CoS_2OH + e^- \qquad (viii)$$
$$CoS_2OH + OH^- \rightleftharpoons CoS_2O + H_2O + e^- \qquad (ix)$$

When NiO interacts with hydroxide ions from the KOH EL, it undergoes a reversible redox reaction to form nickel oxyhydroxide, which facilitates the storage and release of electrons. Similarly, CoS_2 engages in sequential and reversible reactions with hydroxide ions, initially forming CoS_2OH and subsequently converting to CoS_2O while generating water and electrons. The CV plots of NiO and CoS_2@NiO (K4) electrodes were further analyzed to determine the proportion of surface-controlled versus diffusion-controlled charge-storage mechanisms, derived from the relation $i \propto v^b$, where *i* (peak current) and v (scan rate). The parameter '*b*' determined *b* values for the oxidation peaks of nickel oxide and K4 electrodes, which are 0.636

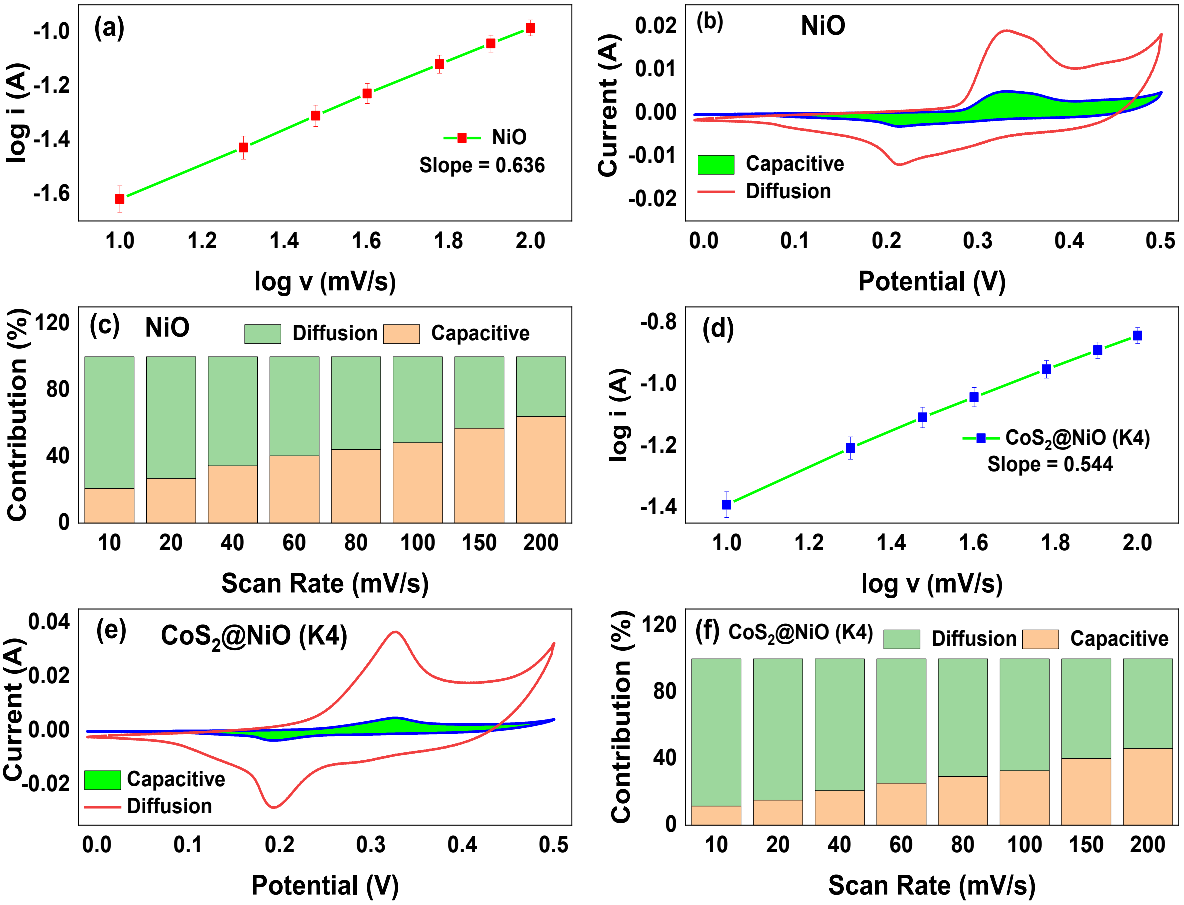

Fig. 6.8 (a) The graph between log (i) vs log (v) plotted for b parameter estimation for NiO. (b) The capacitive and diffusive contributions of NiO electrode at 10 mV/sec. (c) The percentage contribution of diffusive and capacitive current in NiO NPs at different v. (d) The graph between log (i) vs log (v) plotted for b parameter estimation for CoS_2@NiO nanocomposite-based electrode. (e) The capacitive and diffusive contributions of CoS_2@NiO electrode at 10 mV/sec. (f) The percentage contribution of diffusive and capacitive current in CoS_2@NiO electrode at different v.

falls within the range of 0.5 to 1.0, determined from the slope of the log(v) and log(i) plot. A '*b*' value of 1 indicates a purely capacitive response dominated by surface effects, while a '*b*' value of 0.5 indicates a Faradic mechanism. [370,389] Figures 6.8(a) and 8(d) present the and 0.544, sequentially. This indicates that while both electrodes primarily store charge through diffusion or Faradic processes, NiO also exhibits a significant contribution from surface-

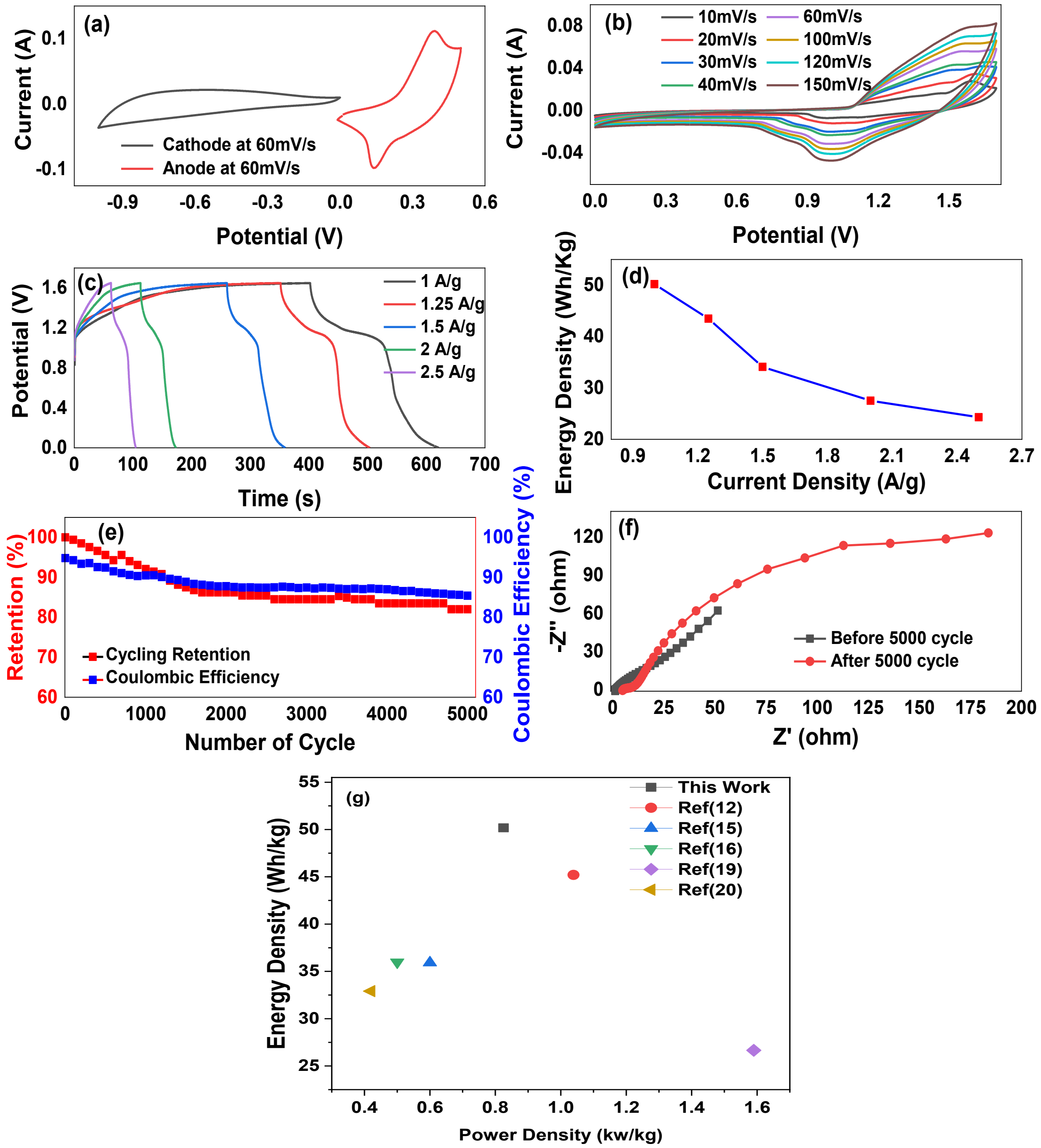

Fig. 6.9 (a) The CV curves of negative electrode and positive electrode obtained at a constant v of 60 mV/s. (b) The CV curves of the device obtained by varying the v while maintaining a potential window of 0 to 1.7 V. (c) The current density dependent GCD curve of the SC device obtained by applying a potential window ranging from 0 to 1.65 V. (f) The variation of E_D of the device with current density. (e) The graph illustrates the variation of percentage retention of Cs and coulombic efficiency with number of cycles. (f) The EIS curve of the device was measured both before and after subjecting it to 5000 cycles of GCD. (g) Ragone plot for compared result with another related paper.

controlled processes. Using Dunn's model, the regions in the CV loops of NiO and CoS_2@NiO representing surface and diffusion-controlled processes are illustrated in Fig. 6.8(b) and 6.8(e). The analysis was conducted at a v of 10 millivolts per second. Figures 6.8(c) and 6.8(f) further display the proportions of these regions at various v. It is evident that at lower v, Faradic processes dominate charge storage because ions have enough time to move into the electrode material and undergo redox reactions, fully utilizing the active material. In contrast, at higher v, the limited time for ion diffusion causes charge storage to shift towards capacitive processes, involving rapid sorption of ions on the electrode surface.

An ASC was assembled using CoS_2@NiO (K4) as the anode and graphite-mixed activated carbon (GMC) as the cathode, denoted as CoS_2@NiO//GMC, to assess its practical utilization. The active materials on cathode and anode electrode were 1 and 2.5 mg respectively. indicating their compatibility for the device. Figure6.9(a) show the CV curves of the anode and cathode at a v of 60 mV/sec. The CV plots of the ASC, recorded at various v, revealed a stable potential window from 0 to 1.7 V, as illustrated in Fig. 6.9(b). The consistent shape of the curves across various v demonstrates that the device performs well over a wide range of operating conditions. Figure 9(c) shows the current dependent GCD curves of the ASC. The capacitance per unit active material's mass of the device was calculated at different current densities, yielding values of 530.90 F/g at 1 A/g, 460 F/g at 1.25 A/g, 360.72 F/g at 1.5 A/g, 290.90 F/g at 2 A/g, and 256.96 F/g at 2.25 A/g. Figure 6.9(d) illustrates how the energy densities of the NSD vary with different current densities, clearly indicating that the E_D reduces as the current density increases. The ASC achieved a notable 50.18 Wh/kg at 0.825 kW/kg. The robustness and durability of the ASC are highlighted by its retention of about 82% of its initial capacitance and approximately 85% of its Coulombic efficiency post 5000 cycles at 2 A/g, as shown in Fig. 6.9(e). Figure 6.9(f) displays the EIS curves of the ASC device pre and post 5000 cycles, showing minimal changes in the Nyquist plots. This indicates the structural and morphological stability of the electrodes, with negligible degradation even after prolonged cycling. The comparison of reported energy densities of devices prepared with similar anode-composite materials, compiled in Table 6.1, clearly showcases the superior performance of the CoS_2@NiO//GMC. Ragone plot for compared result with another related paper showing in fig 9(g).The outstanding performance can be assigned to the synergistic contribution of CoS_2's superior electrical conductivity and NiO's excellent electrochemical stability, resulting in a microporous composite with commendable electrical conductivity and a large SA. These properties enhance the electrode-EL interactions, contributing to the remarkable performance of the developed ASC.

6.4 Conclusion

In conclusion, this investigation demonstrated the significant potential of CoS_2@NiO composite heterostructures as high-efficiency electrode materials for enhancing electrochemical functionality. By harnessing the synergistic interplay of CoS_2's superior electrical conductivity and NiO's remarkable electrochemical stability, we successfully synthesized and optimized the CoS_2@NiO composite through hydrothermal method. The optimized electrode exhibited specific capacity of 475 C/g (1187.5 F/g), significantly outperforming NiO and CoS_2 based electrodes by approximately 46% and 42%, respectively. Our study revealed that at lower v, diffusion-driven processes dominated the charge storage mechanism, while at higher v, surface-controlled processes prevailed. E_D of 50.18 Wh/kg was delivered by the assembled ASC(CoS_2@NiO//GMC) further validated the composite's practical application, at a P_D of 0.825 kW/kg. Additionally, the device maintained a retention rate of 82% after 5000 cycles, indicating robust performance and durability. These findings underscored the transformative impact of compositional tuning and heterostructure formation in optimizing electrochemical behavior, showing the way for future advancements in high-performance ES devices.

Chapter 7

Optimization of CuS@NiO Nanocomposite for Enhanced Charge Storage in Supercapacitors

7.1 Introduction

SCs have garnered considerable attention as a noteworthy ES device due to their exceptional safety, impressive P_D, and long cycle life. The ES capability of SCs is mainly dependent on the electrode materials used [350]. To address the growing need for high P_D and Ed, significant research has focused on MO pseudocapacitive materials as potential candidates for high-performance SCs. Several TMO materials, including Co_3O_4, MoO_3, MnO_2, V_2O_5, NiO, and $NiCo_3O_4$, have been studied. Among these, NiO is notable and favored for its reasonable price, strong chemical and thermal stability, widespread accessibility, and minimal environmental impact [353]. Nevertheless, the intrinsic low conductivity of TMOs can obstruct the movement of ions and electrons, thus restricting their usefulness. To overcome these constraints and improve the efficiency of NiO, it is imperative to investigate alternative materials for ES. Developing innovative hybrid electrodes that can address these limitations is crucial for enhancing the efficiency of NiO-based electrodes [374–376]. An effective approach is the development of heterostructures by combining components with distinct band gaps [377]. Heterostructures exhibit unique physical phenomena and advantages that a single component cannot achieve by leveraging energy level asymmetry. Additionally, the internal field can prevent the recombination of electrons and holes at the contact by effectively separating them. This facilitates multiple steps in the charge extraction process [378,379].

Transition metal sulfides (TMS) have emerged as a popular choice due to their inherent conductivity and layered structure. They have extensive applications in various domains, including photocatalytic processes, ES, and conversion [278]. Several researchers have investigated the combined action of TMOs with TMS, demonstrating notable improvements in Cs, E_D, P_D, and cycling stability. For instance, the Cs values of 781.1 C/g was achieved by the MnO_2@CoS hybrid electrode at2 mA/cm². The utilization of MnO_2@CoS heterostructure composite electrodes in symmetric SC. At 0.597 kW/kg, symmetric SC demonstrate the E_D of 34.72 Wh/kg [391]. The ZnO/CuS composite synthesized via the hydrothermal method. The specific capacity of 1830 mF/cm² was exhibits by ZnO/CuS composite at 2 mA/cm². At 4.26 W/cm², the symmetric SC was achieved an E_D of 0.27 Wh/cm² [392]. At 0.5 A/g, the Mn-doped SnO_2@MoS_2 composite electrode shows an impressive Cs of 242 F/g, with remarkable retention rate of 97% after 5000 cycles [279]. The Cs of 898.9 C/g was exhibited by the ZnO@CoS composite at 3 mA/cm² [382]. At 1 A/g, the Cu_2O/MoS_2/rGO composite demonstrates a significant Cs of 388 F/g and after 3000 cycles retains cyclic stability of 95.6% [360]. The MoS_2@TiO_2 composite synthesized using the hydrothermal process. At 10 mV/s, composite demonstrates a Cs of 210 F/g. Furthermore, MoS_2@TiO_2 composite electrode demonstrate a cyclic stability of 98% after 2000 cycles. At 1.3 kW/kg, MoS_2@NiO composite was demonstrate an E_D of 21 Wh/kg [389]. Cs of 479 F/g and 469 F/g was achieved by the PANI/MoS_2-MnO_2 composite electrode at 5 mV/s and 1 A/g, respectively. At 0.5 kW/kg, the SC device made using the composite electrode demonstrated an E_D of 35.97 Wh/kg, maintaining retention rate of 94.1% after 4000 cycles [358].

TMS are actively researched due to properties such as variable valences, stoichiometric compositions, specific crystal structures, band gap properties, and high extinction coefficients. Copper sulfide, a type of metal chalcogenide, exists in several forms depending on the ratio of copper (Cu) to sulfur (S) in the compound [393,394]. Among various copper sulfides, including Cu_2S, CuS_2, and CuS, CuS emerges as a promising electrode material due to its high electrical conductivity, which is comparable to that of metals (10^{-3} S/cm). [395].

This research aims to improve the ES capability of NiO-based electrodes by synthesizing and characterizing CuS@NiO composites with varying CuS content. This study systematically investigates the synergistic effects of combining NiO with CuS to achieve substantial improvements in specific capacity, E_D, and cycling stability. By methodically varying the CuS composition and rigorously analyzing the electrochemical properties of the resulting composites, this research endeavors to develop advanced hybrid electrodes that mitigate the intrinsic low conductivity of NiO. Furthermore, a hybrid device incorporating optimized CuS@NiO as the anode and expanded graphite and activated charcoal (EGA) as the cathode is assembled and characterized to evaluate its ES capability and durability.

7.2 Materials and methods

7.2.1 Synthesis and electrode fabrication

Synthesis of nickel oxide (NiO): The experiment began by mixing 0.1 M $Ni(NO_3)_2 \cdot 6H_2O$, 0.05 M hexamine, and 0.05 M urea with 90 mL of DI water. Subsequently, the stirring process started using a magnetic stirrer. Next, the solution was subjected to three consecutive irradiation exposures in a microwave for 180 seconds, 120 seconds, and 90 seconds, using a multimode cavity operating at 900 W. Then, the solution was separated by filtration using filter paper, successfully isolating the $Ni(OH)_2$ precipitates. The reaction scheme is given below [353]:

$$NH_3 + H_2O \rightarrow NH_4 + OH \quad (i)$$
$$2Ni(NO_3) \rightarrow Ni^{2+} + 2NO^{3-} \quad (ii)$$
$$Ni^{2+} + 2OH \rightarrow Ni(OH)_2 \quad (iii)$$

The resultant precipitate was subsequently washed through a series of washing processes, which included water, alcohol, and acetone. Then, the $Ni(OH)_2$ precipitate annealed at 300 °C for 2 hours, leading to the development of NiO nanostructures.

Synthesis of CuS: Initially, 500 mg of copper sulfate pentahydrate and 250 mg of thioacetamide were mixed in 80 mL of water using magnetic agitation for a duration of 20 minutes. Afterwards, the solution was poured into an autoclave, which was operated at 180 °C for 8 hours. The reaction scheme is shared below [396]:

$$Cu^{+2} + 2OH^- \rightarrow Cu(OH)_2 \quad (iv)$$
$$CH_3CSNH_2 + OH^- \rightarrow CH_3CN + H_2O + SH^- \quad (v)$$
$$SH^- + OH^- \rightarrow Co^{+2} + 2NO^{-3} \quad (v)$$
$$Cu(OH)_2 + S^{2-} \rightarrow CuS + 2OH^- \quad (vi)$$

Following the cooling process to reach ambient temperature, the solution underwent filtration and subsequent multiple washes using DI water, acetone, and ethanol in order to obtain CuS NPs. Subsequently, the CuS NPs underwent a drying process at 70 °C for 10 hours. The quantity of CuS nanostructures acquired was 350 mg.

Synthesis of the composite CuS/NiO heterostructure:

A total of 400 mg of NiO was homogenized with 80 mL of distilled water by ultrasonication of 1 hour. Subsequently, an equal amount of copper sulfate pentahydrate and thioacetamide was added, and the aforementioned process, as outlined in the synthesis of CuS, was repeated. This procedure resulted in the formation of 20% CuS@NiO after filtration. The same procedure was applied to synthesize additional nanocomposites with 30, 40, and 50% CuS in the CuS@NiO composite, with the corresponding proportions of NiO being 1400, 816.6, 525, and 350 mg, respectively. The resulting specimens with 20, 30, 40, and 50% CuS in the CuS@NiO composite were labelled as C2, C3, C4, and C5, respectively.

7.3 Results and discussion

7.3.1 Structural and morphological analysis

Figure 7.1(a) presents the XRD patterns of CuS NPs. The diffraction peaks corresponding to the (101), (102), (103), (006), (110), (108), and (116) planes are observed at 27.7°, 29.2°, 32.6°, 33.3°, 48.8°, 53.6°, and 59.2°, respectively. These peaks align well with the JCPDS card (no. 78-0880), confirming the successful synthesis of CuS NPs. Figure 7.1(b) shows the XRD patterns of NiO NPs. The peaks at 37.2°, 43.3°, 62.9°, 75.4° and 79.4°, are observed in the diffraction curves of all studied reaction temperatures, displaying the presence of (111), (200), (220), (311) and (222) planes, respectively. These values are consistent with the PDF (ICSD) 01-071-1179, confirming the formation of cubic NiO NPs. Figure 7.1(c) illustrates the XRD patterns of the CuS@NiO (C4) composite. The characteristic peaks of both CuS and NiO are clearly visible, confirming the successful synthesis of the composite material. Figure 7.2(a–f) displays the results of the XPS analysis, examining the elemental composition and oxidation states of the CuS@NiO composite material. The binding energy (B.E.) for Cu 2p3/2 and 2p1/2 orbitals are observed at 932.3 eV and 952.4 eV, respectively (Fig. 2b), with two satellite peaks at 941 eV and 962 eV, indicating the +2-oxidation state of Cu. In Fig. 7.2(c), peaks at 161.3 eV and 162.6 eV for S 2p confirm the -2-oxidation state of sulfur [397,398]. In Fig. 2(d), peaks at 854 eV and 872.9 eV for the Ni $2p_{3/2}$ and Ni $2p_{1/2}$ orbitals, respectively, show deconvoluted peaks at 853.7 eV and 855 eV, indicating the coexistence of Ni's +2 and +3 oxidation states. Additionally, two satellite peaks at B.E. 861.2 eV and 879.3 eV of Ni orbitals are visible. The O 1s spectra in Figure 7.2(e) show peaks at B.E. 531.5 eV and 529.8 eV, further indicating the coexistence of +2 and +3 oxidation states of Ni [398,399]. The visible B.E curve of Ni, O, Cu, and S elements in the XPS analysis confirms the successful formation of CuS@NiO composite materials. Figure 7.3(a-f) shows magnified FESEM images of sample C4, where distinct

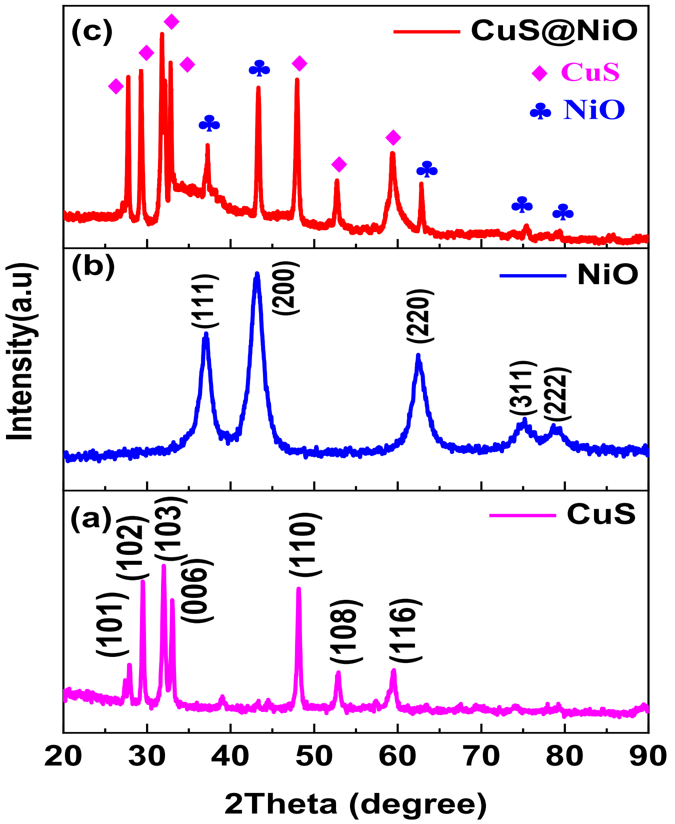

Fig. 7.1 XRD spectrum of (a) CuS, (b) NiO and (c) CuS@NiO.

morphologies of CuS and NiO within the composite are clearly identifiable. In the composite, NiO exhibits a granular morphology, while CuS displays a nanosheet-like morphology. The nanosheet-like structure embedded in granular generally enhances the material's porosity, which probably in turn may improves the electrochemical performance of the composite material C4. EDS mapping of sample C4, shown in Fig. 7.4, provides information on the distribution and presence of the elements Cu, S, Ni, and O in the composite material, which also supports the XRD and XPS results, further confirming the successful formation of CuS@NiO composite materials. The uniform distribution of these elements may facilitate the interaction of active materials with the EL. The SSA of NiO, CuS and C4 hetero nanostructures was meticulously calculated using the BET technique, which involved analyzing the N_2

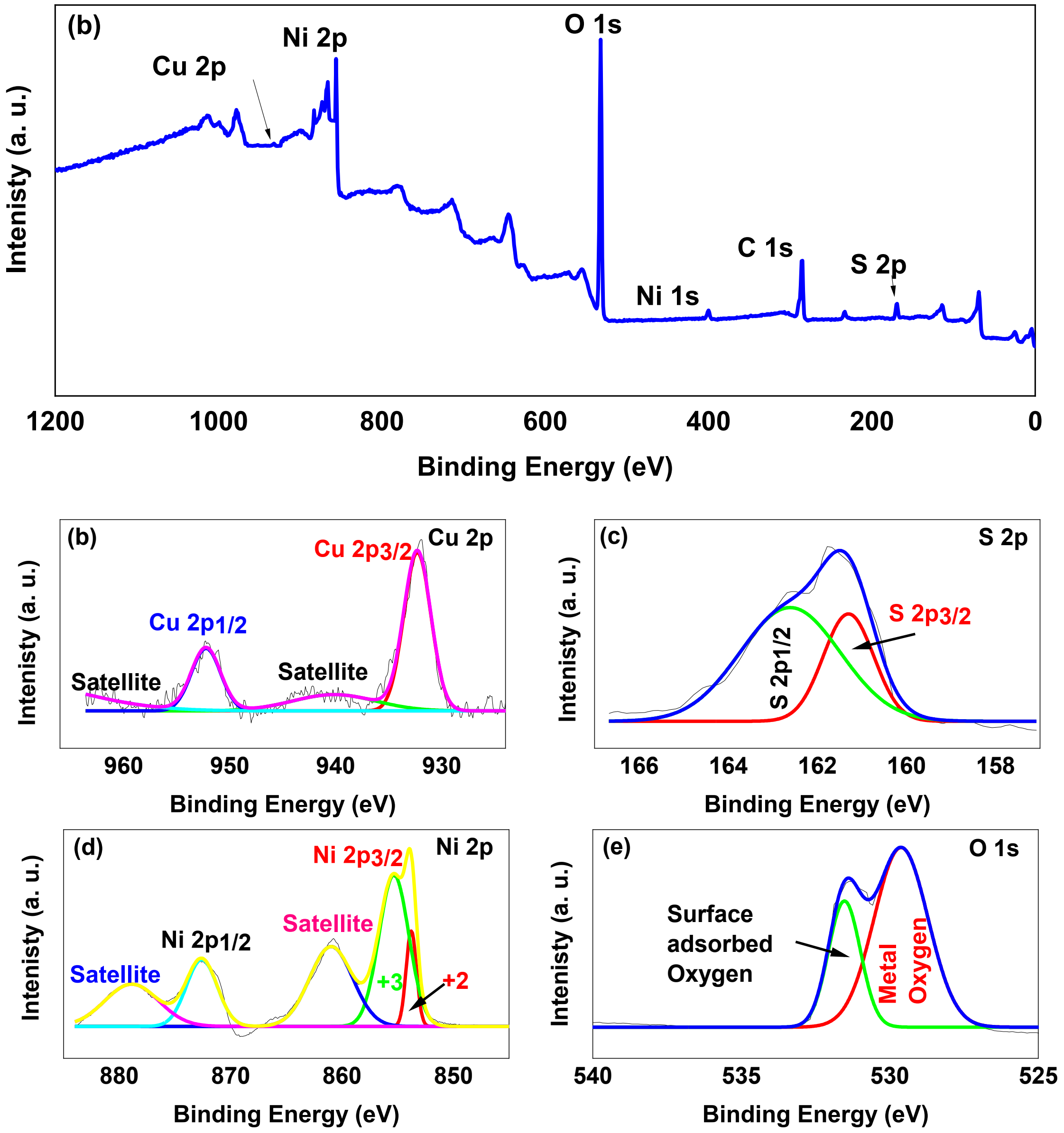

Fig. 7.2 XPS spectra of CuS@NiO (C4) nanocomposite: (a) Survey scan and core-level spectra of (b) Cu 2p, (c) S 2p, (d) Ni 2p, (e) O 1s.

adsorption isotherms at 77 K. The specimens were subjected to a degassing process for 3 hours at 200 °C to remove any adsorbed moisture or gases that could interfere with the measurement. The resulting N_2 adsorption-desorption isotherms exhibited distinct hysteresis loops, indicative of the textural properties of the materials, as depicted in Fig. 7.5(a) and (b), respectively. SSAs derived from the data are 8.686 m^2/g for NiO and 15.068 m^2/g for C4 sample. This indicates

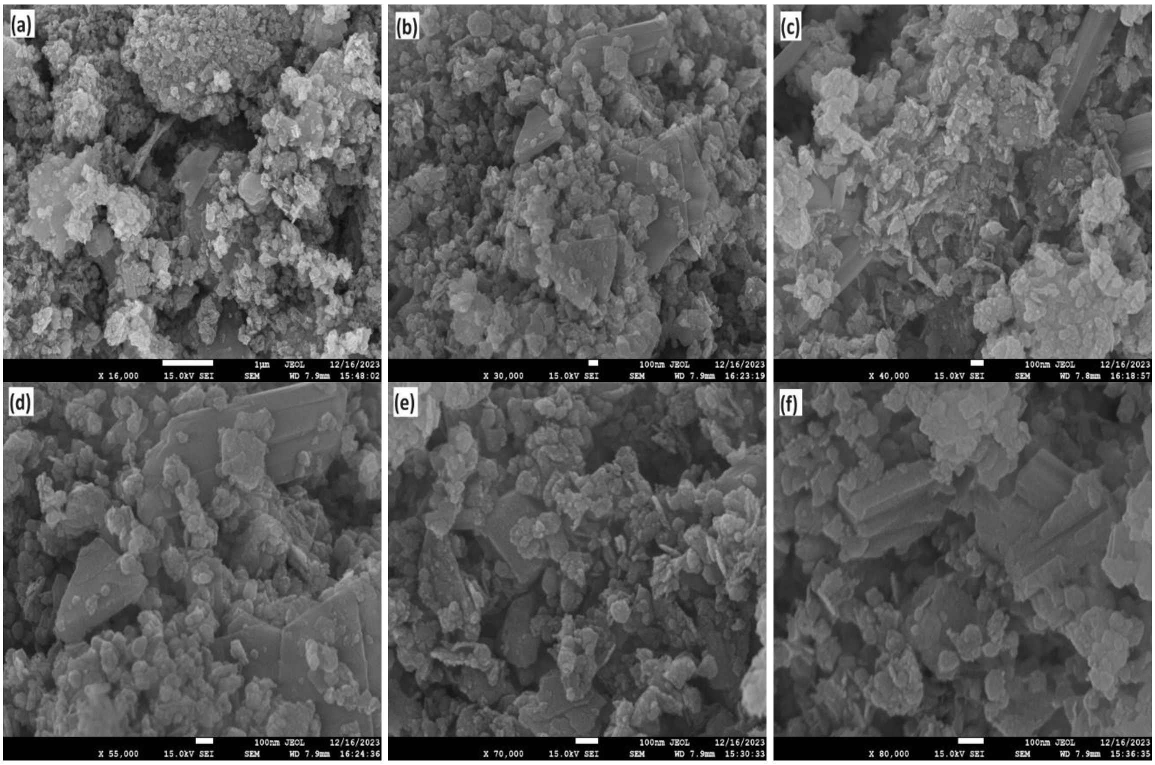

Fig. 7.3. FESEM images of CuS@NiO (C4) nanocomposite at different magnification.

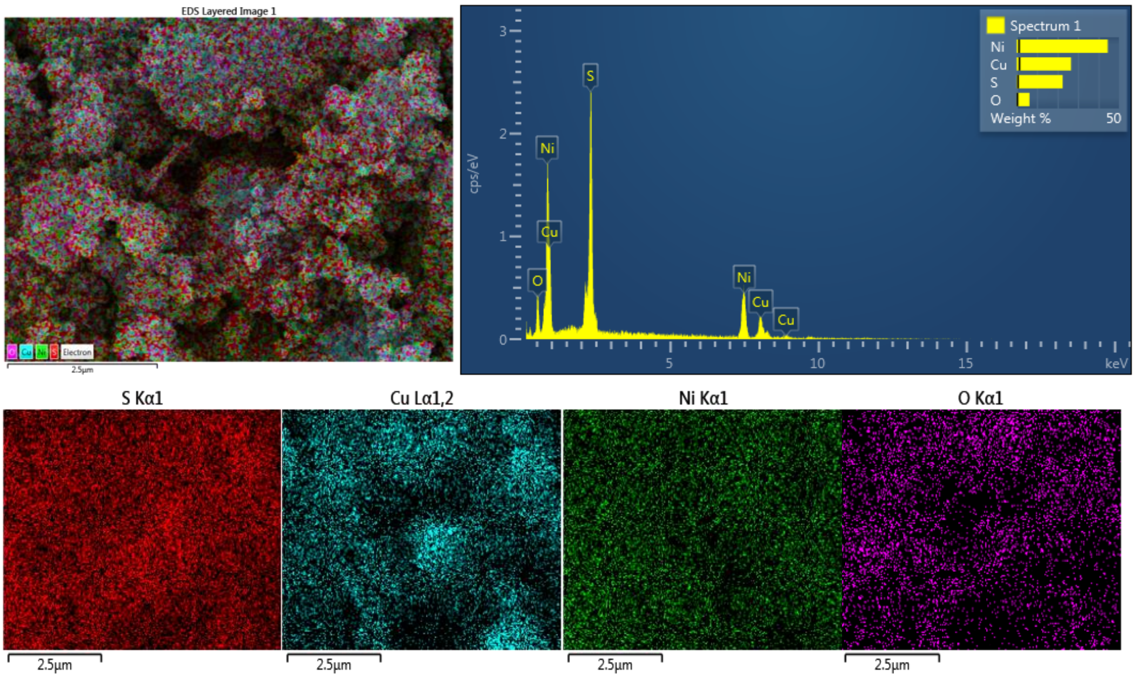

Fig. 7.4. EDS mapping of CuS@NiO (C4) nanocomposite.

that after adding CuS to NiO, the specific SA of the composite increases by approximately 1.73 times. The pore size distribution graphs for NiO and C4 samples are depicted in Fig. 7.5(c) and (d), respectively. For NiO sample, the avg. pore volume and pore radius are 0.038 cm³/g and 1.816 nm, reflecting the mesoporous nature of NiO nanomaterials. For the CuS@NiO (C4) sample, the avg. pore volume and pore radius are 0.150 cm³/g and 0.91 nm, indicating a shift from mesoporous to microporous nature upon CuS incorporation. The decrease in pore diameter and increase in pore volume after composition demonstrate an increase in porosity and availability of more external active sites on the surface of CuS@NiO (C4) composite. Both BET and FESEM characterizations support each other's results, indicating that after the incorporation of CuS in NiO, there is an increase in SA, active sites, and porosity of the material.

7.3.2. Electrochemical analysis

For electrochemical analysis, a three-electrode setup was used to conduct CV analysis on NiO, CuS, and their composite materials (C2, C3, C4, and C5) as potential electrode materials. The CV of all electrodes was performed at a v of 10 mV/s within a potential window from 0 to 0.5 V, as shown in Fig. 7.6(a). The CV curve of the C4 electrode encloses a larger area compared

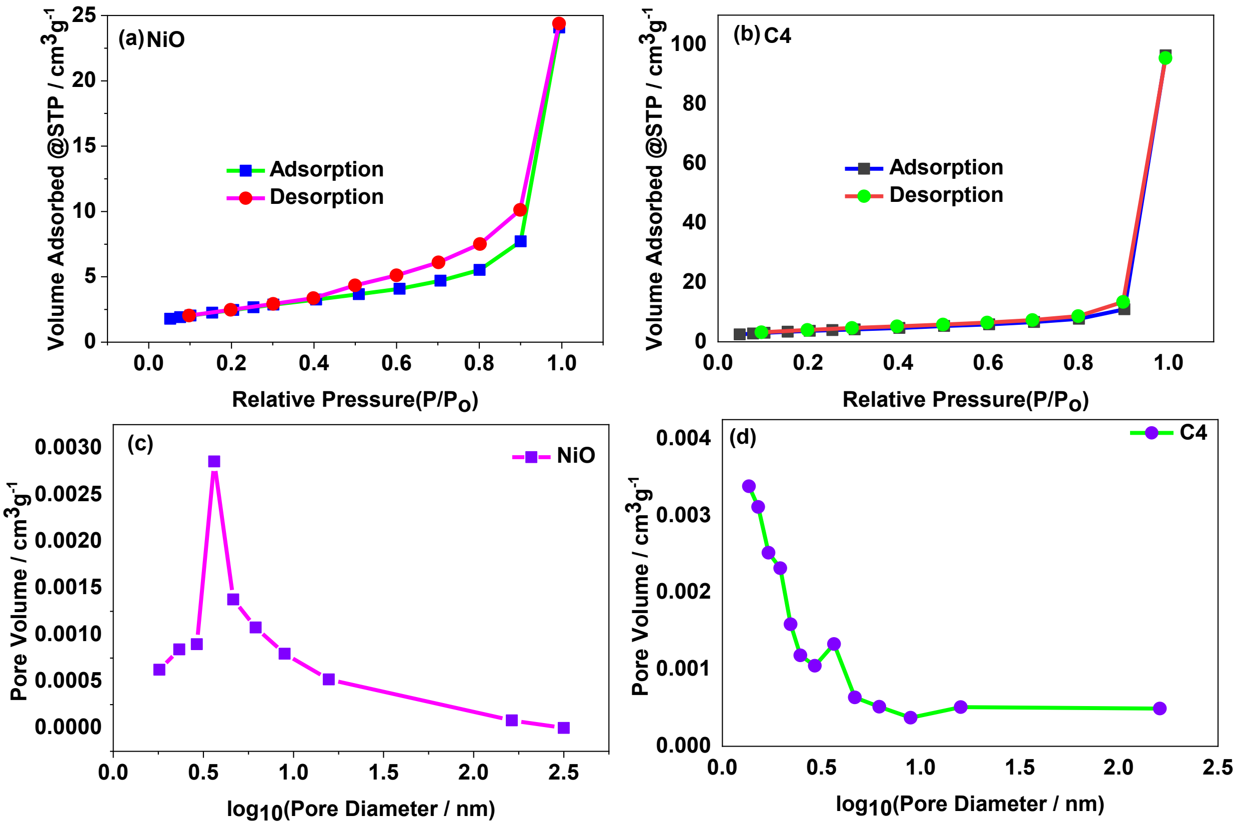

Fig. 7.5. The nitrogen adsorption-desorption isotherm of (a) NiO and (b) CuS@NiO (C4). The variation of pore volume with pore diameter of and (c) NiO and (d) CuS@NiO (C4).

to the other electrodes, indicating a higher charge storage capability of the electrode. Figure 7.6(b) displays the CV curve of sample C4 at different v. From lower to higher v, the CV curves of sample C4 maintain their shape. The GCD results confirm the findings obtained from the CV analysis of the electrodes. Figure 7.6(c) show the GCD curves of CuS, NiO, and their composite electrodes, measured at 1 A/g within a potential range of 0 to 0.4 volts. The CuS@NiO-based electrodes exhibit significantly longer discharge durations compared to the NiO and CuS electrodes, underscoring their superior electrochemical performance. The specific capacities of the CuS, NiO, C2, C3, C4, and C5 electrodes are 237.5 C/g (593.75 F/g), 254.5 C/g (636.25 F/g), 276 C/g (690 F/g), 323 C/g (807.5 F/g), 392 C/g (980 F/g), and 284C/g (710 F/g), respectively. improvement over NiO, underscoring its superior electrochemical

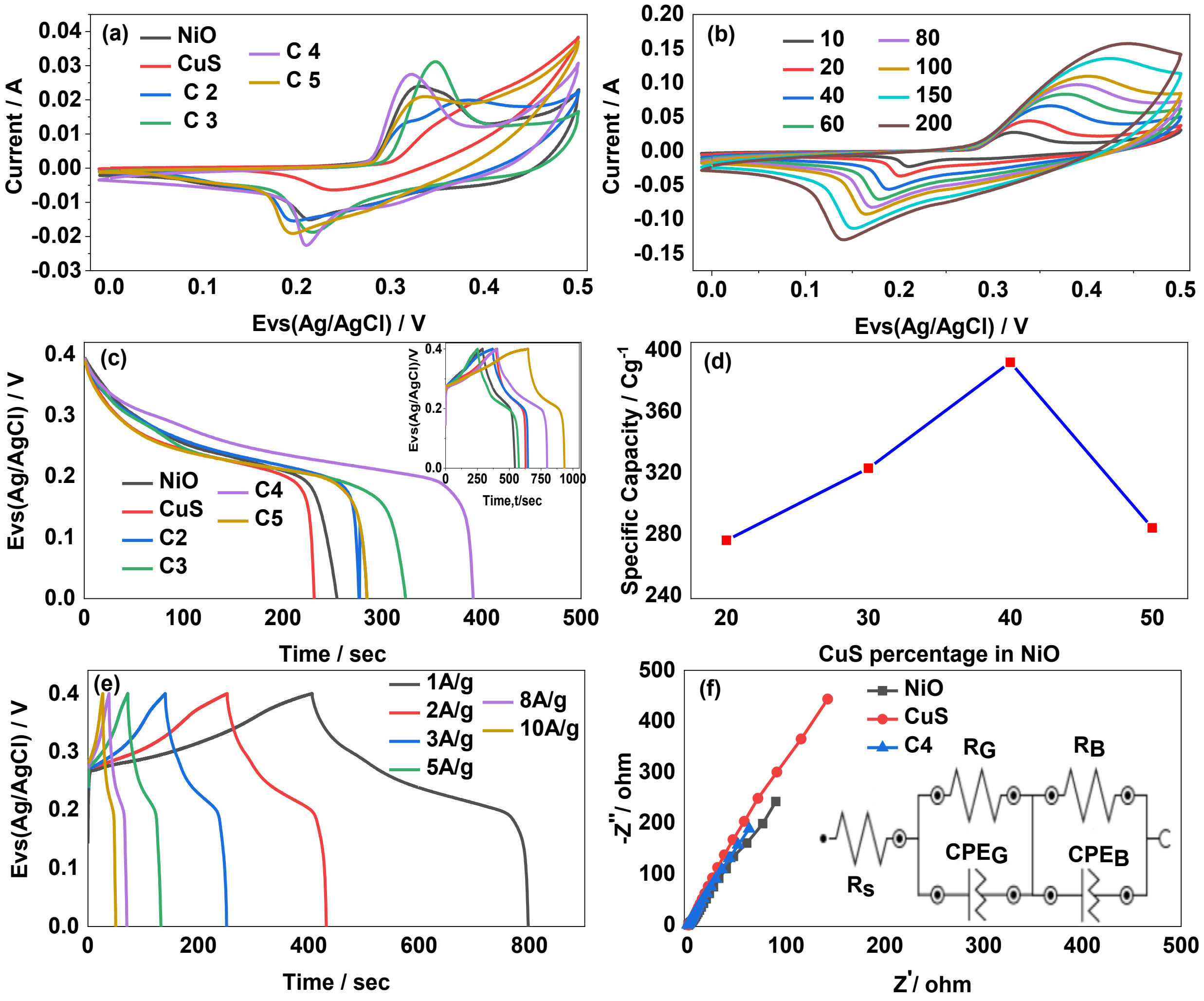

Fig. 7.6 (a) The CV curves of the NiO, CuS, C2, C3, C4, and C5 electrodes obtained at 10 mV/s. (b) The CV curves of the C4 electrode at various v. (c) GCD curves of the NiO, CuS, C2, C3, C4, and C5 at 1 A/g. (d) The variation of specific capacity with the percentage of CuS in composite electrode. (e) The GCD curves of the C4 at current densities. (f) EIS plot of CuS, NiO and C4 electrode (inset shows the equivalent circuit diagrams).

Table 7.1. The values of various components of the equivalent circuit.

Electrode	R_S (ohm)	R_G (ohm)	R_B (ohm)	Ionic conductivity (S/cm)
NiO	1.02	3.95	1900	0.26×10^{-4}
CuS	1.19	2.78	3917	0.12×10^{-4}
CuS@NiO (C4)	0.4	0.657	888	0.56×10^{-4}

Table 7.2 The electrochemical performance of composite electrodes consisting of TMOs and transition metal sulphide.

S. No	Composite	Method	Electrolyte (EL)	Specific capacitance (F/g)	Current density/ v	Energy Density (Wh/kg)	Ref
1	MnO_2@CoS	Electrodeposition method.	3 M KOH	781.1 C/g	2 mA/cm ^{2}	34.72 at 0.597 kW/kg	[390]
2	ZnO@CuS	Hydrothermal	2M KOH	1830 mF/cm^2	2mA/cm^2	0.27 Wh/cm^2 at 4.26W/cm^2	[391]
3	Mn doped SnO_2@MoS_2	Hydrothermal	2 M KOH	242	0.5 A/g.		[379]
4	MoS2@TiO_2	Hydrothermal	1 M sodium sulphate	210	10 mV/sec	21 at 1.3 kW/kg	[389]
5	PANI/MoS_2 MnO_2	Hydrothermal	1M H_2SO_4	479	5mV/sec	35.97 at 0.5 kW/kg	[358]
6	MoS2-RuO2 Composite	Hydrothermal	1 M KOH	972	1 A/g	35.92 at 0.6 kW/kg	[357]
7	CuO/MoS_2	Hydrothermal	2M KOH	268	1A/g	26.66 at 1.59 kW/kg	[361]
8	$NiCo_2O_4$@CoS	Hydrothermal	2M KOH	1902.5	1 A/g	32.91 at 0.42 kW/kg	[383]
9	WO_3-ZnS	microwave assisted wet chemical method	20% KOH solutions	215	1 A/g		[355]
10	CuS@NiO	Hydrothermal	4M KOH	980 (392C/g)	1A/g	44 at 0.82 kW/kg	This Paper

performance. Figure 7.6(e) shows the current density dependent GCD curves of the C4 electrode. The specific capacities of the C4 composite sample are 392, 359, 334.5, 300 Figure 6(d) demonstrates the variation in specific capacity with the percentage of CuS in the composite CuS@NiO electrodes (from C2 to C5). The C4 electrode exhibits enhanced charge storage capacity compared to the other electrodes (C2, C3, and C5) studied. In addition to this, the C4 electrode exhibited a 65.0% enhancement in specific capacity over CuS and a 54.0%, 256, and 240 C/g at 1, 2, 3, 5, 8, and 10 A/g, respectively. At higher current densities, ion diffusion is reduced, leading to a decrease in the rate capability of the electrode by 39% when the current density is increased tenfold. This reduction in capacity at higher current densities is due to concentration polarization caused by ion depletion near the electrode, which reduces the effective driving power for ion migration and, consequently, the electrode capacity. Figure 7.6(f) displays the EIS curves of NiO, CuS, and CuS@NiO (C4) electrodes in a frequency range from 10^{-2} Hz to 10^{5} Hz, with the inset showing the equivalent circuit fit diagram. EIS is crucial for evaluating the electrode's intrinsic resistance, capacitance, and ion diffusion properties, providing a comprehensive understanding of its electrochemical performance. The equivalent circuit diagram consists of a series equivalent resistance (R_S) in line with two reactive elements representing the characteristics of the grain (G) and grain boundaries (B).

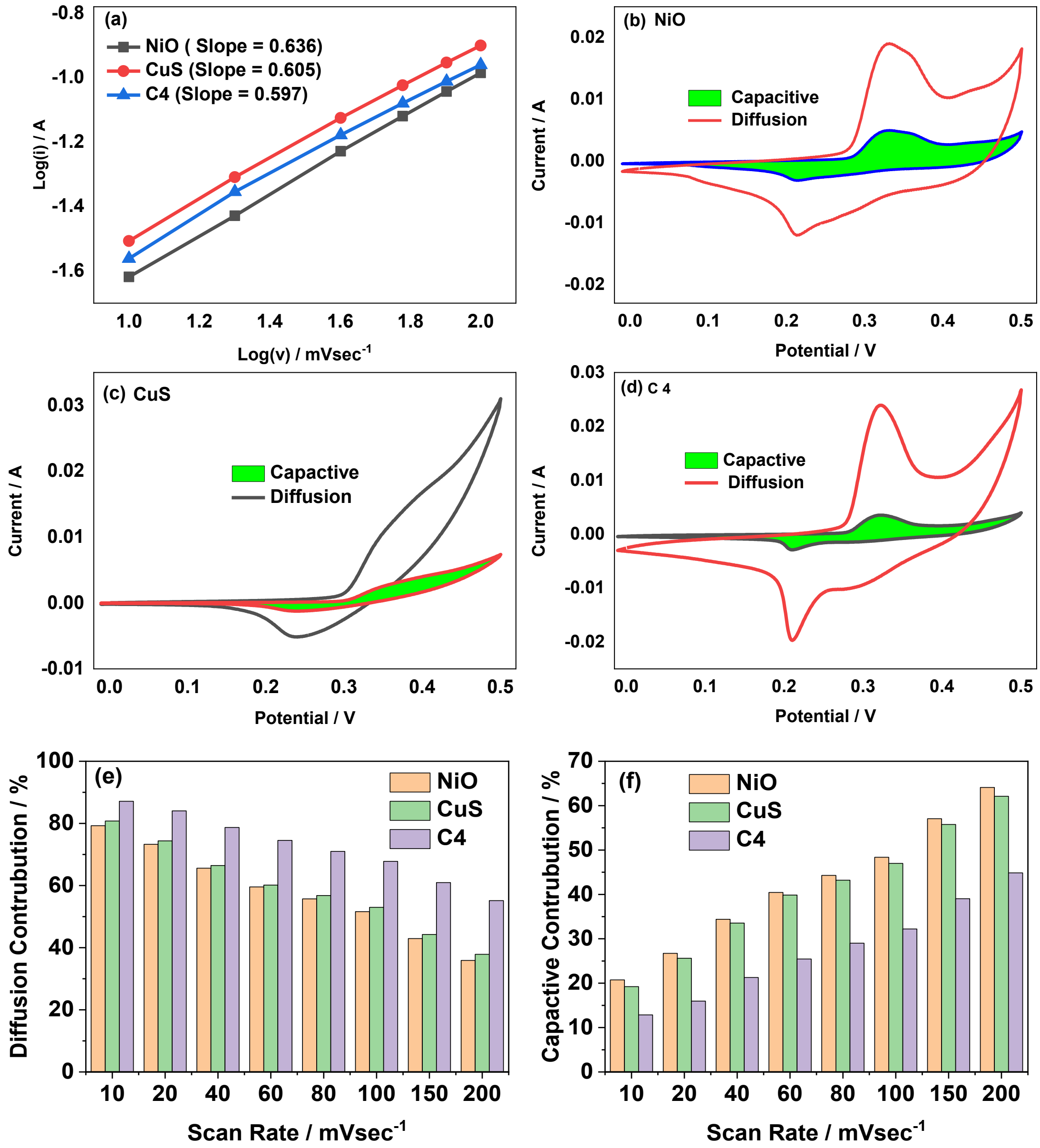

Fig. 7.7 (a) The graph between log (i) vs log (v) for NiO and CuS and C4 electrodes. The capacitive and diffusion contributions electrode of (b) NiO, (c) CuS, (d) and C4 at 10 mV/sec. he graph between (e) diffusion contribution and (f) capacitive contribution versus v of NiO, CuS, and C4 electrodes

Each element contains a resistor (R_G/R_B) connected in parallel with a CPE (CPE_G/CPE_B). The R_S values for NiO, CuS, and C4 electrodes are 1.02, 1.19, and 0.4 ohms, respectively, indicating that the C4 electrode offers less resistance, thus facilitating the movement of charge carriers. The fitted values of the components for NiO, CuS, and C4 electrodes are detailed in Table 7.1. The ionic conductivity of these electrodes was calculated using the fitted values of R_G and R_B. The calculated ionic conductivity values for CuS, NiO, and C4 electrodes are 0.26×10^{-4}, 0.12×10^{-4}, and 0.56×10^{-4} S/cm, respectively. The C4 electrode exhibits higher ionic conductivity and lower series equivalent resistance due to the synergistic effect of the composite, which combines the high electronic conductivity of CuS with the increased surface area of NiO. These results support the findings of CV and GCD analyses. The distribution factors associated with the reactive elements in the C4 electrode are 0.801 and 0.771 for CPE_G and CPE_B, respectively, indicating their capacitive character. Based on the preceding discussion, the following reactions may illustrate NiO and CuS reacting reversibly with hydroxide ions, accompanied by the release of electrons during the charging and discharging processes: [353,392]

$$NiO + OH^- \rightleftharpoons NiOOH + e^- \qquad \text{(viii)}$$
$$CuS + OH^- \rightleftharpoons CuSOH + e^- \qquad \text{(ix)}$$

The CV data is further analysed to determine the relative contributions of surface and diffusion-controlled charge storage mechanisms within the electrodes, using the relationship between peak current (i) and v (v), represented as $i \propto v^b$ [370]. The slope 'b' of log(v) versus log(i) plots as measured from Fig. 7(a), typically ranging from 0.5 to 1.0, is calculated to assess these mechanisms. A b value of 1 indicates a purely capacitive response dominated by surface effects, while a b value of 0.5 indicates a Faradic mechanism. For NiO, CuS, and C4 electrodes, the calculated 'b' values are 0.636, 0.605, and 0.597, respectively. These values suggest that the diffusion-controlled processes dominate in all three electrodes, but it is most prominent in the C4 electrode. The proportions of capacitive and diffusion-controlled contributions in the CV curves of NiO, CuS, and C4 electrodes at a v of 10 mV/sec are traced using Dunn’s equation [389], shown in Fig. 7.7(b-d). Figures 7.7(e) and (f) further illustrate how these proportions vary at different v. For instance, in the NiO electrode, the diffusion-controlled percentage decreases from 79.26% to 35.90%, in CuS electrodes from 80.77% to 37.87%, and in CuS@NiO electrode from 87.14% to 55.14% as the v increases from 10 to 200 mV/sec. Figure 7(f) indicates that the C4 composite electrode primarily stores charge through diffusion processes. At lower v, all three electrodes primarily rely on diffusion processes for charge storage, although NiO and CuS electrodes show a noticeable impact of surface-controlled processes compared to C4 electrode. As v increase, the dominance of diffusion-controlled processes diminishes due to restricted ion diffusion times, leading to a shift towards capacitive processes where charge storage is primarily surface-driven. SC device was fabricated using a CuS@NiO (C4) cathode and an expanded graphite mixed activated charcoal (EGA) anode, denoted as CuS@NiO//EGA, to evaluate its practical application. Fig 7.8(a) displays the CV curves of both the cathode and anode at 60 mV/sec, indicating their compatibility. Figure 7.8(b) showcases the CV performance of the SD at different v within a potential window of 0 to 1.7 V. The CV curves retain their shape from lower to higher v, highlighting the device's outstanding and reliable performance across a wide range of rates. Additionally, the prominent redox peaks suggest the Faradic charge-storage characteristics of the device. Figure 7.8(c) presents the GCD curves of the SD, which exhibit Cs of 465.4, 403.1, 363.6, 290.9, and 242.4 F/g at current densities of 1, 1.25, 1.5, 2, and 2.5 A/g, respectively. The E_D of 44 Wh/kg was demonstrated by the CuS@NiO//EGA device at a P_D of 0.825 kW/kg. Figure 7(d) illustrates the changes in E_D of the SD with varying current densities, showing a decrease in E_D as the current density increases. This decrease is attributed to increased internal resistance or diffusion limitations. Figure 7(e) reveals that CuS@NiO//EGA maintained approximately

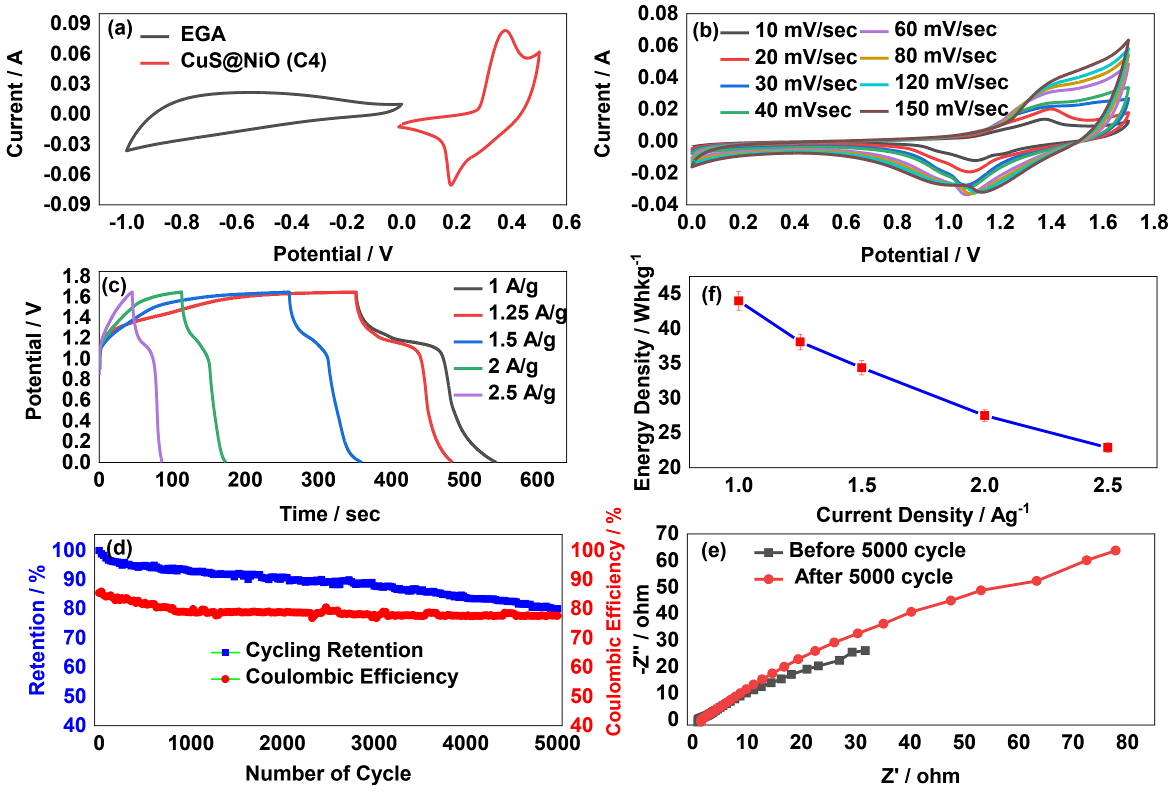

Fig. 7.8 (a) The CV curves of EGA and C4 electrode at 60 mV/s. (b) The CV curves of CuS@NiO//EGA at different v. (c) The GCD curve of CuS@NiO//EGA at various current density. (d) The change in Ed vs current density of CuS@NiO//EGA. (e) The cycling retention and coulombic efficiency up to 5000 cycles. (f) The EIS curve CuS@NiO//EGA before and after 5000 cycles.

80.08% cyclic stability and 77.62% Coulombic efficiency after 5000 cycles at 2 A/g, suggesting robust and stable performance through repeated cycles. Finally, Fig. 7.8(f) displays the EIS plot of the SD before and after 5000 cycles over a frequency range of 10^{-2} Hz to 10^{5} Hz, showing minimal changes and confirming the structural integrity of the electrodes. Table 7.2 compares the electrochemical performance of CuS@NiO (C4) with similar composites of developed with TMS and TMO. Comparing the performance of the CuS@NiO//EGA device with various reported literature reveals its competitive edge in specific capacity and E_D. The CuS@NiO//EGA device demonstrates a specific capacity of 392 C/g and achieves an E_D of 44 Wh/kg at a P_D of 0.825 kW/kg, maintaining a Coulombic efficiency of 77.62% after 5000 cycles. The impressive electrochemical performance of CuS@NiO//EGA is due to the synergistic effects arising from the combination of the higher conductivity of CuS with the enhanced SA and electrochemical stability of NiO. In comparison, the CoS_2/MoS_2 core-shell nanostructure exhibits a higher specific capacity of 781.1 C/g at 2 mA/cm² but a lower E_D of 32.72 Wh/kg at 0.597 kW/kg [390]. The MoS_2-RuO_2 heterostructure achieves an E_D of 35.92 Wh/kg at 0.6 kW/kg [357]. At a higher P_D of 1.599 kW/kg, the CuO/MoS_2 composite, with its synergistic interaction between CuO and MoS_2, reaches an E_D of 26.96 Wh/kg [361]. The 3D core-shell structure $NiCo_2O_4$@CoS heterostructure demonstrates an E_D of 32.91 Wh/kg at 0.425 kW/kg [383]. Thus, the CuS@NiO//EGA device showcases a balanced and robust performance, excelling particularly in E_D for SC applications.

7.4 Conclusion

In conclusion, this investigation demonstrated the significant potential of CuS@NiO composite heterostructures as high-efficiency electrode materials for enhancing electrochemical functionality. By harnessing the synergistic interplay of CuS superior electrical conductivity and NiO's remarkable electrochemical stability, we successfully synthesized and optimized the CuS@NiO composite through hydrothermal method. At 1 A/g, the optimized electrode exhibited specific capacity of 392 C/g (980 F/g). EIS revealed a lower intrinsic resistance of 0.4 ohms for the composite. At lower v, the CuS@NiO electrode primarily relied on diffusion processes for charge storage. As v increased, the dominance of diffusion-controlled processes diminished due to restricted ion diffusion times, leading to a shift towards capacitive processes where charge storage was primarily surface-driven. Additional, E_D of 44 Wh/kg was achieved by the assembled ASC device (CuS@NiO//EGA) at a P_D of 0.825 kW/kg. These findings underscored the potential of the CuS@NiO composite as an advanced electrode material, addressing the critical need for enhanced ES solutions in high-performance SCs.

Chapter 8
Summary and Future Scope

This thesis explores the potential of SCs as an advanced ES solution, focusing on their performance advantages over traditional storage technologies, such as high- P_D, rapid charge/discharge rates, and extended cycle life. Various chapters of the thesis cover fundamental concepts, material innovations, and advanced synthesis methods aimed at optimizing SC performance. The thesis places special emphasis on nickel oxide (NiO) due to its high Cs, stability, and cost-effectiveness. The thesis presents several breakthroughs in material synthesis and composite structures, particularly in NiO-based and heterostructure electrodes. NiO's performance is significantly enhanced through morphological control and the development of composites with materials such as MoS_2, CoS_2, and CuS, resulting in improved charge storage capacities and energy densities. Characterization techniques, including XRD, FESEM, Raman spectroscopy, and electrochemical methods, are used extensively to assess the structural, morphological, and ES capability of electrode materials.

In first research article, NiO materials were optimized by varying the annealing temperature. It was observed that NiO synthesized at an annealing temperature of 110°C exhibited superior electrochemical performance compared to samples annealed at 150°C and 200°C. The decrease in performance at higher temperatures was attributed to the increased crystallite size of the NiO materials. Additionally, the effect of urea concentration on NiO synthesis was investigated. Samples S:1, S:2, S:5, and S:8 were prepared with molar ratios of nickel nitrate hexahydrate to urea of 1:1, 1:2, 1:5, and 1:8, respectively. Among these, sample S:2, synthesized with a nickel nitrate hexahydrate-to-urea ratio of 1:2, demonstrated the best performance. The variation in urea concentration influenced the morphology of NiO, significantly affecting its charge storage capacity. This morphological change resulted from the increased pH of the solution during synthesis, as urea decomposed into ammonia. The study also explored the impact of binder-free versus binder-enriched electrodes on sample S:2. Binder-free electrodes outperformed their binder-enriched counterparts due to lower resistance, as the binder (PVDF) increased electrode resistance, reducing conductivity. At 1 A/g, the binder-free NiO nanosheet electrode demonstrated a specific capacity of 418 C/g (1045 F/g), along with an excellent retention rate of 87.5% after 1,000 cycles at 14 A/g. Additionally, ED of 22.5 Wh/kg was achieved by the ASC at PD of 0.9 kW/kg, showcasing the potential of this electrode material in high-performance ES applications.

Further, the performance of NiO was enhanced by incorporating MoS_2 in MoS_2@NiO composites with MoS_2 concentrations of 10%, 20%, 30%, 40%, and 50%, labeled M1 to M5, respectively. Among these, sample M3 exhibited the best performance, with EIS indicating low resistance and BET analysis revealing an increased surface area. Through systematic structural, morphological, and electrochemical characterizations, the optimized MoS_2@NiO heterostructure-based electrode demonstrated a remarkable specific capacity of 419.5 C/g at 1 A/g, surpassing both MoS_2 and NiO-based electrodes by significant margins. It is revealed that the Faradic or diffusion-controlled process overwhelmingly governs the total charge-storing phenomenon in the MoS_2@NiO based electrode. Leveraging the synergistic interactions between MoS_2 and NiO, the ASC exhibited an impressive ED of 47.43 Wh/kg at 0.825 kW/kg. Notably, the developed device exhibited robust cyclic stability, retaining approximately 80 % of its Cs and around 85 % of Coulombic efficiency after 5000 cycles at 2 A/g.

For enhanced the performance of NiO, CoS_2 was incorporated into CoS_2@NiO composites with concentrations of 20%, 30%, 40%, and 50%, labeled K2 to K5. Among these, sample K4 showed the best performance, with a specific capacity of 475 C/g (1187.5 F/g), outperforming NiO and CoS_2 electrodes by ~46% and ~42%, respectively. EIS analysis highlighted low resistance, and BET studies confirmed enhanced surface area. The K4 electrode demonstrated dominant diffusion-controlled charge storage at lower scan rates and surface-controlled mechanisms at higher scan rates. When integrated into an asymmetric supercapacitor, this composite achieved an energy density of 50.18 Wh/kg at 0.825 kW/kg, maintaining 82% capacity retention and 85% Coulombic efficiency after 5000 cycles.

Finally, the CuS@NiO composite was optimized by varying CuS concentrations at 20%, 30%, 40%, and 50%, labeled C2 to C5, respectively. The C4 electrode demonstrated a high specific capacity of 392 C/g (980 F/g) at 1 A/g. EIS analysis revealed a low intrinsic resistance of 0.4 Ω and high ionic conductivity (0.56×10^{-4} S/cm). The asymmetric supercapacitor achieved an energy density of 44 Wh/kg at 0.825 kW/kg, with a Coulombic efficiency of 77.62% after 5000 cycles.

It was observed during the research that the addition of CoS_2, MoS_2, and CuS to NiO significantly enhanced the electrochemical performance of the resulting composite. When comparing all the different NiO composites in this study, it was found that the CoS_2@NiO composite exhibited the highest enhancement in performance, showing superior energy density and better cyclic stability compared to the others. The performance enhancement of the MoS_2@NiO composite was greater than that of the CuS@NiO composite. Collectively, these findings emphasize the role of compositional and morphological tuning in NiO-based heterostructures, highlighting their potential to significantly advance SC technologies by achieving high energy densities and stable performance across various NiO-based composite configurations.

Future work in this field could focus on further optimizing the structural and compositional properties of NiO-based materials to enhance supercapacitor performance. Exploring alternative doping strategies and incorporating emerging 2D materials like MXenes or graphene derivatives might unlock higher charge storage capacities and improved conductivity. Studies on eco-friendly and scalable synthesis methods, coupled with the development of sustainable binders and electrolytes, would contribute to environmentally responsible ES solutions. Finally, real-world applications, such as wearable electronics or grid-level ES, could be targeted by fabricating flexible, lightweight, and high-performance devices tailored for practical deployment.

Bibliography

[1] L.E. Bell, Cooling, Heating, Generating Power, and Recovering Waste Heat with Thermoelectric Systems, Science (1979) 321 (2008) 1457–1461. https://doi.org/10.1126/science.1158899.

[2] G.J. SNYDER, E.S. TOBERER, Complex thermoelectric materials, in: Materials for Sustainable Energy, Co-Published with Macmillan Publishers Ltd, UK, 2010: pp. 101–110. https://doi.org/10.1142/9789814317665_0016.

[3] P.E. Lokhande, U.S. Chavan, A. Pandey, Materials and Fabrication Methods for Electrochemical Supercapacitors: Overview, Electrochemical Energy Reviews 3 (2020) 155–186. https://doi.org/10.1007/s41918-019-00057-z.

[4] Z.L. Wang, J. Chen, L. Lin, Progress in triboelectric nanogenerators as a new energy technology and self-powered sensors, Energy Environ Sci 8 (2015) 2250–2282. https://doi.org/10.1039/C5EE01532D.

[5] M. Graetzel, R.A.J. Janssen, D.B. Mitzi, E.H. Sargent, Materials interface engineering for solution-processed photovoltaics, Nature 488 (2012) 304–312. https://doi.org/10.1038/nature11476.

[6] K. Moustakas, M. Loizidou, M. Rehan, A.S. Nizami, A review of recent developments in renewable and sustainable energy systems: Key challenges and future perspective, Renewable and Sustainable Energy Reviews 119 (2020) 109418. https://doi.org/10.1016/j.rser.2019.109418.

[7] K.C. Divya, J. Østergaard, Battery energy storage technology for power systems—An overview, Electric Power Systems Research 79 (2009) 511–520. https://doi.org/10.1016/j.epsr.2008.09.017.

[8] J. Zhang, M. Gu, X. Chen, Supercapacitors for renewable energy applications: A review, Micro and Nano Engineering 21 (2023) 100229. https://doi.org/10.1016/j.mne.2023.100229.

[9] S. Yuan, X. Duan, J. Liu, Y. Ye, F. Lv, T. Liu, Q. Wang, X. Zhang, Recent progress on transition metal oxides as advanced materials for energy conversion and storage, Energy Storage Mater 42 (2021) 317–369. https://doi.org/10.1016/j.ensm.2021.07.007.

[10] M. Li, J. Liu, W. Han, Recycling and management of waste lead-acid batteries: A mini-review, Waste Management & Research: The Journal for a Sustainable Circular Economy 34 (2016) 298–306. https://doi.org/10.1177/0734242X16633773.

[11] A. Jain, G. Hautier, S.P. Ong, S. Dacek, G. Ceder, Relating voltage and thermal safety in Li-ion battery cathodes: a high-throughput computational study, Physical Chemistry Chemical Physics 17 (2015) 5942–5953. https://doi.org/10.1039/C5CP00250H.

[12] A.F. Burke, J. Zhao, Past, present and future of electrochemical capacitors: Technologies, performance and applications, J Energy Storage 35 (2021) 102310. https://doi.org/10.1016/j.est.2021.102310.

[13] Y. Liu, X. Peng, Recent advances of supercapacitors based on two-dimensional materials, Appl Mater Today 8 (2017) 104–115. https://doi.org/10.1016/j.apmt.2017.05.002.

[14] K. Thiagarajan, J. Theerthagiri, R.A. Senthil, P. Arunachalam, J. Madhavan, M.A. Ghanem, Synthesis of Ni3V2O8@graphene oxide nanocomposite as an efficient electrode material for supercapacitor applications, Journal of Solid State Electrochemistry 22 (2018) 527–536. https://doi.org/10.1007/s10008-017-3788-8.

[15] A. Kusko, J. Dedad, Stored energy - Short-term and long-term energy storage methods, IEEE Industry Applications Magazine 13 (2007) 66–72. https://doi.org/10.1109/MIA.2007.4283511.

[16] M. Uzunoglu, M.S. Alam, Modeling and Analysis of an FC/UC Hybrid Vehicular Power System Using a Novel-Wavelet-Based Load Sharing Algorithm, IEEE Transactions on Energy Conversion 23 (2008) 263–272. https://doi.org/10.1109/TEC.2007.908366.

[17] M. Inagaki, H. Konno, O. Tanaike, Carbon materials for electrochemical capacitors, J Power Sources 195 (2010) 7880–7903. https://doi.org/10.1016/j.jpowsour.2010.06.036.

[18] A. Burke, Ultracapacitors: why, how, and where is the technology, J Power Sources 91 (2000) 37–50. https://doi.org/10.1016/S0378-7753(00)00485-7.

[19] B.E. Conway, W.G. Pell, Double-layer and pseudocapacitance types of electrochemical capacitors and their applications to the development of hybrid devices, Journal of Solid State Electrochemistry 7 (2003) 637–644. https://doi.org/10.1007/s10008-003-0395-7.

[20] Y. Zhang, H. Feng, X. Wu, L. Wang, A. Zhang, T. Xia, H. Dong, X. Li, L. Zhang, Progress of electrochemical capacitor electrode materials: A review, Int J Hydrogen Energy 34 (2009) 4889–4899. https://doi.org/10.1016/j.ijhydene.2009.04.005.

[21] J.R. Miller, A. Burke, Electrochemical Capacitors: Challenges and Opportunities for Real-World Applications, Electrochem Soc Interface 17 (2008) 53–57. https://doi.org/10.1149/2.F08081IF.

[22] R. Kötz, M. Carlen, Principles and applications of electrochemical capacitors, Electrochim Acta 45 (2000) 2483–2498. https://doi.org/10.1016/S0013-

4686(00)00354-6.

[23] X. Ma, D. Zhu, D. Mo, J. Hou, J. Xu, W. Zhou, The Fabrication of Multilayers of Conducting Polymers and Its High Capacitance Performance Electrode for Supercapacitor, Int J Electrochem Sci 10 (2015) 7941–7954. https://doi.org/10.1016/S1452-3981(23)11067-4.

[24] S. Sarangapani, B. V. Tilak, C. -P. Chen, Materials for Electrochemical Capacitors: Theoretical and Experimental Constraints, J Electrochem Soc 143 (1996) 3791–3799. https://doi.org/10.1149/1.1837291.

[25] H. Randriamahazaka, C. Plesse, D. Teyssié, C. Chevrot, Relaxation kinetics of poly(3,4-ethylenedioxythiophene) in 1-ethyl-3-methylimidazolium bis((trifluoromethyl)sulfonyl)amide ionic liquid during potential step experiments, Electrochim Acta 50 (2005) 1515–1522. https://doi.org/10.1016/j.electacta.2004.10.058.

[26] R.N. Reddy, R.G. Reddy, Synthesis and electrochemical characterization of amorphous MnO2 electrochemical capacitor electrode material, J Power Sources 132 (2004) 315–320. https://doi.org/10.1016/j.jpowsour.2003.12.054.

[27] H. Chen, T.N. Cong, W. Yang, C. Tan, Y. Li, Y. Ding, Progress in electrical energy storage system: A critical review, Progress in Natural Science 19 (2009) 291–312. https://doi.org/10.1016/j.pnsc.2008.07.014.

[28] C. Largeot, C. Portet, J. Chmiola, P.-L. Taberna, Y. Gogotsi, P. Simon, Relation between the Ion Size and Pore Size for an Electric Double-Layer Capacitor, J Am Chem Soc 130 (2008) 2730–2731. https://doi.org/10.1021/ja7106178.

[29] R.N. Reddy, R.G. Reddy, Sol–gel MnO2 as an electrode material for electrochemical capacitors, J Power Sources 124 (2003) 330–337. https://doi.org/10.1016/S0378-7753(03)00600-1.

[30] Q. Huang, X. Wang, J. Li, Characterization and performance of hydrous manganese oxide prepared by electrochemical method and its application for supercapacitors, Electrochim Acta 52 (2006) 1758–1762. https://doi.org/10.1016/j.electacta.2006.01.077.

[31] J. Yan, Q. Wang, T. Wei, Z. Fan, Recent Advances in Design and Fabrication of Electrochemical Supercapacitors with High Energy Densities, Adv Energy Mater 4 (2014). https://doi.org/10.1002/aenm.201300816.

[32] T.S. Bhat, P.S. Patil, R.B. Rakhi, Recent trends in electrolytes for supercapacitors, J Energy Storage 50 (2022) 104222. https://doi.org/10.1016/j.est.2022.104222.

[33] A. Mendhe, H.S. Panda, A review on electrolytes for supercapacitor device, Discov Mater 3 (2023) 29. https://doi.org/10.1007/s43939-023-00065-3.

[34] F. Béguin, V. Presser, A. Balducci, E. Frackowiak, Supercapacitors: Carbons and Electrolytes for Advanced Supercapacitors (Adv. Mater. 14/2014), Advanced Materials 26 (2014) 2283–2283. https://doi.org/10.1002/adma.201470093.

[35] B. Pal, S. Yang, S. Ramesh, V. Thangadurai, R. Jose, Electrolyte selection for supercapacitive devices: a critical review, Nanoscale Adv 1 (2019) 3807–3835. https://doi.org/10.1039/C9NA00374F.

[36] B. Pal, S.G. Krishnan, B.L. Vijayan, M. Harilal, C.-C. Yang, F.I. Ezema, M.M. Yusoff, R. Jose, In situ encapsulation of tin oxide and cobalt oxide composite in porous carbon for high-performance energy storage applications, Journal of Electroanalytical Chemistry 817 (2018) 217–225. https://doi.org/10.1016/j.jelechem.2018.04.019.

[37] M. Galiński, A. Lewandowski, I. Stępniak, Ionic liquids as electrolytes, Electrochim Acta 51 (2006) 5567–5580. https://doi.org/10.1016/j.electacta.2006.03.016.

[38] X. Fang, D. Yao, An Overview of Solid-Like Electrolytes for Supercapacitors, in: Volume 6A: Energy, American Society of Mechanical Engineers, 2013. https://doi.org/10.1115/IMECE2013-64069.

[39] H. OHNO, K. FUKUMOTO, Progress in Ionic Liquids for Electrochemical Reaction Matrices, Electrochemistry 76 (2008) 16–23. https://doi.org/10.5796/electrochemistry.76.16.

[40] G.A. Snook, P. Kao, A.S. Best, Conducting-polymer-based supercapacitor devices and electrodes, J Power Sources 196 (2011) 1–12. https://doi.org/10.1016/j.jpowsour.2010.06.084.

[41] M. Galiński, A. Lewandowski, I. Stępniak, Ionic liquids as electrolytes, Electrochim Acta 51 (2006) 5567–5580. https://doi.org/10.1016/j.electacta.2006.03.016.

[42] H. Sun, G. Zhu, X. Xu, M. Liao, Y.-Y. Li, M. Angell, M. Gu, Y. Zhu, W.H. Hung, J. Li, Y. Kuang, Y. Meng, M.-C. Lin, H. Peng, H. Dai, A safe and non-flammable sodium metal battery based on an ionic liquid electrolyte, Nat Commun 10 (2019) 3302. https://doi.org/10.1038/s41467-019-11102-2.

[43] A. Lewandowski, M. Galiński, Carbon–ionic liquid double-layer capacitors, Journal of Physics and Chemistry of Solids 65 (2004) 281–286. https://doi.org/10.1016/j.jpcs.2003.09.009.

[44] A. Balducci, W.A. Henderson, M. Mastragostino, S. Passerini, P. Simon, F. Soavi, Cycling stability of a hybrid activated carbon//poly(3-methylthiophene) supercapacitor

with N-butyl-N-methylpyrrolidinium bis(trifluoromethanesulfonyl)imide ionic liquid as electrolyte, Electrochim Acta 50 (2005) 2233–2237. https://doi.org/10.1016/j.electacta.2004.10.006.

[45] H. Randriamahazaka, C. Plesse, D. Teyssié, C. Chevrot, Relaxation kinetics of poly(3,4-ethylenedioxythiophene) in 1-ethyl-3-methylimidazolium bis((trifluoromethyl)sulfonyl)amide ionic liquid during potential step experiments, Electrochim Acta 50 (2005) 1515–1522. https://doi.org/10.1016/j.electacta.2004.10.058.

[46] H. Liu, P. He, Z. Li, Y. Liu, J. Li, A novel nickel-based mixed rare-earth oxide/activated carbon supercapacitor using room temperature ionic liquid electrolyte, Electrochim Acta 51 (2006) 1925–1931. https://doi.org/10.1016/j.electacta.2005.06.034.

[47] H.W. Cho, L.R. Hepowit, H.-S. Nam, S.H. Kim, Y.M. Lee, J.H. Kim, K.M. Kim, J.M. Ko, Synthesis and supercapacitive properties of electrodeposited polyaniline composite electrode on acrylonitrile-butadiene rubber as a flexible current collector, Synth Met 162 (2012) 410–413. https://doi.org/10.1016/j.synthmet.2011.12.025.

[48] I. Ryu, M. Yang, H. Kwon, H.K. Park, Y.R. Do, S.B. Lee, S. Yim, Coaxial RuO 2 –ITO Nanopillars for Transparent Supercapacitor Application, Langmuir 30 (2014) 1704–1709. https://doi.org/10.1021/la4044599.

[49] X. Gong, J.P. Cheng, F. Liu, L. Zhang, X. Zhang, Nickel–Cobalt hydroxide microspheres electrodepositioned on nickel cobaltite nanowires grown on Ni foam for high-performance pseudocapacitors, J Power Sources 267 (2014) 610–616. https://doi.org/10.1016/j.jpowsour.2014.05.120.

[50] K.-T. Lee, C.-B. Tsai, W.-H. Ho, N.-L. Wu, Superabsorbent polymer binder for achieving MnO2 supercapacitors of greatly enhanced capacitance density, Electrochem Commun 12 (2010) 886–889. https://doi.org/10.1016/j.elecom.2010.04.012.

[51] H. Lee, H. Kim, M.S. Cho, J. Choi, Y. Lee, Fabrication of polypyrrole (PPy)/carbon nanotube (CNT) composite electrode on ceramic fabric for supercapacitor applications, Electrochim Acta 56 (2011) 7460–7466. https://doi.org/10.1016/j.electacta.2011.06.113.

[52] M. Kang, J.E. Lee, H.W. Shim, M.S. Jeong, W.B. Im, H. Yoon, Intrinsically conductive polymer binders for electrochemical capacitor application, RSC Adv. 4 (2014) 27939–27945. https://doi.org/10.1039/C4RA03261F.

[53] A. Varzi, A. Balducci, S. Passerini, Natural Cellulose: A Green Alternative Binder for High Voltage Electrochemical Double Layer Capacitors Containing Ionic Liquid-Based

Electrolytes, J Electrochem Soc 161 (2014) A368–A375. https://doi.org/10.1149/2.063403jes.

[54] K.-C. Tsay, L. Zhang, J. Zhang, Effects of electrode layer composition/thickness and electrolyte concentration on both specific capacitance and energy density of supercapacitor, Electrochim Acta 60 (2012) 428–436. https://doi.org/10.1016/j.electacta.2011.11.087.

[55] K. Tõnurist, T. Thomberg, A. Jänes, I. Kink, E. Lust, Specific performance of electrical double layer capacitors based on different separator materials in room temperature ionic liquid, Electrochem Commun 22 (2012) 77–80. https://doi.org/10.1016/j.elecom.2012.05.029.

[56] C. Zhong, Y. Deng, W. Hu, J. Qiao, L. Zhang, J. Zhang, A review of electrolyte materials and compositions for electrochemical supercapacitors, Chem Soc Rev 44 (2015) 7484–7539. https://doi.org/10.1039/C5CS00303B.

[57] M. Eikerling, A.A. Kornyshev, E. Lust, Optimized Structure of Nanoporous Carbon-Based Double-Layer Capacitors, J Electrochem Soc 152 (2005) E24. https://doi.org/10.1149/1.1825379.

[58] Y. Zhang, H. Feng, X. Wu, L. Wang, A. Zhang, T. Xia, H. Dong, X. Li, L. Zhang, Progress of electrochemical capacitor electrode materials: A review, Int J Hydrogen Energy 34 (2009) 4889–4899. https://doi.org/10.1016/j.ijhydene.2009.04.005.

[59] A. Clemente, Solid-state, polymer-based, redox capacitors, Solid State Ion 85 (1996) 273–277. https://doi.org/10.1016/0167-2738(96)00070-7.

[60] D.-D. Zhao, S.-J. Bao, W.-J. Zhou, H.-L. Li, Preparation of hexagonal nanoporous nickel hydroxide film and its application for electrochemical capacitor, Electrochem Commun 9 (2007) 869–874. https://doi.org/10.1016/j.elecom.2006.11.030.

[61] L. Xie, G. Sun, F. Su, X. Guo, Q. Kong, X. Li, X. Huang, L. Wan, W. song, K. Li, C. Lv, C.-M. Chen, Hierarchical porous carbon microtubes derived from willow catkins for supercapacitor applications, J Mater Chem A Mater 4 (2016) 1637–1646. https://doi.org/10.1039/C5TA09043A.

[62] E. Frackowiak, F. Béguin, Carbon materials for the electrochemical storage of energy in capacitors, Carbon N Y 39 (2001) 937–950. https://doi.org/10.1016/S0008-6223(00)00183-4.

[63] J. Xu, C. Ruan, P. Li, Y. Xie, Excessive nitrogen doping of tin dioxide nanorod array grown on activated carbon fibers substrate for wire-shaped microsupercapacitor, Chemical Engineering Journal 378 (2019) 122064.

https://doi.org/10.1016/j.cej.2019.122064.

[64] M. Jayalakshmi, K. Balasubramanian, Simple Capacitors to Supercapacitors - An Overview, Int J Electrochem Sci 3 (2008) 1196–1217. https://doi.org/10.1016/S1452-3981(23)15517-9.

[65] S. Asaithambi, P. Sakthivel, M. Karuppaiah, K. Balamurugan, R. Yuvakkumar, M. Thambidurai, G. Ravi, Synthesis and characterization of various transition metals doped SnO2@MoS2 composites for supercapacitor and photocatalytic applications, J Alloys Compd 853 (2021) 157060. https://doi.org/10.1016/j.jallcom.2020.157060.

[66] B. Fang, L. Binder, A Novel Carbon Electrode Material for Highly Improved EDLC Performance, J Phys Chem B 110 (2006) 7877–7882. https://doi.org/10.1021/jp060110d.

[67] H. Choi, H. Yoon, Nanostructured Electrode Materials for Electrochemical Capacitor Applications, Nanomaterials 5 (2015) 906–936. https://doi.org/10.3390/nano5020906.

[68] S.-M. Chen, R. Ramachandran, V. Mani, R. Saraswathi, Recent Advancements in Electrode Materials for the Highperformance Electrochemical Supercapacitors: A Review, Int J Electrochem Sci 9 (2014) 4072–4085. https://doi.org/10.1016/S1452-3981(23)08076-8.

[69] F. Wang, G. Li, J. Zheng, J. Ma, C. Yang, Q. Wang, Hydrothermal synthesis of flower-like molybdenum disulfide microspheres and their application in electrochemical supercapacitors, RSC Adv 8 (2018) 38945–38954. https://doi.org/10.1039/C8RA04350G.

[70] C. Arbizzani, New trends in electrochemical supercapacitors, J Power Sources 100 (2001) 164–170. https://doi.org/10.1016/S0378-7753(01)00892-8.

[71] M. WU, Y. HUANG, C. YANG, J. JOW, Electrodeposition of nanoporous nickel oxide film for electrochemical capacitors, Int J Hydrogen Energy 32 (2007) 4153–4159. https://doi.org/10.1016/j.ijhydene.2007.06.001.

[72] B. WAHDAME, D. CANDUSSO, X. FRANCOIS, F. HAREL, J. KAUFFMANN, G. COQUERY, Design of experiment techniques for fuel cell characterisation and development, Int J Hydrogen Energy 34 (2009) 967–980. https://doi.org/10.1016/j.ijhydene.2008.10.066.

[73] R. Kötz, M. Carlen, Principles and applications of electrochemical capacitors, Electrochim Acta 45 (2000) 2483–2498. https://doi.org/10.1016/S0013-4686(00)00354-6.

[74] M.M. Sk, C.Y. Yue, Synthesis of polyaniline nanotubes using the self-assembly

behavior of vitamin C: a mechanistic study and application in electrochemical supercapacitors, J. Mater. Chem. A 2 (2014) 2830–2838. https://doi.org/10.1039/C3TA14309K.

[75] M.M. Sk, C.Y. Yue, R.K. Jena, Synthesis of graphene/vitamin C template-controlled polyaniline nanotubes composite for high performance supercapacitor electrode, Polymer (Guildf) 55 (2014) 798–805. https://doi.org/10.1016/j.polymer.2013.12.057.

[76] A.G. Pandolfo, A.F. Hollenkamp, Carbon properties and their role in supercapacitors, J Power Sources 157 (2006) 11–27. https://doi.org/10.1016/j.jpowsour.2006.02.065.

[77] F.-X. Ma, L. Yu, C.-Y. Xu, X.W. (David) Lou, Self-supported formation of hierarchical NiCo 2 O 4 tetragonal microtubes with enhanced electrochemical properties, Energy Environ Sci 9 (2016) 862–866. https://doi.org/10.1039/C5EE03772G.

[78] X. Yu, L. Yu, X.W. (David) Lou, Metal Sulfide Hollow Nanostructures for Electrochemical Energy Storage, Adv Energy Mater 6 (2016). https://doi.org/10.1002/aenm.201501333.

[79] L. Yu, B. Guan, W. Xiao, X.W. (David) Lou, Formation of Yolk-Shelled Ni–Co Mixed Oxide Nanoprisms with Enhanced Electrochemical Performance for Hybrid Supercapacitors and Lithium Ion Batteries, Adv Energy Mater 5 (2015). https://doi.org/10.1002/aenm.201500981.

[80] A. Burke, R&D considerations for the performance and application of electrochemical capacitors, Electrochim Acta 53 (2007) 1083–1091. https://doi.org/10.1016/j.electacta.2007.01.011.

[81] T. Kar, V.R. Shetty, S.K. Pasha, K. Deshmukh, S. Godavarthi, M.K. Kesarla, Development of symmetric and asymmetric supercapacitors–a step towards efficient and practical energy storage, in: Smart Supercapacitors, Elsevier, 2023: pp. 405–456. https://doi.org/10.1016/B978-0-323-90530-5.00013-7.

[82] K. Joseph, H. Kasparian, V. Shanov, Carbon Nanotube Fiber-Based Wearable Supercapacitors—A Review on Recent Advances, Energies (Basel) 15 (2022) 6506. https://doi.org/10.3390/en15186506.

[83] S. Alam, M.I. Khan, F. Fiaz, M.Z. Iqbal, F. Alam, Z. Ahmad, H.H. Hegazy, Advancements in asymmetric supercapacitors: Material selection, mechanisms, and breakthroughs with metallic oxides, sulfides, and phosphates, J Energy Storage 72 (2023) 108208. https://doi.org/10.1016/j.est.2023.108208.

[84] F. Beguin, E. Frackowiak, eds., Carbons for Electrochemical Energy Storage and Conversion Systems, CRC Press, 2009. https://doi.org/10.1201/9781420055405.

[85] P. Forouzandeh, V. Kumaravel, S.C. Pillai, Electrode Materials for Supercapacitors: A Review of Recent Advances, Catalysts 10 (2020) 969. https://doi.org/10.3390/catal10090969.

[86] J. Chang, M. Park, D. Ham, S.B. Ogale, R.S. Mane, S.-H. Han, Liquid-phase synthesized mesoporous electrochemical supercapacitors of nickel hydroxide, Electrochim Acta 53 (2008) 5016–5021. https://doi.org/10.1016/j.electacta.2008.01.100.

[87] S.K. Meher, P. Justin, G. Ranga Rao, Microwave-Mediated Synthesis for Improved Morphology and Pseudocapacitance Performance of Nickel Oxide, ACS Appl Mater Interfaces 3 (2011) 2063–2073. https://doi.org/10.1021/am200294k.

[88] Y. Wang, Y. Xia, Electrochemical capacitance characterization of NiO with ordered mesoporous structure synthesized by template SBA-15, Electrochim Acta 51 (2006) 3223–3227. https://doi.org/10.1016/j.electacta.2005.09.013.

[89] M. Zhi, C. Xiang, J. Li, M. Li, N. Wu, Nanostructured carbon–metal oxide composite electrodes for supercapacitors: a review, Nanoscale 5 (2013) 72–88. https://doi.org/10.1039/C2NR32040A.

[90] P. Justin, S.K. Meher, G.R. Rao, Tuning of Capacitance Behavior of NiO Using Anionic, Cationic, and Nonionic Surfactants by Hydrothermal Synthesis, The Journal of Physical Chemistry C 114 (2010) 5203–5210. https://doi.org/10.1021/jp9097155.

[91] D. Qu, H. Shi, Studies of activated carbons used in double-layer capacitors, J Power Sources 74 (1998) 99–107. https://doi.org/10.1016/S0378-7753(98)00038-X.

[92] J.N. Barisci, G.G. Wallace, R.H. Baughman, Electrochemical Characterization of Single-Walled Carbon Nanotube Electrodes, J Electrochem Soc 147 (2000) 4580. https://doi.org/10.1149/1.1394104.

[93] M. Endo, T. Maeda, T. Takeda, Y.J. Kim, K. Koshiba, H. Hara, M.S. Dresselhaus, Capacitance and Pore-Size Distribution in Aqueous and Nonaqueous Electrolytes Using Various Activated Carbon Electrodes, J Electrochem Soc 148 (2001) A910. https://doi.org/10.1149/1.1382589.

[94] B. Fang, L. Binder, A modified activated carbon aerogel for high-energy storage in electric double layer capacitors, J Power Sources 163 (2006) 616–622. https://doi.org/10.1016/j.jpowsour.2006.09.014.

[95] B. Xu, F. Wu, R. Chen, G. Cao, S. Chen, Z. Zhou, Y. Yang, Highly mesoporous and high surface area carbon: A high capacitance electrode material for EDLCs with various electrolytes, Electrochem Commun 10 (2008) 795–797. https://doi.org/10.1016/j.elecom.2008.02.033.

[96] Y. Zhang, H. Feng, X. Wu, L. Wang, A. Zhang, T. Xia, H. Dong, X. Li, L. Zhang, Progress of electrochemical capacitor electrode materials: A review, Int J Hydrogen Energy 34 (2009) 4889–4899. https://doi.org/10.1016/j.ijhydene.2009.04.005.

[97] K.R. Prasad, K. Koga, N. Miura, Electrochemical Deposition of Nanostructured Indium Oxide: High-Performance Electrode Material for Redox Supercapacitors, Chemistry of Materials 16 (2004) 1845–1847. https://doi.org/10.1021/cm0497576.

[98] L.-Z. Fan, J. Maier, High-performance polypyrrole electrode materials for redox supercapacitors, Electrochem Commun 8 (2006) 937–940. https://doi.org/10.1016/j.elecom.2006.03.035.

[99] V. Gupta, N. Miura, High performance electrochemical supercapacitor from electrochemically synthesized nanostructured polyaniline, Mater Lett 60 (2006) 1466–1469. https://doi.org/10.1016/j.matlet.2005.11.047.

[100] A. Laforgue, P. Simon, C. Sarrazin, J.-F. Fauvarque, Polythiophene-based supercapacitors, J Power Sources 80 (1999) 142–148. https://doi.org/10.1016/S0378-7753(98)00258-4.

[101] K. Naoi, S. Suematsu, A. Manago, Electrochemistry of Poly(1,5-diaminoanthraquinone) and Its Application in Electrochemical Capacitor Materials, J Electrochem Soc 147 (2000) 420–426. https://doi.org/10.1149/1.1393212.

[102] M. Mastragostino, C. Arbizzani, L. Meneghello, R. Paraventi, Electronically conducting polymers and activated carbon: Electrode materials in supercapacitor technology, Advanced Materials 8 (1996) 331–334. https://doi.org/10.1002/adma.19960080409.

[103] K.S. Ryu, K.M. Kim, N.-G. Park, Y.J. Park, S.H. Chang, Symmetric redox supercapacitor with conducting polyaniline electrodes, J Power Sources 103 (2002) 305–309. https://doi.org/10.1016/S0378-7753(01)00862-X.

[104] P. Sharma, T.S. Bhatti, A review on electrochemical double-layer capacitors, Energy Convers Manag 51 (2010) 2901–2912. https://doi.org/10.1016/j.enconman.2010.06.031.

[105] É. Naudin, N. El Mehdi, C. Soucy, L. Breau, D. Bélanger, Poly(3-arylthiophenes): Syntheses of Monomers and Spectroscopic and Electrochemical Characterization of the Corresponding Polymers, Chemistry of Materials 13 (2001) 634–642. https://doi.org/10.1021/cm0007656.

[106] P. Sivaraman, A. Thakur, R.K. Kushwaha, D. Ratna, A.B. Samui, Poly(3-methyl thiophene)-Activated Carbon Hybrid Supercapacitor Based on Gel Polymer Electrolyte, Electrochemical and Solid-State Letters 9 (2006) A435.

https://doi.org/10.1149/1.2213357.

[107] R.K. Sharma, A.C. Rastogi, S.B. Desu, Manganese oxide embedded polypyrrole nanocomposites for electrochemical supercapacitor, Electrochim Acta 53 (2008) 7690–7695. https://doi.org/10.1016/j.electacta.2008.04.028.

[108] T.-F. Yi, J. Mei, B. Guan, P. Cui, S. Luo, Y. Xie, Y. Liu, Construction of spherical NiO@MnO2 with core-shell structure obtained by depositing MnO2 nanoparticles on NiO nanosheets for high-performance supercapacitor, Ceram Int 46 (2020) 421–429. https://doi.org/10.1016/j.ceramint.2019.08.278.

[109] Y.-T. Kim, K. Tadai, T. Mitani, Highly dispersed ruthenium oxide nanoparticles on carboxylated carbon nanotubes for supercapacitor electrode materials, J Mater Chem 15 (2005) 4914. https://doi.org/10.1039/b511869g.

[110] R. Fu, Z. Ma, J.P. Zheng, Proton NMR and Dynamic Studies of Hydrous Ruthenium Oxide, J Phys Chem B 106 (2002) 3592–3596. https://doi.org/10.1021/jp013860q.

[111] G. Wang, L. Zhang, J. Zhang, A review of electrode materials for electrochemical supercapacitors, Chem. Soc. Rev. 41 (2012) 797–828. https://doi.org/10.1039/C1CS15060J.

[112] W. Sugimoto, H. Iwata, Y. Murakami, Y. Takasu, Electrochemical Capacitor Behavior of Layered Ruthenic Acid Hydrate, J Electrochem Soc 151 (2004) A1181. https://doi.org/10.1149/1.1765681.

[113] W. Sugimoto, H. Iwata, Y. Yasunaga, Y. Murakami, Y. Takasu, Preparation of Ruthenic Acid Nanosheets and Utilization of Its Interlayer Surface for Electrochemical Energy Storage, Angewandte Chemie International Edition 42 (2003) 4092–4096. https://doi.org/10.1002/anie.200351691.

[114] J. Yan, Q. Wang, T. Wei, Z. Fan, Recent Advances in Design and Fabrication of Electrochemical Supercapacitors with High Energy Densities, Adv Energy Mater 4 (2014). https://doi.org/10.1002/aenm.201300816.

[115] Y. Zhang, H. Feng, X. Wu, L. Wang, A. Zhang, T. Xia, H. Dong, X. Li, L. Zhang, Progress of electrochemical capacitor electrode materials: A review, Int J Hydrogen Energy 34 (2009) 4889–4899. https://doi.org/10.1016/j.ijhydene.2009.04.005.

[116] J.R. Miller, P. Simon, Electrochemical Capacitors for Energy Management, Science (1979) 321 (2008) 651–652. https://doi.org/10.1126/science.1158736.

[117] T.-C. Liu, W.G. Pell, B.E. Conway, Stages in the development of thick cobalt oxide films exhibiting reversible redox behavior and pseudocapacitance, Electrochim Acta 44 (1999) 2829–2842. https://doi.org/10.1016/S0013-4686(99)00002-X.

[118] Y. Shan, L. Gao, Formation and characterization of multi-walled carbon nanotubes/Co3O4 nanocomposites for supercapacitors, Mater Chem Phys 103 (2007) 206–210. https://doi.org/10.1016/j.matchemphys.2007.02.038.

[119] X. Xia, J. Tu, Y. Zhang, Y. Mai, X. Wang, C. Gu, X. Zhao, Freestanding Co3O4 nanowire array for high performance supercapacitors, RSC Adv 2 (2012) 1835. https://doi.org/10.1039/c1ra00771h.

[120] B. Chang, Z. Gu, Y. Guo, Z. Li, B. Yang, Glucose-assisted synthesis of Co3O4 nanostructure with controllable morphologies from nanosheets to nanowires, J Alloys Compd 676 (2016) 26–36. https://doi.org/10.1016/j.jallcom.2016.03.056.

[121] N.-L. Wu, S.-Y. Wang, C.-Y. Han, D.-S. Wu, L.-R. Shiue, Electrochemical capacitor of magnetite in aqueous electrolytes, J Power Sources 113 (2003) 173–178. https://doi.org/10.1016/S0378-7753(02)00482-2.

[122] S.-C. Pang, M.A. Anderson, T.W. Chapman, Novel Electrode Materials for Thin-Film Ultracapacitors: Comparison of Electrochemical Properties of Sol-Gel-Derived and Electrodeposited Manganese Dioxide, J Electrochem Soc 147 (2000) 444. https://doi.org/10.1149/1.1393216.

[123] M. Toupin, T. Brousse, D. Bélanger, Influence of Microstucture on the Charge Storage Properties of Chemically Synthesized Manganese Dioxide, Chemistry of Materials 14 (2002) 3946–3952. https://doi.org/10.1021/cm020408q.

[124] J.-K. Chang, M.-T. Lee, W.-T. Tsai, In situ Mn K-edge X-ray absorption spectroscopic studies of anodically deposited manganese oxide with relevance to supercapacitor applications, J Power Sources 166 (2007) 590–594. https://doi.org/10.1016/j.jpowsour.2007.01.036.

[125] M.-S. Wu, C.-Y. Huang, K.-H. Lin, Electrophoretic deposition of nickel oxide electrode for high-rate electrochemical capacitors, J Power Sources 186 (2009) 557–564. https://doi.org/10.1016/j.jpowsour.2008.10.049.

[126] C.-L. Tang, X. Wei, Y.-M. Jiang, X.-Y. Wu, L. Han, K.-X. Wang, J.-S. Chen, Cobalt-Doped MnO 2 Hierarchical Yolk–Shell Spheres with Improved Supercapacitive Performance, The Journal of Physical Chemistry C 119 (2015) 8465–8471. https://doi.org/10.1021/jp512795g.

[127] A.M. Hashem, H.M. Abuzeid, N. Narayanan, H. Ehrenberg, C.M. Julien, Synthesis, structure, magnetic, electrical and electrochemical properties of Al, Cu and Mg doped MnO2, Mater Chem Phys 130 (2011) 33–38. https://doi.org/10.1016/j.matchemphys.2011.04.074.

[128] G. Wang, L. Liu, L. Zhang, J. Zhang, Nickel, cobalt, and manganese oxide composite as an electrode material for electrochemical supercapacitors, Ionics (Kiel) 19 (2013) 689–695. https://doi.org/10.1007/s11581-013-0872-7.

[129] S. Beke, A review of the growth of V2O5 films from 1885 to 2010, Thin Solid Films 519 (2011) 1761–1771. https://doi.org/10.1016/j.tsf.2010.11.001.

[130] H.Y. Lee, J.B. Goodenough, Ideal Supercapacitor Behavior of Amorphous V2O5·nH2O in Potassium Chloride (KCl) Aqueous Solution, J Solid State Chem 148 (1999) 81–84. https://doi.org/10.1006/jssc.1999.8367.

[131] G. Wang, L. Liu, L. Zhang, J. Zhang, Nickel, cobalt, and manganese oxide composite as an electrode material for electrochemical supercapacitors, Ionics (Kiel) 19 (2013) 689–695. https://doi.org/10.1007/s11581-013-0872-7.

[132] R.S. Kate, S.A. Khalate, R.J. Deokate, Overview of nanostructured metal oxides and pure nickel oxide (NiO) electrodes for supercapacitors: A review, J Alloys Compd 734 (2018) 89–111. https://doi.org/10.1016/j.jallcom.2017.10.262.

[133] P. Saha, N.C.D. Nath, Md.M. Islam, Md.A. Aziz, A.J.S. Ahammad, Recent progress of high-energy density supercapacitors based on nanostructured nickel oxides, Electrochim Acta 504 (2024) 144892. https://doi.org/10.1016/j.electacta.2024.144892.

[134] Y. Chuminjak, S. Daothong, P. Reanpang, J.P. Mensing, D. Phokharatkul, J. Jakmunee, A. Wisitsoraat, A. Tuantranont, P. Singjai, Electrochemical energy-storage performances of nickel oxide films prepared by a sparking method, RSC Adv 5 (2015) 67795–67802. https://doi.org/10.1039/C5RA09408A.

[135] M.S. Kolathodi, M. Palei, T.S. Natarajan, Electrospun NiO nanofibers as cathode materials for high performance asymmetric supercapacitors, J Mater Chem A Mater 3 (2015) 7513–7522. https://doi.org/10.1039/C4TA07075E.

[136] M. Tadic, D. Nikolic, M. Panjan, G.R. Blake, Magnetic properties of NiO (nickel oxide) nanoparticles: Blocking temperature and Neel temperature, J Alloys Compd 647 (2015) 1061–1068. https://doi.org/10.1016/j.jallcom.2015.06.027.

[137] F. Taghizadeh, The Study of Structural and Magnetic Properties of NiO Nanoparticles, Optics and Photonics Journal 06 (2016) 164–169. https://doi.org/10.4236/opj.2016.68B027.

[138] B. Gokul, P. Matheswaran, K.M. Abhirami, R. Sathyamoorthy, Structural and dielectric properties of NiO nanoparticles, J Non Cryst Solids 363 (2013) 161–166. https://doi.org/10.1016/j.jnoncrysol.2012.12.007.

[139] M. Wang, X. Song, S. Dai, W. Xu, Q. Yang, J. Liu, C. Hu, D. Wei, NiO nanoparticles

supported on graphene 3D network current collector for high-performance electrochemical energy storage, Electrochim Acta 214 (2016) 68–75. https://doi.org/10.1016/j.electacta.2016.08.036.

[140] K.K. Purushothaman, I. Manohara Babu, B. Sethuraman, G. Muralidharan, Nanosheet-Assembled NiO Microstructures for High-Performance Supercapacitors, ACS Appl Mater Interfaces 5 (2013) 10767–10773. https://doi.org/10.1021/am402869p.

[141] S. Vijayakumar, S. Nagamuthu, G. Muralidharan, Supercapacitor Studies on NiO Nanoflakes Synthesized Through a Microwave Route, ACS Appl Mater Interfaces 5 (2013) 2188–2196. https://doi.org/10.1021/am400012h.

[142] D. Gyabeng, D.A. Anang, J.I. Han, Honeycomb layered oxide Na3Ni2SbO6 for high performance pseudocapacitor, J Alloys Compd 704 (2017) 734–741. https://doi.org/10.1016/j.jallcom.2017.02.099.

[143] K. Ramasamy, R.K. Gupta, H. Sims, S. Palchoudhury, S. Ivanov, A. Gupta, Layered ternary sulfide CuSbS 2 nanoplates for flexible solid-state supercapacitors, J Mater Chem A Mater 3 (2015) 13263–13274. https://doi.org/10.1039/C5TA03193A.

[144] X. Yan, X. Tong, J. Wang, C. Gong, M. Zhang, L. Liang, Synthesis of mesoporous NiO nanoflake array and its enhanced electrochemical performance for supercapacitor application, J Alloys Compd 593 (2014) 184–189. https://doi.org/10.1016/j.jallcom.2014.01.036.

[145] J. Zhao, Y. Tian, A. Liu, L. Song, Z. Zhao, The NiO electrode materials in electrochemical capacitor: A review, Mater Sci Semicond Process 96 (2019) 78–90. https://doi.org/10.1016/j.mssp.2019.02.024.

[146] Y. Hanifehpour, A. Morsali, B. Mirtamizdoust, S.W. Joo, B. Soltani, Thermolysis synthesis of pure phase NiO from novel sonochemical synthesized Ni(II) nano metal-organic supramolecular architecture, Ultrason Sonochem 37 (2017) 430–435. https://doi.org/10.1016/j.ultsonch.2017.02.003.

[147] A. Gedanken, Using sonochemistry for the fabrication of nanomaterials, Ultrason Sonochem 11 (2004) 47–55. https://doi.org/10.1016/j.ultsonch.2004.01.037.

[148] V. Ramasamy Raja, D. Rani Rosaline, A. Suganthi, M. Rajarajan, Ultrasonic assisted synthesis with enhanced visible-light photocatalytic activity of NiO/Ag3VO4 nanocomposite and its antibacterial activity, Ultrason Sonochem 44 (2018) 73–85. https://doi.org/10.1016/j.ultsonch.2018.02.010.

[149] S. Mohseni Meybodi, S.A. Hosseini, M. Rezaee, S.K. Sadrnezhaad, D. Mohammadyani, Synthesis of wide band gap nanocrystalline NiO powder via a sonochemical method,

Ultrason Sonochem 19 (2012) 841–845. https://doi.org/10.1016/j.ultsonch.2011.11.017.

[150] D. Bokov, A. Turki Jalil, S. Chupradit, W. Suksatan, M. Javed Ansari, I.H. Shewael, G.H. Valiev, E. Kianfar, Nanomaterial by Sol-Gel Method: Synthesis and Application, Advances in Materials Science and Engineering 2021 (2021). https://doi.org/10.1155/2021/5102014.

[151] X. Xia, Y. Zhang, D. Chao, C. Guan, Y. Zhang, L. Li, X. Ge, I.M. Bacho, J. Tu, H.J. Fan, Solution synthesis of metal oxides for electrochemical energy storage applications, Nanoscale 6 (2014) 5008–5048. https://doi.org/10.1039/C4NR00024B.

[152] M.M. Sk, C.Y. Yue, K. Ghosh, R.K. Jena, Review on advances in porous nanostructured nickel oxides and their composite electrodes for high-performance supercapacitors, J Power Sources 308 (2016) 121–140. https://doi.org/10.1016/j.jpowsour.2016.01.056.

[153] N. Duraisamy, A. Numan, S.O. Fatin, K. Ramesh, S. Ramesh, Facile sonochemical synthesis of nanostructured NiO with different particle sizes and its electrochemical properties for supercapacitor application, J Colloid Interface Sci 471 (2016) 136–144. https://doi.org/10.1016/j.jcis.2016.03.013.

[154] S. Chatterjee, R. Maiti, M. Miah, S.K. Saha, D. Chakravorty, NiO Nanoparticle Synthesis Using a Triblock Copolymer: Enhanced Magnetization and High Specific Capacitance of Electrodes Prepared from the Powder, ACS Omega 2 (2017) 283–289. https://doi.org/10.1021/acsomega.6b00384.

[155] S. Pilban Jahromi, A. Pandikumar, B.T. Goh, Y.S. Lim, W.J. Basirun, H.N. Lim, N.M. Huang, Influence of particle size on performance of a nickel oxide nanoparticle-based supercapacitor, RSC Adv 5 (2015) 14010–14019. https://doi.org/10.1039/C4RA16776G.

[156] S.-I. Kim, J.-S. Lee, H.-J. Ahn, H.-K. Song, J.-H. Jang, Facile Route to an Efficient NiO Supercapacitor with a Three-Dimensional Nanonetwork Morphology, ACS Appl Mater Interfaces 5 (2013) 1596–1603. https://doi.org/10.1021/am3021894.

[157] P. Pandurangan, T.N. Parvin, B. Soundiraraju, Y. Johnbosco, M. Ramalingam, M. Bhagavathiachari, S.A. Suthanthiraraj, S.S. Narayanan, Ultrasmall NiO nanoclusters modified with conical Ni(<scp>ii</scp>)-SR staples for high performance supercapacitor applications, New Journal of Chemistry 41 (2017) 6127–6136. https://doi.org/10.1039/C6NJ03678C.

[158] V.S.R. Channu, R. Holze, B. Rambabu, Synthesis and characterization of NiO nanoparticles for electrochemical applications, Colloids Surf A Physicochem Eng Asp 414 (2012) 204–208. https://doi.org/10.1016/j.colsurfa.2012.08.023.

[159] G. Cai, X. Wang, M. Cui, P. Darmawan, J. Wang, A.L.-S. Eh, P.S. Lee, Electrochromo-supercapacitor based on direct growth of NiO nanoparticles, Nano Energy 12 (2015) 258–267. https://doi.org/10.1016/j.nanoen.2014.12.031.

[160] Q. Wei, F. Xiong, S. Tan, L. Huang, E.H. Lan, B. Dunn, L. Mai, Porous One-Dimensional Nanomaterials: Design, Fabrication and Applications in Electrochemical Energy Storage, Advanced Materials 29 (2017). https://doi.org/10.1002/adma.201602300.

[161] R.H. Zhang, T.S. Zhao, H.R. Jiang, M.C. Wu, L. Zeng, V2O5-NiO composite nanowires: A novel and highly efficient carbon-free electrode for non-aqueous Li-air batteries operated in ambient air, J Power Sources 409 (2019) 76–85. https://doi.org/10.1016/j.jpowsour.2018.10.098.

[162] Y. Cui, C. Wang, S. Wu, G. Liu, F. Zhang, T. Wang, Lotus-root-like NiO nanosheets and flower-like NiO microspheres: synthesis and magnetic properties, CrystEngComm 13 (2011) 4930. https://doi.org/10.1039/c1ce05389b.

[163] M. Liu, J. Chang, J. Sun, L. Gao, A facile preparation of NiO/Ni composites as high-performance pseudocapacitor materials, RSC Adv 3 (2013) 8003. https://doi.org/10.1039/c3ra23286g.

[164] R.A. Laudise, J.W. Nielsen, Hydrothermal Crystal Growth, in: 1961: pp. 149–222. https://doi.org/10.1016/S0081-1947(08)60654-2.

[165] F. Jiao, A.H. Hill, A. Harrison, A. Berko, A. V. Chadwick, P.G. Bruce, Synthesis of Ordered Mesoporous NiO with Crystalline Walls and a Bimodal Pore Size Distribution, J Am Chem Soc 130 (2008) 5262–5266. https://doi.org/10.1021/ja710849r.

[166] M.M. Sk, C.Y. Yue, K. Ghosh, R.K. Jena, Review on advances in porous nanostructured nickel oxides and their composite electrodes for high-performance supercapacitors, J Power Sources 308 (2016) 121–140. https://doi.org/10.1016/j.jpowsour.2016.01.056.

[167] M. Ristić, M. Marciuš, Ž. Petrović, S. Musić, Dependence of NiO microstructure on the electrospinning conditions, Ceram Int 40 (2014) 10119–10123. https://doi.org/10.1016/j.ceramint.2014.01.132.

[168] S.R. Hosseini, S. Ghasemi, M. Kamali-Rousta, S.R. Nabavi, Preparation of NiO nanofibers by electrospinning and their application for electro-catalytic oxidation of ethylene glycol, Int J Hydrogen Energy 42 (2017) 906–913. https://doi.org/10.1016/j.ijhydene.2016.09.116.

[169] P.P. Dorneanu, A. Airinei, N. Olaru, M. Homocianu, V. Nica, F. Doroftei, Preparation and characterization of NiO, ZnO and NiO–ZnO composite nanofibers by

electrospinning method, Mater Chem Phys 148 (2014) 1029–1035. https://doi.org/10.1016/j.matchemphys.2014.09.014.

[170] D. Su, H. Kim, W. Kim, G. Wang, Mesoporous Nickel Oxide Nanowires: Hydrothermal Synthesis, Characterisation and Applications for Lithium-Ion Batteries and Supercapacitors with Superior Performance, Chemistry – A European Journal 18 (2012) 8224–8229. https://doi.org/10.1002/chem.201200086.

[171] F.I. Dar, K.R. Moonoosawmy, M. Es-Souni, Morphology and property control of NiO nanostructures for supercapacitor applications, Nanoscale Res Lett 8 (2013) 363. https://doi.org/10.1186/1556-276X-8-363.

[172] A. Liu, H. Che, Y. Mao, Y. Wang, J. Mu, C. Wu, Y. Bai, X. Zhang, G. Wang, Template-free synthesis of one-dimensional hierarchical NiO nanotubes self-assembled by nanosheets for high-performance supercapacitors, Ceram Int 42 (2016) 11435–11441. https://doi.org/10.1016/j.ceramint.2016.04.080.

[173] S. Xiong, C. Yuan, X. Zhang, Y. Qian, Mesoporous NiO with various hierarchical nanostructures by quasi-nanotubes/nanowires/nanorodsself-assembly: controllable preparation and application in supercapacitors, CrystEngComm 13 (2011) 626–632. https://doi.org/10.1039/C002610G.

[174] B. Ren, M. Fan, Q. Liu, J. Wang, D. Song, X. Bai, Hollow NiO nanofibers modified by citric acid and the performances as supercapacitor electrode, Electrochim Acta 92 (2013) 197–204. https://doi.org/10.1016/j.electacta.2013.01.009.

[175] M. Kundu, L. Liu, Binder-free electrodes consisting of porous NiO nanofibers directly electrospun on nickel foam for high-rate supercapacitors, Mater Lett 144 (2015) 114–118. https://doi.org/10.1016/j.matlet.2015.01.032.

[176] A. Paravannoor, R. Ranjusha, A.M. Asha, R. Vani, S. Kalluri, K.R.V. Subramanian, N. Sivakumar, T.N. Kim, S. V. Nair, A. Balakrishnan, Chemical and structural stability of porous thin film NiO nanowire based electrodes for supercapacitors, Chemical Engineering Journal 220 (2013) 360–366. https://doi.org/10.1016/j.cej.2013.01.063.

[177] B. Vidhyadharan, N.K.M. Zain, I.I. Misnon, R.A. Aziz, J. Ismail, M.M. Yusoff, R. Jose, High performance supercapacitor electrodes from electrospun nickel oxide nanowires, J Alloys Compd 610 (2014) 143–150. https://doi.org/10.1016/j.jallcom.2014.04.211.

[178] L. Zang, J. Zhu, Y. Xia, Facile Synthesis of Porous NiO Nanofibers for High-Performance Supercapacitors, J Mater Eng Perform 23 (2014) 679–683. https://doi.org/10.1007/s11665-013-0797-3.

[179] B. Wang, J.S. Chen, Z. Wang, S. Madhavi, X.W. (David) Lou, Green Synthesis of NiO

Nanobelts with Exceptional Pseudo-Capacitive Properties, Adv Energy Mater 2 (2012) 1188–1192. https://doi.org/10.1002/aenm.201200008.

[180] M. Yao, Z. Hu, Z. Xu, Y. Liu, P. Liu, Q. Zhang, Template synthesis and characterization of nanostructured hierarchical mesoporous ribbon-like NiO as high performance electrode material for supercapacitor, Electrochim Acta 158 (2015) 96–104. https://doi.org/10.1016/j.electacta.2014.12.058.

[181] M. Zhang, Q. Li, D. Fang, I.A. Ayhan, Y. Zhou, L. Dong, C. Xiong, Q. Wang, NiO hierarchical hollow nanofibers as high-performance supercapacitor electrodes, RSC Adv 5 (2015) 96205–96212. https://doi.org/10.1039/C5RA17011G.

[182] F. Lei, T. Le, G. Rong, Controllable preparation of NiO macrotubes from NiC2O4 and its application in supercapacitors, CrystEngComm 13 (2011) 7246. https://doi.org/10.1039/c1ce05735a.

[183] H. Xiao, S. Yao, H. Liu, F. Qu, X. Zhang, X. Wu, NiO nanosheet assembles for supercapacitor electrode materials, Progress in Natural Science: Materials International 26 (2016) 271–275. https://doi.org/10.1016/j.pnsc.2016.05.007.

[184] D. Yue, C. Guo, X. Yan, R. Wang, M. Fang, Y. Wu, X. Qian, Y. Zhao, Secondary battery inspired NiO nanosheets with rich Ni(III) defects for enhancing persulfates activation in phenolic waste water degradation, Chemical Engineering Journal 360 (2019) 97–103. https://doi.org/10.1016/j.cej.2018.11.201.

[185] Y. Zhu, H. Guo, Y. Wu, C. Cao, S. Tao, Z. Wu, Surface-enabled superior lithium storage of high-quality ultrathin NiO nanosheets, J Mater Chem A Mater 2 (2014) 7904. https://doi.org/10.1039/c4ta00257a.

[186] B. Zhao, J. Song, T. Fang, P. Liu, Z. Jiao, H. Zhang, Y. Jiang, Hydrothermal method to prepare porous NiO nanosheet, Mater Lett 67 (2012) 24–27. https://doi.org/10.1016/j.matlet.2011.09.057.

[187] Y. Jiang, Z. Jia, W. Zhang, H. Suo, In Situ Hydrothermal Synthesis of Nickel Oxide Nanostructures by Thermal Decomposition and its Electrochemical Property, J Inorg Organomet Polym Mater 23 (2013) 1043–1047. https://doi.org/10.1007/s10904-013-9877-y.

[188] J.M. Xu, J.P. Cheng, The advances of Co 3 O 4 as gas sensing materials: A review, J Alloys Compd 686 (2016) 753–768. https://doi.org/10.1016/j.jallcom.2016.06.086.

[189] J. Mei, T. Liao, Z. Sun, Two-dimensional metal oxide nanosheets for rechargeable batteries, Journal of Energy Chemistry 27 (2018) 117–127. https://doi.org/10.1016/j.jechem.2017.10.012.

[190] K. Liu, M.A. Anderson, Porous Nickel Oxide/Nickel Films for Electrochemical Capacitors, J Electrochem Soc 143 (1996) 124–130. https://doi.org/10.1149/1.1836396.

[191] W. Xing, F. Li, Z. Yan, G.Q. Lu, Synthesis and electrochemical properties of mesoporous nickel oxide, J Power Sources 134 (2004) 324–330. https://doi.org/10.1016/j.jpowsour.2004.03.038.

[192] Y. Zhang, L. Li, H. Su, W. Huang, X. Dong, Binary metal oxide: advanced energy storage materials in supercapacitors, J Mater Chem A Mater 3 (2015) 43–59. https://doi.org/10.1039/C4TA04996A.

[193] H.I. Lee, J.H. Kim, S.H. Joo, H. Chang, D. Seung, O.-S. Joo, D.J. Suh, W.-S. Ahn, C. Pak, J.M. Kim, Ultrafast production of ordered mesoporous carbons via microwave irradiation, Carbon N Y 45 (2007) 2851–2854. https://doi.org/10.1016/j.carbon.2007.08.031.

[194] J.-F. Zhu, Y.-J. Zhu, Microwave-Assisted One-Step Synthesis of Polyacrylamide−Metal (M = Ag, Pt, Cu) Nanocomposites in Ethylene Glycol, J Phys Chem B 110 (2006) 8593–8597. https://doi.org/10.1021/jp060488b.

[195] Y. Wang, Z. Iqbal, S. Mitra, Rapid, low temperature microwave synthesis of novel carbon nanotube–silicon carbide composite, Carbon N Y 44 (2006) 2804–2808. https://doi.org/10.1016/j.carbon.2006.03.036.

[196] M. Khairy, S.A. El-Safty, Mesoporous NiO nanoarchitectures for electrochemical energy storage: influence of size, porosity, and morphology, RSC Adv 3 (2013) 23801. https://doi.org/10.1039/c3ra44465a.

[197] H. Xiao, F. Qu, X. Wu, Ultrathin NiO nanoflakes electrode materials for supercapacitors, Appl Surf Sci 360 (2016) 8–13. https://doi.org/10.1016/j.apsusc.2015.10.171.

[198] N. Behm, D. Brokaw, C. Overson, D. Peloquin, J.C. Poler, High-throughput microwave synthesis and characterization of NiO nanoplates for supercapacitor devices, J Mater Sci 48 (2013) 1711–1716. https://doi.org/10.1007/s10853-012-6929-6.

[199] X. Zhang, W. Shi, J. Zhu, W. Zhao, J. Ma, S. Mhaisalkar, T.L. Maria, Y. Yang, H. Zhang, H.H. Hng, Q. Yan, Synthesis of porous NiO nanocrystals with controllable surface area and their application as supercapacitor electrodes, Nano Res 3 (2010) 643–652. https://doi.org/10.1007/s12274-010-0024-6.

[200] Z. Zhu, J. Ping, X. Huang, J. Hu, Q. Chen, X. Ji, C.E. Banks, Hexagonal nickel oxide nanoplate-based electrochemical supercapacitor, J Mater Sci 47 (2012) 503–507. https://doi.org/10.1007/s10853-011-5826-8.

[201] T. Alammar, O. Shekhah, J. Wohlgemuth, A.-V. Mudring, Ultrasound-assisted synthesis of mesoporous β-Ni(OH)2 and NiO nano-sheets using ionic liquids, J Mater Chem 22 (2012) 18252. https://doi.org/10.1039/c2jm32849f.

[202] C. Yuan, Template-free synthesis of ultrathin mesoporous NiO nanosheets and their application in supercapacitors, Mater Res Bull 48 (2013) 840–843. https://doi.org/10.1016/j.materresbull.2012.11.077.

[203] X. Sun, G. Wang, J.-Y. Hwang, J. Lian, Porous nickel oxide nano-sheets for high performance pseudocapacitance materials, J Mater Chem 21 (2011) 16581. https://doi.org/10.1039/c1jm12734a.

[204] Q. Sun, S. Bao, Effects of Reaction Temperature on Microstructure and Advanced Pseudocapacitor Properties of NiO Prepared via Simple Precipitation Method, Nanomicro Lett 5 (2013) 289–295. https://doi.org/10.1007/BF03353760.

[205] M. Liu, J. Chang, J. Sun, L. Gao, A facile preparation of NiO/Ni composites as high-performance pseudocapacitor materials, RSC Adv 3 (2013) 8003. https://doi.org/10.1039/c3ra23286g.

[206] K.K. Purushothaman, I. Manohara Babu, B. Sethuraman, G. Muralidharan, Nanosheet-Assembled NiO Microstructures for High-Performance Supercapacitors, ACS Appl Mater Interfaces 5 (2013) 10767–10773. https://doi.org/10.1021/am402869p.

[207] C. Yuan, J. Li, L. Hou, L. Yang, L. Shen, X. Zhang, Facile growth of hexagonal NiO nanoplatelet arrays assembled by mesoporous nanosheets on Ni foam towards high-performance electrochemical capacitors, Electrochim Acta 78 (2012) 532–538. https://doi.org/10.1016/j.electacta.2012.06.044.

[208] H. Xiao, S. Yao, H. Liu, F. Qu, X. Zhang, X. Wu, NiO nanosheet assembles for supercapacitor electrode materials, Progress in Natural Science: Materials International 26 (2016) 271–275. https://doi.org/10.1016/j.pnsc.2016.05.007.

[209] A.D. Jagadale, V.S. Kumbhar, D.S. Dhawale, C.D. Lokhande, Potentiodynamically deposited nickel oxide (NiO) nanoflakes for pseudocapacitors, Journal of Electroanalytical Chemistry 704 (2013) 90–95. https://doi.org/10.1016/j.jelechem.2013.06.020.

[210] Y. Zheng, H. Ding, M. Zhang, Preparation and electrochemical properties of nickel oxide as a supercapacitor electrode material, Mater Res Bull 44 (2009) 403–407. https://doi.org/10.1016/j.materresbull.2008.05.002.

[211] S. Vijayakumar, S. Nagamuthu, G. Muralidharan, Supercapacitor Studies on NiO Nanoflakes Synthesized Through a Microwave Route, ACS Appl Mater Interfaces 5

(2013) 2188–2196. https://doi.org/10.1021/am400012h.

[212] M. Fan, B. Ren, L. Yu, Q. Liu, J. Wang, D. Song, J. Liu, X. Jing, L. Liu, Facile growth of hollow porous NiO microspheres assembled from nanosheet building blocks and their high performance as a supercapacitor electrode, CrystEngComm 16 (2014) 10389–10394. https://doi.org/10.1039/C4CE01242A.

[213] V. Senthilkumar, F.B. Kadumudi, N.T. Ho, J.-W. Kim, S. Park, J.-S. Bae, W.M. Choi, S. Cho, Y.S. Kim, NiO nanoarrays of a few atoms thickness on 3D nickel network for enhanced pseudocapacitive electrode applications, J Power Sources 303 (2016) 363–371. https://doi.org/10.1016/j.jpowsour.2015.11.034.

[214] Y. Zhang, J. Wang, H. Wei, J. Hao, J. Mu, P. Cao, J. Wang, S. Zhao, Hydrothermal synthesis of hierarchical mesoporous NiO nanourchins and their supercapacitor application, Mater Lett 162 (2016) 67–70. https://doi.org/10.1016/j.matlet.2015.09.123.

[215] S.A. Abbas, K.-D. Jung, Preparation of mesoporous microspheres of NiO with high surface area and analysis on their pseudocapacitive behavior, Electrochim Acta 193 (2016) 145–153. https://doi.org/10.1016/j.electacta.2016.02.054.

[216] D. Du, Z. Hu, Y. Liu, Y. Deng, J. Liu, Preparation and characterization of flower-like microspheres of nano-NiO as electrode material for supercapacitor, J Alloys Compd 589 (2014) 82–87. https://doi.org/10.1016/j.jallcom.2013.11.176.

[217] M. Yao, Z. Hu, Y. Liu, P. Liu, Z. Ai, O. Rudolf, 3D hierarchical mesoporous roselike NiO nanosheets for high-performance supercapacitor electrodes, J Alloys Compd 648 (2015) 414–418. https://doi.org/10.1016/j.jallcom.2015.06.098.

[218] J. Wang, Y. Zhang, P. Wan, T. Li, D. Hou, S. Hussain, H. Shao, Nanosheet-assembled hollow NiO ball-flower for high-performance supercapacitor, Journal of Materials Science: Materials in Electronics 27 (2016) 8020–8026. https://doi.org/10.1007/s10854-016-4798-5.

[219] S.-I. Kim, J.-S. Lee, H.-J. Ahn, H.-K. Song, J.-H. Jang, Facile Route to an Efficient NiO Supercapacitor with a Three-Dimensional Nanonetwork Morphology, ACS Appl Mater Interfaces 5 (2013) 1596–1603. https://doi.org/10.1021/am3021894.

[220] Y. Wang, B. Chang, D. Guan, K. Pei, Z. Chen, M. Yang, X. Dong, Preparation of nanospherical porous NiO by a hard template route and its supercapacitor application, Mater Lett 135 (2014) 172–175. https://doi.org/10.1016/j.matlet.2014.07.150.

[221] F. Cao, G.X. Pan, X.H. Xia, P.S. Tang, H.F. Chen, Synthesis of hierarchical porous NiO nanotube arrays for supercapacitor application, J Power Sources 264 (2014) 161–167. https://doi.org/10.1016/j.jpowsour.2014.04.103.

[222] C.-Y. Cao, W. Guo, Z.-M. Cui, W.-G. Song, W. Cai, Microwave-assisted gas/liquid interfacial synthesis of flowerlike NiO hollow nanosphere precursors and their application as supercapacitor electrodes, J Mater Chem 21 (2011) 3204. https://doi.org/10.1039/c0jm03749d.

[223] M. Fan, B. Ren, L. Yu, Q. Liu, J. Wang, D. Song, J. Liu, X. Jing, L. Liu, Facile growth of hollow porous NiO microspheres assembled from nanosheet building blocks and their high performance as a supercapacitor electrode, CrystEngComm 16 (2014) 10389–10394. https://doi.org/10.1039/C4CE01242A.

[224] U.M. Patil, R.R. Salunkhe, K.V. Gurav, C.D. Lokhande, Chemically deposited nanocrystalline NiO thin films for supercapacitor application, Appl Surf Sci 255 (2008) 2603–2607. https://doi.org/10.1016/j.apsusc.2008.07.192.

[225] F. Yu, L. Zhu, T. You, F. Wang, Z. Wen, Preparation of chestnut-like porous NiO nanospheres as electrodes for supercapacitors, RSC Adv 5 (2015) 96165–96169. https://doi.org/10.1039/C5RA17122A.

[226] M. Karuppaiah, P. Sakthivel, S. Asaithambi, R. Murugan, G.A. babu, R. Yuvakkumar, G. Ravi, Solvent dependent morphological modification of micro-nano assembled Mn2O3/NiO composites for high performance supercapacitor applications, Ceram Int 45 (2019) 4298–4307. https://doi.org/10.1016/j.ceramint.2018.11.104.

[227] Q. Li, J. Guo, D. Xu, J. Guo, X. Ou, Y. Hu, H. Qi, F. Yan, Electrospun N-Doped Porous Carbon Nanofibers Incorporated with NiO Nanoparticles as Free-Standing Film Electrodes for High-Performance Supercapacitors and CO 2 Capture, Small 14 (2018). https://doi.org/10.1002/smll.201704203.

[228] W. Xu, B. Mu, A. Wang, Facile fabrication of well-defined microtubular carbonized kapok fiber/NiO composites as electrode material for supercapacitor, Electrochim Acta 194 (2016) 84–94. https://doi.org/10.1016/j.electacta.2016.02.072.

[229] J. Jia, F. Luo, C. Gao, C. Suo, X. Wang, H. Song, X. Hu, Synthesis of La-doped NiO nanofibers and their electrochemical properties as electrode for supercapacitors, Ceram Int 40 (2014) 6973–6977. https://doi.org/10.1016/j.ceramint.2013.12.024.

[230] T.V. Thi, A.K. Rai, J. Gim, J. Kim, High performance of Co-doped NiO nanoparticle anode material for rechargeable lithium ion batteries, J Power Sources 292 (2015) 23–30. https://doi.org/10.1016/j.jpowsour.2015.05.029.

[231] D. Han, X. Jing, J. Wang, P. Yang, D. Song, J. Liu, Porous lanthanum doped NiO microspheres for supercapacitor application, Journal of Electroanalytical Chemistry 682 (2012) 37–44. https://doi.org/10.1016/j.jelechem.2012.06.016.

[232] G. Boopathi, G.G. Karthikeyan, S.M. Jaimohan, A. Pandurangan, A.L.F. de Barros, Dopant Effects of Gd 3+ on the Electrochemical Pseudocapacitive Characteristics of Electroactive Mesoporous NiO Electrodes for Supercapacitors, The Journal of Physical Chemistry C 122 (2018) 9257–9274. https://doi.org/10.1021/acs.jpcc.7b11643.

[233] P.E. Saranya, S. Selladurai, Mesoporous 3D network Ce-doped NiO nanoflakes as high performance electrodes for supercapacitor applications, New Journal of Chemistry 43 (2019) 7441–7456. https://doi.org/10.1039/C9NJ00097F.

[234] G. Srikesh, A.S. Nesaraj, Chemical synthesis of Co and Mn co-doped NiO nanocrystalline materials as high-performance electrode materials for potential application in supercapacitors, Ceram Int 42 (2016) 5001–5010. https://doi.org/10.1016/j.ceramint.2015.12.013.

[235] K. Sathishkumar, N. Shanmugam, N. Kannadasan, S. Cholan, G. Viruthagiri, Synthesis and characterization of Cu2+ doped NiO electrode for supercapacitor application, J Solgel Sci Technol 74 (2015) 621–630. https://doi.org/10.1007/s10971-015-3641-4.

[236] S. Hussain, P. Wan, N. Aslam, G. Qiao, G. Liu, M. Wang, Ag-doped NiO porous network structure on Ni foam as electrode for supercapacitors, Journal of Materials Science: Materials in Electronics 29 (2018) 1759–1765. https://doi.org/10.1007/s10854-017-8084-y.

[237] P. Lu, F. Liu, D. Xue, H. Yang, Y. Liu, Phase selective route to Ni(OH)2 with enhanced supercapacitance: Performance dependent hydrolysis of Ni(Ac)2 at hydrothermal conditions, Electrochim Acta 78 (2012) 1–10. https://doi.org/10.1016/j.electacta.2012.03.183.

[238] Y. Zhang, J. Wang, P. Wan, J. Ye, S. Hussain, H. Wei, D. Hou, Ag2O loaded NiO ball-flowers for high performance supercapacitors, Mater Lett 177 (2016) 71–75. https://doi.org/10.1016/j.matlet.2016.04.169.

[239] C. Wei, Y. Huang, M. Chen, J. Yan, W. Yao, X. Chen, Fabrication of porous nanosheets assembled from NiCo2O4/NiO electrode for electrochemical energy storage application, J Colloid Interface Sci 504 (2017) 1–11. https://doi.org/10.1016/j.jcis.2017.05.027.

[240] H. Wang, Q. Ren, D.J.L. Brett, G. He, R. Wang, J. Key, S. Ji, Double-shelled tremella-like NiO@Co3O4@MnO2 as a high-performance cathode material for alkaline supercapacitors, J Power Sources 343 (2017) 76–82. https://doi.org/10.1016/j.jpowsour.2017.01.042.

[241] T. Wang, J. Liu, Y. Ma, S. Han, C. Gu, J. Lian, P- N heterojunction NiO/ZnO electrode

with high electrochemical performance for supercapacitor applications, Electrochim Acta 392 (2021) 138976. https://doi.org/10.1016/j.electacta.2021.138976.

[242] X. Zhao, X. Liu, F. Li, M. Huang, MnO2@NiO nanosheets@nanowires hierarchical structures with enhanced supercapacitive properties, J Mater Sci 55 (2020) 2482–2491. https://doi.org/10.1007/s10853-019-04112-4.

[243] T.-F. Yi, J. Mei, Y. Xie, S. Luo, Hybrid porous flower-like NiO@CeO2microspheres with improved pseudocapacitiveproperties, Electrochim Acta 297 (2019) 593–605. https://doi.org/10.1016/j.electacta.2018.12.037.

[244] Y. Zuo, J.-J. Ni, J.-M. Song, H.-L. Niu, C.-J. Mao, S.-Y. Zhang, Y.-H. Shen, Synthesis of Co3O4/NiO nanofilms and their enhanced electrochemical performance for supercapacitor application, Appl Surf Sci 370 (2016) 528–535. https://doi.org/10.1016/j.apsusc.2016.02.193.

[245] R. Xu, J. Lin, J. Wu, M. Huang, L. Fan, Z. Xu, Z. Song, A high-performance pseudocapacitive electrode material for supercapacitors based on the unique NiMoO4/NiO nanoflowers, Appl Surf Sci 463 (2019) 721–731. https://doi.org/10.1016/j.apsusc.2018.08.172.

[246] J.H. Lee, J.Y. Lim, C.S. Lee, J.T. Park, J.H. Kim, Direct growth of NiO nanosheets on mesoporous TiN film for energy storage devices, Appl Surf Sci 420 (2017) 849–857. https://doi.org/10.1016/j.apsusc.2017.05.216.

[247] Y. Zhao, N. Jiang, X. Zhang, J. Guo, Y. Li, L. Gao, H. Wang, T. Ma, Low-cost, large-scale, one-pot synthesis of C/Ni3(NO3)2(OH)4 composites for high performance supercapacitor, Mater Chem Phys 217 (2018) 291–299. https://doi.org/10.1016/j.matchemphys.2018.06.082.

[248] R. Qu, S. Tang, X. Qin, J. Yuan, Y. Deng, L. Wu, J. Li, Z. Wei, Expanded graphite supported Ni(OH)2 composites for high performance supercapacitors, J Alloys Compd 728 (2017) 222–230. https://doi.org/10.1016/j.jallcom.2017.08.270.

[249] D.H. Shin, J.S. Lee, J. Jun, J. Jang, Fabrication of amorphous carbon-coated NiO nanofibers for electrochemical capacitor applications, J. Mater. Chem. A 2 (2014) 3364–3371. https://doi.org/10.1039/C3TA14900E.

[250] J. Xu, L. Li, F. He, R. Lv, P. Yang, A Novel double-shelled C@NiO hollow microsphere: Synthesis and application for electrochemical capacitor, Electrochim Acta 148 (2014) 211–219. https://doi.org/10.1016/j.electacta.2014.10.061.

[251] K. Tao, P. Li, L. Kang, X. Li, Q. Zhou, L. Dong, W. Liang, Facile and low-cost combustion-synthesized amorphous mesoporous NiO/carbon as high mass-loading

pseudocapacitor materials, J Power Sources 293 (2015) 23–32. https://doi.org/10.1016/j.jpowsour.2015.05.004.

[252] S. Vijayakumar, S. Nagamuthu, G. Muralidharan, Porous NiO/C Nanocomposites as Electrode Material for Electrochemical Supercapacitors, ACS Sustain Chem Eng 1 (2013) 1110–1118. https://doi.org/10.1021/sc400152r.

[253] X. Yang, Y. Zhang, G. Wu, C. Zhu, W. Zou, Y. Gao, J. Tian, Z. Zheng, Nanoelectrical investigation and electrochemical performance of nickel-oxide/carbon sphere hybrids through interface manipulation, J Colloid Interface Sci 469 (2016) 287–295. https://doi.org/10.1016/j.jcis.2016.02.031.

[254] Z. Wang, H. Qiang, Z. Zhu, J. Liu, C. Chen, D. Zhang, Facile Synthesis of Nitrogen-Doped Mesoporous Hollow Carbon Nanospheres for High-Performance Supercapacitors, ChemElectroChem 5 (2018) 2242–2249. https://doi.org/10.1002/celc.201800597.

[255] G.S. Gund, D.P. Dubal, S.S. Shinde, C.D. Lokhande, Architectured Morphologies of Chemically Prepared NiO/MWCNTs Nanohybrid Thin Films for High Performance Supercapacitors, ACS Appl Mater Interfaces 6 (2014) 3176–3188. https://doi.org/10.1021/am404422g.

[256] A.S. Adekunle, K.I. Ozoemena, B.O. Agboola, MWCNTs/metal (Ni, Co, Fe) oxide nanocomposite as potential material for supercapacitors application in acidic and neutral media, Journal of Solid State Electrochemistry 17 (2013) 1311–1320. https://doi.org/10.1007/s10008-012-1978-y.

[257] B. Gao, C. Yuan, L. Su, L. Chen, X. Zhang, Nickel oxide coated on ultrasonically pretreated carbon nanotubes for supercapacitor, Journal of Solid State Electrochemistry 13 (2009) 1251–1257. https://doi.org/10.1007/s10008-008-0658-4.

[258] Z. Zhang, P. Zhang, D. Zhang, H. Lin, Y. Chen, A new strategy for the preparation of flexible macroscopic graphene fibers as supercapacitor electrodes, Mater Des 157 (2018) 170–178. https://doi.org/10.1016/j.matdes.2018.07.043.

[259] C. Wu, S. Deng, H. Wang, Y. Sun, J. Liu, H. Yan, Preparation of Novel Three-Dimensional NiO/Ultrathin Derived Graphene Hybrid for Supercapacitor Applications, ACS Appl Mater Interfaces 6 (2014) 1106–1112. https://doi.org/10.1021/am404691w.

[260] Z.B. Wen, F. Yu, T. You, L. Zhu, L. Zhang, Y.P. Wu, A core–shell structured nanocomposite of NiO with carbon nanotubes as positive electrode material of high capacitance for supercapacitors, Mater Res Bull 74 (2016) 241–247. https://doi.org/10.1016/j.materresbull.2015.10.035.

[261] B. Zhao, H. Zhuang, T. Fang, Z. Jiao, R. Liu, X. Ling, B. Lu, Y. Jiang, Self-assembly of NiO/graphene with three-dimension hierarchical structure as high performance electrode material for supercapacitors, J Alloys Compd 597 (2014) 291–298. https://doi.org/10.1016/j.jallcom.2014.01.192.

[262] D. Xiang, X. Liu, X. Dong, A facile synthetic method and electrochemical performances of nickel oxide/carbon fibers composites, J Mater Sci 52 (2017) 7709–7718. https://doi.org/10.1007/s10853-017-1019-4.

[263] J. Lv, Z. Wang, H. Miura, Facile synthesis of mesoporous NiO nanoflakes on graphene foam and its electrochemical properties for supercapacitor application, Solid State Commun 269 (2018) 45–49. https://doi.org/10.1016/j.ssc.2017.10.005.

[264] K. Xu, R. Zou, W. Li, Q. Liu, T. Wang, J. Yang, Z. Chen, J. Hu, Carbon-coated mesoporous NiO nanoparticles as an electrode material for high performance electrochemical capacitors, New Journal of Chemistry 37 (2013) 4031. https://doi.org/10.1039/c3nj00890h.

[265] A. Liu, H. Zhang, G. Wang, J. Zhang, S. Zhang, Sandwich-like NiO/rGO nanoarchitectures for 4 V solid-state asymmetric-supercapacitors with high energy density, Electrochim Acta 283 (2018) 1401–1410. https://doi.org/10.1016/j.electacta.2018.07.099.

[266] L. Jinlong, Z. Wang, L. Tongxiang, Y. Meng, K. Suzuki, H. Miura, The effect of graphene coated nickel foam on the microstructures of NiO and their supercapacitor performance, Journal of Electroanalytical Chemistry 799 (2017) 595–601. https://doi.org/10.1016/j.jelechem.2017.07.013.

[267] Q. Li, Q. Wei, L. Xie, C. Chen, C. Lu, F.-Y. Su, P. Zhou, Layered NiO/reduced graphene oxide composites by heterogeneous assembly with enhanced performance as high-performance asymmetric supercapacitor cathode, RSC Adv 6 (2016) 46548–46557. https://doi.org/10.1039/C6RA04998B.

[268] Y. Feng, H. Zhang, Y. Zhang, Y. Bai, Y. Wang, Novel peapod NiO nanoparticles encapsulated in carbon fibers for high-efficiency supercapacitors and lithium-ion batteries, J Mater Chem A Mater 4 (2016) 3267–3277. https://doi.org/10.1039/C5TA09699E.

[269] G. Wang, L. Zhang, J. Zhang, A review of electrode materials for electrochemical supercapacitors, Chem. Soc. Rev. 41 (2012) 797–828. https://doi.org/10.1039/C1CS15060J.

[270] S.A. Razali, S.R. Majid, Electrochemical performance of binder-free NiO-PANI on

etched carbon cloth as active electrode material for supercapacitor, Mater Des 153 (2018) 24–35. https://doi.org/10.1016/j.matdes.2018.04.074.

[271] Y.H. Navale, S.T. Navale, I.A. Dhole, F.J. Stadler, V.B. Patil, Specific capacitance, energy and power density coherence in electrochemically synthesized polyaniline-nickel oxide hybrid electrode, Org Electron 57 (2018) 110–117. https://doi.org/10.1016/j.orgel.2018.02.037.

[272] B. Sun, X. He, X. Leng, Y. Jiang, Y. Zhao, H. Suo, C. Zhao, Flower-like polyaniline–NiO structures: a high specific capacity supercapacitor electrode material with remarkable cycling stability, RSC Adv 6 (2016) 43959–43963. https://doi.org/10.1039/C6RA02534J.

[273] X. Wu, Q. Wang, W. Zhang, Y. Wang, W. Chen, Nano nickel oxide coated graphene/polyaniline composite film with high electrochemical performance for flexible supercapacitor, Electrochim Acta 211 (2016) 1066–1075. https://doi.org/10.1016/j.electacta.2016.06.026.

[274] S.R. Nalage, S.T. Navale, V.B. Patil, Polypyrrole-NiO hybrid nanocomposite: Structural, morphological, optical and electrical transport studies, Measurement 46 (2013) 3268–3275. https://doi.org/10.1016/j.measurement.2013.06.049.

[275] H. Vijeth, S.P. Ashokkumar, L. Yesappa, M. Vandana, H. Devendrappa, Hybrid core-shell nanostructure made of chitosan incorporated polypyrrole nanotubes decorated with NiO for all-solid-state symmetric supercapacitor application, Electrochim Acta 354 (2020) 136651. https://doi.org/10.1016/j.electacta.2020.136651.

[276] K. Han, Y. Liu, H. Huang, Q. Gong, Z. Zhang, G. Zhou, Tremella-like NiO microspheres embedded with fish-scale-like polypyrrole for high-performance asymmetric supercapacitor, RSC Adv 9 (2019) 21608–21615. https://doi.org/10.1039/C9RA03046H.

[277] W. Ji, J. Ji, X. Cui, J. Chen, D. Liu, H. Deng, Q. Fu, Polypyrrole encapsulation on flower-like porous NiO for advanced high-performance supercapacitors, Chemical Communications 51 (2015) 7669–7672. https://doi.org/10.1039/C5CC00965K.

[278] F. Wang, G. Li, J. Zheng, J. Ma, C. Yang, Q. Wang, Hydrothermal synthesis of flower-like molybdenum disulfide microspheres and their application in electrochemical supercapacitors, RSC Adv 8 (2018) 38945–38954. https://doi.org/10.1039/C8RA04350G.

[279] S. Asaithambi, P. Sakthivel, M. Karuppaiah, K. Balamurugan, R. Yuvakkumar, M. Thambidurai, G. Ravi, Synthesis and characterization of various transition metals doped

SnO2@MoS2 composites for supercapacitor and photocatalytic applications, J Alloys Compd 853 (2021) 157060. https://doi.org/10.1016/j.jallcom.2020.157060.

[280] O. Moradlou, H. Sharifpour, Interconnected NiCo2S4 - coated NiO nanosheet arrays as electrode materials for high-performance supercapacitors, J Energy Storage 32 (2020) 101886. https://doi.org/10.1016/j.est.2020.101886.

[281] Y. Wang, A. Pan, Y. Zhang, J. Shi, J. Lin, S. Liang, G. Cao, Heterogeneous NiS/NiO multi-shelled hollow microspheres with enhanced electrochemical performances for hybrid-type asymmetric supercapacitors, J Mater Chem A Mater 6 (2018) 9153–9160. https://doi.org/10.1039/C8TA01866A.

[282] Y. Yang, S. Li, F. Liu, J. Wen, N. Zhang, S. Wang, K. Liu, Enhanced performance of multi-dimensional CoS nanoflake/NiO nanosheet architecture with synergetic effect for asymmetric supercapacitor, Nanotechnology 29 (2018) 455401. https://doi.org/10.1088/1361-6528/aadd63.

[283] T. Yi, Y. Li, S. Qi, P. Peng, Y. Zhu, Y. Xie, Construction of Porous ZnS@Co 3 S 4 @NiO Nanosheets Hybrid Materials for High-Performance Pseudocapacitor Electrode by Morphology Reshaping, Adv Sustain Syst 4 (2020). https://doi.org/10.1002/adsu.202000090.

[284] S.-Y. Kim, C.V.V.M. Gopi, A.E. Reddy, H.-J. Kim, Facile synthesis of a NiO/NiS hybrid and its use as an efficient electrode material for supercapacitor applications, New Journal of Chemistry 42 (2018) 5309–5313. https://doi.org/10.1039/C7NJ05145J.

[285] J. Epp, X-ray diffraction (XRD) techniques for materials characterization, in: Materials Characterization Using Nondestructive Evaluation (NDE) Methods, Elsevier, 2016: pp. 81–124. https://doi.org/10.1016/B978-0-08-100040-3.00004-3.

[286] C. Hu, X. Dang, S. Hu, Studies on adsorption of cetyltrimethylammonium bromide at carbon paste electrode and the enhancement effect in thyroxine reduction by voltammetry and electrochemical impedance spectroscopy, Journal of Electroanalytical Chemistry 572 (2004) 161–171. https://doi.org/10.1016/j.jelechem.2004.06.009.

[287] R.S. Almenares Reyes, A. Alujas Díaz, C.A. Leyva Rodríguez, L. Poll Legrá, L.A. Pérez García, S. Betancourt Rodríguez, F. Arcial Carratalá, J.F. Martirena Hernández, Clay Deposits from the Northeastern of Cuba: Characterization, Evaluation, and Use as a Source of Supplementary Cementitious Materials, in: 2020: pp. 49–56. https://doi.org/10.1007/978-981-15-2806-4_6.

[288] P.B. Hirsch, Elements of X-Ray Diffraction, Physics Bulletin 8 (1957) 237–238. https://doi.org/10.1088/0031-9112/8/7/008.

[289] A.A. Bunaciu, E. gabriela Udriştioiu, H.Y. Aboul-Enein, X-Ray Diffraction: Instrumentation and Applications, Crit Rev Anal Chem 45 (2015) 289–299. https://doi.org/10.1080/10408347.2014.949616.

[290] A.A. Bunaciu, E. gabriela Udriştioiu, H.Y. Aboul-Enein, X-Ray Diffraction: Instrumentation and Applications, Crit Rev Anal Chem 45 (2015) 289–299. https://doi.org/10.1080/10408347.2014.949616.

[291] M.J. Pelletier, Quantitative Analysis Using Raman Spectrometry, Appl Spectrosc 57 (2003) 20A-42A. https://doi.org/10.1366/000370203321165133.

[292] S.P. Mulvaney, C.D. Keating, Raman Spectroscopy, Anal Chem 72 (2000) 145–158. https://doi.org/10.1021/a10000155.

[293] F. Ascencio, A. Bobadilla, R. Escudero, Study of NiO nanoparticles, structural and magnetic characteristics, Applied Physics A 125 (2019) 279. https://doi.org/10.1007/s00339-019-2579-8.

[294] I. Burmistrov, D. Agarkov, I. Tartakovskii, V. Kharton, S. Bredikhin, Performance Optimization of Cermet SOFC Anodes: An Evaluation of Nanostructured NiO, ECS Trans 68 (2015) 1265–1274. https://doi.org/10.1149/06801.1265ecst.

[295] S.L. Erlandsen, C. Frethem, Y. Chen, Field Emission Scanning Electron Microscopy (FESEM) Entering the 21st Century: Nanometer Resolution and Molecular Topography of Cell Structure, J Histotechnol 23 (2000) 249–259. https://doi.org/10.1179/his.2000.23.3.249.

[296] C. Sant'Anna, L. Campanati, C. Gadelha, D. Lourenço, L. Labati-Terra, J. Bittencourt-Silvestre, M. Benchimol, N.L. Cunha-e-Silva, W. Souza, Improvement on the visualization of cytoskeletal structures of protozoan parasites using high-resolution field emission scanning electron microscopy (FESEM), Histochem Cell Biol 124 (2005) 87–95. https://doi.org/10.1007/s00418-005-0786-1.

[297] D.C. Joy, J.B. Pawley, High-resolution scanning electron microscopy, Ultramicroscopy 47 (1992) 80–100. https://doi.org/10.1016/0304-3991(92)90186-N.

[298] L. Frank, M. Hovorka, Š. Mikmeková, E. Mikmeková, I. Müllerová, Z. Pokorná, Scanning Electron Microscopy with Samples in an Electric Field, Materials 5 (2012) 2731–2756. https://doi.org/10.3390/ma5122731.

[299] S. Sharma, H.I. Rasool, V. Palanisamy, C. Mathisen, M. Schmidt, D.T. Wong, J.K. Gimzewski, Structural-Mechanical Characterization of Nanoparticle Exosomes in Human Saliva, Using Correlative AFM, FESEM, and Force Spectroscopy, ACS Nano 4 (2010) 1921–1926. https://doi.org/10.1021/nn901824n.

[300] B.C. Ang, I.I. Yaacob, I. Nurdin, Investigation of Fe 2 O 3 /SiO 2 Nanocomposite by FESEM and TEM, J Nanomater 2013 (2013). https://doi.org/10.1155/2013/980390.

[301] G. Zadora, Z. Brożek-Mucha, SEM–EDX—a useful tool for forensic examinations, Mater Chem Phys 81 (2003) 345–348. https://doi.org/10.1016/S0254-0584(03)00018-X.

[302] Z. Brozek-Mucha, A. Jankowicz, Evaluation of the possibility of differentiation between various types of ammunition by means of GSR examination with SEM–EDX method, Forensic Sci Int 123 (2001) 39–47. https://doi.org/10.1016/S0379-0738(01)00518-7.

[303] M. Scimeca, S. Bischetti, H.K. Lamsira, R. Bonfiglio, E. Bonanno, Energy Dispersive X-ray (EDX) microanalysis: A powerful tool in biomedical research and diagnosis, European Journal of Histochemistry (2018). https://doi.org/10.4081/ejh.2018.2841.

[304] M. Liu, J.M. Cowley, Structures of carbon nanotubes studied by HRTEM and nanodiffraction, Ultramicroscopy 53 (1994) 333–342. https://doi.org/10.1016/0304-3991(94)90046-9.

[305] F. Xudong, Q. Hua, P. Julin, L.A. Bursill, HRTEM analysis of nanodomain textures in PMN, Integrated Ferroelectrics 9 (1995) 233–242. https://doi.org/10.1080/10584589508012928.

[306] C. Tao, W. Hejing, Z. Xiaoping, Z. Nan, SAED and HRTEM Investigation of Palygorskite, Acta Geologica Sinica - English Edition 82 (2008) 385–391. https://doi.org/10.1111/j.1755-6724.2008.tb00588.x.

[307] S. Tougaard, Practical guide to the use of backgrounds in quantitative XPS, Journal of Vacuum Science & Technology A 39 (2021). https://doi.org/10.1116/6.0000661.

[308] M. Eddaoudi, Characterization of Porous Solids and Powders: Surface Area, Pore Size and Density By S. Lowell (Quantachrome Instruments, Boynton Beach), J. E. Shields (C. W. Post Campus of Long Island University), M. A. Thomas, and M. Thommes (Quantachrome In-struments). Kluwer Academic Publishers: Dordrecht, The Netherlands. 2004. xiv + 348 pp. $159.00. ISBN 1-4020-2302-2., J Am Chem Soc 127 (2005) 14117–14117. https://doi.org/10.1021/ja041016i.

[309] S. Ho, A.G. Jacob, A brief overview of X-ray photoelectron spectroscopy characterization of thin films, Res J Chem Environ 28 (2023) 142–160. https://doi.org/10.25303/281rjce1420160.

[310] J. Matthew, Surface analysis by Auger and x-ray photoelectron spectroscopy. D. Briggs and J. T. Grant (eds). IMPublications, Chichester, UK and SurfaceSpectra, Manchester, UK, 2003. 900 pp., ISBN 1-901019-04-7, 900 pp, Surface and Interface Analysis 36 (2004) 1647–1647. https://doi.org/10.1002/sia.2005.

[311] M.P. Seah, The quantitative analysis of surfaces by XPS: A review, Surface and Interface Analysis 2 (1980) 222–239. https://doi.org/10.1002/sia.740020607.

[312] M. Thommes, K. Kaneko, A. V. Neimark, J.P. Olivier, F. Rodriguez-Reinoso, J. Rouquerol, K.S.W. Sing, Physisorption of gases, with special reference to the evaluation of surface area and pore size distribution (IUPAC Technical Report), Pure and Applied Chemistry 87 (2015) 1051–1069. https://doi.org/10.1515/pac-2014-1117.

[313] EC08, A. A. N. (2011). Basic overview of the working principle of a potentiostat/galvanostat (PGSTAT)–Electrochemical cell setup. Metrohm Autolab. BV, 1-3.

[314] A. Bard, L. Faulkner, Electrochemical Methods – Fundamental and Applications, 2nd Edition, John Wiley and sons

[315] B. Ranjan, G. Kumar Sharma, G. Malik, A. Kumar, D. Kaur, In-situ sputtered 2D-MoS 2 nanoworms reinforced with molybdenum nitride towards enhanced Na-ion based supercapacitive electrodes, Nanotechnology 32 (2021) 455402. https://doi.org/10.1088/1361-6528/ac1bdf.

[316] M.M. Vadiyar, S.C. Bhise, S.S. Kolekar, J.-Y. Chang, K.S. Ghule, A. V. Ghule, Low cost flexible 3-D aligned and cross-linked efficient ZnFe 2 O 4 nano-flakes electrode on stainless steel mesh for asymmetric supercapacitors, J Mater Chem A Mater 4 (2016) 3504–3512. https://doi.org/10.1039/C5TA09022A.

[317] V. Augustyn, P. Simon, B. Dunn, Pseudocapacitive oxide materials for high-rate electrochemical energy storage, Energy Environ Sci 7 (2014) 1597. https://doi.org/10.1039/c3ee44164d.

[318] Q. Yang, Q. Li, Z. Yan, X. Hu, L. Kang, Z. Lei, Z.-H. Liu, High performance graphene/manganese oxide hybrid electrode with flexible holey structure, Electrochim Acta 129 (2014) 237–244. https://doi.org/10.1016/j.electacta.2014.02.113.

[319] J. Li, Y. Chen, Y. Liu, Research on a Stand-alone Photovoltaic System with a Supercapacitor as the Energy Storage Device, Energy Procedia 16 (2012) 1693–1700. https://doi.org/10.1016/j.egypro.2012.01.262.

[320] Y. Zhang, H. Feng, X. Wu, L. Wang, A. Zhang, T. Xia, H. Dong, X. Li, L. Zhang, Progress of electrochemical capacitor electrode materials: A review, Int J Hydrogen

Energy 34 (2009) 4889–4899. https://doi.org/10.1016/j.ijhydene.2009.04.005.

[321] F. Shi, L. Li, X. Wang, C. Gu, J. Tu, Metal oxide/hydroxide-based materials for supercapacitors, RSC Adv. 4 (2014) 41910–41921. https://doi.org/10.1039/C4RA06136E.

[322] X.L. Guo, M. Kuang, F. Dong, Y.X. Zhang, Monodispersed plum candy-like MnO 2 nanosheets-decorated NiO nanostructures for supercapacitors, Ceram Int 42 (2016) 7787–7792. https://doi.org/10.1016/j.ceramint.2016.01.213.

[323] L. Pei, Y. Yang, H. Chu, J. Shen, M. Ye, Self-assembled flower-like FeS2/graphene aerogel composite with enhanced electrochemical properties, Ceram Int 42 (2016) 5053–5061. https://doi.org/10.1016/j.ceramint.2015.11.178.

[324] X. Wu, S. Yao, Flexible electrode materials based on WO3 nanotube bundles for high performance energy storage devices, Nano Energy 42 (2017) 143–150. https://doi.org/10.1016/j.nanoen.2017.10.058.

[325] Y. Liu, P. Hu, H. Liu, J. Song, A. Umar, X. Wu, Toward a high performance asymmetric hybrid capacitor by electrode optimization, Inorg Chem Front 6 (2019) 2824–2831. https://doi.org/10.1039/C9QI00927B.

[326] D. Zhao, M. Dai, H. Liu, K. Chen, X. Zhu, D. Xue, X. Wu, J. Liu, Sulfur-Induced Interface Engineering of Hybrid NiCo 2 O 4 @NiMo 2 S 4 Structure for Overall Water Splitting and Flexible Hybrid Energy Storage, Adv Mater Interfaces 6 (2019). https://doi.org/10.1002/admi.201901308.

[327] W. Deng, Y. Liu, Y. Zhang, F. Lu, Q. Chen, X. Ji, Enhanced electrochemical capacitance of nanoporous NiO based on an eggshell membrane, RSC Adv 2 (2012) 1743. https://doi.org/10.1039/c2ra00885h.

[328] X. Yan, X. Tong, J. Wang, C. Gong, M. Zhang, L. Liang, Synthesis of mesoporous NiO nanoflake array and its enhanced electrochemical performance for supercapacitor application, J Alloys Compd 593 (2014) 184–189. https://doi.org/10.1016/j.jallcom.2014.01.036.

[329] E.L. Miller, R.E. Rocheleau, Electrochemical Behavior of Reactively Sputtered Iron-Doped Nickel Oxide, J Electrochem Soc 144 (1997) 3072–3077. https://doi.org/10.1149/1.1837961.

[330] B. Subramanian, M. Mohamed Ibrahim, V. Senthilkumar, K.R. Murali, VS. Vidhya, C. Sanjeeviraja, M. Jayachandran, Optoelectronic and electrochemical properties of nickel oxide (NiO) films deposited by DC reactive magnetron sputtering, Physica B Condens Matter 403 (2008) 4104–4110. https://doi.org/10.1016/j.physb.2008.08.014.

[331] Q. Li, L.-S. Wang, B.-Y. Hu, C. Yang, L. Zhou, L. Zhang, Preparation and characterization of NiO nanoparticles through calcination of malate gel, Mater Lett 61 (2007) 1615–1618. https://doi.org/10.1016/j.matlet.2006.07.113.

[332] A. Aslani, V. Oroojpour, M. Fallahi, Sonochemical synthesis, size controlling and gas sensing properties of NiO nanoparticles, Appl Surf Sci 257 (2011) 4056–4061. https://doi.org/10.1016/j.apsusc.2010.11.174.

[333] S.D. Dhas, P.S. Maldar, M.D. Patil, A.B. Nagare, M.R. Waikar, R.G. Sonkawade, Annasaheb. V. Moholkar, Synthesis of NiO nanoparticles for supercapacitor application as an efficient electrode material, Vacuum 181 (2020) 109646. https://doi.org/10.1016/j.vacuum.2020.109646.

[334] A. Ali, M. Ammar, A. Mukhtar, T. Ahmed, M. Ali, M. Waqas, M.N. Amin, A. Rasheed, 3D NiO nanowires@NiO nanosheets core-shell structures grown on nickel foam for high performance supercapacitor electrode, Journal of Electroanalytical Chemistry 857 (2020) 113710. https://doi.org/10.1016/j.jelechem.2019.113710.

[335] S. Ci, Z. Wen, Y. Qian, S. Mao, S. Cui, J. Chen, NiO-Microflower Formed by Nanowire-weaving Nanosheets with Interconnected Ni-network Decoration as Supercapacitor Electrode, Sci Rep 5 (2015) 11919. https://doi.org/10.1038/srep11919.

[336] F. Cao, G.X. Pan, X.H. Xia, P.S. Tang, H.F. Chen, Synthesis of hierarchical porous NiO nanotube arrays for supercapacitor application, J Power Sources 264 (2014) 161–167. https://doi.org/10.1016/j.jpowsour.2014.04.103.

[337] D. Du, Z. Hu, Y. Liu, Y. Deng, J. Liu, Preparation and characterization of flower-like microspheres of nano-NiO as electrode material for supercapacitor, J Alloys Compd 589 (2014) 82–87. https://doi.org/10.1016/j.jallcom.2013.11.176.

[338] Z.H. Ibupoto, S. Elhag, M.S. AlSalhi, O. Nur, M. Willander, Effect of Urea on the Morphology of Co 3 O 4 Nanostructures and Their Application for Potentiometric Glucose Biosensor, Electroanalysis 26 (2014) 1773–1781. https://doi.org/10.1002/elan.201400116.

[339] S. Pilban Jahromi, A. Pandikumar, B.T. Goh, Y.S. Lim, W.J. Basirun, H.N. Lim, N.M. Huang, Influence of particle size on performance of a nickel oxide nanoparticle-based supercapacitor, RSC Adv 5 (2015) 14010–14019. https://doi.org/10.1039/C4RA16776G.

[340] A. Allagui, A.H. Alami, E.A. Baranova, R. Wüthrich, Size-dependent capacitance of NiO nanoparticles synthesized with cathodic contact glow discharge electrolysis, J Power Sources 262 (2014) 178–182. https://doi.org/10.1016/j.jpowsour.2014.03.104.

[341] F. Ascencio, A. Bobadilla, R. Escudero, Study of NiO nanoparticles, structural and magnetic characteristics, Applied Physics A 125 (2019) 279. https://doi.org/10.1007/s00339-019-2579-8.

[342] I. Burmistrov, D. Agarkov, I. Tartakovskii, V. Kharton, S. Bredikhin, Performance Optimization of Cermet SOFC Anodes: An Evaluation of Nanostructured NiO, ECS Trans 68 (2015) 1265–1274. https://doi.org/10.1149/06801.1265ecst.

[343] M. Saraf, K. Natarajan, S.M. Mobin, Emerging Robust Heterostructure of MoS 2 –rGO for High-Performance Supercapacitors, ACS Appl Mater Interfaces 10 (2018) 16588–16595. https://doi.org/10.1021/acsami.8b04540.

[344] E. Cuervo-Reyes, C.P. Scheller, M. Held, U. Sennhauser, A Unifying View of the Constant-Phase-Element and Its Role as an Aging Indicator for Li-Ion Batteries, J Electrochem Soc 162 (2015) A1585–A1591. https://doi.org/10.1149/2.0791508jes.

[345] P. Kumar, S. Sharma, S. Jabeen, K.S. Samra, Hybrid microwave annealing assisted synthesis of MoS2-RGO nanostructures: Optimization and characterization for application in supercapacitors, Electrochim Acta 426 (2022) 140738. https://doi.org/10.1016/j.electacta.2022.140738.

[346] S. Vijayakumar, S. Nagamuthu, G. Muralidharan, Supercapacitor Studies on NiO Nanoflakes Synthesized Through a Microwave Route, ACS Appl Mater Interfaces 5 (2013) 2188–2196. https://doi.org/10.1021/am400012h.

[347] Q.Q. Li, R.H. Fan, K.L. Yan, K. Sun, X.A. Wang, M. Chen, P.T. Xie, Preparation of NiO Microspheres by Hydrothermal Method and its Electrochemical Capacitive Properties, Materials Science Forum 814 (2015) 81–85. https://doi.org/10.4028/www.scientific.net/MSF.814.81.

[348] W. Yu, X. Jiang, S. Ding, B.Q. Li, Preparation and electrochemical characteristics of porous hollow spheres of NiO nanosheets as electrodes of supercapacitors, J Power Sources 256 (2014) 440–448. https://doi.org/10.1016/j.jpowsour.2013.12.110.

[349] S.S. Gunasekaran, A. Gopalakrishnan, R. Subashchandrabose, S. Badhulika, Phytogenic generation of NiO nanoparticles as green-electrode material for high performance asymmetric supercapacitor applications, J Energy Storage 37 (2021) 102412. https://doi.org/10.1016/j.est.2021.102412.

[350] L. Niu, Y. Wang, F. Ruan, C. Shen, S. Shan, M. Xu, Z. Sun, C. Li, X. Liu, Y. Gong, In situ growth of NiCo2S4@Ni3V2O8 on Ni foam as a binder-free electrode for asymmetric supercapacitors, J Mater Chem A Mater 4 (2016) 5669–5677. https://doi.org/10.1039/c6ta00078a.

[351] J. Xu, C. Ruan, P. Li, Y. Xie, Excessive nitrogen doping of tin dioxide nanorod array grown on activated carbon fibers substrate for wire-shaped microsupercapacitor, Chem Eng J 378 (2019). https://doi.org/10.1016/j.cej.2019.122064.

[352] Y. Wang, Y. Xie, Electroactive FeS2-modified MoS2 nanosheet for high-performance supercapacitor, J Alloys Compd 824 (2020). https://doi.org/10.1016/j.jallcom.2020.153936.

[353] S. Sheokand, P. Kumar, S. Jabeen, K.S. Samra, 3D highly porous microspherical morphology of NiO nanoparticles for supercapacitor application, J Solid State Electrochem 27 (2023) 727–738. https://doi.org/10.1007/s10008-022-05366-w.

[354] T. Wang, J. Liu, Y. Ma, S. Han, C. Gu, J. Lian, P- N heterojunction NiO/ZnO electrode with high electrochemical performance for supercapacitor applications, Electrochim Acta 392 (2021). https://doi.org/10.1016/j.electacta.2021.138976.

[355] P. Palanisamy, K. Thangavel, S. Murugesan, S. Marappan, M. Chavali, P.F. Siril, D.V. Perumal, Investigating the synergistic effect of hybridized WO3-ZnS nanocomposite prepared by microwave-assisted wet chemical method for supercapacitor application, J Electroanal Chem 833 (2019) 93–104. https://doi.org/10.1016/j.jelechem.2018.11.026.

[356] N. Chaudhary, A. Kumar, S. Imtiyaz, M. Khanuja, Architectural Design of Electrode Material for Supercapacitor Application Based on a MoS 2 /CeO 2 Heterostructure Synthesized by Facile Hydrothermal Technique , ECS J Solid State Sci Technol 10 (2021) 053005. https://doi.org/10.1149/2162-8777/ac02a3.

[357] M. Manuraj, J. Chacko, K.N. Narayanan Unni, R.B. Rakhi, Heterostructured MoS2-RuO2 nanocomposite: A promising electrode material for supercapacitors, J Alloys Compd 836 (2020). https://doi.org/10.1016/j.jallcom.2020.155420.

[358] H. Heydari, M. Abdouss, S. Mazinani, A.M. Bazargan, F. Fatemi, Electrochemical study of ternary polyaniline/MoS2−MnO2 for supercapacitor applications, J Energy Storage 40 (2021). https://doi.org/10.1016/j.est.2021.102738.

[359] D. Kasinathan, P. Prabhakar, P. Muruganandam, B.R. Wiston, A. Mahalingam, G. Sriram, Solution Processed NiO/MoS2 Heterostructure Nanocomposite for Supercapacitor Electrode Application, Energies 16 (2023). https://doi.org/10.3390/en16010335.

[360] P.S. Selvamani, J.J. Vijaya, L.J. Kennedy, B. Saravanakumar, M. Bououdina, High-performance supercapacitor based on Cu2O/MoS2/rGO nanocomposite, Mater Lett 275 (2020). https://doi.org/10.1016/j.matlet.2020.128095.

[361] G.P. Awasthi, M.B. Poudel, M. Shin, K.P. Sharma, H.J. Kim, C. Yu, Facile synthesis of

a copper oxide/molybdenum disulfide heterostructure for asymmetric supercapacitors of high specific energy, J Energy Storage 42 (2021). https://doi.org/10.1016/j.est.2021.103140.

[362] W. Shang, Y. Tan, L. Kong, F. Ran, Fundamental Triangular Interaction of Electron Trajectory Deviation and P-N Junction to Promote Redox Reactions for the High-Energy-Density Electrode, ACS Appl Mater Interfaces 12 (2020) 29404–29413. https://doi.org/10.1021/acsami.0c08299.

[363] X.H. Zhang, C. Wang, M.Q. Xue, B.C. Lin, X. Ye, W.N. Lei, HYDROTHERMAL SYNTHESIS AND CHARACTERIZATION OF ULTRATHIN MoS 2 NANOSHEETS, n.d.

[364] D. Zhang, Y. Jin, Y. Cao, Facile synthesis and ammonia gas sensing properties of NiO nanoparticles decorated MoS2 nanosheets heterostructure, J Mater Sci Mater Electron 30 (2019) 573–581. https://doi.org/10.1007/s10854-018-0323-3.

[365] G. Cheng, Y. Yan, R. Chen, From Ni-based nanoprecursors to NiO nanostructures: Morphology-controlled synthesis and structure-dependent electrochemical behavior, New J Chem 39 (2015) 676–682. https://doi.org/10.1039/c4nj01398k.

[366] T. Alamro, M.K. Ram, Polyethylenedioxythiophene and molybdenum disulfide nanocomposite electrodes for supercapacitor applications, Electrochim Acta 235 (2017) 623–631. https://doi.org/10.1016/j.electacta.2017.03.102.

[367] J. Yan, S. Wang, Y. Chen, M. Yuan, Y. Huang, J. Lian, J. Qiu, J. Bao, M. Xie, H. Xu, H. Li, Y. Zhao, Smart in situ construction of NiS/MoS2 composite nanosheets with ultrahigh specific capacity for high-performance asymmetric supercapacitor, J Alloys Compd 811 (2019). https://doi.org/10.1016/j.jallcom.2019.151915.

[368] Y. Chen, W.K. Pang, H. Bai, T. Zhou, Y. Liu, S. Li, Z. Guo, Enhanced Structural Stability of Nickel-Cobalt Hydroxide via Intrinsic Pillar Effect of Metaborate for High-Power and Long-Life Supercapacitor Electrodes, Nano Lett 17 (2017) 429–436. https://doi.org/10.1021/acs.nanolett.6b04427.

[369] M. Saraf, K. Natarajan, S.M. Mobin, Microwave assisted fabrication of a nanostructured reduced graphene oxide (rGO)/Fe2O3 composite as a promising next generation energy storage material, RSC Adv 7 (2017) 309–317. https://doi.org/10.1039/c6ra24766k.

[370] Z. Xu, S. Sun, Y. Han, Z. Wei, Y. Cheng, S. Yin, W. Cui, High-Energy-Density Asymmetric Supercapacitor Based on a Durable and Stable Manganese Molybdate Nanostructure Electrode for Energy Storage Systems, ACS Appl Energy Mater 3 (2020) 5393–5404. https://doi.org/10.1021/acsaem.0c00393.

[371] Y. Wang, Y. Song, Y. Xia, Electrochemical capacitors: Mechanism, materials, systems, characterization and applications, Chem Soc Rev 45 (2016) 5925–5950. https://doi.org/10.1039/c5cs00580a.

[372] Z.A. Hrbe, S.W. Hashim, Tungsten disulfide-nickel oxide hybrids as high-performance supercapacitors, J Met Mater 32 (2022) 86–92. https://doi.org/10.55713/jmmm.v32i3.1519.

[373] D. Liang, Z. Tian, J. Liu, Y. Ye, S. Wu, Y. Cai, C. Liang, MoS2 nanosheets decorated with ultrafine Co3O4 nanoparticles for high-performance electrochemical capacitors, Electrochim Acta 182 (2015) 376–382. https://doi.org/10.1016/j.electacta.2015.09.085.

[374] Q.H. Ren, Y. Zhang, H.L. Lu, Y.P. Wang, W.J. Liu, X.M. Ji, A. Devi, A.Q. Jiang, D.W. Zhang, Atomic Layer Deposition of Nickel on ZnO Nanowire Arrays for High-Performance Supercapacitors, ACS Appl Mater Interfaces 10 (2018) 468–476. https://doi.org/10.1021/acsami.7b13392.

[375] X. Jia, X. Wu, B. Liu, Formation of ZnCo2O4@MnO2 core-shell electrode materials for hybrid supercapacitor, Dalton Transactions 47 (2018) 15506–15511. https://doi.org/10.1039/c8dt03298j.

[376] F.N. Tuzluca, Y.O. Yesilbag, M. Ertugrul, Synthesis of In 2 O 3 nanostructures with different morphologies as potential supercapacitor electrode materials, Appl Surf Sci 427 (2018) 956–964. https://doi.org/10.1016/j.apsusc.2017.08.127.

[377] Y. Zheng, T. Zhou, C. Zhang, J. Mao, H. Liu, Z. Guo, Boosted Charge Transfer in SnS/SnO 2 Heterostructures: Toward High Rate Capability for Sodium-Ion Batteries , Angewandte Chemie 128 (2016) 3469–3474. https://doi.org/10.1002/ange.201510978.

[378] O. Voznyy, B.R. Sutherland, A.H. Ip, D. Zhitomirsky, E.H. Sargent, Engineering charge transport by heterostructuring solution-processed semiconductors, Nat Rev Mater 2 (2017). https://doi.org/10.1038/natrevmats.2017.26.

[379] D. Sharma, S. Upadhyay, V.R. Satsangi, R. Shrivastav, U. V. Waghmare, S. Dass, Nanostructured BaTiO3/Cu2O heterojunction with improved photoelectrochemical activity for H2 evolution: Experimental and first-principles analysis, Appl Catal B 189 (2016) 75–85. https://doi.org/10.1016/j.apcatb.2016.02.037.

[380] W. Chen, T. Wei, L.E. Mo, S. Wu, Z. Li, S. Chen, X. Zhang, L. Hu, CoS2 nanosheets on carbon cloth for flexible all-solid-state supercapacitors, Chemical Engineering Journal 400 (2020). https://doi.org/10.1016/j.cej.2020.125856.

[381] J. Ning, T. Zhang, Y. He, C. Jia, P. Saha, Q. Cheng, Co3O4@CoS core-shell nanosheets on carbon cloth for high performance supercapacitor electrodes, Materials 10 (2017).

https://doi.org/10.3390/ma10060608.

[382] S. Ding, X. Li, X. Jiang, Q. Hu, Y. Yan, Q. Zheng, D. Lin, Core-shell nanostructured ZnO@CoS arrays as advanced electrode materials for high-performance supercapacitors, Electrochim Acta 354 (2020). https://doi.org/10.1016/j.electacta.2020.136711.

[383] W.D. Wang, X.F. Li, P.P. Zhang, B.Q. Wang, S.H. Gong, X.C. Wang, F. Liu, J.P. Cheng, Preparation of NiCo2O4@CoS heterojunction composite as electrodes for high-performance supercapacitors, Journal of Electroanalytical Chemistry 891 (2021). https://doi.org/10.1016/j.jelechem.2021.115257.

[384] K. Wu, W. Wang, X. Guo, C. Wang, Q. Han, Y. Yang, Facile and fast template-free synthesis of octahedron and hollow sphere CoS2 by microwave-assisted hydrothermal method, Results Phys 7 (2017) 1683–1688. https://doi.org/10.1016/j.rinp.2017.05.004.

[385] P. Wei, H. Xie, X. Zhu, R. Zhao, L. Ji, X. Tong, Y. Luo, G. Cui, Z. Wang, X. Sun, CoS2 Nanoparticles-Embedded N-Doped Carbon Nanobox Derived from ZIF-67 for Electrocatalytic N2-to-NH3 Fixation under Ambient Conditions, ACS Sustain Chem Eng 8 (2020) 29–33. https://doi.org/10.1021/acssuschemeng.9b06272.

[386] X. Hu, P. Tan, R. Dong, M. Jiang, L. Lu, Y. Wang, H. Liu, Y. Liu, J. Xie, J. Pan, A Novel Metal–Organic Framework Intermediated Synthesis of Heterogeneous CoS2/CoS Porous Nanosheets for Enhanced Oxygen Evolution Reaction, Energy Technology 9 (2021). https://doi.org/10.1002/ente.202000961.

[387] J. Song, C. Zhang, J. Zhang, H. Zhou, L. Chen, L. Bian, A. Yuan, Construction of CoS2-N-C sheets anchored on 3D graphene network for lithium storage performances, Journal of Nanoparticle Research 21 (2019). https://doi.org/10.1007/s11051-019-4522-5.

[388] S. Liu, D. Gao, J. Li, K.S. Hui, Y. Yin, K.N. Hui, S. Chan Jun, Phosphorus dual-site driven CoS2@S, N co-doped porous carbon nanosheets for flexible quasi-solid-state supercapacitors, J Mater Chem A Mater 7 (2019) 26618–26630. https://doi.org/10.1039/c9ta09646a.

[389] M. Iqbal, N.G. Saykar, A. Arya, I. Banerjee, P.S. Alegaonkar, S.K. Mahapatra, High-performance supercapacitor based on MoS2@TiO2 composite for wide range temperature application, J Alloys Compd 883 (2021). https://doi.org/10.1016/j.jallcom.2021.160705.

[390] Q. Hu, M. Tang, M. He, N. Jiang, C. Xu, D. Lin, Q. Zheng, Core-shell MnO2@CoS nanosheets with oxygen vacancies for high-performance supercapattery, J Power Sources 446 (2020). https://doi.org/10.1016/j.jpowsour.2019.227335.

[391] S. Zhai, K. Jin, M. Zhou, Z. Fan, H. Zhao, X. Li, Y. Zhao, F. Ge, Z. Cai, A novel high performance flexible supercapacitor based on porous carbonized cotton/ZnO nanoparticle/CuS micro-sphere, Colloids Surf A Physicochem Eng Asp 584 (2020). https://doi.org/10.1016/j.colsurfa.2019.124025.

[392] S. Zhai, K. Jin, M. Zhou, Z. Fan, H. Zhao, X. Li, Y. Zhao, F. Ge, Z. Cai, A novel high performance flexible supercapacitor based on porous carbonized cotton/ZnO nanoparticle/CuS micro-sphere, Colloids Surf A Physicochem Eng Asp 584 (2020). https://doi.org/10.1016/j.colsurfa.2019.124025.

[393] N.M. Farag, M.A. Deyab, A.M. El-Naggar, A.M. Aldhafiri, M.B. Mohamed, Z.K. Heiba, Exploring the functional properties of CuCo2O4/CuS nanocomposite as improved material for supercapacitor electrode, Journal of Materials Research and Technology 10 (2021) 1415–1426. https://doi.org/10.1016/j.jmrt.2020.12.083.

[394] Y. Ma, J. Hao, H. Liu, W. Shi, J. Lian, Facile synthesis clusters of sheet-like Ni3S4/CuS nanohybrids with ultrahigh supercapacitor performance, J Solid State Chem 282 (2020). https://doi.org/10.1016/j.jssc.2019.121088.

[395] W. Zhou, J. Miao, X. Yan, Y. Li, Y. Zhu, W. Zhang, M. Zhang, W. Zhu, M.S. Javed, J. Pan, S. Hussain, Boosted electrochemical performance of CuS anchored on carbon cloth as an integrated electrode for quasi-solid-state flexible supercapacitor, Journal of Electroanalytical Chemistry 897 (2021). https://doi.org/10.1016/j.jelechem.2021.115610.

[396] H.W. Lee, N.M. Shinde, P. V. Shinde, J.M. Yun, P.K. Song, K.H. Kim, High energy and power density of self-grown CuS@Cu2O core-shell supercapattery positrode, Journal of Solid State Electrochemistry 23 (2019) 2609–2617. https://doi.org/10.1007/s10008-019-04351-0.

[397] J. Zhang, Y. Zhao, Y. Zhang, J. Li, M.R. Babaa, N. Liu, Z. Bakenov, Synthesis of microflower-like vacancy defective copper sulfide/reduced graphene oxide composites for highly efficient lithium-ion batteries, Nanotechnology 31 (2020). https://doi.org/10.1088/1361-6528/ab57f6.

[398] D. Zhang, Y. Jin, Y. Cao, Facile synthesis and ammonia gas sensing properties of NiO nanoparticles decorated MoS2 nanosheets heterostructure, Journal of Materials Science: Materials in Electronics 30 (2019) 573–581. https://doi.org/10.1007/s10854-018-0323-3

[399] S. Sheokand, P. Kumar, S. Sharma, K.S. Samra, Augmented electrochemical capacities

of microporous MoS2@NiO heterostructures, Electrochim Acta 497 (2024) 144521. https://doi.org/10.1016/j.electacta.2024.144521.

List of Publications

1. S. Sheokand, P. Kumar, S. Jabeen, K.S. Samra, 3D highly porous microspherical morphology of NiO nanoparticles for supercapacitor application, J. Solid State Electrochem 27 (2023) 727–738. https://doi.org/10.1007/s10008-022-05366-w.
2. S. Sheokand, P. Kumar, S. Sharma, K.S. Samra, Augmented electrochemical capacities of microporous MoS2@NiO heterostructures, Electrochim Acta 497 (2024) 144521. https://doi.org/10.1016/j.electacta.2024.144521.
3. S. Sheokand, P. Kumar, S. Sharma, K.S. Samra, High efficiency CoS_2@NiO heterostructures: Synthesis, characterization, and electrochemical performance, J Energy Storage 114 (2025) 115771. https://doi.org/10.1016/j.est.2025.115771.
4. S. Sheokand, P. Kumar, K.S. Samra, Optimization of CuS@NiO nanocomposite for enhanced charge storage in supercapacitors, J Appl Electrochem 55 (2025) 1765–1778. https://doi.org/10.1007/s10800-025-02267-4.

Other Publications

1. S. Jabeen, P. Kumar, S. Sheokand, K.S. Samra, Mesoporous Ni doped MnMoO4 nanoparticles for high performance asymmetric supercapacitors, J Energy Storage 93 (2024) 112464. https://doi.org/10.1016/j.est.2024.112464.